Synthesis and Characterization of Spin-Chain Compounds of the $AM_2V_2O_8$ Type

I n a u g u r a l - D i s s e r t a t i o n

zur

Erlangung des Doktorgrades
der Mathematisch-Naturwissenschaftlichen Fakultät
der Universität zu Köln

vorgelegt von

Sandra Niesen

aus Köln

Köln 2015

Berichterstatter:	Priv.-Doz. Dr. Thomas Lorenz
	Prof. Dr. Markus Braden
Vorsitzender der Prüfungskomission:	Prof. Dr. Ladislav Bohatý
Tag der mündlichen Prüfung:	13. Januar 2015

die sonne rutscht vom dach
mit ihrem nackten arsch
voll roter striemen und

ich schlafe bis auf weiteres
auf der tenne des waldes
mit einem in der krone

Raoul Schrott [1]

Contents

1 Introduction

The physics of low-dimensional spin-systems is strongly driven by quantum fluctuations and reveals anomalous ground-state properties with prospect of quantum-critical behavior as well as unusual excitations. For a long time the field of low-dimensional magnetism was a purely theoretical one with a wide variety of theoretical techniques developing [2]. Up to now the research on low-dimensional magnets is a field of discoveries and new phenomena and is an exemplary field of solid state research, where theoretical approaches and experimental progress work hand in hand concerning the synthesis and analysis of corresponding crystals showing low-dimensional magnetism.

As a fingerprint of low-dimensional magnetism the Mermin Wagner theorem [3] predicts the absence of long-range (anti-)ferromagnetic order, which breaks a continuous symmetry, for one- and two-dimensional systems at finite temperature [4]. However, in real crystals competing energy scales and more complex coupling scenarios yield a plethora of interesting (ordering) phenomena. In the field of two-dimensional magnetism, planar arrangements of spins are in the focus of interest such as Skyrmions [5]. In this context, (geometric) spin frustration very often plays an eminent role and leads to interesting phenomena.

Various spin ladders, for example $(C_5H_{12}N)_2CuBr_4$ [6] or the $(Sr, Ca, La)_{14}Cu_{24}O_{41}$ compounds [7–9], are representatives of compounds to be put between one and two dimensions. The one-dimensional case holds a wide range of spin chains, which are a vivid research topic, like the first inorganic spin-Peierls system $CuGeO_3$ [10], due to diverse magnetic anisotropies and/or magnetic frustration resulting from competing interactions. Here, external parameters like pressure, magnetic field etc. not only yield significant changes of the excitation spectrum but also quantum phase transitions. Besides low-dimensionality and frustration, the reduction of the spin quantum number vitally increases the incidence of quantum fluctuations. Therefore, in the field of low-dimensional systems $S = 1/2$ (e.g. Cu^{2+}) and $S = 1$ (e.g. Ni^{2+}) materials are investigated, for example one of the first described $S = 1/2$ quantum spin chain $CuCl_2{\cdot}NC_5H_5$ [11] or the $S = 1$ Haldane chain $SrNi_2V_2O_8$ [12, 13].

As an application of one-dimensional magnetism one can think of cooling devices made from materials, where the heat transport is naturally anisotropic and that unidirectionally transport the heat away from the heat source. And of course, the understanding of the physics in one dimension might be transferred to the understanding of the field of, e.g., the 2-dimensional high-temperature cuprate superconductors [14] where spin fluctuations play an eminent role.

This thesis concerns a particularly interesting class of low-dimensional spin-chain systems which can be described by the general formula $AM_2V_2O_8$. These compounds belong to the quasi-one dimensional magnets and an outstanding feature of this compound class is, that it comprises many different magnetic phases, ranging from the effective spin-1/2 Ising chain (e.g. $BaCo_2V_2O_8$ [15, 16]), to the nearly isotropic spin-5/2 Heisenberg chain (e.g. $BaMn_2V_2O_8$ [17, 18]), and it even holds space to the synthesis of new compounds [19]. The $AM_2V_2O_8$ compounds have an alkaline earth metal ion on the A^{2+} site and a transition metal with partially filled 3d shell on the M^{2+} site and belong to the group of alkaline earth oxometallates. The magnetism is fully carried by the local moments of the transition metal since in these compounds the oxidation number of vanadium is 5+ and the vanadium is, thus, nonmagnetic. The MO_6 octahedra form screw chains running along the c axis separated by the vanadium and barium ions.

Only few low-dimensional compounds are known that realize a high spin of $S = 5/2$ like e.g. $BaMn_2O_3$ [20] or $CsMnCl_3 \cdot 2H_2O$ [21, 22]. The only recently synthesized compound $SrMn_2V_2O_8$ [19] and the related $BaMn_2V_2O_8$ are the isotropic Heisenberg versions of the $AM_2V_2O_8$ compounds. Here, the first single crystal investigations on these Heisenberg chains will be presented. Both compounds are canted antiferromagnets at low temperatures where the transition temperatures are of the order of 40 K [18, 19]. The influence of a magnetic field on T_N is investigated.

The main emphasis of this thesis, however, lies on the antiferromagnetic effective spin-1/2 Ising chain $BaCo_2V_2O_8$. The magnetic susceptibility is highly anisotropic and indicates one-dimensional spin-correlations. Below $T_N = 5.4$ K the system enters a Néel-ordered phase due to finite inter-chain coupling. Additionally and until recently undetected, the magnetic transition is accompanied by a structural transition from tetragonal to orthorhombic [23]. In the ordered phase, the antiferromagnetic spins are oriented along c, i.e. along the direction of the distorted CoO_6 octahedra which form screw chains. For magnetic fields applied along the magnetic easy axis, the Néel order is strongly suppressed already for low magnetic fields where the system enters an incommensurate phase [24]. Only few studies of $BaCo_2V_2O_8$ for other field directions were published so far. A detailed analysis of this topic is presented in this thesis. Actually, for fields perpendicular to the easy axis an additional anisotropy occurs [23]. Here, the field dependence of the transition temperature for fields along the tetragonal axes, i.e. $H \,||\, [1\,0\,0]$ ($H \,||\, [0\,1\,0]$), is quite different from that for the magnetic field rotated by 45°, i.e. for $H \,||\, [1\,1\,0]$. This in-plane anisotropy yields very different phase diagrams for the field directions $H \,||\, [1\,1\,0]$ and $H \,||\, [1\,0\,0]$.

Another aim of this thesis lies on the influence of several substitutions on the magnetic phase diagrams of $BaCo_2V_2O_8$. The structure of $BaCo_2V_2O_8$ suggests two kinds of substitutions. One is the substitution between the spin chains realized by the partial exchange of barium ions by strontium. $SrCo_2V_2O_8$ is a known, but poorly investigated compound. Moreover, despite the closeness to $BaCo_2V_2O_8$ a different magnetic structure was proposed for magnetic fields parallel and perpendicular to the c axis [25]. Partial and complete substitution of Ba by Sr can clarify the question whether $BaCo_2V_2O_8$ and $SrCo_2V_2O_8$ behave similar in magnetic field or not. Furthermore, this substitution introduces (structural) disorder into the system and may yield a tool to gradually change the relevant couplings within the system. Therefore, sam-

ples with three substitution levels (10 %, 50 % and 90 %) as well as pure $SrCo_2V_2O_8$ have been synthesized and characterized. The magnetic phase phase diagrams of the $Ba_{1-x}Sr_xCo_2V_2O_8$ series will be presented for different field directions.

The other kind of substitution directly manipulates the magnetic subsystem of $BaCo_2V_2O_8$, i.e. the CoO_6 screw chains. Four compounds, $BaCo_{1.9}Mn_{0.1}V_2O_8$, $BaCo_{1.9}Ni_{0.1}V_2O_8$, $BaCo_{1.9}Cu_{0.1}V_2O_8$ and $BaCo_{1.9}Mg_{0.1}V_2O_8$, have been investigated. Depending on the dopant M, a more or less pronounced segmentation of the spin chains may occur. For non-magnetic Mg, doping of non-magnetic impurities on the quasi-one dimensional antiferromagnetic spin chain plays a role as a model system for theoretical predictions concerning the influence of impurities on the magnetism of low-dimensional magnets [26, 27].

This thesis is structured as follows. Chapter 2 gives an introduction to some general concepts of low-dimensional spin systems and quantum critical behavior. This is followed by an overview of the diffraction techniques and experimental setups that were employed to measure the thermodynamic properties. Also, the class of compounds with the general formula $AM_2V_2O_8$ will be introduced in more detail and embedded in the theoretical background. Chapter 3 deals with the topic of single crystal preparation by the floating-zone method in a mirror furnace in general and more specific for the compounds that were grown in the scope of this thesis. The following chapters deal with the experimental results. The two nearly isotropic spin-5/2 Heisenberg systems $BaMn_2V_2O_8$ and $SrMn_2V_2O_8$ are presented in Chapter 4, followed by a study of the spin-1/2 Ising chain $BaCo_2V_2O_8$ in Chapter 5. The influence of the different types of substitutions, represented by the $Ba_{1-x}Sr_xCo_2V_2O_8$ and $BaCo_{1.9}M_{0.1}V_2O_8$ series, is the topic of Chapter 6. A summary of this work is followed by the appendices where further growth processes and measurements which exceed the main part of this work are presented.

2 Theory and Experiment

2.1 Low-dimensional Spin Systems

A lot of theoretical and experimental effort has been put into the field of low-dimensional magnetism in the last decades. The physics in three-dimensionally coupled systems is completely different from those in two- or one-dimensional ones. The Mermin Wagner theorem [3] predicts the absence of long-range order in low-dimensional systems with a continuous, isotropic symmetry above zero temperature [4]. Here, strong spin fluctuations, which occur without any energy loss, release the entropy of the system when the temperature is reduced, resulting in the destruction of long-range order. Only if significant anisotropies are present, a rotation of the spins costs energy and a long-range order is stabilized. Especially in low-dimensional spin systems the interplay of competing interactions within more complex coupling scenarios yields a variety of interesting (ordering) phenomena. In real crystals at one point always a long-range order sets in where other coupling energies (e.g. inter-chain coupling) become relevant. As a typical fingerprint of low dimensionality, for example, the magnetic susceptibility shows a broad maximum at a temperature that is of the order of the relevant short-range magnetic correlations.

In a low-dimensional spin system, localized moments couple via an exchange energy J along only one preferred direction. One of the most established models to describe such systems is the isotropic Heisenberg model where an electron system in a crystal field is reduced to an effective, direct exchange between pairs of spins, i.e.

$$\mathcal{H}_H = \sum_{\langle i,j \rangle} J \mathbf{S}_i \mathbf{S}_j, \tag{2.1}$$

where J is the exchange coupling and $\mathbf{S}_i$, $\mathbf{S}_j$ are the spins at sites i and j. Often the summation can be reduced to nearest (NN) or next nearest neighbors (NNN). This model is widely examined, but still of ongoing interest. If spin-orbit coupling is coming into play the spins are no longer isotropic and diverse anisotropies develop. One of the models describing an anisotropic spin chain with NN interaction is the XXZ model

$$\mathcal{H}_{XXZ} = \sum_i J \left\{ S_i^z S_{i+1}^z + \epsilon \left(S_i^x S_{i+1}^x + S_i^y S_{i+1}^y \right) \right\} + g \mu_\mathrm{B} \mathbf{H} \cdot \mathbf{S}_i, \tag{2.2}$$

with the anisotropy factor ϵ, the g factor, the Bohr magneton μ_B and $\mathbf{H}$ the external

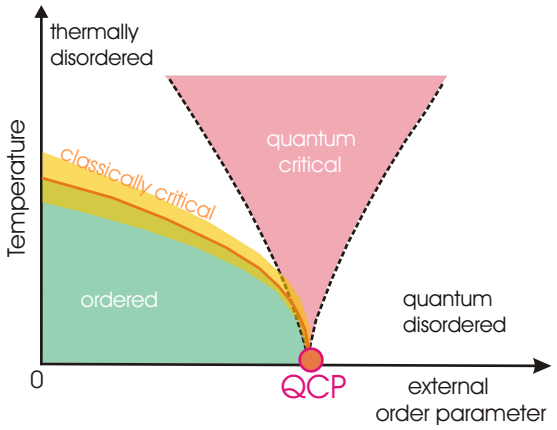

Figure 2.1: Schematic phase diagram of a quantum critical system. The green area gives the region of classical order which can be classically broken by thermal fluctuations. Depending on an external order parameter strong quantum fluctuations are enhanced giving rise to a quantum critical cone (pink). Also, the enhanced quantum fluctuations lead to a quantum disordered state at $T = 0$.

magnetic field. In principle three main cases are distinguished to categorize a spin system by their anisotropy factor ϵ. For $\epsilon = 1$ one gets back to the isotropic Heisenberg case. For $\epsilon >> 1$, the XY case is reached with a spin coupling mainly within a plane. In the other direction, i.e. for $\epsilon = 0$, an Ising system is realized where the spins are coupled only along z. An even more complex model taking the characteristics of $BaCo_2V_2O_8$ into account is presented in Section 5.4.2. The topic of low-dimensional spin systems is described in detail,e.g. in Refs. 2, 28–30.

Quantum Criticality

All systems discussed above are mostly investigated for an external magnetic field applied along z. Due to the conserved rotational symmetry around z, this case is more easily modeled than the case of an application perpendicular to z where the field breaks the rotational symmetry, which gives rise to potential quantum phase transitions and exotic ground states. Some popular one-dimensional spin-chain systems showing quantum criticality are $LiHoF_4$ [31] and $CoNb_2O_6$ [32, 33] which are text-book examples for the Ising model in a transverse field. Classically a phase transition is driven by thermal fluctuations. Quantum fluctuations result from Heisenberg's uncertainty principle and are of the energetic order $\hbar\omega$. In principle, quantum fluctuations are present in all phase transitions, but for $T > 0\,\mathrm{K}$ they are negligible compared to thermal fluctuations ($E \approx k_\mathrm{B}T$). A quantum phase transition is a non-thermally driven transition of the quantum-mechanical ground state due to a symmetry-breaking external parameter, e.g. the magnetic field or pressure, which can induce quantum fluctuations and drive the system through a quantum critical point (QCP). At the quantum critical point a phase transition occurs at $T = 0\,\mathrm{K}$. In the region of such a QCP, quantum fluctuations can dominate the physical properties also at finite temperatures represented by a quantum critical cone in Figure 2.1. Magnetic insulators are a class of systems that can be treated conceptually comparatively easy and in particular theoretical predictions can be made for effectively one-dimensional systems. The influence of quantum fluctuations increases with decreasing spin number, with decreasing dimensionality and in the presence of increasing frustration. Thus, a quantitative comparison between theory and experiment is possible and a field of vivid research in the field of low-dimensional spin systems has evolved [34, 35]. Comprehensive literature can be found, e.g. in Refs. 36, 37.

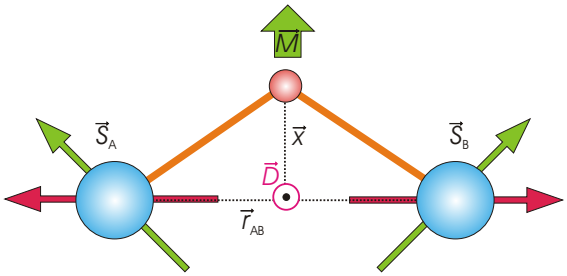

Figure 2.2: Two antiferromagnetic spins (pink arrows) coupled via an oxygen (red) are canting due to Dzyaloshinskii-Moriya interaction (green arrows) in a plane perpendicular to the Dzyaloshinskii-Moriya vector $\vec{D}$, resulting in a weak ferromagnetic net-magnetization.

Dzyaloshinskii-Moriya interaction

Dzyaloshinskii-Moriya interactions are discussed in literature for some of the $AM_2V_2O_8$ compounds. They occur as a correction due to the spin-orbit interaction. Two spins $\mathbf{S}_\mathrm{A}$ and $\mathbf{S}_\mathrm{B}$ (Fig. 2.2, pink arrows) are indirectly coupled via an oxygen (red). The spin-orbit interaction can produce an excited state in one of the magnetic ions such that there is an exchange interaction between the excited state of one ion and the ground state of the second ion. This antisymmetric exchange interaction is also known as Dzyaloshinskii-Moriya interaction and the according Hamiltonian is given as

$$\mathcal{H}_\mathrm{DM} = \mathbf{D}(\mathbf{S}_\mathrm{A} \times \mathbf{S}_\mathrm{B}), \tag{2.3}$$

with the Dzyaloshinskii-Moriya vector $\mathbf{D} \propto \mathbf{x} \times \mathbf{r}_\mathrm{AB}$, where $\mathbf{r}_\mathrm{AB}$ is the connecting vector between the spins and $\mathbf{x}$ is the displacement of the ligand, i.e. the oxygen. $\mathbf{D}$ only vanishes if the crystal field has an inversion symmetry with respect to the center of the inter-spin distance $\mathbf{r}_{AB}$. The Dzyaloshinskii-Moriya interaction favors a perpendicular spin alignment in a plane perpendicular to $\mathbf{D}$. This may result in a slight canting of the spins. In an antiferromagnet this small canting perpendicular to the spin-axis yields a weak ferromagnetic net-magnetization.

2.2 Diffraction Techniques

Structure determination by diffraction techniques can be carried out on solids with periodical formation of the atoms, i.e. on single crystals. The typical microscopic structures are of the order of Å and for the resolution of those structures radiation with a wave length of the same order is needed. In case of X-ray diffraction the typical energy is given by some keV and provides, thus, a suitable wave length.

Two equivalent descriptions of diffraction processes on a single crystal are given by the Bragg description and the von Laue description. The commonly known Bragg law $2 \cdot d_{hkl} \cdot \sin\theta = n \cdot \lambda$ describes constructive interference when the optical retardation given by the scattering angle θ and the distance d_{hkl} equals an even number of the wavelength of the incident beam. The von Laue condition equivalently describes constructive interference under the condition that the change in the wave vector $\Delta\mathbf{k} = \mathbf{k}^{initial} - \mathbf{k}^{final}$ has to be equal to a reciprocal lattice vector $\mathbf{G}$, that means $\Delta\mathbf{k} = \mathbf{G}$. $\mathbf{G}$ can be written in a basis of primitive lattice vectors of the reciprocal lattice,i.e. $\mathbf{G} = v_1\mathbf{b}_1 + v_2\mathbf{b}_2 + v_3\mathbf{b}_3$. Thus, applying the scalar product between $\Delta\mathbf{k}$,

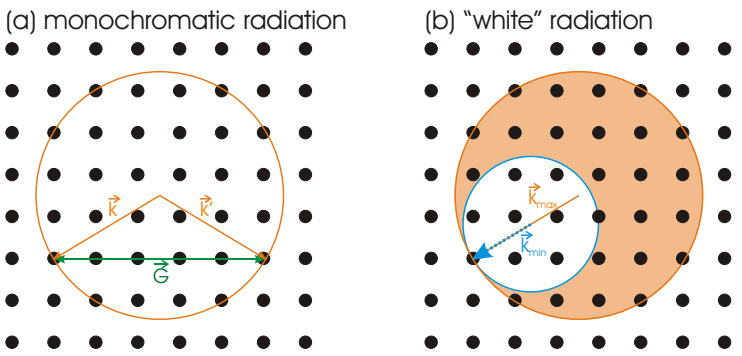

Figure 2.3: Ewald construction for monochromatic radiation (a) and for "white" radiation (b) as used for the Laue camera.

$\mathbf{G}$ and the primitive lattice vectors $\mathbf{a}_i$ leads to

$$\mathbf{a}_i \cdot \Delta\mathbf{k} = 2\pi v_i, \quad i = 1, 2, 3. \tag{2.4}$$

This can be interpreted geometrically. The equation $\mathbf{a}_1 \cdot \Delta\mathbf{k} = 2\pi v_1$ means that the vector $\Delta\mathbf{k}$ must be located on the surface of a cone around the direction $\mathbf{a}_1$. Since all of the three equations have to be fulfilled simultaneously, $\Delta\mathbf{k}$ must lie on the intersection of three cones which is a very rigid condition. Figure 2.3 illustrates the fulfillment of the Laue condition through the Ewald construction in the two dimensional case for (a) monochromatic radiation and (b) for white radiation. In case of monochromatic radiation, constructive interference is obtained from only those reciprocal lattice vectors that lie on a circle with radius $\Delta\mathbf{k}$ while for white radiation all lattice points that are located in the space between the Ewald spheres with $\mathbf{k}_{min}$ and $\mathbf{k}_{max}$ fulfill the von Laue condition.

EDX

Energy Dispersive X-ray analysis (EDX) allows the determination of a sample's chemical composition. Usually, this technique is performed within a scanning electron microscope (SEM) where the primary electrons are accelerated and focused onto small spots on the sample surface. Depending on the energy and the absorption properties of the sample the electrons penetrate by a few μm and either scatter elastically or (partially) deposit their energy by inelastic scattering. The created hole is then filled again by a higher-energy electron accompanied by the emission of X-ray radiation with an energy characteristic for the element. Depending on the shells of the hole and the higher-energy electron, different transitions (typically called $K_\alpha, K_\beta, L_\alpha$..) are triggered. In EDX, the focus lies on the quantitative analysis of the element-specific X-ray radiation emitted from the sample. The energy-resolved intensities are counted and the obtained spectrum is compared to standards via a sophisticated modeling. In an ideal setup one can distinguish sample compositions down to $\sim 0.1\%$. However, several factors influence the reliability of the technique. First, non-conductive samples like the ones investigated in this thesis have to be coated with a conductive material to prevent surface charge accumulation. A side-effect of this coating is, however, that (depending on the coating material) the radiation emitted by the sample is partially absorbed by the coating. This effect drastically increases for the light elements and

the uncertainty of the coating thickness enters the sample's composition error in multiples. Thus, the determination of the oxygen content of a sample is very difficult, whereas heavier elements can be determined very well. Further errors are introduced by imperfectness of the sample, e.g. surface roughness or geometric effects.

Due to the high spatial resolution of the SEM, the sample composition can be mapped very precisely for different positions on the sample. Therefore, measurements were typically performed at about ten different position in order to identify possible grains of impurities. All samples were prepared on an aluminum sample holder covered with a two-sided conductive tape. Measurements have been performed by the technician I. Simons and B.Sc. P. Warzanowski, who introduced several optimizations to the microscope and to the EDX [38].

Laue Camera

In the Laue camera white X-ray radiation with $\frac{2\pi}{k_{max}} = \lambda_{min} \leq \lambda \leq \lambda_{max} = \frac{2\pi}{k_{min}}$ (Wolfram source) is used. The Laue camera is used to verify the crystallinity of a sample and for the orientation of crystals for cutting. Here, the setup is aligned in a reflection mode which means that the sample is mounted in a defined distance in front of a detector plate and the incoming beam. The resulting picture is a snapshot of the reciprocal space and specific for the symmetry, the lattice constants and the orientation of the crystal. Exemplary patterns of the three most interesting crystal planes of $BaCo_2V_2O_8$ namely (1 0 0), (1 1 0), and (0 0 1) are shown in Figure 2.4. To check the crystallinity of a sample several pictures at different spots of a plane surface are taken. If all of them are equal one can conclude that this surface is most probably one domain. The opposite surface should show the same picture under π rotation around the horizontal or vertical axis. If both surfaces are of good quality and the patterns of both sides are equivalent the whole sample can be called single crystalline.

The program Clip [39] is used for indexation of the reflections and for calculation of the necessary rotations for the orientation in a certain direction. The sample has to be tilted and rotated until the wanted reflection is in the middle of the picture. Usually, the sample is mounted on a goniometer and is first fixed only by some modeling clay until the rough orientation is done. The goniometer has a horizontal angular range of 30° and vertically 15° only. When orientation is completed the sample is fixed by aceton-soluble glue (UHU hart). This glue is completely hard after drying (min. 3 hours) so that the sample will not move under physical treatment. The sample is cut in the inside hole saw perpendicular to the pictured surface. After cutting the glue can easily be removed in acetone, given that the sample does not react with the glue or the solvent used for cooling the saw.

X-ray Powder Diffraction

In powder X-ray diffraction (PXRD) a single wavelength is used in combination with a powder sample which provides a statistic distribution of crystallites that fulfill the scattering condition. With help of the PXRD the material can be tested with respect to its composition and phase purity.

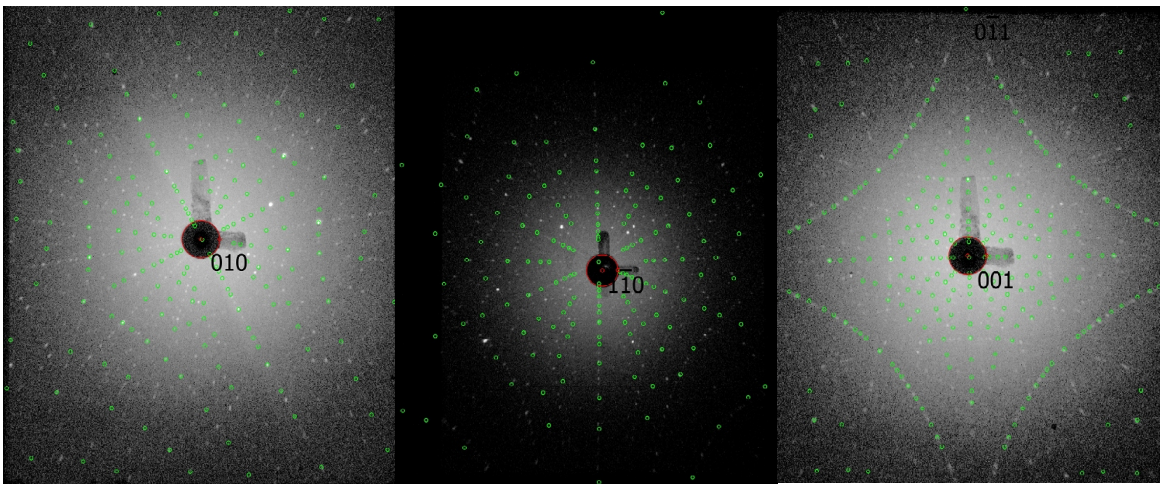

Figure 2.4: Laue pictures of $BaCo_2V_2O_8$ for the lattice directions [0 1 0], [1 1 0], and [0 0 1]. The left and the right picture show an orientation with less than 0.3° deviation while the intensity of the [1 1 0] direction shows some deviation of about 1°. The dark area in the middle is the direction of the incident beam where the plate is covered by a copper beam collimator. The "L" shaped marks are marks of conductive silver varnish on the photo plate to keep track of the orientation of the photo plate.

D5000

Polycrystalline samples, i.e. powders of single crystals, were investigated on a two-circle diffractometer in order to refine the lattice parameters. Two diffractometers are available in the Institute, the so called *D5000* and the *Praktikums-D5000*. Most X-ray diffractograms have been measured with the first setup. Here, one can choose between a chrome anode ($k_{\alpha1}$: $\lambda_1 = 2.289726$ Å, $k_{\alpha2}$: $\lambda_2 = 2.293651$ Å) and a copper anode ($k_{\alpha1}$: $\lambda_1 = 1.5405929$ Å, $k_{\alpha2}$: $\lambda_2 = 1.5444274$Å) [40], with a zirconium filter to exclude k_β radiation. The advantage of using a chrome anode is a higher resolution but a decreased 2θ range and intensity, and vice versa for the copper source. Therefore, depending on the 2θ range (Cu: $12° < 2\theta < 120°$) and the resolution one is interested in, the X-ray source is chosen. Only the room temperature setup was used within this work, but setups for low- and high-temperature measurements do exist. The obtained diffractograms can either be compared to literature data (e.g. the online data base ICSD [41]) of the existing compound or in case of a new compound to a similar one which has the expected symmetry. A refinement of lattice constants and other parameters was done with FULLPROF [42] using a pseudo-Voigt model. In Section 3.3, the powder patterns were subtracted by the (refined) background. The measured intensity, the calculated intensity and the difference between both were normalized to the maximum intensity of the measured pattern.

For the D5000 the sample is prepared on a microscope object glass. Only a small amount of powder is necessary and has to be ground very carefully to prevent from a non-statistic distribution of all crystal orientations. The powder is prepared with diffilene oil (which brings some underground) or way better with acetone on the glass plate.

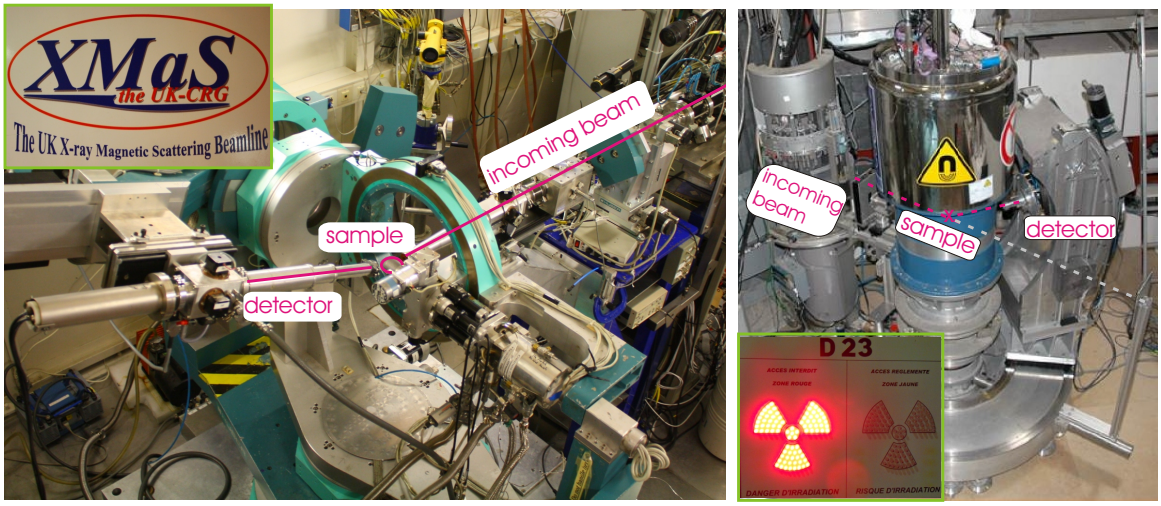

Figure 2.5: Pictures of the XMaS beamline at ESRF (left) and the D23 facility at ILL (right), both located in Grenoble (France).

ID22

ID22 is a high-resolution powder diffraction beamline at the European Synchrotron Radiation Facility (ESRF) in Grenoble, France and operates in an energy range of 6 -80 keV. The beamline is located at an undulator and equipped with a diffractometer that makes use of the spinning-capillary technique which reduces preferred orientation effects. The facility is equipped with a Si_{111} monochromator and a bank of 9 detectors operating parallel and preceded by Si_{111} analyzer crystals [43].

Single Crystal X-ray Diffraction at XMaS

For single crystal X-ray diffraction (SCXRD), single crystalline samples and a monochromatic radiation are used, which means that crystal and detector have to be brought exactly into position in three dimensions in order to observe a distinct reflection.

The UK-CRG X-ray Magnetic Scattering (XMaS) beamline is located at the bending magnet BM28 at the ESRF and provides an 11-axis Huber diffractometer. The facility is equipped for high-resolution (wide-angle) and magnetic single-crystal diffraction and a cryostat where 2 K is the base temperature [44, 45]. In order to access high-Q reflections the focused monochromatic radiation was set to 14 keV, thus a wavelength of $\lambda = 0.886$ Å was used for the experiment. In principle also a 1 T electromagnet or a 4 T superconducting magnet can be used in this facility but were not used in our experiment. The left panel of Figure 2.5 shows the XMaS diffractometer.

Neutron Diffraction at D23

Magnetic neutron scattering makes use of the fact that neutrons are scattered by the nuclei as well as by magnetic structures. Thus, always a superposition of both types of scattering is observed. In the case of elastic neutron scattering, i.e. without energy

transfer, incoming and outcoming beam are of the same absolute value and $k_i = k_f$. The scattering vector $\mathbf{Q}$ is defined by $\mathbf{k}_i + \mathbf{Q} = \mathbf{k}_f$. The scattered intensity I is proportional to the square of the scattering amplitude A, i.e.

$$I(\mathbf{Q}) \propto |A(\mathbf{Q})|^2 = \left| \sum_{\mathbf{G}} n_{\mathbf{G}} \int e^{i(\mathbf{G}-\mathbf{Q})\cdot\mathbf{r}} \mathrm{d}V \right|^2 , \tag{2.5}$$

where $\mathbf{G}$ is the reciprocal lattice vector and $n_{\mathbf{G}}$ are the Fourier components of the scattering density $n(\mathbf{r})$. The scattering condition $\mathbf{Q} = \mathbf{G}$ is analog to Bragg's law. For a sample with a certain volume V_Z and N unit cells we find

$$I(\mathbf{Q}) \propto |A(\mathbf{Q})|^2 = \left| N \int_{V_Z} n(\mathbf{r}) e^{i\mathbf{Q}\cdot\mathbf{r}} \mathrm{d}V \right|^2 = N \left| F(\mathbf{G}) \right|^2 . \tag{2.6}$$

For neutron scattering the atom form factor is $F(\mathbf{G}) = \sum_j b_j e^{i\mathbf{Q}\cdot\mathbf{r}}$, where b_j is the scattering length, which is the Fourier transform of the nuclear distribution and of the magnetic structure within a unit cell. Detailed descriptions of the field of neutron scattering are found, e.g. in Refs. 46–48.

D23 is a CEA-CRG single crystal thermal neutron diffractometer at the Institut Laue Langevin (ILL) in Grenoble, France. Due to its high flux (3.6×10^6 n/cm^2/s) and its good signal-to-noise ratio, the diffractometer is used for the determination of magnetic structures and maps of magnetic densities. Magnetic phase diagrams can be investigated by means of high magnetic fields, high pressures and low temperatures.

A picture of the instrument is shown in the right panel of Figure 2.5. The neutron beam goes through the first monochromator which defines the wavelength. The incident wavelength is 1-3 Å for unpolarized neutrons ($\lambda \approx 1.3$Å for Cu_{200} [49]) and 1.2 -2.4 Å for polarized neutrons. After the second, Heusler monochromator the beam hits the sample and the reflections are measured at the detector. The sample position can be slightly corrected within the xy plane but not along z. The cryostat, i.e. the sample, can be rotated around the angle γ (in xy plane) with a range of $-124° < \gamma < 127°$. The detector can be rotated in the angles ω (in xy plane) and ν (in z direction) with angular ranges of $-184° < \omega < 184°$ and $-28° < \nu < 29°$ [49]. Not the whole angular range can be used due to the pillars of the magnet.

The great advantage of this diffractometer is the additional sample environments that can be attached. Here, a 12 T split coil magnet was used within a dilution insert that is put inside a VTI (Variable Temperature Insert) to reach base temperatures of about 40 mK. Therefore, D23 was very suitable to study $BaCo_2V_2O_8$ at low temperatures and high magnetic fields. Two proposals on D23 (No. 5-41-706 and No. 5-41-757) for the investigation of $BaCo_2V_2O_8$ in transverse magnetic fields have been approved. The results of those beam times are presented in Section 5.4.2.

The sample had to be mounted on the sample holder with an orientation of the a axis parallel to the field direction. Since it was necessary to reach magnetic fields above 10 T combined with very low temperatures of about 50 mK the sample had to fit into the dilution insert. A schematic picture of the insert is given in Figure 2.6. The

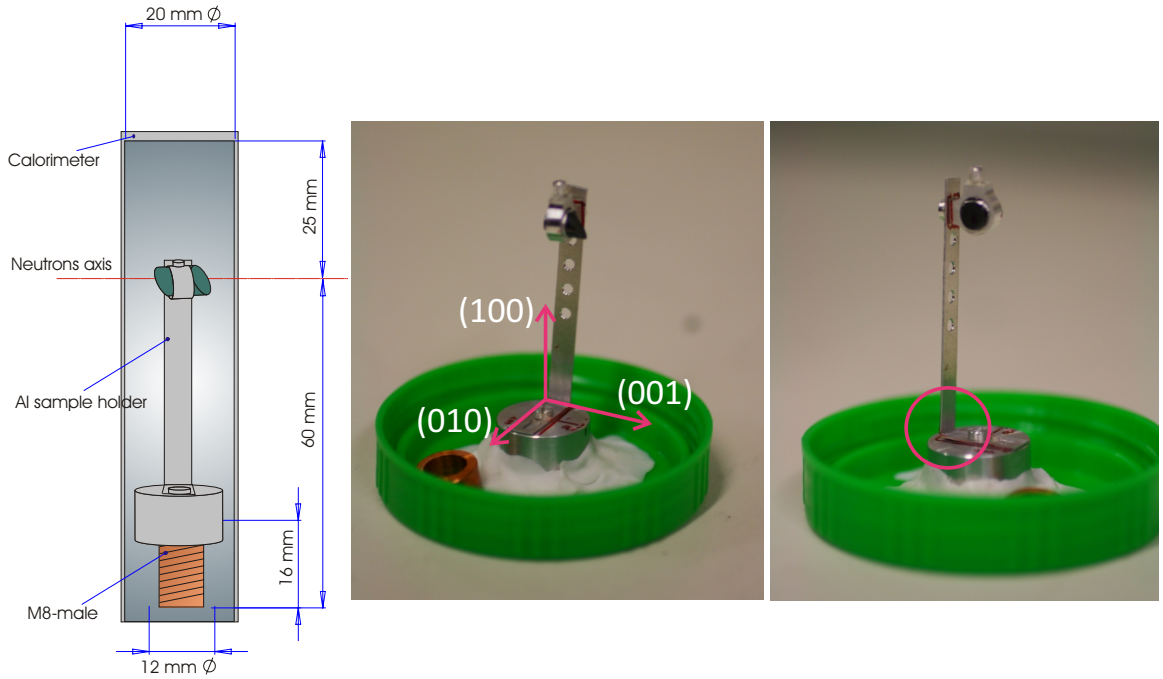

Figure 2.6: The left sketch shows the sample mounting and corresponding dimensions in the dilution insert. The photos show sample SN0133 of $BaCo_2V_2O_8$ prepared for single crystal neutron diffraction on D23 (pictured after the first beamtime). The arrows give the orientation of the sample with respect to the sample holder. After the first beamtime the sample holder was tilted out of the a axis (see circle right picture).

maximum diameter of the sample holder is 12 mm to be put on a male pin with M8 thread. A sample holder made of copper is recommended for better thermal coupling competing with aluminum which is invisible for the neutrons and enhances the signal to noise ratio.

The sample was mounted on an aluminum holder, as shown in Figure 2.6, which consists of an aluminum cylinder of 12 mm diameter and 10 mm height. Here, the sample was pressed into the aluminum ring that was fixed at the pin. The orientation must be done by hand and eye and the sample needs to be fixed well to prevent it from moving out of the orientation due to transportation or the measurement itself. Here the sample was fixed with a screw in the ring and some glue points of UHU hart were added to fix the screws as well. The pictures have been taken before the sample was inserted for the second beamtime. The red arrows give the orientation of the sample. The orientation suffered maybe due to the extracting procedure of the first time or because of the magnetic moment induced during the measurements. The wave length were $\lambda = 1.2765$ Å and $\lambda = 1.279$ Å for the first and second beamtime, respectively. Due to activation of the cobalt, the sample had to be stored at ILL. The storage number is 2981. The estimated storage time for a pure cobalt sample of about 5 cm^3 for an exposition to a neutron beam for one day is about 24 years in comparison to e.g. barium with less than 150 hours. The prompt activation after 2 minutes of exposure is $1.9 \cdot 10^6$ Bq/g (Ba: $< 2.9 \cdot 10^3$ Bq/g) [47].

2.3 Thermodynamic Properties

The Gibbs free energy G is given by a Legendre transformation of the inner energy U of a system. The natural variables of G are the temperature T, pressure p and the magnetic field H,

$$G(N,T,p,H) = U - TS + pV - HM, \quad \text{with} \quad \mathrm{d}G = -S\mathrm{d}T + V\mathrm{d}p + \mu\mathrm{d}N, \tag{2.7}$$

where S is the entropy, V the volume and M the magnetization of the system. A characteristic of a first-order phase transition is a discontinuity in at least one of the first derivatives of those quantities. In case of a second-order phase transition the quantities S, V and M are continuous while at least one of the second derivatives shows a discontinuity. The thermodynamic properties that can be derived experimentally are, e.g.,the magnetic susceptibility χ, the heat capacity c or the thermal expansion coefficient α discussed below.

Magnetization

The magnetic susceptibility χ is given by

$$\chi = \left(\frac{\partial M}{\partial H}\right)_T = -\frac{1}{V}\left(\frac{\partial^2 G}{\partial H^2}\right)_T. \tag{2.8}$$

The measurement of the magnetization is the very basic measurement technique when dealing with magnetic materials. The magnetization $\vec{M}$ is the macroscopic net magnetic moment of a sample with respect to the sample volume $\vec{M} = \frac{N}{V}\vec{m}$, i.e. it expresses the density of permanent or induced magnetic dipole moments in the material. The origin of the magnetic moment on an atom is attributed to the total angular momentum $\vec{J} = \vec{L} + \vec{S}$, which is the sum of the spin angular momentum $\vec{S}$ of the electrons and the orbital angular momentum $\vec{L}$.

The relation between the magnetization and the external magnetic field in a simple paramagnet is given as $\vec{M} = \chi\vec{H}$ where χ is the volume magnetic susceptibility which reflects the response of a magnetic material to a magnetic field. A diamagnet contains no unpaired electrons and the effect of an applied magnetic field is an induced magnetic moment which opposes the external field. A paramagnet contains unpaired electrons and, thus, a finite magnetic moment which are without an outer field randomly directed. Applying a magnetic field yields a field induced magnetization which aligns parallel with the field depending on the strength of the field. This picture becomes quite more colorful if interactions between magnetic ions or magnetic ions within a crystal field are of importance and long-range ordering of the moments becomes possible.

In the II. Department of Physics, three different setups for measuring the magnetization are available- a Quantum Design (QD) MPMS, a QD PPMS with a VSM and a homebuilt magnetometer. The method of measuring the magnetic moment is different for each setup. The MPMS setup is based on on a superconducting quantum inter-

ference device (SQUID) and measures the magnetic response of the sample indirectly but with very high resolution. Here, the sample is moved within superconducting pickup coils which induces a flux change. Via a flux transformer the flux change induces a voltage in the SQUID (superconducting ring with two intersections) via the DC- Josephson effect. The maximum magnetic field reachable is 7 T in a temperature range from 2 K to 350 K. MPMS measurements have partly been carried out by the technician S. Heijligen. For a measurement in the MPMS the samples are prepared in a straw where the straw axis is aligned along the axis of the magnetic field. Therefore, the maximum size for a sample is given by the dimensions of the straw with a diameter of about 3 mm. The sample is mounted with adhesive tape (tesa film). The sample orientation is checked in a microscope, but there is also a holder available to check the orientation in the Laue camera. For samples with a very high magnetic moment the preparation with adhesive tape is not suitable. Here, a preparation where the sample is glued on a copper wire is recommended.

The Vibrating Sample Magnetometer (VSM) is an option to the Physical Property Measurement System (PPMS). Here, the sample is vibrating between 2 pick-up coils. Caused by the movements of the magnetic sample the changing magnetic flux induces a modulated voltage, which is proportional to the magnetic moment of the sample. The temperature range in this setup is 2 K to 400 K with a maximum magnetic field of 14 T. The VSM sample holder is a flat teflon bar on which the sample is glued on a fixed position. The sample is vibrated with about 40 Hz. The sample dimensions of the sample holder should be of max. 3 mm width. In all setups the sample shape has to be regarded due to demagnetization effects.

The home-built Faraday magnetometer is a setup that was constructed and modified in the Diploma theses of D. Löwen and S. Scharffe [50, 51] and is mainly built of a capacitive dilatometer in a gradient magnetic field. The sample is fixed on one of the capacitor plates and and the capacitor is mounted in the magnetic field gradient of a cryomagnet. This magnetic-field gradient induces a force $-\vec{\nabla}(\vec{\mu} \cdot \vec{B})$ on the capacitor plate. Therefore, the magnetization is reflected in a change of the capacitance which can be measured with high resolution using an AC capacitance bridge (Andeen Hagerling, AH2550). Depending on the cryomagnet and the insert used, magnetic fields up to 17 T and base temperatures down to 250 mK can be reached.

Heat Capacity

The specific heat is defined as the amount of heat (per unit mass) that is required to raise the temperature by a given amount, $C = \frac{\Delta Q}{\Delta T}$. The heat capacity is the second derivative of the Gibbs free energy with respect to the temperature and, thus, the first derivative of the entropy:

$$c_p = \left(\frac{\partial S}{\partial T}\right)_p = \frac{1}{V}\left(\frac{\partial^2 G}{\partial T^2}\right)_p . \tag{2.9}$$

Hence, the measurement of the specific heat is a suitable tool to estimate the entropy of a system. Two methods for measuring the heat capacity are common, the quasi-adiabatic heat pulse method and the relaxation method. The latter was used in the

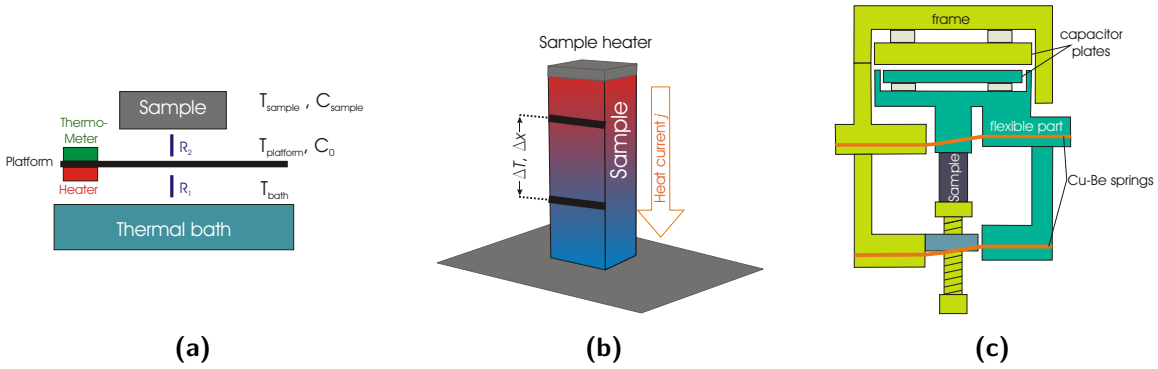

Figure 2.7: (a) Principle setup for heat-capacity measurements at low temperatures with the relaxation method. (b) Principle setup for measurements of the thermal conductivity via standard steady state method. (c) Principle setup of a capacitive dilatometer. The dilatometer consists of a a frame to which one capacitor plate is fixed (light green). The flexible part (green) provides the second capacitor plate to which the sample is attached with a screw. Both parts are connected via Cu-Be springs.

two employed setups. The principle setup is shown in Figure 2.7 (a). The sample is connected through a thermal resistance R_1 to a bath of constant temperature T_{bath} and the sample temperature T_{sample} is monitored as a function of time via the thermometer that is attached to the sample platform. Sample and platform are thermally connected via R_2. First T_{sample} is stabilized and at a certain time t_1 the heating power is raised by ΔP and an exponential rising of the temperature (time constant τ) is induced. At a time t_2 the heating power is switched back to the original value and an exponential relaxation of the temperature back to T_0 follows. The heat capacity is given by the relaxation time τ, the temperature gradient ΔT and the heating power ΔP:

$$C = \tau \cdot \frac{\Delta P}{\Delta T}. \tag{2.10}$$

A detailed discussion of this method is given in, e.g., Ref. 52. Two setups for the measurement of the specific heat are available in the II. Department of Physics. One is a specific heat device for the PPMS where temperatures down to 2 K and magnetic fields up to 14 T are available. The other setup was built by O. Breunig [52] and is constructed for the use in the HELIOX insert to reach temperatures down to 250 mK or in a dilution fridge where even lower temperatures are reachable. To provide a good thermal connection between sample and platform it is necessary that the sample has a smooth surface. The sample should not extent a diameter of about 5 mm and a thickness of about 1 mm or even thinner to partially compensate low thermal conductivity of some samples. For measurements in a magnetic field one has to keep the magnetic moment of the sample in mind because the platform is movable to some extent and the sample could be tilted out of the field or, in worst case, the sample holder could be broken. The sample is "glued" on the platform with a small amount of Apiezon grease, which gives, together with the platform itself, an addenda to the data that is measured in a separate run and subtracted from the data.

Thermal Conductivity

The thermal conductivity κ was measured via the so-called steady state method. The thermal conductivity κ relates to heat current $\vec{j}$ and a temperature gradient $\vec{\nabla}T$ over the samples as follows:

$$\vec{j} = -\kappa\vec{\nabla}T. \tag{2.11}$$

In the anisotropic case, κ is a second-rank tensor which is temperature dependent and the unit of κ is given as [W/m ·K]. A special interest lies in magnetic heat transport, κ_{mag}, which is under vivid debate, e.g. in spin-ice systems [53]. More details may be found elsewhere, e.g. in Ref. 54.

The principle setup of the steady state method used for this measurements is depicted in Figure 2.7 (b). As the thermal conductivity in one dimension can be described as

$$j = \frac{P}{A} = \kappa\frac{\Delta T}{\Delta x}, \tag{2.12}$$

a heat current j is given through the ratio of the power P of a sample heater and the sample cross section A. The temperature gradient $\frac{\Delta T}{\Delta x}$ over the sample is assumed to be constant and the temperature difference ΔT is measured between two fixed contacts in the distance Δx. The sample needs well defined surfaces because it is contacted on three planes. Typical dimensions are $3 \times 1 \times 1\text{mm}^3$ and the direction of the heat current should be the longest axis of the sample. A more detailed discussion of the thermal conductivity measurements can be found in the PhD thesis of G. Kolland [53] who performed measurements on $BaCo_2V_2O_8$ and related systems to which will be referred to.

Thermal Expansion and Magnetostriction

In terms of the Gibbs free energy, the thermal expansion coefficient is given as:

$$\alpha_i = \frac{1}{L_i}\left(\frac{\partial V}{\partial T}\right)_p = \frac{1}{L_i}\left(\frac{\partial^2 G}{\partial T \partial p_i}\right), \tag{2.13}$$

where the index i signals the direction of the expansion. The thermal expansion and the field-dependent expansion (= magnetostriction) can be measured in a capacitive dilatometer with very high resolution. In capacitance dilatometry a length change of the sample is translated into a change in the distance of the capacitor plates and, thus, into a change in the capacitance. The basic setup of a capacitance dilatometer that is based on the construction of Brändli and Griessen [55] is shown in Figure 2.7 (c). The dilatometer consists of two capacitor plates, one fixed to the frame (green) and one is flexibly connected via Cu-Be springs (blue). In detail, one of the capacitor plates is larger than the other one and both of them are surrounded by electrically grounded rings in order to suppress geometrical effects and stray fields, respectively. The sample is mounted between the flexible part, i.e. one capacitor plate, and a screw. If the sample expands by ΔL the capacitor plate adapts, resulting in a change of capacitance from an initial value C_0 to C_1. The measured change in capacitance is

easily related to ΔL by

$$\Delta L = \epsilon_0 \pi r^2 \left(\frac{1}{C_0} - \frac{1}{C_1} \right), \tag{2.14}$$

with the dielectric constant ϵ_0, the radius of the capacitor plates r, the start capacity C_0, and the capacity with changed field/temperature C_1.

The actual dilatometer consists of very pure copper which provides a good thermal coupling. The measured length changes ΔL ($\approx 10^{-9}$m) are always referred to the start value L_0 ($\approx 10^{-3}$m) so that the relative length change $\Delta L/L$ is of the order 10^{-6}. Often the changes of the relative length when close to a phase transition are more obvious in the derivatives of the length changes with respect to the temperature and the field, that are called the thermal expansion coefficient α and the magnetostriction coefficient λ:

$$\alpha_i = \frac{\partial}{\partial T} \left(\frac{\Delta L_i}{L_0} \right) \tag{2.15}$$

$$\lambda_i = \frac{\partial}{\partial H} \left(\frac{\Delta L_i}{L_0} \right). \tag{2.16}$$

Three different dilatometers were used within this work, all of them home-built [56–58]. Most measurements have been carried out on a dilatometer that was operated in the HELIOX insert where base temperatures down to 250 mK can be reached and depending on the cryomagnet a magnetic field up to 17 T can be applied. Some of the measurements were carried out in the VTI insert, where the minimum temperature is 2 K.

Zero-field measurements of the thermal expansion with small uniaxial pressures that will be discussed in Chapter 5.2 were measured in the so-called TADNULL setup [56]. Here, the dilatometer is mounted within a glass cryostat which is pre-cooled with liquid nitrogen and finally cooled with liquid helium. Via lowering the vapor pressure a base temperature of 2 K can be reached. The temperature ramp is caused by the natural warming process of the system to room temperature. Data are recorded only up to 180 K because of non-reproducible cell effects for higher temperatures.

Special on this setup is that the start capacity can be varied externally via a screw. Therefore, one can apply small uniaxial pressures on the sample depending to the base capacitance. With increasing base capacitance $C_0 \propto 1/d_0$ (d_0: base distance between the capacitor plates) the uniaxial pressure along the sample increases. Knowing the spring constant of the dilatometer that was determined by M. Seher [59] to $D \approx 5 \pm 1$kN/m, which was found reasonably temperature independent, the force on the sample can be estimated:

$$F = D \cdot \delta L = D \epsilon_0 \pi r^2 \left(\frac{1}{C_0} - \frac{1}{C_1} \right). \tag{2.17}$$

The sample areas are usually in the range of a few mm^2 and the applied pressure p_i can, thus, be varied around ≈ 0.5 MPa.

3 Crystal Preparation

> Crystal synthesis means
> to breath certain properties
> into matter under great effort
> in order to elicit them
> skilfully of yonder afterwards.

In solid-state physics the use of (large) single crystals in macroscopic measurements is inevitable. Moreover, crystal engineering is necessary to produce made-to-measure materials of high quality with respect to their chemical composition, their cristallinity, and their intrinsic and macroscopic geometries. Crystal growth is a temporally regulated heterogeneous chemical reaction leading into a crystalline state that can be, roughly, classified by the initial phase it starts from, i.e. if the crystal is grown from a gas phase, a solution, a melt or a solid-state reaction [60, 61]. For each method, chemistry holds a large variety of crystal growth techniques and the crystal growth by a floating zone, i.e. by a traveling melt, is one of them.

In the first part of this chapter the main aspects of crystal growth by the traveling melt method in a floating-zone mirror furnace will be presented. This method was used to grow single crystals of the $AM_2V_2O_8$ compounds that are introduced in Section 3.2. In the following sections the individual growth attempts are explained including used chemicals and according reaction equation as well as pictures of the successfully grown crystals. Main characterization by X-ray powder diffraction and resulting lattice parameters will also be given in these sections. Section 3.3.1 deals with the particular crystal growth processes of $BaCo_2V_2O_8$, followed by those of several substitutions either on the barium site (Sec. 3.3.2) or on the cobalt site (Sec. 3.3.3). In Section 3.3.4 the growth processes for the non-magnetic variants $(Ba,Sr)(Mg,Zn)_2V_2O_8$ are presented. Section 3.3.5 describes the crystal growth of $BaMn_2V_2O_8$ and $SrMn_2V_2O_8$, which are the (nearly) isotropic Heisenberg variants of the $AM_2V_2O_8$ spin-chain compounds. Further growth processes of systems that do not relate to the topics that will be discussed in Chapters 4 to 6, e.g. $LiCuVO_4$, $La_{1-x}Sr_xCoO_3$, or $(Dy_{1-x}Ho_x)_2Ti_2O_7$, can be found in the Appendix A.

3.1 Floating-Zone Method

The crystal growth by the floating-zone technique is but one technique amongst others to grow large single crystals. One big application of the floating-zone technique (besides the Czochralski method) is the commercial growth of large Silicon single crystals [62]. Here, the heat mechanism is a radio frequency electromagnetic field. In mirror furnaces conventional optical heating or laser heating is used as heat mechanism. In the application of crystal growth of designed materials containing metal oxides the crystal growth in an optically heated mirror furnace is a common technique. In principle two different floating-zone techniques can be distinguished. One of them is the pedestral growth which is comparable to the Czochralski top-seed method but with the advantage of the absence of a crucible, higher pulling times and higher achievable temperatures. Another technique is the crystal growth as it will be described below. Detailed information about several crystal growth methods and especially about the crystal growth by the floating-zone method can be found in textbooks, e.g. Refs. 62–64.

Preceding the actual growth process in the mirror furnace, pre-reactions have to be carried out as well as a rod preparation for use in the mirror furnace. In a short abstract the process of preparations as used in this thesis consists of following steps:

A. Choosing chemicals as educts and balancing the reaction equation

B. Calculating the amount of educts

C. Stoichiometric weighing in the educts

D. Mixing and grinding

E. Solid-state pre-reaction

F. Mixing and grinding

G. Rod preparation

H. Sintering

In most cases, there is more than one possibility to choose chemicals and reaction equations to grow a certain material. The choice of the educts should ensure that the melting points of the educts are in a similar temperature range. Otherwise, already during the first heating process it may happen that one of the educts will be volatile and in the end be missing in the reaction product. Some chemicals like manganese oxide, for example, show a tendency to evaporate easily already at comparably low temperatures. One possible solution for that problem would be to weigh in an extra amount of this material to provide the correct stoichiometry in the end product. Those strongly evaporating compounds are candidates for handling without pre-reactions to minimize evaporation. The measure of the extra amount of a material that needs to be added depends on the temperatures and growth velocities and has to be verified empirically. Another point is to keep in mind the valence of the used chemicals and

their favored oxidation states. In case of the $AM_2V_2O_8$ compounds the oxidation number of the transition metal should finally be 2+.

Solid-state reactions serve as pre-reactions of the stoichiometrically weighed in educts. A pre-reaction is advantageous (if evaporation is not a problem) because the chemical reaction does not take place in the mirror furnace. A rod of already reacted material is much more homogeneous in its composition.

After balancing the reaction equation, calculating the amount of educts and accordingly weighing in the chemicals, the mixture is usually pestled carefully in an agate mortar by hand. For the solid-state pre-reaction the alloy is put in a corundum (melting point: 2054 °C [65]) or platinum (melting point: 1768.3 °C [65]) crucible. The appearance of blue coloring of corundum crucibles indicates a reaction of cobalt with corundum, therefore, usually a platinum crucible is chosen for the $AM_2V_2O_8$ compounds. A box furnace is used for the pre-reaction of the mixture. There, the samples are heated to temperatures below the melting point for a solid-state reaction which is below ≈ 1100 °C for the $AM_2V_2O_8$ compounds under atmospheric air.

For the crystal growth in a mirror furnace the powder has to be pressed into rod shape. Several techniques are suitable, but here a drainage flexible tube (from medical supply) which is closed by a knot on one end, is put into a test glass. Through a hole at the bottom the test glass can be evacuated and the rubber tube is sucked at the walls so that it can be filled with the powder. After filling, the tube is closed by a buckler and with the help of a small needle the tube is evacuated. Removing air from the sample is of particular need because the powder rod is put in a hydrostatic press applying pressures of about 2 kbar. After removing the rod from the press and from the rubber tube, the rod is usually put in a platinum "ship" and sintered for several hours. Alternatively, a corundum ship can be used with some additional powder put between bearing surface and the rod to prevent the bar material from reacting with corundum. The diameter of the sintered rod is from about 4 mm to 6 mm. It is cut with a side cutter into a feed rod of about 1 cm and a seed rod of about 5 cm length.

Mirror Furnace

The mirror furnace (see Fig. 3.1) provides several advantages compared to other techniques. First of all it works without any crucibles and it is a contact-free technique which is of advantage for chemicals which are highly reactive or have a high melting point. Figure 3.1 (a) shows a picture of the heating unit of the 4-mirror furnace FZ-T10000-H-VI from Crystal Systems Inc. that is used for crystal growth in this thesis. The basic setup of a mirror furnace is shown in panel (b). The heating unit of this mirror furnace consists of four or, in other models, of two ellipsoidal mirrors with halogen lamps (depicted in yellow). Ideally, they are positioned at one of the two focal points of each mirror. The mirrors are aligned such that their second focal points coincide at a single point where the melting zone in the sample shall develop. The size of the melting zone depends, *inter alia*, on the dimensions of the spiral filament of the halogen lamps which usually increases with increasing lamp power. Therefore, it is advisable to choose the lamps with lowest sufficient power because a smaller melting zone is more stable. Other parameters and their influence on the stability of the melt will be discussed below.

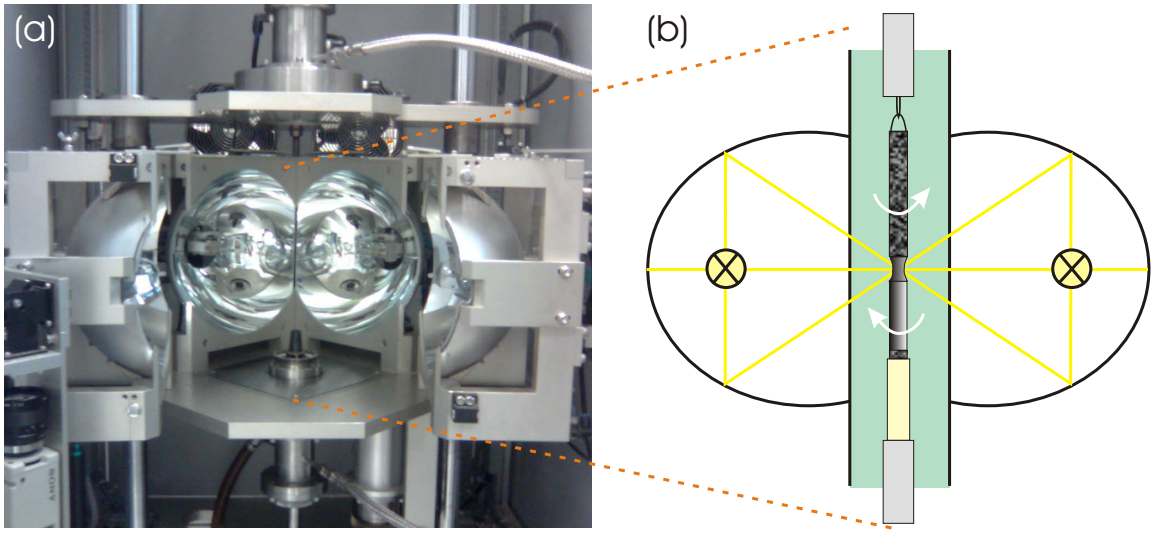

Figure 3.1: Panel (a) depicts the heating unit of the actual four-mirror furnace used in this thesis. The schematic view of a mirror furnace is shown in (b). Two or four ellipsoidal mirrors with halogen lamps on one focus (yellow) combine their second focus points at the same site. A feed rod and a seed rod (black) are attached to the rotating upper and lower shaft (gray), respectively. The sample system is in a closed quartz tube (light green) where specific atmospheres and pressures can be realized.

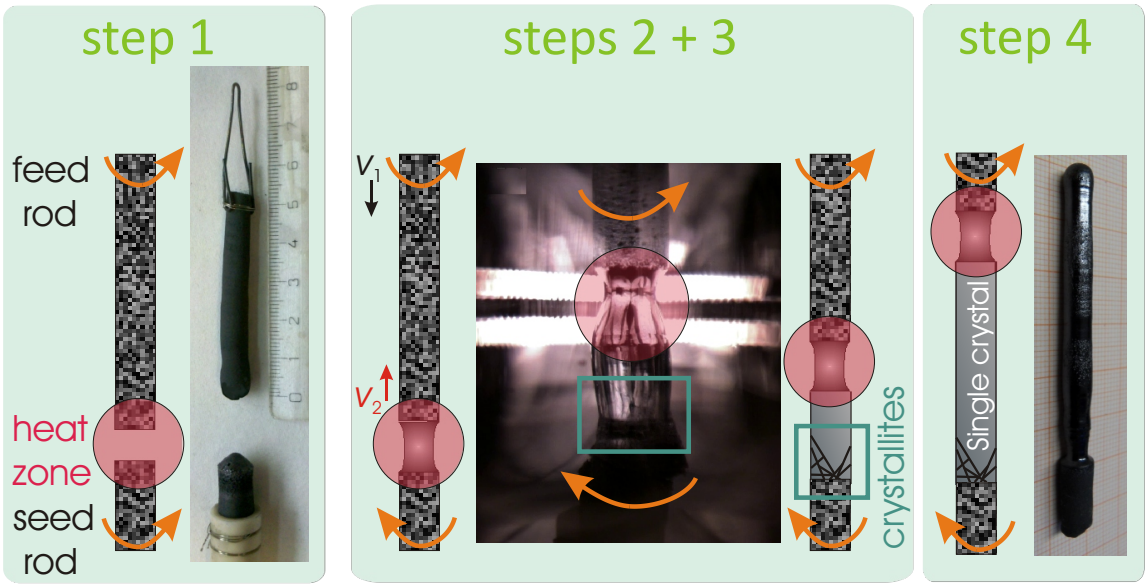

Figure 3.2: The idealized main steps of the nucleation process occurring during crystal growth in a mirror furnace. In step 1, the seed rod and feed rod are heated (red zone). In step 2, a melting zone is built up, the rods move with velocities v_1, v_2 and are rotated in opposite directions. In step 3, crystallites are growing and grain selection proceeds. In the last step a large (ideally) single crystal grows through grain selection.

The sample chamber is enclosed by a quartz tube (*cf.* Fig. 3.1), where a variety of atmospheres can be realized. One can either evacuate the sample chamber, or apply pressures up to 10 bar with ambient air or special reductive (e.g. forming gas, N_2/H_2), oxidizing (e.g. oxygen) or neutral/inert (e.g. argon) gases. The sample chamber can either be filled with a constant amount of gas or one can work with a gas flow. In cases of strong evaporation of rod material a gas flow can prevent a pollution of the glass tube and, thus, a loss of heating power.

The seed rod is mounted on the lower shaft (*cf.* Fig. 3.1) and can consist of a ceramic sample, i.e. a sintered rod as described above, or a single crystal with a certain orientation which enhances the probability that the emerging crystal grows along this chosen direction. The feed rod is attached to the upper shaft and can consist just of the pressed and maybe sintered educts in cases where the material is treated without pre-reaction. Otherwise, the rod is also a ceramic rod of the wanted composition. In case of the twice-scanning method the same rod is used twice or even more often. After the first scan, the rod usually becomes a polycrystal or a single crystal of poor crystallinity. Both shafts can be rotated against each other for a better heat circulation, and can be independently moved vertically which gives the speed of the growth process and the diameter of the resulting crystal. Until both rods are locally molten the shafts are usually rotated concordantly to prevent accidental damage of the rods. Afterwards, an inverse rotation is preferable to provide a thorough stirring of the melt. The rotation is commonly given in rounds per minute [r/min]. Within the melt, several kinds of convection occur such as natural convection, forced convection by the rod rotation, and Marangoni convection (see e.g. Ref. 62) that superimpose and influence the temperature distribution and, hence, the stability of the melt.

Figure 3.2 shows the schematic nucleation process during the crystal growth in a mirror furnace split in four steps. First, feed rod and seed rod are heated up (red zone) until they locally melt. Then they are moved towards each other, such that in the second step a stable melting zone develops. The feed (v_1) and the seed rod (v_2) are now moved such that effectively the heating zone travels though the feed rod. By choice of the velocity difference, one can influence the thickness of the resulting crystal. If, for example, the feed rod has a higher velocity than the seed rod more material is molten and the resulting crystal becomes thicker, and vice versa. This is also of importance if the density ρ_{feed} of the feed rod material is much smaller than that of the resulting crystal $\rho_{crystal}$. The picture in the middle of Fig. 3.2 is a snapshot which was taken during a crystal growth. The spiral filaments in the background, the sample and the melting zone in the foreground are clearly visible. In the best case, crystallites of the wanted composition are growing and a grain selection occurs with one grain ‘"winning”. As a rule of thumb, the occurrence of facets during the growth process is an indication for good single crystallinity. At the end, the ideal result is a large single crystal (step 4) like the one shown in the right panel. Due to the grain selection process, one can expect that the tip of a crystal is of better quality than the bottom, a fact that should be kept in mind for further sample preparation.

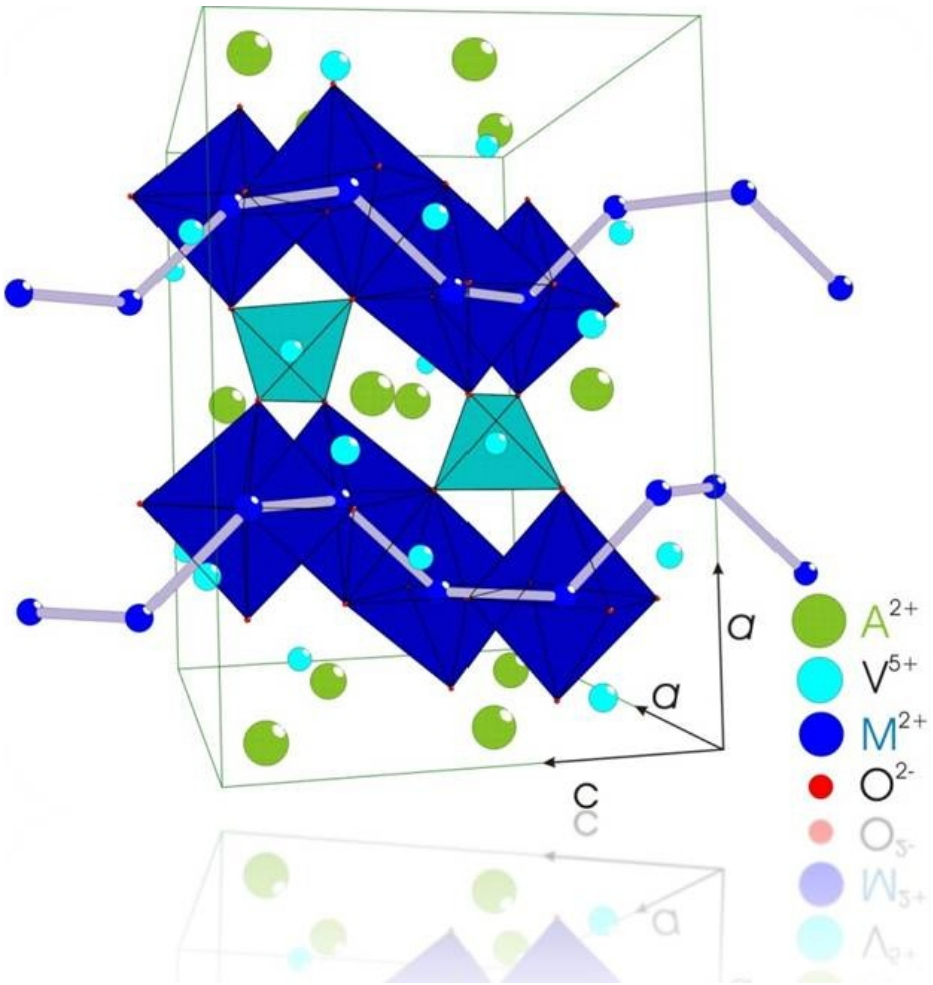

Figure 3.3: Crystal structure of most of the $AM_2V_2O_8$ compounds. Neighboring screw chains of different helicity are formed by CoO_6 octahedra (dark blue) along the c axis separated by nonmagnetic A^{2+} ions (green) and VO_4 tetrahedra (light blue).

3.2 Compounds of the $AM_2V_2O_8$ Type

The mother compound of this group of compounds is $SrNi_2V_2O_8$ that crystallizes in the tetragonal space group $I4_1cd$ (No. 110). Most of the $AM_2V_2O_8$ compounds related to this thesis are isostructural. Chemically these compounds can be classified into the group of alkaline-earth oxometallates.

The principle structural features will now be discussed on the example of $BaCo_2V_2O_8$ crystallizing in the symmetrically higher space group $I4_1/acd$ (No. 142) that is the compound of main interest in this work. Space group No. 110 is a maximal non-isomorphic subgroup of space group no. 142 or, the other way around, No. 142 is the minimal translational equal supergroup of No. 110. The structure $I4_1/acd$ can also be written as $I\ 4_1/a\ 2/c\ 2/d$ and in detail this means that the structure contains [66–69]:

- body centering (I), corresponding to a translation of $(1/2, 1/2, 1/2)$,
- an axial a (b) glide plane $(0\,0\,1)$ which is a glide reflection through the plane with the glide vector $\vec{a}/2$ (and $\vec{b}/2$, due to the tetragonal symmetry)

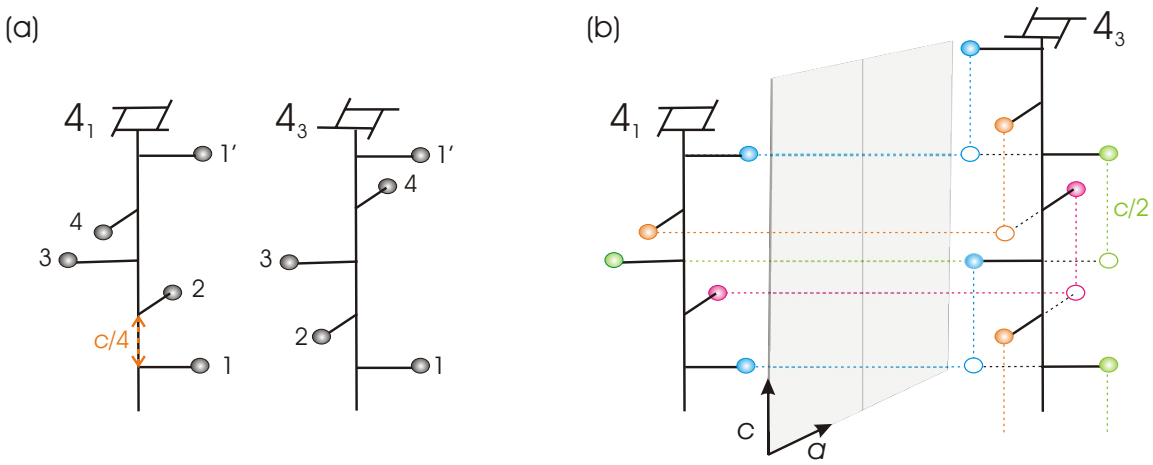

Figure 3.4: (a) 4_1 and 4_3 screw axes. (b) Applying a glide mirror plane to 4_1 yields the 4_3 screw axis. Open symbols represent the position after mirroring. For the correct position a translation of $c/2$ has to be added.

- a 4_1 screw axis with anticlockwise rotation along [0 0 1],
- a 2_1 screw axis along [1 0 0],
- an axial c glide plane (1 0 0) which is a glide reflection through the plane with the glide vector $\vec{c}/2$,
- a diamond glide plane perpendicular to the xy diagonal, i.e. $(1\,\bar{1}\,0)$, (1 1 0), (in centered cells only) one quarter unit cell edge in each direction which is always occurring in pairs of alternating glide vectors, e.g. $(\vec{a} \pm \vec{b})/4$.

In particular, the $AM_2V_2O_8$ compounds contain screw chains of edge sharing MO_6 octahedra which are running along the c axis of the tetragonal crystal structure as shown in Figure 3.3. Along the 4_1 chain the octahedra are rotated by 90° and translated by $\frac{1}{4}c$. The M site is occupied by a small transition metal, M^{2+}= Mn, (Fe,) Co, Ni, Cu, (Zn) or the smallest of the alkaline earth, magnesium. Depending on the transition metal ion M^{2+}, the various members of $AM_2V_2O_8$ represent spin-chain materials with different spin quantum number and anisotropy.

In the ab plane, the chains are spatially separated by nonmagnetic A^{2+} ions, where A = Ba, Sr or Pb (green in Fig. 3.3), which has an oxygen coordination of twelve, and V^{5+} ions in a tetrahedral oxygen coordination (light blue). The detailed oxygen coordination of the M^{2+} and A^{2+} ions is discussed in detail in the respective Chapters 4 to 6. Depending on the size of the non-magnetic ions the distance between the spin chains is changed. The unit cell contains 16 M^{2+} ions within 4 chains. Along the tetragonal axis neighboring chains have different helicity, i.e. one finds two types of chains namely a 4_1 and a 4_3 axis, see Figure 3.4 (a). The combination of the 4_1 screw axis with anti-clockwise rotation and the glide mirror plane c yields the second type of chains which have a clockwise rotation. The 4_3 chain is enantiomorphous to the 4_1 screw axis meaning that they can be transformed into each other through a mirror plane. In the present case, in addition to the mirroring the transformation

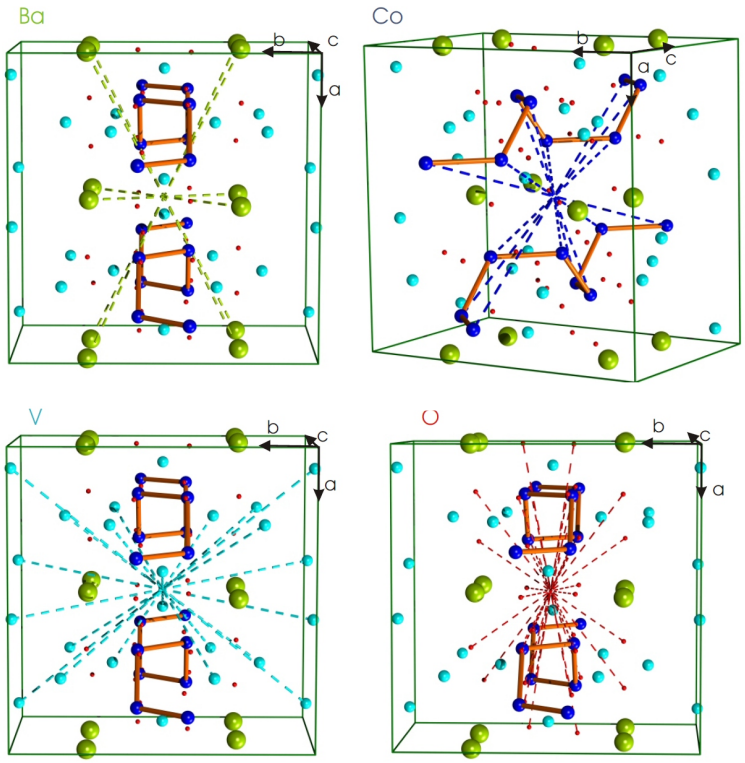

Figure 3.5: Structure of $BaCo_2V_2O_8$ with emphasis on the inversion center. Each picture shows the inversion of another ion (Ba, Co, V, O) of the unit cell.

contains a shift of $c/2$ along c. Figure 3.4 (b) illustrates the construction of the 4_3 screw chain from the 4_1 screw chain. Open symbols represent the position after the mirror transformation. The final position is achieved after translation by $c/2$ along the axis. Along the ab plane diagonal the chains have the same helicity and the chains are transformed into each other by applying the body centering I simply by translation of $(1/2, 1/2, 1/2)$. The crucial difference between the two space groups $I4_1/acd$ and $I4_1cd$ is the loss of the glide mirror plane a coming along with the loss of the centrosymmetry. Figure 3.5 depicts the inversion center in the structure of $BaCo_2V_2O_8$ represented for each Ba, Co, V and O. The loss of this inversion symmetry gives rise to more degrees of freedom for the ions within the unit cell, e.g. there are 4 different oxygen positions in space group No. 110 instead of only 2 in No. 142. Apart from this, it is nearly impossible to distinguish between both space groups in the refinement of X-ray powder diffraction pattern.

Table 3.2 at the end of this section gives an overview over all $AM_2V_2O_8$ type compounds with A = Ba, Sr or Pb which are ordered with increasing spin number of the transition metal on the M site. Not all imaginable compounds are existing yet, those are depicted in gray. Existence has been checked by literature, e.g. the ICSD database. For the known compounds the structure and the lattice constants are given in rows 3-5. In the *Comment* some main features of the compound such as a general description of the magnetic behavior, Néel temperature, the potential synthesis as single crystal (sc) or powder (pw), and references are listed. A more detailed description of the several compounds will be given below.

Ion		CN 6	CN 10	CN 11	CN 12
rare earth	Pb^{2+}		1.4	1.45	1.49
alkaline-earth metal	Ba^{2+}		1.52	1.57	1.61
	Sr^{2+}		1.36	–	1.44
	Ca^{2+}		1.23	–	1.34
	Mg^{2+}	0.72	–	–	–
transition metal	Mn^{2+}	0.83			
	Fe^{2+}	0.78			
	Co^{2+}	0.745			
	Zn^{2+}	0.74			
	Cu^{2+}	0.73			
	Ni^{2+}	0.69			

Table 3.1: Atomic radii of the respective alkali metal, rare-earth and alkaline-earth metal and transition-metal ions. The radii are given in Å (taken from Ref. 70) depending on the coordination number (CN) of the ions with oxidation number 2+. Other coordination for the transition metals are possible, but not listed here.

Mg, $S = 0$

The alkaline-earth metal Mg^{2+} is suitable to enter the M site within $AM_2V_2O_8$ because its ionic radius for a coordination number of 6 is in the same range than that of the transition metals (*cf.* Tab. 3.1). However, only one compound with magnesium on the M site is known in literature, namely $BaMg_2V_2O_8$ [15]. According to literature, $BaMg_2V_2O_8$ is isostructural to $BaCo_2V_2O_8$ (space group No. 142) with lattice parameters $a = 12.4189(8)$ Å and $c = 8.4657(3)$ Å. Small single crystals were grown by the spontaneous nucleation method. Due to its electronic configuration [Ne] with no partially filled shell $BaMg_2V_2O_8$ is the perfect non-magnetic reference system to the magnetic $AM_2V_2O_8$ compounds in order to distinguish magnetic behavior from non-magnetic background. The crystal growth of $BaMg_2V_2O_8$ and $SrMg_2V_2O_8$ was achieved in this work and will be discussed in Section 3.3.4.

Zn, $S = 0$

An occupation of the M site by Zn^{2+} would also lead to a non-magnetic variant of the $AM_2V_2O_8$ compounds but with a configuration [Ar] $3d^{10}$. However, none of the possible compositions (Ba, Sr, Pb)$Zn_2V_2O_8$ is known in literature so far. Only other vanadates containing Zn, for example $Ba_2ZnV_2O_8$ [71] or $AZn_2V_2O_7$ with $A =$ Ba, Sr [72] are existing (see also appendix A). Crystal growth attempts of $BaZn_2V_2O_8$ and $SrZn_2V_2O_8$ will also be discussed in Section 3.3.4.

Cu, $S = 1/2$

Copper has a configuration [Ar] $3d^9$ when present in oxidation number 2+ which results in a spin quantum number of $S = 1/2$. Co^{2+} is Jahn-Teller active and may influence the oxygen coordination within the compound. In fact, only one of the

copper compounds is known in literature, which is $BaCu_2V_2O_8$ [73]. $BaCu_2V_2O_8$ is also tetragonal but belongs to space group $I42d$ (No. 122) which is a subgroup of space group No. 142. Due to a strong Jahn-Teller effect, the Cu^{2+} ions have quasiplanar (4+1+1) coordination bridged by oxygen ions forming one-dimensional linear chains made of edge-sharing pairs of CuO4 square-plaquettes, i.e. dimer chains, where the exchange via the 2 different V sites plays an important role (*cf.* detailed discussion in Refs. 74, 75). The lattice constants are $a = 12.7439(37)$ Å and $c = 8.1480(34)$ Å [73]. $BaCu_2V_2O_8$ is a quasi-one-dimensional gaped alternating spin chain [75] and single crystals of this compound were grown by top seed method [76].

Ni, $S = 1$

Ni^{2+} has a configuration of [Ar] $3d^8$ and, therefore, a spin $S = 1$. A lot of research has been done on the nickel compounds $BaNi_2V_2O_8$, $SrNi_2V_2O_8$ and $PbNi_2V_2O_8$. Most of the investigations on $SrNi_2V_2O_8$ in literature have been measured only on powders or very small single crystals of $SrNi_2V_2O_8$. Only recently large single crystals of $SrNi_2V_2O_8$ have been successfully grown by the traveling solvent floating zone technique [12, 13]. The structure of $SrNi_2V_2O_8$ belongs to space group $I4_1cd$ (No. 110) with lattice constants $a = 12.1617(13)$ Å and $c = 8.3247(14)$ Å [77]. The latest reports describe $SrNi_2V_2O_8$ as a Haldane chain and confirm a non-magnetic spin-singlet ground state, e.g. [13, 78]. The magnetic easy axis is the c axis and the system shows magnetic anisotropy with field-induced magnetic order above the critical fields $H^{\perp c} \simeq 12$ T and $H^{\parallel c} \simeq 21$ T at $T = 4.2$ K due to closing of the gaps by the Zeeman splitting [13]. $PbNi_2V_2O_8$ is isostructural to $SrNi_2V_2O_8$ with slightly larger lattice constants ($a = 12.249(3)$ Å and $c = 8.354(2)$ Å [79]) due to the larger ionic size of the Pb and it is a Haldane chain [80]. Up to now, only measurements on (oriented) powder samples have been reported [81]. $BaNi_2V_2O_8$, however, falls out of the scheme because its structure belongs to the rhombohedral space group $R3\bar{H}$ (No. 148) with lattice constants $a = 5.028\,99(4)$ Å and $c = 22.3450(2)$ Å [82, 83]. Single crystals of this compound exist and the system can be described as a 2D honeycomb antiferromagnet with a Néel temperature of $T_N = 50$ K [83].

Co, $S = 3/2$

Co^{2+} has configuration [Ar] $3d^7$ and $S = 3/2$, assuming the high-spin state. All three cobalt compounds $BaCo_2V_2O_8$, $SrCo_2V_2O_8$ and $PbCo_2V_2O_8$ exist. The lattice constants of $BaCo_2V_2O_8$, which is the main-topic compound of this thesis, are $a = 12.4441(6)$ Å and $c = 8.4153(10)$ Å [15]. The system crystallizes in space group $I4_1/acd$ (No. 142). Single crystals of $BaCo_2V_2O_8$ can be grown by different techniques [15, 23, 84–86]. Even if cobalt has a spin of 3/2, the antiferromagnet $BaCo_2V_2O_8$ is effectively described as a quasi-one-dimensional spin-1/2 Ising system with a Néel temperature of ≈ 5.5 K. A detailed description of the structural and magnetic properties of $BaCo_2V_2O_8$ are given in Chapter 5. Single crystals of $SrCo_2V_2O_8$ can be grown by different techniques [86–88]. It crystallizes in space group $I4_1cd$ with lattice constants $a = 12.267(1)$ Å and $c = 8.424(1)$ Å [87]. $SrCo_2V_2O_8$ is also described as an Ising antiferromagnet with a Néel temperature of ≈ 5 K [25, 86]. A second transition at 3 K

was reported and assumed as a transition into a canted antiferromagnetic state [89]. Amongst others, Chapter 6 presents a study of $SrCo_2V_2O_8$. For $PbCo_2V_2O_8$ only polycrystals are known from literature. The crystal structure is $I4_1cd$ with lattice constants $a = 12.3482(5)$ Å and $c = 8.4378(3)$ Å) [90]. $PbCo_2V_2O_8$ is a quasi-one-dimensional canted antiferromagnet with a Néel temperature of $T_N = 4$ K [90, 91].

Mn, $S = 5/2$

Mn^{2+} is of configuration [Ar] $3d^5$ with spin $S = 5/2$. $BaMn_2V_2O_8$ and $SrMn_2V_2O_8$ are known in literature [17, 19]. The structure of $BaMn_2V_2O_8$ is contradictorily reported as isostructural to $BaCo_2V_2O_8$ (No. 142) with $a = 12.5563(14)$ Å and $c = 8.5942(9)$ Å [17] or to $SrNi_2V_2O_8$ (No. 110) with lattice constants $a = 12.267(1)$ Å and $c = 8.424(1)$ Å [18]. $BaMn_2V_2O_8$ is a quasi one-dimensional canted antiferromagnet with relatively high Néel temperature $T_N = 37$ K. In literature, the magnetic properties were derived only on powder samples. $SrMn_2V_2O_8$ belongs to the space group No. 110 and has lattice constants of $a = 12.4422(9)$ Å and $c = 8.6833(6)$ Å [19]. This compound also is a canted antiferromagnet with $T_N = 43$ K and nearly isotropic magnetism. A more detailed discussion of both compounds will be given in Chapter 4 .

Fe, $S = 0$ or 2

A spin chain with iron on the M site would be of interest because iron with an oxidation number of 2+ ($3d^6$) can occur, in principle, with two different spin states. In the low-spin configuration the system is nonmagnetic with $S = 0$ whereas in the high-spin state $S = 2$ is realized. Therefore, a spin-state transition between both configurations would be possible. Unfortunately, none of these compounds can be found in literature which might be caused by the affinity of iron for higher oxidation states. Attempts to grow $BaFe_2V_2O_8$ have been carried out in the course of this thesis, but were not successful [92].

Table 3.2: Overview of the $AM_2V_2O_8$ compounds with A=Ba, Sr, Pb and M=Zn, Cu, Ni, Co, Mn, Fe or Mg. (sc= single crystal, pw= powder, af= antiferromagnet, Q-1D= quasi-1-dimensional)

	Name	Structure	a [Å]	c [Å]	Comment
Mg	$BaMg_2V_2O_8$	$I4_1/acd$ (No. 142)	12.4189(8)	8.4657(3)	sc [15], pw [53]; non-magnetic
$S = 0$	$Sr/PbMg_2V_2O_8$				unknown
Zn	$Ba/Sr/PbZn_2V_2O_8$				unknown
$S = 0$					
Cu	$BaCu_2V_2O_8$	$I\bar{4}2d$ (No. 122)	12.7439(37)	8.1480(34)	sc [73]; 1D alternating chain
$S = \frac{1}{2}$	$Sr/PbCu_2V_2O_8$				unknown
Ni	$BaNi_2V_2O_8$	$R\bar{3}$ (No. 148)	5.02899(4)	22.3450(2)	sc [83]; 2D honeycomb af (γ=120°); $T_N = 50\,K$
$S = 1$	$SrNi_2V_2O_8$	$I4_1cd$ (No. 110)	12.1617(13)	8.3247(14)	sc [13]; 1D Haldane chain
	$PbNi_2V_2O_8$	$I4_1cd$ (No. 110)	12.249(3)	8.354(2)	pw [79]; 1D Haldane chain
Co	$BaCo_2V_2O_8$	$I4_1/acd$ (No. 142)	12.4441(6)	8.4153(10)	sc [15]; 1D eff. S=1/2 Ising chain, $T_N = 5.5\,K$
$S = \frac{3}{2}$	$SrCo_2V_2O_8$	$I4_1cd$ (No. 110)	12.267(1)	8.424(1)	sc [87]; 1D canted af Ising chain, $T_N = 5\,K$
	$PbCo_2V_2O_8$	$I4_1cd$ (No. 110)	12.3482(5)	8.4378(3)	pw [90]; 1D canted af Ising chain, $T_N = 4\,K$
Mn	$BaMn_2V_2O_8$	$I4_1/acd$ (No. 142)	12.5563(14)	8.5942(9)	sc [17]; 1D canted af Heisenberg chain, $T_N = 37\,K$
$S = \frac{5}{2}$	$SrMn_2V_2O_8$	$I4_1cd$ (No. 110)	12.4422(9)	8.6833(6)	sc [19]; 1D canted af Heisenberg chain, $T_N = 43\,K$
	$PbMn_2V_2O_8$				unknown
Fe	$Ba/Sr/PbFe_2V_2O_8$				unknown
$S = 0; 2$					

Figure 3.6: Samples of $BaCo_2V_2O_8$: P1A is the sample grown by a spontaneous nucleation method. The arrow indicates the c direction and the flat surface is a (1 1 0) plane. SN0107 is a polycrystal. SN0089 has a rough surface, polycrystal. SN0133 has a very smooth surface due to very slow crystal growth. This sample was used in the neutron studies. SN0075 is a single crystal. In this picture, part of the crystal was cut and prepared for specific heat measurements.

3.3 Crystal Growth Processes

For completeness, some reaction processes that were carried out in the period of my diploma thesis [92] are mentioned here. This concerns particularly the growth of $BaCo_2V_2O_8$ (P1A, see below) by the spontaneous nucleation method, growth attempts of $BaZn_2V_2O_8$ (Section 3.3.4), and the growth processes of $BaMn_2V_2O_8$ and $SrMn_2V_2O_8$ in Section 3.3.5. Samples that are marked by a * were not used for the measurements presented in the following chapters due to their poor quality.

3.3.1 $BaCo_2V_2O_8$

$BaCo_2V_2O_8$ is the hub of this thesis and most of the other grown crystals are based on the interest in this compound. $BaCo_2V_2O_8$ is an effective Ising spin 1/2 chain compound. Small single crystals of this compound were first synthesized by Wichmann and Müller-Buschbaum in 1986 [15] by spontaneous nucleation, i.e., by self-flux mediated crystal growth. In literature, single crystals were synthesized with this method until 2011 when the first single crystal growth by the floating-zone method was reported [86].

In analogy to the spontaneous nucleation in literature, the precursors $BaCO_3$ (Merck $\geq$ 99 %), Co_3O_4 (Alfa Aesar 99.5 %) and V_2O_5 (Strem Chemicals 99.5 %) have been mixed in the molar ratio of 3:2:3.

$$3\ BaCO_3 + 2\ Co_3O_4 + 3\ V_2O_5 \rightarrow 3\ BaCo_2V_2O_8 + 3\ CO_2\uparrow + O_2\uparrow \qquad (3.1)$$

After grinding, the mixture was put into a corundum vessel and heated with a temperature rate of 100 °C/h up to 1050 °C which is above the melting point of about 1038 °C (derived via DTA measurements [92]). The cooling process was done extremely slow with a rate of only 1 °C/h to give the incongruent melt a chance to crystallize into the wanted composition. Below 950 °C the sample was cooled down fast (100 °C/h). The entire reaction process needed five days. Small, mm-sized crystals could be extracted

and the largest one of them (labeled P1A) is depicted in Figure 3.6. The longest axis ($\approx$ 2 mm) of this crystal could be identified as the c axis and the plane shown is perpendicular to the [1 1 0] direction. Single crystals grown with this method seem to grow always in this configuration which is of experimental significance (see Chapter 5). The powder pattern of sample P1A is shown in Figure 3.7 (a) and the resulting lattice parameters using space group No. 142 are given in Tab 3.3.

The following subsections discuss the growth attempts of large single crystals of $BaCo_2V_2O_8$ in a mirror furnace. The first attempt to grow $BaCo_2V_2O_8$ in the mirror furnace was actually done during my diploma thesis. However, some time and effort was needed to find growth parameters that provide a sample with a smooth surface and of good crystallinity. Table 3.3 gives an overview over the processes and the resulting lattice parameters. The powder pattern of all the $BaCo_2V_2O_8$ samples are summarized in Figure 3.7.

SN0075

The precursor of SN0075 was prepared according to Eq. (3.1). The mixture was heated in a platinum crucible to 930 °C for about 35 hours with intermediate grinding. The material was pressed to a bar that was sintered at 950 °C for 11 hours. Twice scanning of the sample was performed in the mirror furnace. In the first run an argon atmosphere with 4 bar pressure was chosen. A tiny crucible with pure titanium was added in order to purify the gas, as titanium strongly reacts with oxygen. 300 W lamps were chosen and a power of about 52 % was sufficient to establish a stable melt. The rods were rotating with 15 r/min in opposite sense and the growth velocity was varied from 5 mm/h to 12 mm/h. Since the resulting sample did not have a smooth surface which got worse with increasing growth velocity a much slower growth velocity of 2 mm/h to 4 mm/h was chosen for the second run (300 W lamps, Ar 2 bar, $\pm$15 r/min) and the lamp power could be held a little lower than before. A polycrystal of mainly c-oriented grains was used as a seed. The resulting crystal still did not have a smooth surface but cutting the rod and investigation of the inner surfaces via Laue camera showed the single crystallinity of the sample. A part of it, already cut in shape for further measurements, is shown in Figure 3.6.

SN0089*

The pre-reaction of SN0089 according to Eq. (3.1) was performed in a platinum crucible at 950 °C for twelve hours. The material pressed into a bar and sintered for another twelve hours at the same temperature. The rod was treated twice in the mirror furnace and both times 300 W lamps were chosen. This time the atmosphere was chosen to be ambient air and normal pressure to test the influence of the atmosphere, e.g., on the stability of the melt. The rod rotation was increased to about $\pm 20 - 25$ r/min. During the first (second) run the growth velocity was kept at 3 mm/h (7 mm/h). The resulting crystal is shown in Figure 3.6 and it turned out to suffer from inner stress, as the crystal showed a lot of crinkles.

SN0107*

In case of SN0107, $BaCO_3$ was replaced by $Ba(OH)_2{\cdot}8\ H_2O$ (Sigma Aldrich, $\geq 98\,\%$) which is more reactive:

$$3\ (Ba(OH)_2 \cdot 8\ H_2O) + 2\ Co_3O_4 + 3\ V_2O_5 \rightarrow 3\ BaCo_2V_2O_8 + 27\ H_2O \uparrow + O_2 \uparrow \quad (3.2)$$

The precursor was put in a platinum crucible and heated to 900 °C for 15 h. The temperature was chosen a little lower than before because the material is pretty hard after the pre-reaction which increases the amount of physical work for grinding. During the rod pressing the sample got wet due to a leakage in the rubber tube. The material was dried, pressed again and put into the mirror furnace with part of a single-cristalline sample as seed. This time a very slow growth velocity of only 0.5 mm/h was chosen (300 W, air, ambient pressure). Rotation was kept inverse with a slower rotation for the upper rod than the lower one. The power had to be varied from 43 % to 54 % because the stability of the melt was disturbed by gas bubbles that were forming inside the melt. Those bubbles were removed by carefully under-cooling the melt temporarily and evacuating the sample chamber but there is a high risk that the melt breaks down completely, what actually happened once. The resulting sample is also shown in Figure 3.6. The cut surfaces show a lot of crinkles but a slightly smoother surface than SN0089.

SN0133

The best single crystal of $BaCo_2V_2O_8$ grown in the mirror furnace is SN0133. The precursor according to Eq. (3.1) was put in a platinum crucible covered with a corundum lit and heated up to 700 °C for two days with intermediate grinding. The bar was pressed and sintered (Pt ship) at 850 °C. Actually, this sample was put in the mirror furnace three times with 300 W lamps under ambient air. The first two runs again showed the gas-bubble problem mentioned above. The counter rotation was kept comparatively slow (6 r/min to 14 r/min) with the lower seed rod slower than the feed rod. With every run the lamp power could be decreased, additionally preventing gas bubbles. Because the melt broke down some times in the first growth, which was carried out very slowly, the second run was performed very fast to homogenize the rod for the third run. In this last run the rotation was kept at 11 r/min for the feed rod and only 6 r/min for the seed rod, the growth velocity was 0.5 mm/h. Still, this run was not completely unproblematic because the furnace ran for almost three days and it was necessary to lower the power several times during this run. The resulting crystal (see Fig. 3.6) had a smooth and shiny surface and turned out to be of good crystalline quality.

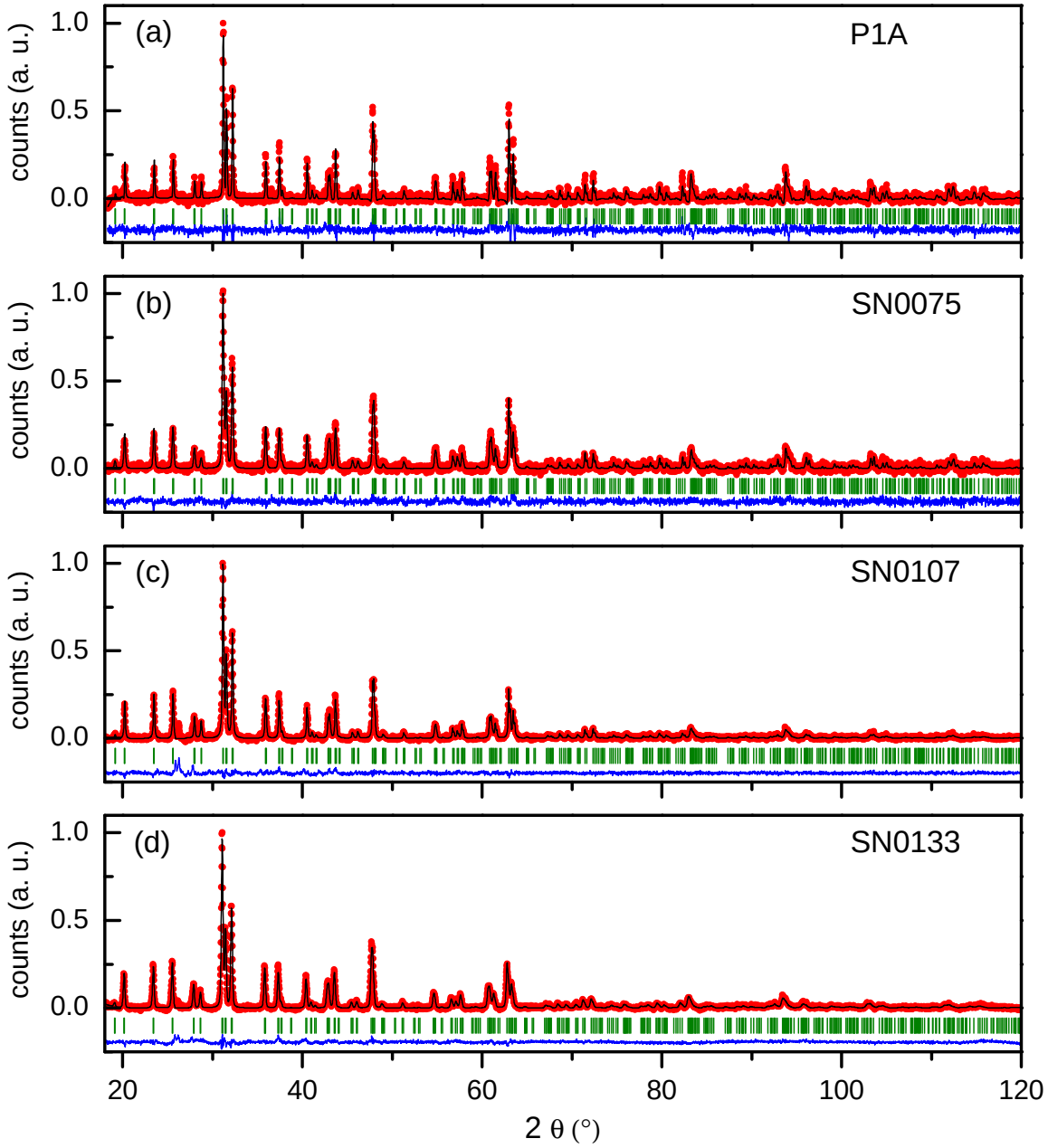

Figure 3.7: X-ray powder patterns of the $BaCo_2V_2O_8$ samples (a) P1A, (b) SN0075, (c) SN0107, and (d) SN0133. Green bars are the calculated Bragg positions, red points are the measured data, the black line is the calculated intensity, and the blue line gives the difference between measurements and calculation.

3.3.2 $Ba_{1-x}Sr_xCo_2V_2O_8$

In order to study the influence of disorder in $BaCo_2V_2O_8$, induced by substitution of the smaller strontium on the barium site, several attempts to grow single crystals with different substitution levels have been made. Single crystals with three different intermediate substitution levels as well as complete substitution were realized. Probably due to the smaller strontium (see Tab. 3.1), the structure of $SrCo_2V_2O_8$ lacks

Table 3.3: Several growth processes of $BaCo_2V_2O_8$ and the $Ba_{1-x}Sr_xCo_2V_2O_8$ series and the obtained lattice parameters from X-ray powder diffraction compared to literature data. The Sr content is represented by x. Samples were grown via the floating-zone (FZ) method or spontaneous nucleation (sn) method. The resulting samples were either single crystals (sc) or polycrystals (pc) of varying quality.

$x =$	Sample	Method	Comment	$a = b$ (Å)	c (Å)	χ^2
0	P1A	sn, Eq. (3.1)	sc	12.4310(5)	8.4029(4)	2.3
0	SN0075	FZ, Eq. (3.1)	sc	12.4300(7)	8.4026(5)	1.4
0	SN0089*	FZ, Eq. (3.1)	pc/stressed sc	–	–	–
0	SN0107*	FZ, Eq. (3.2)	pc	12.4323(5)	8.4044(4)	1.7
0	SN0133	FZ, Eq. (3.1)	sc	12.4664(7)	8.4263(5)	2.2
0	$BaCo_2V_2O_8$	sn	Ref. 15	12.4441(6)	8.4153(10)	
0.1	SN0061*	sn, Eq. (3.3)	small sc	–	–	–
0.1	SN0087	FZ, Eq. (3.3)	sc	12.4086(4)	8.3973(3)	1.3
0.5	SN0091	FZ, Eq. (3.3)	sc	12.3546(5)	8.4023(3)	1.3
0.9	SN0111	FZ, Eq. (3.4)	fractured sc	12.2767(2)	8.4110(2)	1.5
1	SNxx04*	sn, Eq.(3.3)	small, twinned sc	–	–	–
1	SN0093*	FZ, Eq.(3.3)	fractured sc	12.2554(8)	8.4119(5)	1.3
1	SN0135	FZ, Eq.(3.3)	sc	12.2594(5)	8.4146(4)	1.4
1	$SrCo_2V_2O_8$	sn	Ref. 87	12.267(1)	8.424(1)	

centrosymmetry and belongs to space group No. 110. For the powder pattern refinement space group No. 142 was used for a Sr content up to 50 % and No. 110 above. Anyway, the refinement with both space groups yield basically the same values for the lattice constants. To clarify that issue single-crystal X-ray diffraction refinement could be performed which was not carried out during this work. For a final discussion about the influence of the Sr substitution on the crystal structure this should be done in future. Although $SrCo_2V_2O_8$ is closely related to $BaCo_2V_2O_8$ and known from literature [25, 87–89], the compound is hardly investigated compared to $BaCo_2V_2O_8$. A detailed motivation for this project and the detailed study of these compounds are given in Section 6.1. Table 3.3 comprises the key data of the crystal growth and the resulting lattice constants from the X-ray powder diffraction refinement (see Fig. 3.8).

$Ba_{0.9}Sr_{0.1}Co_2V_2O_8$ (SN0061*)

The first growth attempt of $Ba_{1-x}Sr_xCo_2V_2O_8$ with $x = 0.1$ has been done via the spontaneous nucleation method in analogy to the growth reported for $x = 0$. The educts $BaCO_3$, $SrCO_3$ (Alfa Aesar 99.99 %), Co_3O_4 and V_2O_5 have been mixed in the ratio $0.9 : 0.1 : \frac{2}{3} : 1$ according to Eq. (3.3) ($x = 0.1$) and put in a corundum crucible (part of this mixture was used for SN0087 and kept aside).

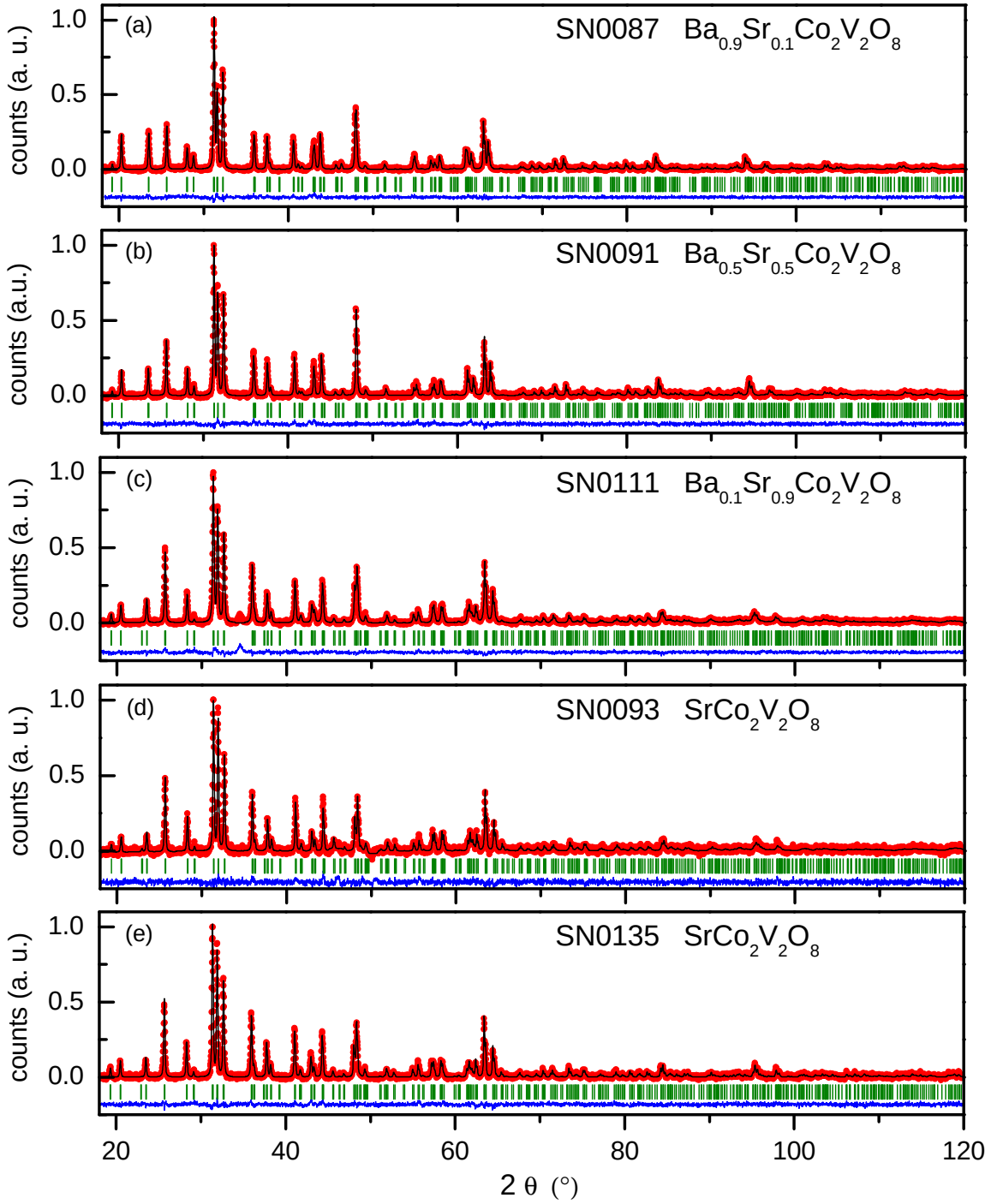

Figure 3.8: X-ray powder diffraction patterns of the strontium substituted samples (a) $Ba_{0.9}Sr_{0.1}Co_2V_2O_8$, (b) $Ba_{0.5}Sr_{0.5}Co_2V_2O_8$, (c) $Ba_{0.1}Sr_{0.9}Co_2V_2O_8$ and pure $SrCo_2V_2O_8$ (d)-(e). Green bars are the calculated Bragg positions, red points are the measured data, the black line is the calculated intensity, and the blue line gives the difference between measurements and calculation.

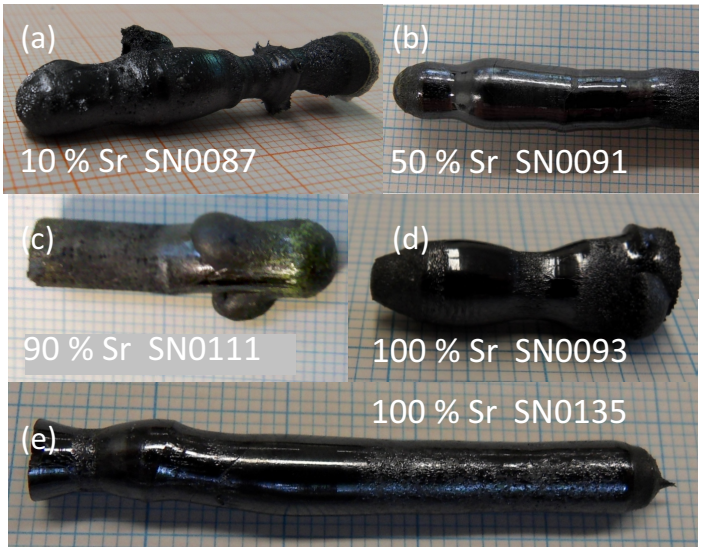

Figure 3.9: Grown single crystals with different Sr content x: $x = 0.1$ SN0087, $x = 0.5$ SN0091, $x = 0.9$ SN0111 and the pure $SrCo_2V_2O_8$ samples SN0093 and SN0135. All of them are single crystals.

$$(1-x)\ BaCO_3 + x\ SrCO_3 + \frac{2}{3}\ Co_3O_4 + V_2O_5 \longrightarrow$$
$$Ba_{1-x}Sr_xCo_2V_2O_8 + CO_2\uparrow + \frac{1}{3}\ O_2\uparrow \quad (3.3)$$

The mixture was heated to 1050 °C with a rate of 100 °C/h and kept there for about 10 h. The cooling rate was only 1 °C/h down to 900 °C from where the sample was cooled to room temperature with a rate of 100 °C/h. The reaction product was a bunch of dark colored, small, about 1 mm^3 sized, and heavily conjoined crystallites of irregular shape.

$Ba_{0.9}Sr_{0.1}Co_2V_2O_8$ (SN0087)

The mixture for this sample, according to Eq. (3.3) with $x = 0.1$, was put in a platinum crucible and heated to 900 °C where it was kept for one day. After grinding and pressing, the rod was sintered at 900 °C in a corundum ship for one day. Two runs in the mirror furnace with 300 W in a mixture of 80 % Ar / 20 % O_2 under ambient pressure were done for this sample. The first run was performed with a growth rate of 7 mm/h which was obviously too fast because judging from the porous surface and a lot of crinkles due to inner stress. The second run was carried out with growth velocities around 3 mm/h. The establishment of a stable melt was difficult what is reflected by the irregular crystal shape (see Fig. 3.9). However, part of the sample was of good single-crystalline quality.

$Ba_{0.5}Sr_{0.5}Co_2V_2O_8$ (SN0091)

The educts were mixed according to Eq. (3.3) with $x = 0.5$ and heated in a platinum crucible to 900 °C for 10 hours. Afterwards, the sample was carefully ground and pressed into a rod that was sintered in a corundum ship with extra powder between ship and rod for 40 hours at 900 °C. Three runs in the mirror furnace with basically

the same parameters as for SN0087 were necessary to grow the crystal. Here as well, it was not that easy to establish a stable melt and the system developed gas bubbles during the growth processes. In the last run with a growth velocity of only 0.5 mm/h a single crystal with a smooth and shiny surface was grown (see Fig. 3.9).

$Ba_{0.1}Sr_{0.9}Co_2V_2O_8$ (SN0111)

A mixture with the composition of 10 % Ba and 90 % Sr was prepared according to Eq. (3.4). The mixture was heated to 950 °C for 28 h in a platinum crucible with intermediate grinding. The pressed rod was sintered in a corundum ship with extra powder between bottom and rod at the same temperature for another 15 h.

$$0.1\ BaCO_3 + 0.9\ SrCO_3 + 2\ CoCO_3 + V_2O_5 \longrightarrow Ba_{0.1}Sr_{0.9}Co_2V_2O_8 + 3\ CO_2 \uparrow \quad (3.4)$$

After the first run in the mirror furnace (300 W lamps, ambient air, 2.5 mm/h) the resulting sample was very stressed and melted a second time with part of it as seed rod. The growth velocity was kept at 0.5 mm/h and yielded a crystal of about 2 cm length shown in Figure 3.9. The sample is that short because, unfortunately, the melt broke down during the growth process.

$SrCo_2V_2O_8$ (SN0093)

My first growth attempt of $SrCo_2V_2O_8$ was done during my diploma thesis via spontaneous nucleation method, labeled here as SNxx04, but did not yield crystals of usable shape due to drastically conjoined crystallites (*cf.* SN0061) [92]. Sample SN0093 was grown in three runs in the mirror furnace. The precursor was mixed according to Eq. (3.3) with $x = 1$ and heated in a platinum crucible to 900 °C and kept there for 12 h. After pressing, the rod was sintered at 900 °C for one day. For the first growth in the mirror furnace (ambient air, gas flow, 2 mm/h to 7 mm/h) 1000 W lamps were used because of the furnace configuration at that time. In the second run those lamps were used again yielding a very rough surface. This time an atmosphere of 80 % Ar and 20 % O_2 with gas flow and 1.5 bar pressure were used, following Ref. 88. The growth velocity was kept relatively high at 17 mm/h to 25 mm/h. In the third run 300 W lamps, atmospheric air at ambient pressure and very slow growth velocities of 0.5 mm/h to 2 mm/h were chosen. The resulting sample was a stressed single crystal of short length due to break-down of the melt (see Fig. 3.9).

$SrCo_2V_2O_8$ (SN0135)

The precursors, according to Eq. (3.3) ($x = 1$), have been mixed in the ratio 3:2:3 and were put into a platinum crucible that was covered by a corundum lit. The mixture was first heated within 6 h to 700 °C, kept there for 30 h. After intermediate grinding the sample was heated to 850 °C for 10 h. In the third step, the powder was pressed to a rod and sintered at 950 °C for 15 h in a corundum ship with powder between rod and ship. The crystal growth in the mirror furnace was performed in two runs where 300 W lamps and air under ambient pressure were used. The first run was carried out very fast with 27 mm/h to compact the material. In the second run, part of the sample

Table 3.4: Growth processes and obtained lattice constants of the $BaCo_{2-y}M_{2y}V_2O_8$ series with M =Mg, Cu, Ni, Mn. All samples were grown via floating-zone (FZ) method. The resulting samples were either single crystals (sc) or polycrystals (pc) of varying quality.

$M =$	$y =$	Sample	Method	Comment	$a = b$ (Å)	c (Å)	χ^2
Mg	0.1	SN0103*	FZ, Eq. (3.5)	pc, impurities	–	–	–
Mg	0.05	SN0109	FZ, Eq. (3.5)	sc	12.3570(7)	8.4042(5)	2.5
Cu	0.05	SN0123	FZ, Eq. (3.6)	sc, impurities	12.4492(6)	8.3912(5)	2.4
Ni	0.05	SN0141	FZ, Eq. (3.7)	sc, impurities	12.436(1)	8.406(1)	6.1
Mn	0.05	SN0131	FZ, Eq. (3.6)	sc	12.4490(4)	8.4222(3)	4.5

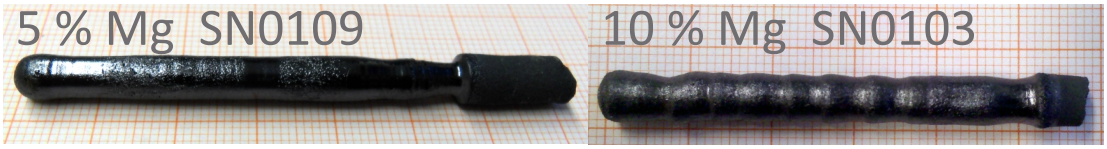

Figure 3.10: $BaCo_{1.9}Mg_{0.1}V_2O_8$ single crystal SN0109. A substitution of 10 % was not successful and the resulting sample was polluted with grains of MgO. Note the wiggled shape of the rod.

SN0093 was used as seed rod. The sample was grown very slowly with a velocity of 0.7 mm/h. The resulting crystal is shown in Figure 3.9 and is of good single crystalline quality.

3.3.3 $BaCo_{2-2y}M_{2y}V_2O_8$, M= Mg, Cu, Mn, Ni

Replacing Co partly by other transition metals or non-magnetic ions is a substitution into the magnetic subsystem. Inducing impurities into the spin chains results in a segmentation of the chains into finite segments and influences the magnetic behavior of the system (see Chapter 6.2). Magnesium was chosen as non-magnetic impurity and the transition metals copper, nickel, and manganese were chosen to vary the spin quantum number. The main aspects of the crystal growth and obtained lattice constants are summarized in Table 3.4. The according X-ray powder patterns are shown in Figure 3.12.

$BaCo_{1.8}Mg_{0.2}V_2O_8$ (SN0103*)

Mg is an alkaline earth like barium and strontium but in a 6-fold coordination its ionic radius is comparable to that of cobalt (see Tab. 3.1) and should, therefore, be able to enter this site. A substitution with 10 % of magnesium was the first attempt and a mixture was prepared according to Eq. (3.5) with $y = 0.1$:

$$3\ (Ba(OH)_2 \cdot 8\ H_2O) + (2-2y)\ Co_3O_4 + 2y\ Mg(OH)_2 + 3\ V_2O_5 \rightarrow$$
$$3\ BaCo_{2-2y}Mg_{2y}V_2O_8 + (27+2y)\ H_2O \uparrow + (1-2y)\ O2 \uparrow . \quad (3.5)$$

The more reactive $Ba(OH)_2 \cdot 8\,H_2O$ and $Mg(OH)_2$ were used to prevent a formation of the very stable MgO during the reaction process. The mixture was heated to 950 °C in a platinum crucible and kept there for 14 h. After grinding and compressing to a rod, the sample was sintered at the same temperature for 30 h. The rod was scanned twice in the mirror furnace (300 W lamps, ambient air) with growth velocities of 5 mm/h in the first run and much slower with 0.5 mm/h in the second run. One big issue during the growth process was the heterogeneous melting of the material. The resulting wiggled shape of the crystal rod (see Fig. 3.10) gives evidence that the melt periodically changed its composition. Cutting the crystal showed that grains of white color, most probably the extremely stable MgO, polluted the sample.

$BaCo_{1.9}Mg_{0.1}V_2O_8$ (SN0109)

A mixture was prepared according to Eq. (3.5) with a lower substitution level of $y = 0.05$. The mixture was heated in a platinum crucible to 900 °C for 6 h. After intermediate grinding and heating at 600 °C for another 6 h, the resulting material was ground, pressed into a rod and sintered at 800 °C in a corundum ship with extra powder between rod and bottom. The rod was grown in two runs in the mirror furnace (300 W lamps, ambient air) with a growth velocity of 2 mm/h in the first run. Figure 3.10 shows the sample SN0109 after the first run in the mirror furnace. The sample already shows a partly smooth surface and no wiggled shape but was very stressed inside and had a lot of crinkles. Therefore, part of the rod was used as seed rod for the second run where a growth velocity of 1.4 mm/h lead to a single crystal of good crystalline quality.

$BaCo_{1.9}Cu_{0.1}V_2O_8$ (SN0123)

A substitution of 5 % Cu into $BaCo_2V_2O_8$ was prepared according to Eq. (3.6) (CuO: Alfa Aesar 99.995 %):

$$BaCO_3 + 1.9\ CoCO_3 + 0.1\ CuO + V_2O_5 \rightarrow BaCo_{1.9}Cu_{0.1}V_2O_8 + 2.9\ CO_2 \uparrow . \quad (3.6)$$

The mixture was pre-reacted in a platinum crucible at 800 °C for 26 h with intermediate grinding. The pressed rod was sintered at 600 °C for 50 h and was processed in the mirror furnace (300 W lamps, ambient air) twice. The first run was carried out fast (15 mm/h) to compact the rod. The second run was carried out very slowly with 0.6 mm/h and yielded a single crystal with a shiny and smooth surface and of good crystalline quality (see Fig. 3.11). The X-ray powder diffraction pattern, Fig.3.12 (b), shows an indication of small impurities in the low-angle region (yellow area).

Figure 3.11: Single crystals of $BaCo_{1.9}Cu_{0.1}V_2O_8$ (SN0123), $BaCo_{1.9}Mn_{0.1}V_2O_8$ (SN0131) and $BaCo_{1.9}Ni_{0.1}V_2O_8$ (SN0141).

$BaCo_{1.9}Ni_{0.1}V_2O_8$ (SN0141)

A mixture for a nickel substitution of 5 % was produced according to Eq. (3.7) (NiO: Alfa Aesar 99.998 %) and pre-reacted in a platinum crucible at 900 °C for 10 hours.

$$3\ BaCO_3 + 1.9\ Co_3O_4 + 0.1 \cdot 3\ NiO + 3\ V_2O_5 \rightarrow 3\ BaCo_{1.9}Ni_{0.1}V_2O_8 + 3\ CO_2\uparrow + 0.95\ O_2\uparrow \quad (3.7)$$

A rod was pressed and sintered in a platinum ship at the same temperature for 10 hours. The rod was scanned twice in the mirror furnace (300 W lamps, ambient air) with a very fast first run (27 mm/h) and a very slow second run with a growth velocity of 0.5 mm/h. The resulting crystal is shown in Figure 3.11 (right panel) and shows a partly smooth surface but is stressed inside and seems to contain small impurities (yellow areas) according to the powder pattern.

$BaCo_{1.9}Mn_{0.1}V_2O_8$ (SN0131)

A sample with a substitution of 5 % manganese was prepared according to Eq. (3.6) using MnO(Aldrich 99 %) instead of CuO: The mixture was pre-reacted in a platinum crucible at 800 °C for 26 h with intermediate grinding. The pressed rod was sintered at 600 °C for 50 h and processed in the mirror furnace twice (300 W lamps, ambient air). The growth velocity in the first run was fast with 8 mm/h to 15 mm/h. The growth was interfered by the upcoming of gas bubbles in the melt. The second run was carried out very slowly with a growth velocity of 0.5 mm/h. The resulting single crystal of about 4 cm length can be seen in the bottom left panel of Figure 3.11 (SN0131).

3.3.4 Non-magnetic Reference Systems

A non-magnetic reference system with the same structure as $BaCo_2V_2O_8$ would be of great interest to separate magnetic from non-magnetic phenomena. Suitable candidates are the $(Ba/Sr)(Mg/Zn)_2V_2O_8$ compounds. Only one of them, $BaMg_2V_2O_8$, was reported to be synthesized so far [15]. Several attempts to grow these crystals were unfortunately not successful. The growth attempts are summarized in Table 3.5. First attempts have been done with the educt MgO but this material is, in fact, much too stable to react. Therefore, magnesium hydroxide $Mg(OH)_2$ (Alfa Aesar, ≥ 95 %)

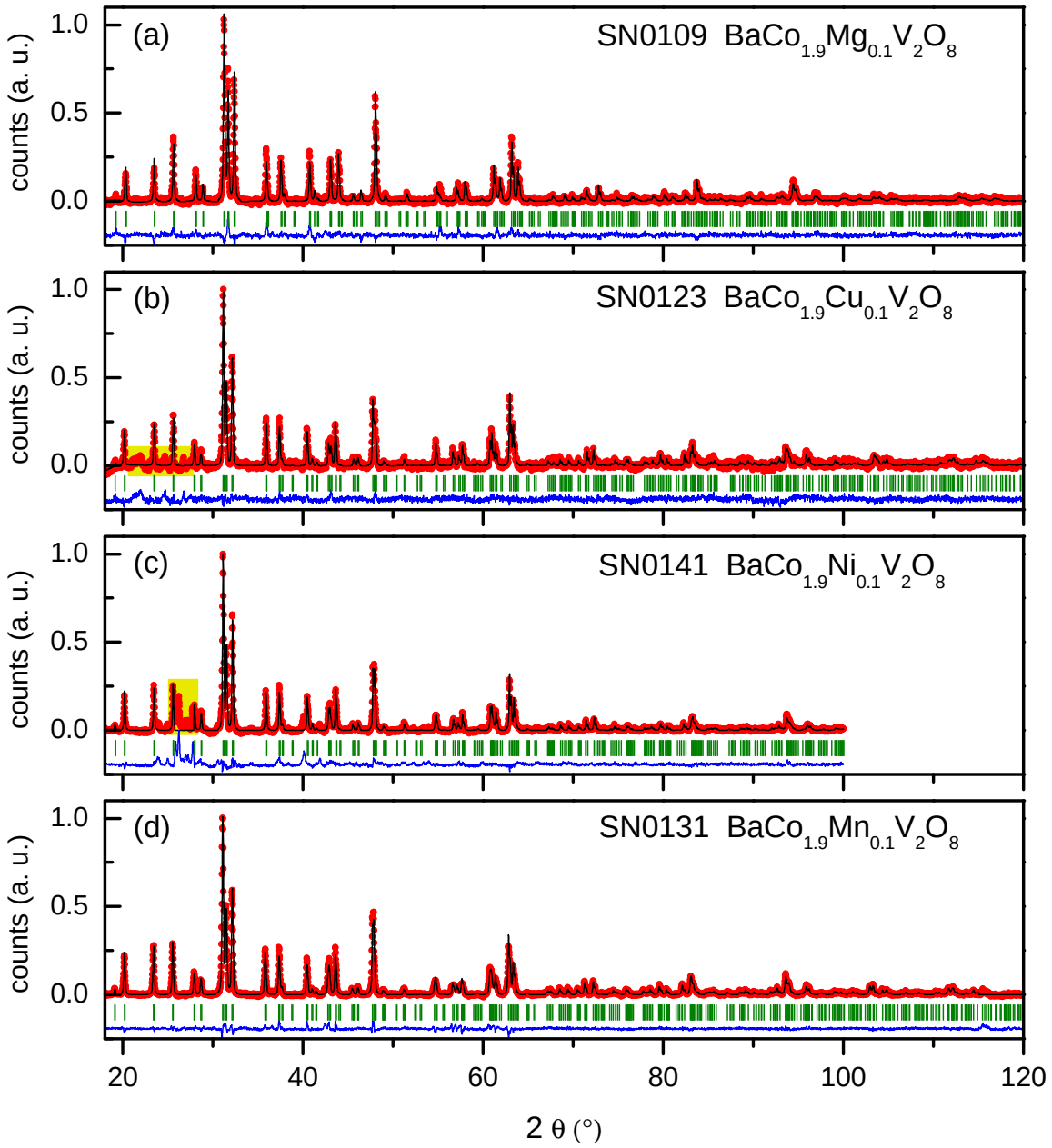

Figure 3.12: X-ray powder diffraction patterns of the $BaCo_{1.9}M_{0.1}V_2O_8$ series with each 5 % of Mg (a), Cu (b), Ni (c), and Mn (e), respectively. Yellow areas mark impurity peaks in the low-angle region. Green bars are the calculated Bragg positions, red points mark the measured data, the black line is the calculated intensity, and the blue line gives the difference between measurements and fit.

with a suitable melting point of 839 °C [65] was chosen. To enhance the reactivity also barium hydroxide $Ba(OH)_2{\cdot}8\ H_2O$ (Sigma Aldrich,≥98 %) was used.

Growth attempts of $BaMg_2V_2O_8$ were tried with several starting reaction equations and several heating processes that can be found in Table 3.5. Maybe, the first three attempts were not reacted thoroughly enough because the results were consisting of several constituents of different colors. For, e.g., sample SN0115 two heating cycles

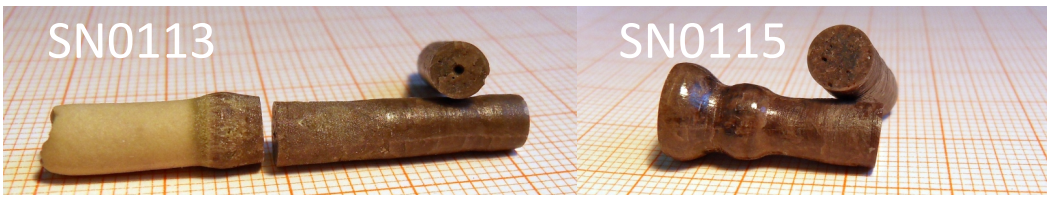

Figure 3.13: Unsuccessful growth attempts of the non-magnetic reference systems $SrMg_2V_2O_8$ (SN0113) and $BaMg_2V_2O_8$ (SN0115) that were grown in the mirror furnace. The material is inhomogeneous in color and not single phased. Note the hole in the middle of the rod of SN0113.

with intermediate grinding were necessary to let the mixture react into a single phase. The mixture for sample SN0115 was first slowly heated to 630 °C and kept there for 10 h. Further heating to a temperature of 800 °C followed where it was kept for another 10 h. After that reaction the product seemed not to be single phase because it was of white color with brown grains. Therefore, it was carefully ground and heated to 950 °C for ten hours. The sample was again heavily compressed and the resulting powder sample was of light yellow color. The X-ray powder pattern is shown in Figure 3.12 (a) and the obtained lattice parameters from the refinement using space group No. 142 (as suggested by literature) are $a = 12.4015(3)$ Å $c = 8.4552(2)$ Å ($\chi^2 = 5$) (Ref. $a = 12.4189(8)$ Å $c = 8.4657(17)$ Å [15]). A pressed powder sample of SN0115 was used for reference measurements of the specific heat (*cf.* Ch. 4).

Also, part of this sample was prepared for the mirror furnace and a rod was sintered at 900 °C for one day. The growth in the mirror furnace was carried out with 300 W lamps in ambient air. The growth velocity was kept at 6.6 mm/h and a stable melt could be established. However, the resulting sample was not single crystalline as can be seen in the right panel of Figure 3.13.

In an analogous way, attempts to grow a sample of $SrMg_2V_2O_8$ yielded the same problems concerning impurities, see left panel of Figure 3.13. Thus, this project was not pursued further.

3.3.5 $Ba/SrMn_2V_2O_8$

Because Mn^{2+} is of $3d^5$ configuration and has a large spin of $S = 5/2$ $BaMn_2V_2O_8$ as well as $SrMn_2V_2O_8$ are a nearly isotropic Heisenberg chain variant of the $AM_2V_2O_8$ compounds (see Chapter 4). For low spin quantum numbers the physics is strongly influenced by quantum fluctuations, while for higher spins a more classical behavior is expected. Because of this and because only few spin-chain compounds containing Mn^{2+} have been studied so far the synthesis of both compounds was of particular interest.

$BaMn_2V_2O_8$

$BaMn_2V_2O_8$ was first synthesized in 1992 by von Postel and Müller-Buschbaum [17] by a solid-state reaction just below the melting point (1100 °C) in an argon atmosphere. Small, dark-red crystals could be grown and the crystal structure was refined

Table 3.5: Growth attempts of non-magnetic reference systems (Ba,Sr)$Mg_2V_2O_8$ and (Ba,Sr)$Zn_2V_2O_8$. All of them were grown with a solid-state reaction. SN0113 and SN0115 were additionally processed in the mirror furnace.

Sample		Comment
$BaMg_2V_2O_8$	SN0095*	$BaCO_3 + 2\,MgO + V_2O_5 \rightarrow BaMg_2V_2O_8 + CO_2\uparrow$
	SN0097*	$Ba(OH)_2 \cdot 8H_2O + 2\,MgO + V_2O_5 \rightarrow BaMg_2V_2O_8 + 9 \cdot H_2O\uparrow$
	SN0099*	$Ba(OH)_2 \cdot 8H_2O + 2 \cdot Mg(OH)_2 + V_2O_5 \rightarrow BaMg_2V_2O_8 + 9 \cdot H_2O\uparrow$
	SN0115	$BaV_2O_6 + 2 \cdot Mg(OH)_2 \rightarrow BaMg_2V_2O_8 + 2H_2O\uparrow$
$SrMg_2V_2O_8$	SN0101*	$SrCO_3 + 2 \cdot Mg(OH)_2 + V_2O_5 \rightarrow SrMg_2V_2O_8 + 2 \cdot H_2O\uparrow + CO_2\uparrow$
	SN0113*	$SrV_2O_6 + 2 \cdot Mg(OH)_2 \rightarrow SrMg_2V_2O_8 + 2 \cdot H_2O\uparrow$
$SrZn_2V_2O_8$	SN0117*	$SrV_2O_6 + 2 \cdot ZnO \rightarrow SrZn_2V_2O_8$
$BaZn_2V_2O_8$	SNxx *	$BaV_2O_6 + 2 \cdot ZnO \rightarrow BaZn_2V_2O_8$

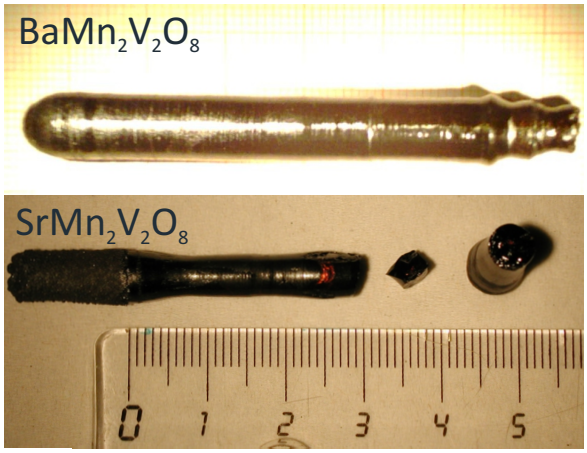

Figure 3.14: Samples of $BaMn_2V_2O_8$ (top panel) and $SrMn_2V_2O_8$ (bottom panel). Both crystals developed shiny surfaces and are of dark orange colour.

as $I4_1/acd$ (No. 142) with lattice constants $a = 12.5563(14)$ Å and $c = 8.5942(9)$ Å. A lower symmetry $I4_1cd$ (No. 110) with different lattice constants $a = 12.267(1)$ Å and $c = 8.424(1)$ Å was reported later by He *et. al.* [18]. Only powder studies on magnetization and specific heat can be found in literature [18]. Therefore, it was of interest to grow large single crystals for more specific investigations.

This thesis, or rather the former Diploma thesis [92], contains the first report of single crystal growth of $BaMn_2V_2O_8$ in a mirror furnace. The first reaction step was the synthesis of BaV_2O_6 (Eq. (3.9)). A platinum crucible served as reaction vessel and the temperature was kept at 800 °C for one hour. In the second step the product was mixed with MnO in the molar ratio 1:2, see Eq. (3.9) ($BaCO_3$: Merck ≥ 99 %, V_2O_5: Strem Chemicals 99.5 %, MnO: Aldrich ≥ 99 %).

$$BaCO_3 + V_2O_5 \rightarrow BaV_2O_6 + CO_2\uparrow \tag{3.8}$$

$$BaV_2O_6 + 2\,MnO \rightarrow BaMn_2V_2O_8 \tag{3.9}$$

After homogenization the powder mixture was pressed into a seed and feed rod and prepared for single crystal growth in the mirror furnace. The rods were prepared without further pre-reaction or sintering to prevent from evaporation of the manganese. The crystal was grown with 150 Watt lamps and at 1 bar argon atmosphere. To purify the argon gas a small corundum crucible was attached at the base of the seed bar that was filled with metallic titanium. Heating up the titanium enhances its reactivity and small rests of O_2 and/or N_2 in the argon gas are bound. The sample had a stable melt and the resulting crystal (see Fig. 3.14) was of about 7 cm length and 8 mm diameter and had a shiny surface.

For the X-ray powder diffraction, part of the crystal was carefully ground into a dark-orange powder. The lattice constants are $a = 12.6163(7)$ Å and $c = 8.6692(5)$ Å and the used space group is the centrosymmetric $I4_1/acd$ ($\chi^2 = 3$). The powder pattern is shown is shown in Figure 3.15 (a). Besides magnetization, specific heat, thermal expansion, and magnetostriction measurements, neutron powder diffraction at different temperatures was carried out on this compound, see Section 4.1.

$SrMn_2V_2O_8$

To the best of my knowledge, until recently $SrMn_2V_2O_8$ was not known in literature. In analogy to $BaCo_2V_2O_8$ and $SrCo_2V_2O_8$ the synthesis of $SrMn_2V_2O_8$ was attempted as attendance to the known compound $BaMn_2V_2O_8$. As a precursor for the main synthesis, SrV_2O_6 was synthesized by a solid-state reaction according to Eq. (3.11). The mixture of $SrCO_3$ (Alfa Aesar 99.99 %) and V_2O_5 was heated up in a platinum crucible and kept at 1000 °C for three hours. Subsequently, SrV_2O_6 was mixed with MnO in the molar ratio of 1:2.

$$SrCO_3 + V_2O_5 \rightarrow SrV_2O_6 + CO_2 \uparrow \tag{3.10}$$

$$SrV_2O_6 + 2\ MnO \rightarrow SrMn_2V_2O_8 \tag{3.11}$$

After homogenization in an agate mortar the powder mixture was pressed into a seed and feed rod to start the reaction directly in the mirror furnace (300 W lamps, argon, ambient pressure). The resulting single crystal is shown in the lower part of Figure 3.14. One can already see the orange color of the crystal at the top of the main part of the sample. Part of the cm-sized crystal was crushed into a dark orange powder for X-ray diffraction. Using the tetragonal non-centrosymmetric space group $I4_1cd$ (No. 110) the obtained cell parameters are $a = 12.4422(9)$ Å and $c = 8.6833(6)$ Å [19]. The refined powder pattern is shown in Figure 3.15 (b).

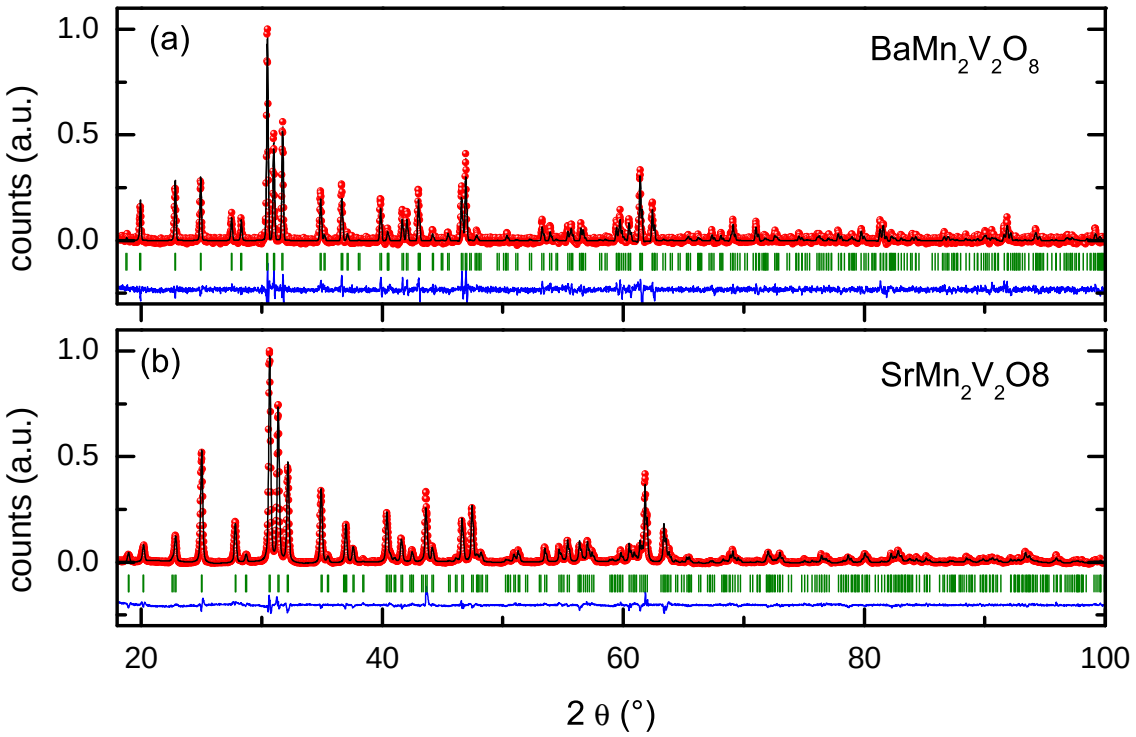

Figure 3.15: X-ray powder diffraction patterns of (a) $BaMn_2V_2O_8$ and (b) $SrMn_2V_2O_8$ refined with the space groups $I4_1/acd$ and $I4_1cd$, respectively. Green bars are calculated Bragg positions, measured data are red points, black lines is the fitted intensity, and the blue lines give the difference between measurements and fit.

4 $S = 5/2$ Heisenberg chains

Due to the increasing importance of quantum fluctuations for small spin quantum numbers one is mostly interested in $S = 1/2$ or $S = 1$ systems while a more classical behavior is expected for larger spins. Only few low-dimensional magnets with a large spin of $S = 5/2$ have been investigated so far, e.g., a clinopyroxene $CaMnGe_2O_6$ [93], the spin-ladder compound $BaMn_2O_3$ [20], or $CsMnCl_3 \cdot 2H_2O$ which is a Heisenberg spin chain [21, 22]. With $BaMn_2V_2O_8$ and $SrMn_2V_2O_8$ two additional spin-chain systems are introduced into that group of low-dimensional magnets with a large spin.

4.1 $BaMn_2V_2O_8$

4.1.1 Introduction

Small single crystals of the compound were first synthesized in 1992 using a spontaneous nucleation method [17]. $BaMn_2V_2O_8$ represents a nearly isotropic Heisenberg $S = 5/2$ system within the group of the $AM_2V_2O_8$ compounds. The large spin of 5/2 corresponds to a half-filled $3d$ shell and, thus, according to Hund's rules $L = 0$. Therefore, anisotropy due to spin-orbit coupling should be absent. Up to now, only one publication is available which concerns the physical properties of this compound [18] which was carried out on a powder sample. Figure 4.1 shows the field and temperature dependent magnetization and the specific heat of $BaMn_2V_2O_8$ as reported

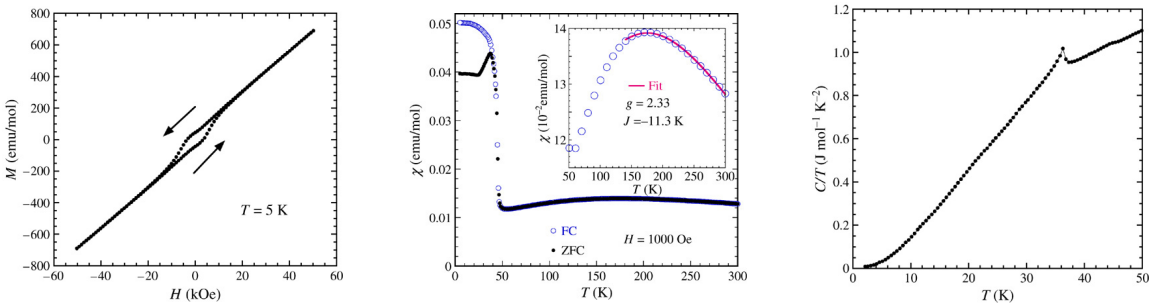

(a) **(b)** **(c)**

Figure 4.1: Literature data of $BaMn_2V_2O_8$ [18] measured on a powder sample. (a) Field dependent magnetization $M(H)$ (left) measured at 5 K. (b) Magnetic susceptibility $\chi(T)$ for a zfc (black) and a fc (blue) measurement. (c) Specific heat $\frac{c(T)}{T}$ in zero magnetic field.

in Ref. 18. The field dependent magnetization shows a nearly linear behavior in the higher field range but a hysteresis in the low field-range of about ± 1 T. $BaMn_2V_2O_8$ is described as a one-dimensional spin-chain system showing a typical maximum in the T-dependence of the magnetization around 170 K. A significant difference between zero-field cooled (zfc) and field cooled (fc) data below the relatively high ordering temperature of $T_N = 37$ K is observed. A canted antiferromagnetic state is reported below T_N. Dzyaloshinskii-Moriya interactions were used to explain a spin canting. The specific heat $c(T)/T$ measured in zero magnetic field, shows a clear anomaly at T_N and an additional kink at 47 K which was interpreted as the onset of long range ordering [18].

This thesis presents the first investigation of $BaMn_2V_2O_8$ on large single crystals that were grown by the floating zone method in a mirror furnace (see Sec. 3.3.5). After a discussion of the crystal structure, direction dependent measurements of the thermodynamic properties of $BaMn_2V_2O_8$ on a single crystal will be presented. $BaMn_2V_2O_8$ was investigated by means of specific heat, magnetization, thermal conductivity [53] and thermal expansion/magnetostriction measurements.

Structure

The two papers about $BaMn_2V_2O_8$ (Refs. 17, 18) state two different space groups for the structure of $BaMn_2V_2O_8$. Postel *et al.* [17] report the centrosymmetric structure $I4_1/acd$ (No. 142) such that $BaMn_2V_2O_8$ is isostructural to $BaCo_2V_2O_8$. Ref. 18 was published later about the magnetic properties and reports the non-centrosymmetric space group $I4_1cd$ (No. 110). Both structures are closely related and were already introduced in Chapter 2.1 (cf. Fig. 3.3 p. 24). Due to the structural closeness it is not possible to unambiguously distinguish them in an X-ray powder pattern. The centrosymmetric space group $I4_1/acd$ has two different oxygen positions whereas in the non-centrosymmetric space group $I4_1cd$ four different oxygen positions are present which yields more degrees of freedom in the refinement of a neutron or X-ray powder pattern. In case of X-rays one has to keep in mind that this technique is not very sensitive to the oxygen positions, whereas the vanadium is nearly invisible in a neutron experiment.

For the powder refinement presented in Section 3.3.5 the centrosymmetric space group $I4_1/acd$ was used as originally reported in Ref. 17. Anyway, the lattice constants do not vary significantly when the other space group is used. The obtained lattice constants agree well with the values reported by Postel et al. [17], see Table 4.1, but are slightly higher.

In order to observe the onset of magnetic order in $BaMn_2V_2O_8$ a neutron powder diffraction study in zero magnetic field was performed at different temperatures above and below the transition temperature of 37 K. The measurements were carried out at the D2B facility at ILL, Grenoble [94] by J. Brand. The incident wavelength was 1.59 Å. Powder pattern were obtained for four different temperatures, i.e. at 2 K, 45 K, 150 K and 290 K. The FULLPROF refinement of the powder pattern carried out by J. Brand showed a better result when using the non-centrosymmetric space group $I4_1cd$. The refined pattern as well as the different Ba–O, Mn–O and V–O bond lengths as a function of temperature are shown in the Appendix, Figures B.1 and B.2. There

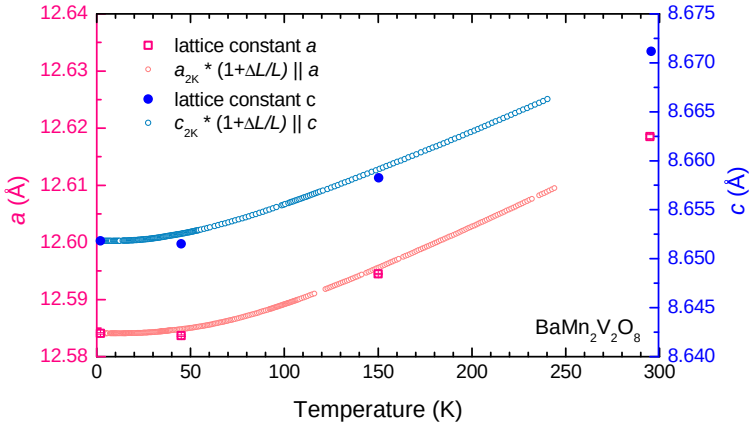

Figure 4.2: Temperature dependant lattice constants a (red) and c (blue) of $BaMn_2V_2O_8$ obtained by neutron powder diffraction. For comparison the respective thermal expansions $\Delta L/L$ for both directions are included ($\circ$).

Source	$a = b$ (Å)	c (Å)
Postel et al. [17]	12.5563(14)	8.5942(9)
He et al. [18]	12.267(1)	8.424(1)
XPD	12.6163(7)	8.6692(5)
NPD (JB)	12.6185(4)	8.6712(3)
NPD (MV)	12.6229(2)	8.6740(1)

Table 4.1: Lattice constants of $BaMn_2V_2O_8$ at room temperature as given in literature and obtained from X-ray powder diffraction (XPD) and by neutron powder diffraction (NPD) carried out by J. Brand (JB) and M. Valldor (MV) [95].

are no additional magnetic peaks occurring below T_N, i.e. at 2 K. Within the pattern the reflections do neither split nor change in position except for the normal thermal expansion, thus, $BaMn_2V_2O_8$ does not undergo a significant structural distortion. Judging from that, the structure remains the same over the whole temperature range and no purely magnetic peaks are observable. The refined temperature dependent lattice constants a and c, Figure 4.2, provide mainly the normal thermal expansion. The respective thermal expansion measurements $\Delta L/L$ are included for comparison, i.e. $x_{2\,K} \cdot (1 + \frac{\Delta l}{L})$, where $x_{2\,K}$ is the lattice constant a or c at $T = 2\,K$.

Because the spin structure of $BaMn_2V_2O_8$ is not known in literature up to now, an experiment for the determination of the spin structure by single crystal neutron diffraction was carried out at HEIDI, München, by A.C. Komarek in collaboration with M. Valldor. This experiment should, in principle, also answer the question which space group is present. However, due to, among others, technical problems the magnetic structure determination is pending and the issue which space group is present in the lattice structure could not be answered unambiguously.

Table 4.1 gives an overview of the lattice constants at room temperature given in literature and the data obtained by X-ray powder diffraction (XPD) method and neutron powder and single crystal diffraction studies that were carried out and analyzed by J. Brand and M. Valldor/ A.C. Komarek, respectively [95]. Larger lattice constants than reported in literature are obtained in all three independent measurements. Especially, they differ significantly from those reported by He et al..

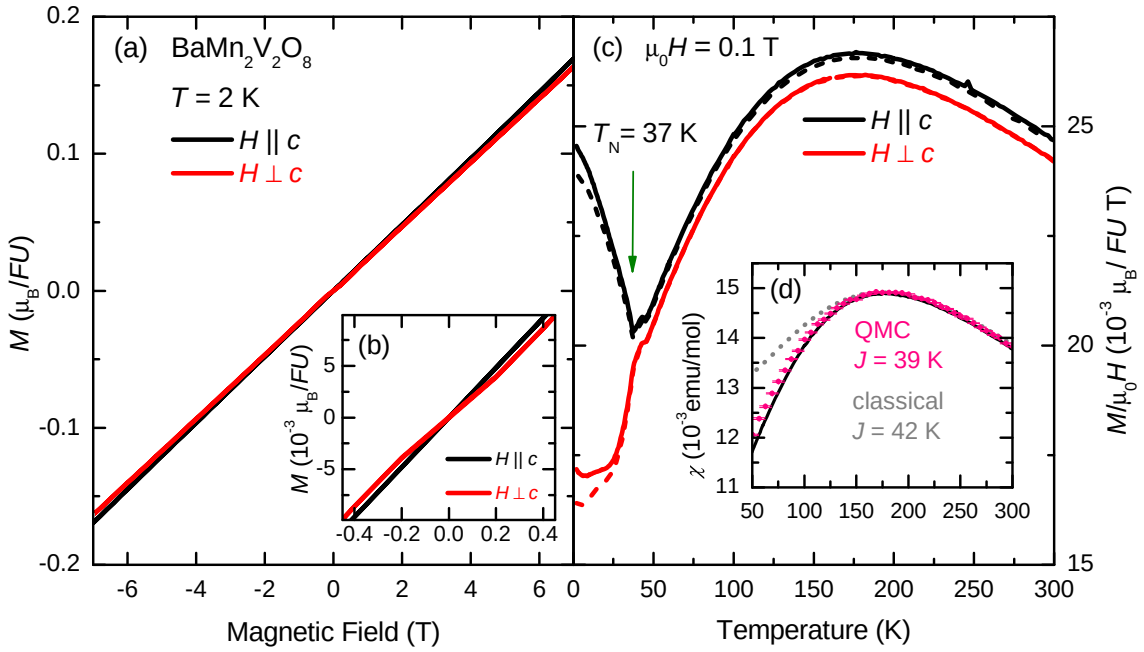

Figure 4.3: (a) Field dependent magnetization of $BaMn_2V_2O_8$ for magnetic field $H \,||\, c$ (black) and $H \perp c$ (red) at 2 K. The inset (b) shows an enlargement of the low field region. Panel (c) shows the temperature dependent magnetization $\frac{M}{\mu_0 H}(T)$ in an external magnetic field of 0.1 T for fc (solid lines) and zfc (dashed lines) measurements. (d) The same curve for $H \,||\, c$ (fc) in units of (emu/mol) in comparison with a QMC fit (pink circles) for a spin-5/2 chain (see text).

4.1.2 Magnetic (An-) Isoptropy and Modeling

Figure 4.3 shows the magnetization of $BaMn_2V_2O_8$ for magnetic fields applied along the c axis (black) and perpendicular to c (red) [1]. For both field directions a linear dependence on the magnetic field is seen. A magnetization of about $0.17\,\mu_B/FU$ at the maximum magnetic field of 7 T is reached. This value is consistent with the powder literature measurements and corresponds to less than 2 % of the expected fully polarized magnetization of about $M_{Sat} = 10\,\mu_B/FU$ for two magnetic Mn^{2+} ions. The fact that $M(7\,T, 2\,K)$ is much smaller than the saturation value M_{Sat} proofs an antiferromagnetic coupling of the magnetic ions. Inset (b) shows an enlargement of the same data in the low field region. While for $H \,||\, c$ the curve goes linearly through zero, the magnetization for $H \perp c$ is s-shaped in the field range of ± 0.2 T.

The temperature dependent magnetization, shown in panel (c) of Figure 4.3, is isotropic in the high-temperature range and shows a broad maximum around 170 K in good agreement with Ref. 18. This maximum confirms the low-dimensionality of the magnetic system and indicates the presence of short-range correlations. A small kink around $T = 47$ K is observed. The onset of magnetic order, however, is reflected in a prominent anomaly at $T_N = 37$ K (green arrow). Below the transition temperature, the $H \,||\, c$ curve (black) shows a slight increase with decreasing temperature. For

[1] Because of the expected isotropic behavior of $BaMn_2V_2O_8$ the field direction perpendicular to the c axis was not fixed to a certain crystallographic direction as it is necessary in $BaCo_2V_2O_8$.

application of the magnetic field perpendicular to c (red) the magnetization decreases below T_N. In an antiferromagnet, the susceptibility below T_N depends on the direction of the magnetic field and an orientation of the spins perpendicular to the magnetic field is energetically favorable. Because $\chi^{||} < \chi^{\perp}$, i.e. the susceptibility parallel to the magnetic easy direction is smaller than the susceptibility perpendicular to it, the susceptibility of $BaMn_2V_2O_8$ suggests that the moments prefer an alignment within the *ab*. Therefore, in the low field region one identifies $\chi_{||c} = \chi^{\perp}$ and $\chi_{\perp c} = \chi^{||}$ (see Sec. 4.1.3).

In Figure 4.3 (c) fc and zfc measurements are presented by solid and dashed lines, respectively. For both field directions, the zfc data are slightly reduced compared to the fc data by roughly the same amount. In literature, a weak ferromagnetic signal was claimed to be observed in the difference of fc and zfc susceptibility measurements and a remanent magnetization was found [18]. This ferromagnetic contribution was supposed to be caused by the antisymmetric Dzyaloshinskii-Moriya interaction due to the non-centrosymmetric crystal structure of $BaMn_2V_2O_8$. Moreover, in this reference a small kink around 47 K was observed in specific heat measurements which was identified as the onset of long range order. At the same temperature the magnetization data presented in this thesis also show a small kink, but taking the s-shape of $M(H)$ and the small differences between fc and zfc data of $M(T)$, these signals are rather caused by a small impurity, especially as the specific heat as well as the thermal conductivity (see below) do not show any anomaly at 47 K. The above presented magnetization data do not give evidence for a spin canting and, thus, there is no argument for Dzyaloshinskii-Moriya interactions within $BaMn_2V_2O_8$. Probably, the amount of impurities was simply larger in the polycrystalline sample of Ref. 18.

The transition temperature T_N is also reflected in an anomaly of the specific heat. Figure 4.4 (a) displays $c_p(T)/T$ of $BaMn_2V_2O_8$ (blue) in zero field measured from 2 K to 300 K. The curve matches the data published in Ref. 18 and reveals a sharp anomaly at 37 K but no additional kink at 47 K. Included in this figure are similar data of a pressed powder sample of the non-magnetic reference substance $BaMg_2V_2O_8$ (gray closed symbols). This reference system is supposed to be a suitable model system for the underlying phononic background. The resulting magnetic specific heat $c_{\mathrm{mag}} = c_{\mathrm{BaMn}}(T) - c_{\mathrm{BaMg}}(A \cdot T)$, derived by subtracting the reference from the $BaMn_2V_2O_8$ data, is shown in panel (c) and reveals a maximum around 70 K. Note, that the temperature of the subtracted reference data was scaled by a factor of 0.87 (open symbols, panel (a)) such that the total entropy of this magnetic part, i.e. $S_{mag} = \int \frac{c_{\mathrm{mag}}}{T} \mathrm{dT}$ shown in panel (d), matches the theoretically expected value of $R \ln 6$ (dashed line) for a magnetic spin $S = 5/2$ system.

Further information about the phononic system of $BaMn_2V_2O_8$ reveals the thermal conductivity which was investigated in Refs. 23, 53. The thermal conductivity $\kappa_{||c}(T)$ is significantly larger than $\kappa_{\perp c}(T)$ over the whole temperature range, particularly also below the transition. The anisotropy of κ can most probably be attributed to the tetragonal structure of $BaMn_2V_2O_8$ which leads to anisotropic phonon branches. Both curves show a large maximum around 11 K but the transition into the Néel ordered phase is reflected only in a small kink of $\kappa_{\perp c}(T)$. The thermal conductivity may, thus, be basically unaffected by scattering on magnetic excitations as suggested by the absence of a sharp anomaly. $BaMn_2V_2O_8$ shows a very different behavior,

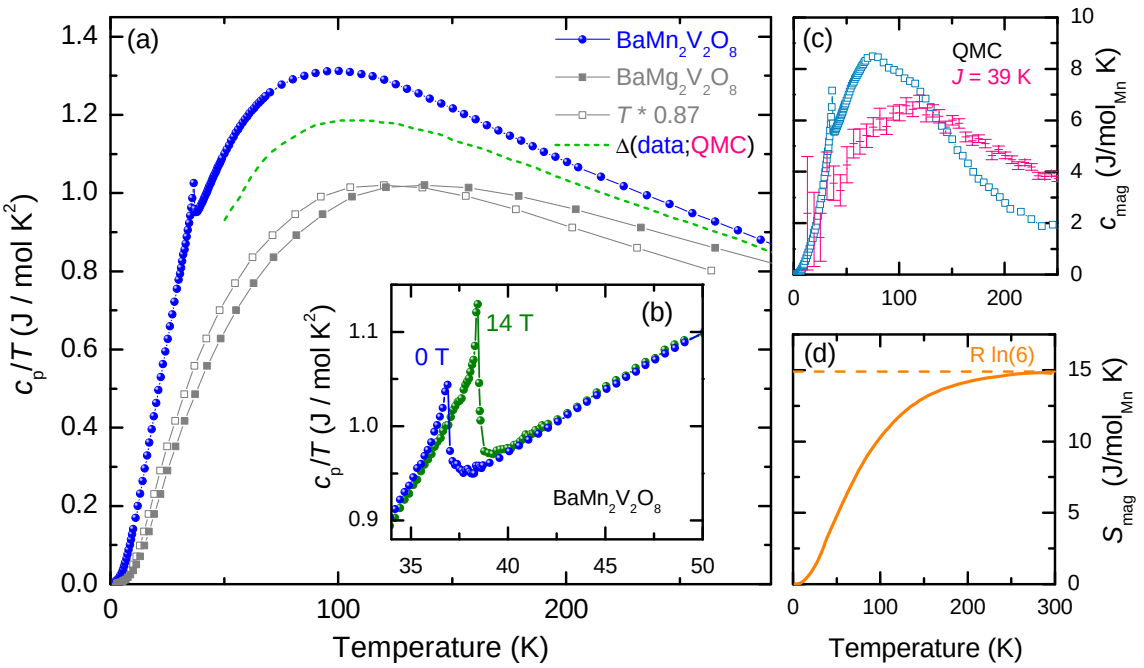

Figure 4.4: (a) Zero-field specific heat $c_p(T)/T$ of $BaMn_2V_2O_8$ (blue) and of the non-magnetic reference system $BaMg_2V_2O_8$ (gray). Open symbols show the $BaMg_2V_2O_8$ data with a rescaled temperature scale (see text). The inset (b) shows the specific heat for 0 T (blue) and 14 T (green). Panel (c) shows the difference $c_{\mathrm{mag}} = c_{\mathrm{BaMn}} - c_{\mathrm{BaMg}}$ and according QMC fits. Panel (d) shows the magnetic entropy S_{mag} and the theoretical value of $R \ln 6$ (dashed line) for high temperatures.

compared to the thermal conductivity of $BaCo_2V_2O_8$ [23, 53, 96]. In $BaCo_2V_2O_8$ a sharp anomaly was observed at the Néel transition and a strong anisotropy was found below the transition.

QMC Modeling

Figure 4.5 summarizes different simulations of the magnetic susceptibility made for a spin-5/2 Heisenberg chain. These simulations yield a theoretical magnetic susceptibility χ_{calc} as a function of the reduced temperature $T' = T/J$. In this representation the quantities are dimensionless. The classical model by Fisher [97] assuming the limit of $S \to \infty$ was rewritten by Kim et al. [98] in terms of an energy scale $J \cdot S(S+1)$ for arbitrary J. The resulting curve is depicted as a dashed line in Figure 4.5 yielding a maximum at $\simeq 4.17$.

Kim et al. also published a Quantum Monte Carlo (QMC) calculation of a spin-5/2 chain using system sizes up to the order of 10^6. The data by Kim et al. ($\triangledown$) suffer from an error introduced by the digitizing of data and furthermore only few data points are presented close to the maximum of χ. This introduces a rather pronounced error while fitting the data, because the absolute value of the maximum is very sensitive to small changes in J. Therefore, Quantum Monte Carlo calculations of a spin 5/2 chain using the ALPS code [99] were performed by O. Breunig [95] in order to describe the susceptibility of $BaMn_2V_2O_8$. The simulation was carried out for different chain

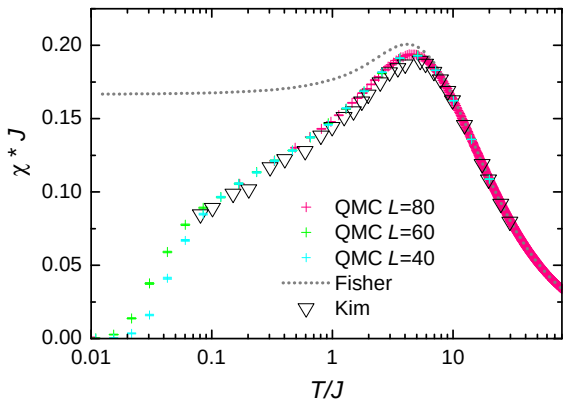

Figure 4.5: Different simulations of the magnetic susceptibility $\chi_{\mathrm{calc}} = \chi \cdot J$ of a spin-5/2 chain as a function of $T' = T/J$. The plot compares the classical result by Fisher [97] (dashed line) with the numerical Monte Carlo results by Kim et al. [98] ($\triangledown$) and our QMC simulation based on the ALPS code [99] performed for different chain lengths of $L = 40$ (pink), 60 (green) and 80 (blue) to estimate the onset of finite size effects.

lengths up to $L = 80$ to estimate the onset of finite size effects. The results of these QMC simulations for $L = 40, 60$ and 80 are also shown in Figure 4.5 as crosses. Within the temperature range, where finite-size effects in the calculations are negligible, the three QMC simulations almost lie on top of each other. The QMC calculations feature a maximum at $T/J \simeq 4.34$.

Fitting a measured susceptibility χ_{meas} by χ_{calc} as a function of a rescaled temperature T' is to derive the proper value of J which fits the model to the data by dividing χ_{calc} by J and multiplying the temperature scale T' by J, i.e.

$$\chi_{meas} = 2 \cdot \frac{g^2 N_{\mathrm{A}} \mu_{\mathrm{B}}^2}{k_{\mathrm{B}}} \cdot \frac{\chi_{\mathrm{calc}}(T' \cdot J)}{J}, \tag{4.1}$$

where the prefactor $\frac{g^2 N_{\mathrm{A}} \mu_{\mathrm{B}}^2}{k_{\mathrm{B}}} \approx 1.50\,\mathrm{emu/mole\ K}$ stems from a unit conversion assuming $g = 2$, which is expected for Mn^{2+} ($S = 5/2$, $L = 0$). Since the simulation takes only one magnetic ion into account and the unit cell comprises two magnetic ions, a factor of 2 has to be included. The inset (d) of Figure 4.3 shows the same $H \,||\, c$ magnetization data (black) in units of (emu/mole) and the resulting fit with the QMC date and $L = 80$ (pink) for an antiferromagnetic inter-chain interaction $J = 39\,\mathrm{K}$. Deviations between measurement and fit occur for temperatures below 50 K which is the region where the magnetic order sets in. Using the classical model yields a slightly higher coupling of $J' \simeq 42\,\mathrm{K}$ (gray dotted line) which results from the lower lying maximum of the model (see above) but the deviations to the data are much stronger directly below the maximum. Moreover, the shown line had to be corrected by a slightly enhanced g factor of 2.04 to match the data. The strong deviations of the classical results arises due to the fact that the classical limit of $S \to \infty$ fully neglects quantum fluctuations that reduce the magnetization to smaller values.

In Ref. 18 the susceptibility (above $T = 170\,\mathrm{K}$) of $BaMn_2V_2O_8$ was fitted by the spin-5/2 linear chain model citing Refs. 21, 97. He et al. report a coupling constant of $\tilde{J} = -11\,\mathrm{K}$ and an enhanced g factor of 2.33. The different sign of J can easily be explained by a different sign convention but my classical treatment of the data yields a roughly 4 times larger value of J. This could be explained by the very unlikely case of $J = 4\tilde{J}$ convention used in Ref. 18. However, the enhanced g factor of 2.33 is about 30 % larger than the correction factor needed to match the data (see above). However, the QMC calculation presented here yields the better description of the $BaMn_2V_2O_8$

susceptibility with $J = 39\,\mathrm{K}$.

The same QMC simulation was done for the magnetic specific heat c_{mag} which is shown in Figure 4.4 (c). The green points are results using $J = 39\,\mathrm{K}$ as obtained from χ. The maximum of the fit does not match the maximum of c_{mag}. The description of the specific heat is much more complicated due to some aspects: It is difficult to separate the magnetic specific heat by subtracting the reference data which might not fully describe the phononic part of the specific heat since the scaling factor has a large impact on the position of the data maximum. Furthermore, the fixing of the magnetic entropy to $R \ln 6$ at $T = 300\,\mathrm{K}$ and, thus, the chosen scaling of the reference data might not be valid. Figure 4.4 (a) shows the difference between the data and the QMC result (dashed green line) representing an idealized reference. It is obvious that the chosen reference data of $BaMg_2V_2O_8$ can not be easily scaled on this curve. Thus, the reference data and the chosen scaling are not suitable to extract a magnetic specific heat for $BaMn_2V_2O_8$.

4.1.3 Field Dependence and Spin Flop

The influence of magnetic fields on the transition temperature of $BaMn_2V_2O_8$ was studied by the specific heat, thermal expansion, and magnetostriction measurements for magnetic fields applied along c and perpendicular to c.

The inset (b) of Figure 4.4 shows an enlargement of the specific heat around the transition temperature in zero magnetic field (black) and in an applied external magnetic field of 14 T (green). The anomaly and, thus, the onset of long-range magnetic order is shifted only weakly by an amount of $\approx 0.1\,\mathrm{K/T}$ to higher temperatures. The same behavior is observed in thermal expansion measurements shown in Figure 4.6 for $H \,||\, c$ and $H \perp c$. The transition is signaled only by a small kink in the relative length change $\Delta L/L$. The thermal expansion coefficient α, shown in panels (b) and (d), shows an anomaly in both field directions which is slightly broader for $H \,||\, c$ but pretty sharp for $H \perp c$. The anomaly's maximum was identified with the transition temperature.

The magnetostriction for $H \,||\, c$ is shown in panel (e) for temperatures below (blue) and above (green, red) the transition temperature. No anomaly can be observed for this field direction due to the flat phase boundary suggested by the thermal expansion measurements. All curves behave roughly quadratically with increasing field, as shown in $\Delta L/L$ vs. $(\mu_0 H)^2$, see panel (f), which is reasonable due to the linear dependence of M on small magnetic fields [2]. However, the magnetostriction for $H \perp c$, panels (f)-(g), introduces a new aspect. Below the transition temperature, the relative length change shows a steep increase in the low field region which is reflected by an anomaly in the magnetostriction coefficient λ. The maxima of these anomalies, panel (d), are shifted to lower magnetic fields with increasing temperature. This difference of the magnetostriction for magnetic fields parallel and perpendicular to the c axis suggests a spin-flop transition. In an antiferromagnet the susceptibility perpendicular to the magnetic easy direction is larger than that for a parallel alignment ($\chi^{\perp} > \chi^{||}$). In small fields the magnetic spins always favor to be perpendicular to the external

[2] $\frac{\partial \Delta L}{\partial H} = -\frac{\partial M}{\partial p} = -\frac{\partial}{\partial p}\chi \cdot H$, with $M = \chi \cdot H$; thus $\Delta L \propto \frac{\partial \chi}{\partial p} \cdot H^2$.

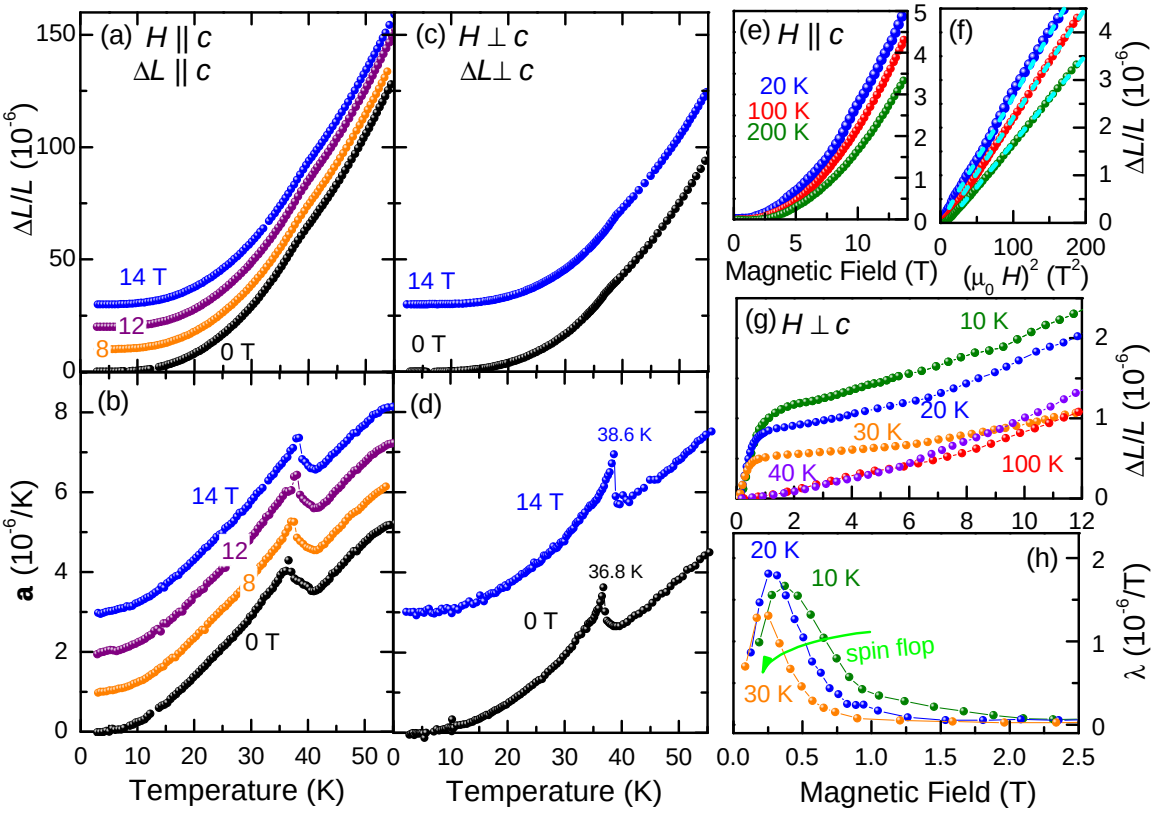

Figure 4.6: Thermal expansion and the thermal expansion coefficient α of $BaMn_2V_2O_8$ for $H \,||\, c$ (a)-(b) and $H \perp c$ (c)-(d). The magnetostriction for $H \,||\, c$ (e) shows no anomaly and increases roughly quadratically with the magnetic field as seen in the linear increase with $(\mu_0 H)^2$ (dashed line) (f). For $H \perp c$ (g), $\Delta L(H)/L$ shows a shoulder in the low-field region below T_N reflected in an anomaly in the magnetostriction coefficient λ (h). Note, that the curves in (a)-(d) are offset to each other for clarity by 10^{-5} and 10^{-6}/K, respectively.

field which is energetically favorable in an antiferromagnetic alignment because for a parallel alignment of spins and field the system can not gain Zeeman energy. A spin flop is a metamagnetic transition where for such a parallel alignment, at a critical value H_{SF}, the spins rotate such that a perpendicular alignment is achieved. With increasing magnetic field the spins are then canting continuously into the field. To verify a spin-flop transition in $BaMn_2V_2O_8$, the temperature dependent magnetization was measured for several weak magnetic fields applied within the *ab* plane as shown in Figure 4.7. The onset of the Néel order is reflected in a sharp turning-point at T_N that changes its sign for a magnetic field around 0.3 T. With increasing magnetic field from 0.1 T to 0.5 T the spins can, thus, be flopped and the spin-flop field H_{SF} is comparatively small. These experimental results of a spin-flop transition in $BaMn_2V_2O_8$ further confirm the above discussed preferred orientation of the spins within the *ab* plane.

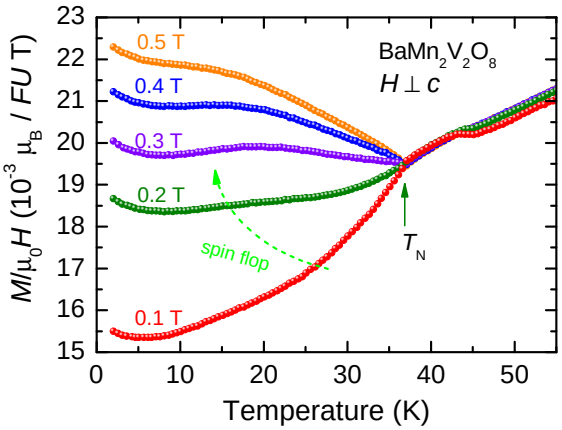

Figure 4.7: Temperature dependent magnetization $M(T)/\mu_0 H$ of $BaMn_2V_2O_8$ (a) for magnetic field perpendicular to the c axis at low magnetic fields up to 0.5 T.

Table 4.2: Atom positions of the constituents of $SrMn_2V_2O_8$ obtained by single crystal X-ray diffraction at room temperature using space group $I4_1cd$ [19, 92].

Atom	Site	x	y	z
Ba	8a	0	0	0
V	16b	0.26406(4)	0.07899(4)	0.0779(1)
Mn	16b	0.33080(4)(1)	0.33215(4)	0.21024(9)
O1	16b	0.1408(2)	0.4981(2)	-0.0080(3)
O2	16b	0.1533(2)	0.6869(2)	0.7009(3)
O3	16b	0.3239(2)	0.4995(2)	0.1710(3)
O4	16b	0.3328(2)	0.1560(2)	0.2124(3)

4.2 $SrMn_2V_2O_8$

4.2.1 Introduction

While $BaMn_2V_2O_8$ was known in literature, $SrMn_2V_2O_8$ had not been synthesized until the research in that field started in 2009 during my diploma thesis [92]. The single crystal growth, a characterization of the structure, and the basic thermodynamic properties were published in their main aspects in Ref. 19 (Niesen et al.) in 2011.

Structure

The structure of $SrMn_2V_2O_8$ was obtained by X-ray powder diffraction and single crystal X-ray diffraction which yield the non-centrosymetric space group No. 110. Thus, $SrMn_2V_2O_8$ is the non-centrosymmetric variant of $BaMn_2V_2O_8$ similar to the case of $SrCo_2V_2O_8$ and $BaCo_2V_2O_8$ (see Sec. 6.1). The lattice constants, obtained by powder X-ray diffraction, are $a = 12.4422(9)$ Å and $c = 8.6833(6)$ Å. The single crystal refinement was carried out by M. Valldor. Table 4.2 gives the refined atom positions of $SrMn_2V_2O_8$. A more detailed table of the refinement parameters and the refined atom positions can be found in the Appendix B, Table B.1. The structure was confirmed only recently by a neutron powder diffraction study which basically reports the same atom positions [100]. The structural peculiarities of $SrMn_2V_2O_8$ can be visualized in the oxygen coordination of the alkaline earth ion Sr and the oxygen

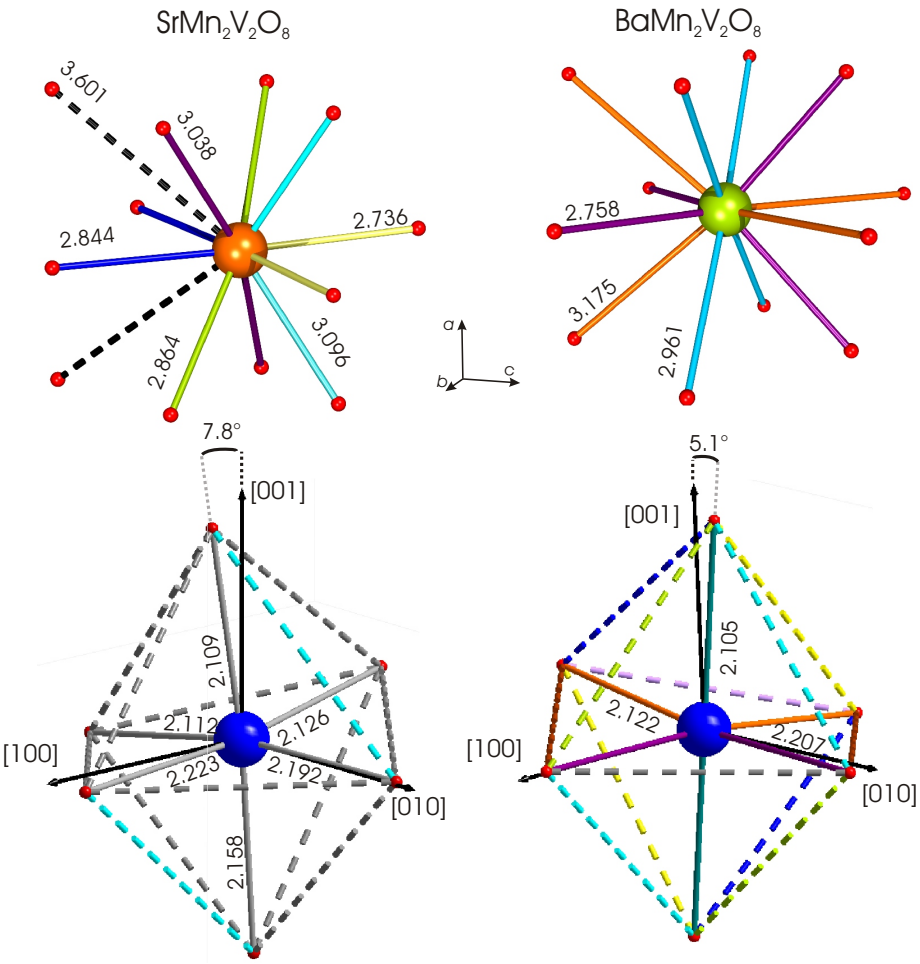

Figure 4.8: Building blocks of $SrMn_2V_2O_8$ (left) and $BaMn_2V_2O_8$ (right). The Sr-cubeoctahedron formed by the 12-fold oxygen coordination reveals two elongated bond lengths compared to the cubeoctahedron of $BaMn_2V_2O_8$. All bond lengths are given in Å, equal distances have equal colors within each picture. The MnO_6 octahedron is strongly distorted and reveals nearly no equal bond lengths.

coordination of the Mn^{2+} as shown in Figure 4.8 in comparison with the respective building blocks of $BaMn_2V_2O_8$ taken from Ref. 17. The 12-fold oxygen coordination of Sr and Ba forms a cubeoctahedron wherein the bond lengths range from 2.647 Å to 3.601 Å for $SrMn_2V_2O_8$. Due to the fact that two of the bond lengths (dashed lines) are significantly longer than the others, the Sr position is off-center of the polyhedron and the coordination is almost lowered to ten. This suggests that the strontium ion is too small to maintain all symmetries of this site compared to barium. The MnO_6 octahedron of $SrMn_2V_2O_8$ (left) shows a large distortion with practically no identical bond lengths (except one pair, blue) which are, thus, depicted in gray. O–O bonds are depicted as dashed lines, the Mn–O bonds are marked as solid lines. For the MnO_6 octahedron in $BaMn_2V_2O_8$ equal colors reflect equal bond lengths. For $SrMn_2V_2O_8$ a significantly enhanced tilt of the upper apical oxygen is observed with respect to the crystallographic c axis. The angle is increased from 5.1° in the $BaMn_2V_2O_8$ case to 7.8° in $SrMn_2V_2O_8$. In the discussion of anisotropies within $BaCo_2V_2O_8$ this angle

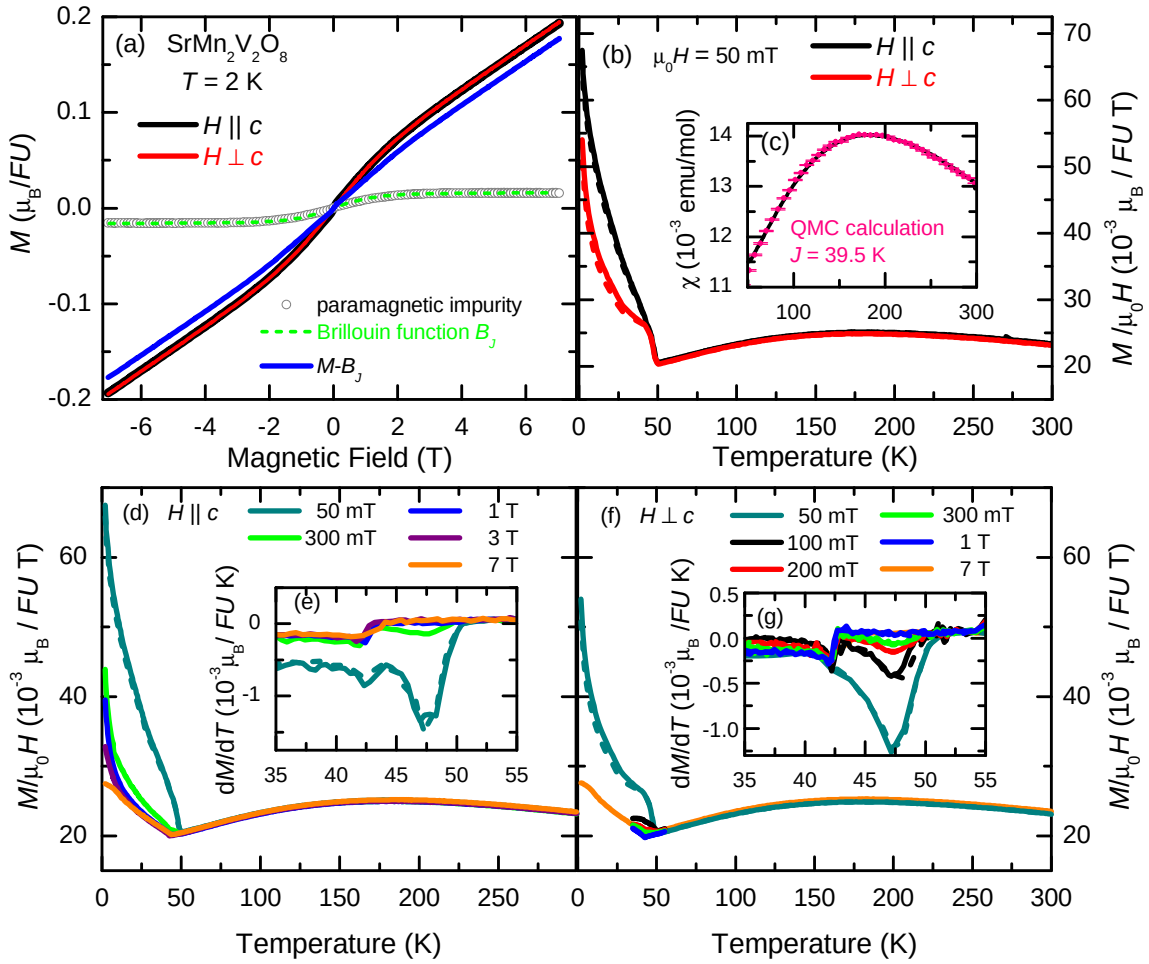

Figure 4.9: Field (a) and temperature dependent (b) magnetization of $SrMn_2V_2O_8$ for magnetic fields parallel (black) and perpendicular to c (red). The magnetization is isotropic for both field directions and shows a s-shape. A moment of about $0.2\,\mu_B/FU$ at 7 T. Temperature dependent magnetization of $SrMn_2V_2O_8$ in several magnetic fields parallel (d) and perpendicular to c (f). The insets (e) and (g) show the derivatives which reflect both anomalies at 42 K and 47 K.

plays an important role (see Sec. 5.4).

4.2.2 Characterization

The magnetization of $SrMn_2V_2O_8$, Figure 4.9, is shown for magnetic fields applied along the c axis (black) and perpendicular to c (red). For both field directions an s-shaped dependence on the magnetic field is seen, both curves lie exactly on top of each other. A linear fit can be made in the field range of 4 T to 7 T. Subtracting the linear fit from the curves yields a paramagnetic contribution (grey circles) of about $0.016\,\mu_B/FU$ at 7 T which can be matched with a Brillouin function (green line). Subtracting vice versa the Brillouin part from the measurements yields a linear $(M - B_J)$ curve (blue) with a magnetization of about $0.18\,\mu_B/FU$ at 7 T which is less than 2 % of a fully polarized magnetization of about $10\,\mu_B/FU$ for two magnetic

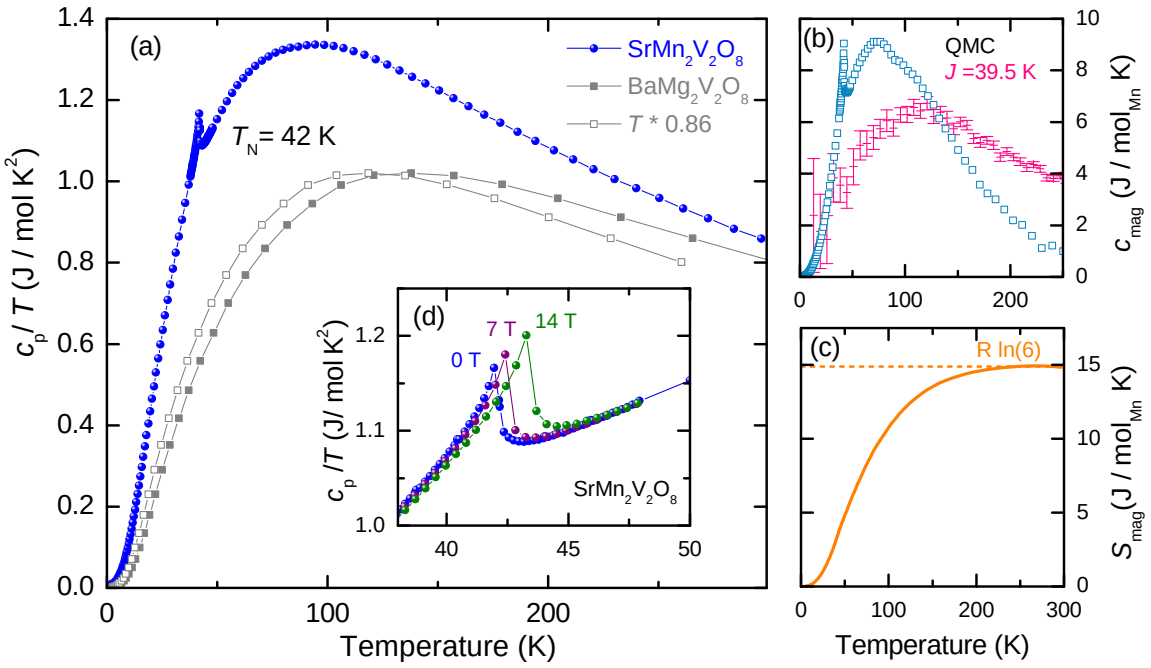

Figure 4.10: (a) Zero-field specific heat $c_p(T)/T$ of $SrMn_2V_2O_8$ (blue) and of the non-magnetic reference system $BaMg_2V_2O_8$ (gray). Open symbols represent the temperature-rescaled $BaMg_2V_2O_8$ data (see text). The inset (b) shows the specific heat for 0, 7 and 14 T. Panel (c) shows the difference $c_{mag} = c_{SrMn} - c_{BaMg}$ and according QMC fits. Panel (d) shows the magnetic entropy S_{mag} of the system and the expected $R \ln 6$ limit for high temperatures (dashed line).

Mn^{2+} ions.

Panel (b) shows the temperature dependent magnetization in an external magnetic field of 50 mT for $H \,||\, c$ (black) and $H \perp c$ (red). In the high-temperature paramagnetic regime the susceptibility is isotropic for both field directions and shows a very broad maximum around 180 K. Two kinks can be observed at 47 K and 42 K. The curves for both field directions coincide until they separate at 42 K. Field cooled (solid lines) and zero field cooled (dashed lines) measurements do not show a significant difference. Below the transition, however, the curves show an increase with decreasing temperature for both field directions. Figure 4.9 shows the temperature dependent magnetization measured at several magnetic fields up to 7 T for $H \,||\, c$ (d) and $H \perp c$ (f). Cooling below T_N, the magnetization is enhanced for all applied fields up to 7 T. The maximum value at lowest temperature, however, is decreased for higher applied fields. In contrast to $BaMn_2V_2O_8$, the magnetization of $SrMn_2V_2O_8$ appears to have no preferred direction or a possible spin flop field lies below 50 mT. The insets (e) and (g) show the temperature derivatives dM/dT which again reveal two significant anomalies located at 42 K and 47 K. The anomaly at 47 K can be suppressed by weak magnetic fields of 300 mT in both field directions. The other anomaly at 42 K remains visible up to 7 T and is nearly unaffected by this field.

With help of the specific heat one is able to answer the question which of the anomalies belongs to a real magnetic ordering. Figure 4.10 shows $c_p(T)/T$ of $SrMn_2V_2O_8$ (blue) which reveals a sharp anomaly at 42 K confirming this temperature as the

onset of long-range magnetic order. Applying magnetic fields up to 14 T shifts the transition to 43.3 K which means a positive shift of less than 0.1 K/T, *cfs.* inset (d). The magnetic specific heat c_{mag} was obtained by subtracting the temperature-rescaled reference curve of the nonmagnetic $BaMg_2V_2O_8$. The scaling factor was chosen such that magnetic entropy $S_{\mathrm{mag}} = \int \frac{c\mathrm{mag}}{T} \mathrm{d}T$ matches $R \ln 6$ in the high-temperature limit in analogy to the discussion in Section 4.1.2.

Modeling

Figure 4.9 (c) shows the analogous fit to the susceptibility of $SrMn_2V_2O_8$ by the QMC simulation as discussed before for $BaMn_2V_2O_8$. The data could be fitted well with a coupling constant $J = 39.5$ K which is slightly higher than in $BaMn_2V_2O_8$. With this coupling constant the overall curvature is matched well but shows a deviation of less than 5 % in the absolute value. Therefore, the shown fit was carried out with $g = 1.954$. Alternative sources for this deviation can be possible due to experimental uncertainties of the small magnetic field of 50(2) mT or errors made when weighing the sample.

In panel (b) of Figure 4.10 the magnetic specific heat c_{mag} (blue) is compared to the QMC simulations ($L = 80$). Using the coupling constant $J = 39.5$ K (pink) which was extracted from the susceptibility, the maximum of the specific heat is not matched. Analogously, the reference substance $BaMg_2V_2O_8$ is probably not suitable as reference system of $SrMn_2V_2O_8$.

Table 4.3: Summarized parameters of $BaMn_2V_2O_8$ and $SrMn_2V_2O_8$.

	a (Å)	c (Å)	T_N (K)	χ_{max} ($10^{-3}\mu_B/FU$T)	$T(\chi_{max})$ (K)	H_{SF} (mT)	$\frac{\partial T_N}{\partial H}$ (mK/T)	J (K)
$BaMn_2V_2O_8$	12.62	8.67	37	26.5	170	300	100	39
$SrMn_2V_2O_8$	12.44	8.68	42	25	180	–	90	39.5

4.3 Magnetic Phase Diagrams and Conclusion

The first single-crystal investigations of the Heisenberg spin-chain systems $BaMn_2V_2O_8$ and $SrMn_2V_2O_8$ are presented here. The compounds crystallize in tetragonal space groups. The value of the lattice constant c is almost identical for both compounds, but due to the different ionic size of Ba^{2+} and Sr^{2+}, the lattice constant a and, hence, the mean inter-chain distance is smaller for $SrMn_2V_2O_8$ as expected (see also Tab. 4.3).

The field- and temperature dependent magnetization reveal a nearly isotropic behavior for both $BaMn_2V_2O_8$ (see Fig. 4.3) and $SrMn_2V_2O_8$ (see Fig. 4.9) for the field directions parallel and perpendicular to the c axis. Also, the magnetic susceptibility reveals low-dimensional nearly isotropic behavior in form of a maximum at 170 K and 180 K, respectively. The hysteresis in the magnetization of $BaMn_2V_2O_8$ reported in Ref. 18 is not observed. This hysteresis has been caused most probably by impurities. The magnetization of $SrMn_2V_2O_8$ presented here, shows an s-shaped curvature that also originates from a small paramagnetic impurity. Using QMC simulations for a spin-5/2 chain, the susceptibility for the Mn compounds could be fitted well with an antiferromagnetic coupling constant of $J \approx 39$ K (see Tab. 4.3). However, $BaMn_2V_2O_8$ shows weak anisotropies below T_N for fields below $H_{SF} = 300$ mT where a spin-flop transition for $H \perp c$ exists below H_{SF} which was confirmed in magnetization and magnetostriction measurements. In this low-field region the spins prefer to orient within the ab plane. However, the microscopic proof for that spin arrangement has to be given by neutron diffraction experiments. For $SrMn_2V_2O_8$, an anomaly in the magnetic susceptibility is located at $T = 42$ K and was confirmed as a bulk transition by specific heat measurements. The high ordering temperatures of both systems can be attributed to the large magnetic spin of $S = 5/2$ due to the inferior role of spin fluctuations that otherwise, i.e. for small S, suppress the development of long-range order and lead to lower ordering temperatures. A possible spin-flop field for $SrMn_2V_2O_8$ is estimated to be lower than 50 mT, a model of the spin structure can not be figured out with the present data set. However, the zero-field magnetic structure of $SrMn_2V_2O_8$ was resolved by Bera et al. recently [100]. According to this report, the spin structure of $SrMn_2V_2O_8$ contains antiferromagnetic spin chains along c that are ordered ferromagnetically within each ab plane. It is very likely that a similar spin structure is also present in $BaMn_2V_2O_8$.

The temperature *vs.* magnetic field phase diagrams for $BaMn_2V_2O_8$ and $SrMn_2V_2O_8$ depicted in Figure 4.11 were derived from the data sets presented above. Since the anisotropy of T_N for magnetic fields parallel and perpendicular to c is very weak, the phase boundary (green area) suits both field directions for each compound. In case

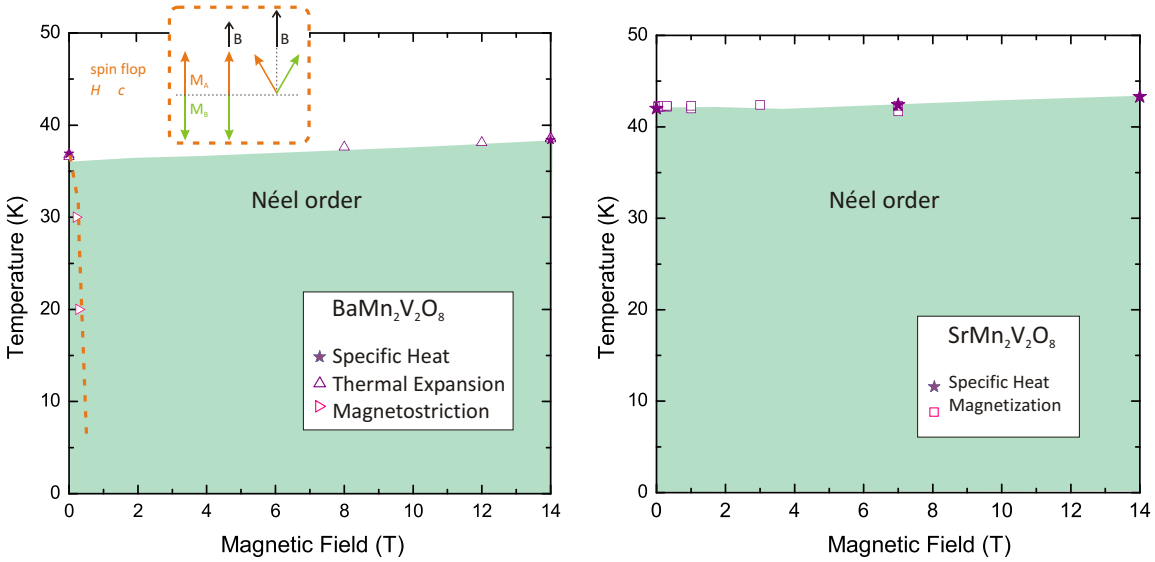

Figure 4.11: Magnetic phase diagrams of $BaMn_2V_2O_8$ (left) and $SrMn_2V_2O_8$ (right) obtained by the specific heat ($\star$), the thermal expansion ($\triangle$), the magnetostriction ($\triangleleft$) and the magnetization ($\square$). The yellow area in the $BaMn_2V_2O_8$ phase diagram marks the spin flop region for $H \perp c$.

of $BaMn_2V_2O_8$ the dashed line in the phase diagram marks the spin flop region for the field direction $H \perp c$. The phase boundaries T_N (B) show a weak positive field dependence of $dT_N/(d\mu_0 H) \approx 0.1\,\mathrm{K/T}$. This increase agrees with expectations given by an Ehrenfest relation, namely

$$\frac{dT_N}{d\mu_0 H} = -T_N \frac{\Delta \frac{\partial M}{\partial T}}{\Delta c_p}. \tag{4.2}$$

For $\mu_0 H > 0.3\,\mathrm{T}$ the anomaly in $\frac{\partial M}{\partial T}$ is negative for all field directions and the anomaly in the specific heat is always positive. Thus, due to the minus sign in the equation, an overall positive field dependence for the transition temperature is expected for $BaMn_2V_2O_8$ and $SrMn_2V_2O_8$.

5 Ising chain $BaCo_2V_2O_8$

The physical properties of $BaCo_2V_2O_8$ are vitally connected to its structural peculiarities and in particular to the screw chain arrangement of the magnetic ions. The introduction 5.1 gives an overview of the structural features and introduces the basic magnetic properties of $BaCo_2V_2O_8$ from literature. In Section 5.2 a lattice distortion due to magneto-elastic coupling when entering the Néel ordered phase in zero-magnetic field will be reported. When applying magnetic fields, the field direction has a selective role because of the strong magnetic anisotropy of $BaCo_2V_2O_8$. The field induced suppression of the Néel order for field directions parallel to the easy axis c will be discussed in Section 5.3. Section 5.4 handles the in-plane anisotropy that can be observed for magnetic fields perpendicular to c.

5.1 Introduction

Structure

$BaCo_2V_2O_8$ crystallizes in the tetragonal space group $I4_1/acd$ (No. 142) with lattice parameters $a = 12.444(1)$ Å and $c = 8.415(3)$ Å. The atom positions and their Wycoff sites are summarized in Table 5.1 [15]. The structure, as introduced in Section 3.2, contains screw chains of edge-sharing CoO_6 octahedra that are running along the c axis. Those chains are separated by Ba^{2+} and V^{5+} ions. Both Ba^{2+} and V^{5+} are non-magnetic, the magnetism within $BaCo_2V_2O_8$ is determined completely by the cobalt. The vanadium is tetrahedrally coordinated by four oxygen ions but is of minor interest here[1]. The left side of Figure 5.1 shows the 12-fold oxygen coordination

[1] Ideta et al. show in their ^{51}V NMR study of the spin-dynamics in the ordered state that there are two V sites experiencing different internal magnetic fields, see Ref. 101.

Atom	Site	x	y	z
Ba	8a	1/4	3/8	0.61(2)
V	16e	0.0800(2)	0	1/4
Co	16f	0.1689(1)	0.4189(1)	1/8
O1	32g	0.157(1)	0.074(1)	0.383(1)
O2	32g	0.498(1)	0.087(1)	0.347(1)

Table 5.1: Atom positions of the constituents within $BaCo_2V_2O_8$ according to Ref. 15 using space group $I4_1/acd$.

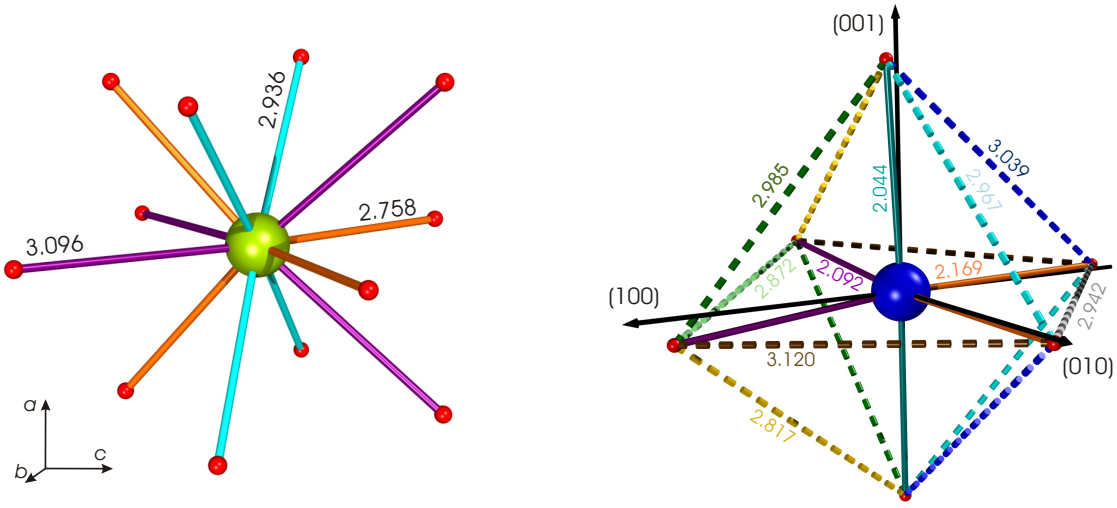

Figure 5.1: Oxygen coordination of the Ba ion within $BaCo_2V_2O_8$ (left). Three different bond lengths (given in Å) lead to a 12-fold coordination in a regular cubeoctahedron. A CoO_6 octahedron within $BaCo_2V_2O_8$ (right). The solid bars indicate the three different Co-O bond-lengths (given in Å). O-O bonds are depicted by dashed lines. Equal colors mark equal bond lengths within each picture.

of the barium ion forming a symmetric cubeoctahedron. The oxygen coordination of the cobalt is even more interesting due to the peculiarities of the CoO_6 octahedra. The right side of Figure 5.1 shows an octahedron with its different bond lengths given in Å[2]. Crystallographic axes are added to visualize the more complicated distortion of the octahedron. The solid bars indicate the three different Co-O bond lengths that occur in pairs. The bonds along c are the shortest ones (cyan) meaning that the octahedron is compressed along the c axis. The bond defined by the upper apical O and Co shall be named as the local axis (cf. Sec. 5.4.2). However, the angle between both bonds is less than 180° and a tilt of the local axis with respect to the global axis can be observed. The other two bonds (purple and orange) are pointing more or less along the crystallographic a and b axes. The corresponding oxygen-oxygen bonds are plotted by dashed lines. Within the ab plane, three different O-O bond lengths are present, one of them occurring in an opposing pair. The out-of-plane O-O bonds are all occurring in pairs.

Figure 5.2 shows the cobalt ions with their oxygen coordinations in the ab planes only. One observes that the cobalt and oxygen ions are forming parquets. All of these parquets seem to have one "wing" that lies above or below a certain ab plane given by the z positions of the cobalt ions (1/8, 3/8, 5/8, or 7/8). Actually, none of the oxygen lies perfectly within the plane, but only one oxygen deviates more than Si0.02Å from the cobalt z position. Resulting from this arrangement the octahedra are distorted and no longer symmetric. As former explained in Section 3.2, the edge-sharing octahedra form to two types of chains that differ in their helicity. One type of chains obeys the 4_1 screw chain: to get the next octahedron's position and orientation the octahedron has to be rotated by $\pi/2$ around an axis along c and shifted a quarter

[2]Crystallographic data are taken from ICSD No. 60580 [15].

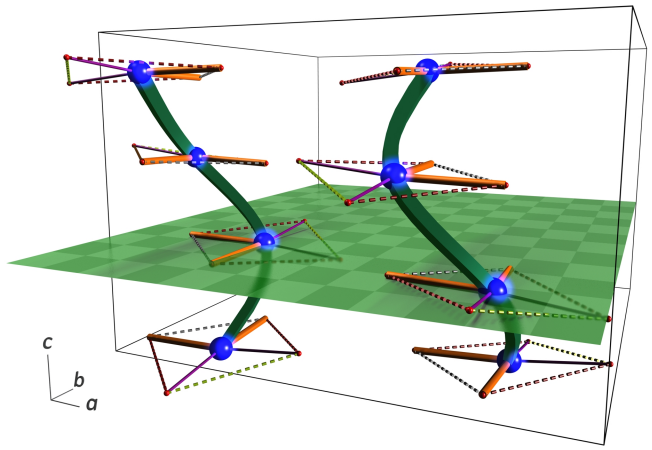

Figure 5.2: Oxygen coordination of the cobalt ions within the *ab* planes. The coordination is not lying perfectly with in a certain *ab* plane and has a tilting wing. The tilt out of the *ab* plane occurs in different directions every second layer. Two of the four screw axes within a unit cell are shown which are counter rotating .

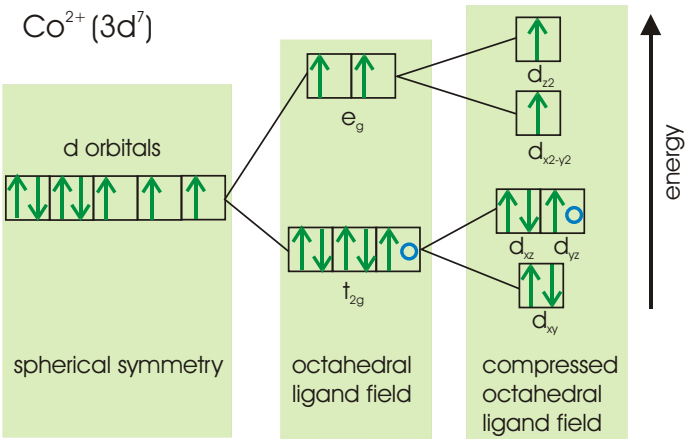

Figure 5.3: Schematic energy splitting of the d orbitals for different octahedral ligand fields. The green arrows give the arrangement of the Co^{2+} ($3d^7$) spins within a compressed octahedron assuming a high spin configuration.

of the lattice constant along c. The second type rotates clockwise with increasing z value as a 4_3 screw axis (cf. Ref. 24).

In summary, the CoO_6 octahedron within $BaCo_2V_2O_8$ is strongly distorted and not simply compressed along c. The different Co-O bond-lengths lead to non-orthogonal angles and the octahedral axes (cf. Fig. 5.1 cyan, purple, orange) are tilted with respected to the crystallographic axes. Especially this tilt will be of importance for the presence of an in-plane anisotropy according to Ref. 96 which will be discussed in Section 5.4.

Ising Anisotropy

Figure 5.3 shows a Co^{2+} ($3d^7$) electronic configuration in different ligand fields. Beginning with a spherical symmetry of a free ion (left) where all 3d energy levels are degenerate, the energy levels are split by an octahedral ligand field and the three t_{2g} levels are energetically lowered (middle). Assuming that the spins realize a $S = 3/2$ high spin state, according to Hund's first rule, the lower lying t_{2g} orbitals are only partially filled. In case of $BaCo_2V_2O_8$ the CoO_6 octahedra are compressed along the c axis, which results in a further splitting of the t_{2g} levels in a singlet and a doublet.

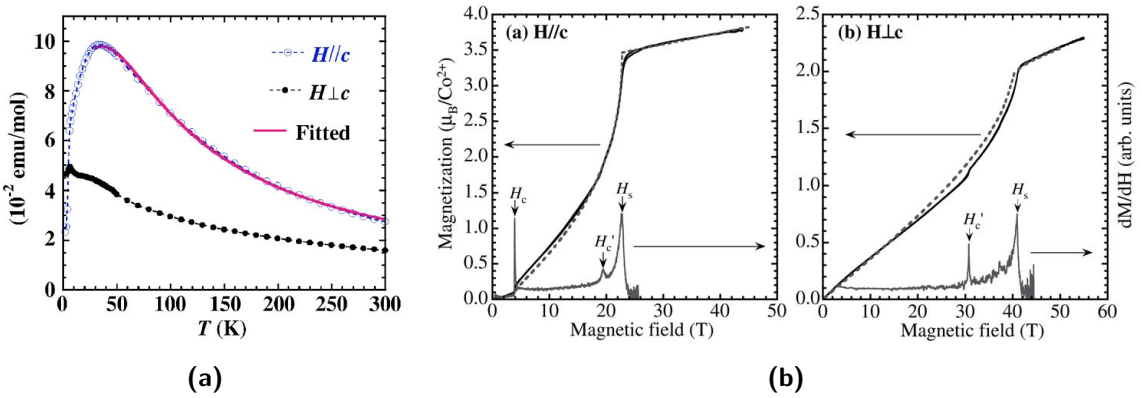

Figure 5.4: Magnetic susceptibility χ (left) of $BaCo_2V_2O_8$ for $H = 1\,\mathrm{T}$ parallel and perpendicular c [16]. (High-) field-dependent magnetization of $BaCo_2V_2O_8$ [102] for H parallel (middle) and perpendicular c (right) at $T = 1.3\,\mathrm{K}$.

The partially filled doublet, i.e. the single hole, yields an effective orbital moment $\tilde{l} = 1$ and results in an anisotropy of the magnetic moment with c as the magnetic easy axis. This Ising anisotropy of $BaCo_2V_2O_8$ was experimentally confirmed first in temperature dependent magnetization measurements [84], see Figure 5.4. Above the ordering temperature the temperature dependent magnetization is very anisotropic for magnetic field applied along c and perpendicular to it, $\chi^{\|c}(T) \approx 2 \cdot \chi^{\perp c}(T)$ identifying the c axis as the easy axis. This is also reflected in low-temperature high-field magnetization data [102], also shown in Fig. 5.4, where the saturation field is $H_{sat}^{\|c} \approx 0.5 \cdot H_{sat}^{\perp c}$ and the saturation magnetization $M_{sat}^{\|c} \approx 1.5 \cdot M_{sat}^{\perp c}$. The magnetic susceptibility $\chi^{\|c}$ shows the typical maximum for low-dimensional spin systems around 35 K. This maximum signals short-range magnetic correlations due to the dominant magnetic exchange within the screw chains, the intra-chain exchange. Because of the dominance of the intra-chain coupling $BaCo_2V_2O_8$ represents a model system of a (quasi-) one dimensional antiferromagnetic effective Ising $S = 1/2$ chain. The XXZ Hamiltonian (2.2)

$$\mathcal{H}_{XXZ} = \sum_i J \left\{ S_i^z S_{i+1}^z + \epsilon \left(S_i^x S_{i+1}^x + S_i^y S_{i+1}^y \right) \right\} + g\mu_\mathrm{B} \mathbf{H} \cdot \mathbf{S}_i$$

is suitable to describe such a system (cf. Sec. 2.1). From the analysis of the low-temperature magnetization the dominant intra-chain exchange $J/k_\mathrm{B} \simeq 65\,\mathrm{K}$, the anisotropy factor $\epsilon \approx 0.5$, and the anisotropic g factors $g^{\|c} \simeq 6.3$ and $g^{\perp c} \simeq 3.2$ were derived [102]. Three-dimensional antiferromagnetic long-range order (3D af LRO) sets in at $T_\mathrm{N} \simeq 5.5\,\mathrm{K}$ due to finite inter-chain couplings. A pronounced anisotropy for magnetic fields along and perpendicular to the c axis has been reported [103, 104]. The magnetic phase diagram of $BaCo_2V_2O_8$ for magnetic fields applied along the magnetic easy axis has been studied by several techniques [24, 103–111]. In this field direction, T_N rapidly decreases in the field range up to 4 T. Above this field an incommensurate (IC) magnetic phase with a weakly field-dependent transition temperature $T_\mathrm{IC} \approx 1\,\mathrm{K}$ develops [24]. Former investigations applied a maximum field of about 9 T, the data presented in Section 5.3 present an extension of the phase diagram up to a maximum

field of 17 T investigated by means of thermal expansion measurements.

The field direction perpendicular to the magnetic easy axis was, until recently, not in the focus of interest. For $H \perp c$ a rather weak decrease of the Néel temperature $\partial T_N/\partial H \approx -0.1\,\mathrm{T/K}$ has been reported up to a maximum field of 9 T by Z. He et al. [103]. A much stronger decrease of $\partial T_N/\partial H \approx -1\,\mathrm{T/K}$ in the field range between 8 T to 10 T, however, was reported by Zhao et al. [104], which was interpreted as a new phase within that field direction. It has to be noted, that in most of the studies for $H \perp c$ the explicit direction of the magnetic field within the *ab* plane has not been given [16, 84, 86, 102, 103, 110, 112]. The in-plane anisotropy within $BaCo_2V_2O_8$ for a field direction along [1 0 0] and [1 1 0], that was found in the course of this thesis, is the topic of Section 5.4.

Spin Structure

Figure 5.5 summarizes some of the structural features [15] mentioned above together with the spin structure of the antiferromagnetic order according to Refs. 24, 109. Two exemplary chains of the edge-sharing octahedra with their complete oxygen coordination are depicted in the upper region in blue with their different helicities indicated by the green arrows. Below, four of the chains are represented without the coordinating oxygen ions, but including the spins of the cobalt ions which are shown as orange and pink arrows according to their respective orientation. According to Refs. 24, 109, the cobalt spins are antiferromagnetically ordered along *c* with a propagation vector $\vec{k}_{AF} = (1, 0, 0)$. Within a certain *ab* plane, e.g. the blue one in the front, the nearest neighbor spins point either in the same (pink, pink) or in the opposite (pink, orange) direction for the [1 0 0] or the [0 1 0] axis, respectively. This spin arrangement results in a magnetic structure that contains different domains with respect to the two *a*-axes orientations which are rotated by an angle of 90° and translated by the symmetry operation $c/4$ with respect to each other. As a result, the symmetry of the magnetic structure is less than tetragonal [24].

The blue dashed and green dotted lines in Fig. 5.5 represent exemplary nearest neighbor (NN) inter-chain couplings $J^{\perp}_{NN}$ within the plane perpendicular to the dominant intra-chain coupling. The notation $J^{\perp}_{n}$ is used to distinguish the in-plane inter-chain interactions from the dominant intra-chain interaction J of the hamiltonian (2.2) that acts along the chain direction. As can be seen for two consecutive *ab* planes ($z = 1/8$ blue and $z = 3/8$ green) this arrangement of $J^{\perp}_{NN}$ is different for different cobalt positions. Expanding the arrangement of $J^{\perp}_{NN}$ within a certain plane shows that, in fact, the NN interactions form a geometrical arrangement similar as shown in Figure 5.6. The colored circles represent the Co-spins pointing out (●) and into (●) the plane while the dashed blue lines represent the *NN* inter-chain coupling $J^{\perp}_{NN}$. Those couplings are competing with corresponding next-nearest neighbor NNN inter-chain couplings $J^{\perp}_{NNN}$, depicted as green solid lines. Moreover, $J^{\perp}_{NN}$ and $J^{\perp}_{NNN}$ are not oriented exactly parallel to the tetragonal *a* axes and the ⟨110⟩ directions, but these directions are symmetry axes of $J^{\perp}_{NN}$ and $J^{\perp}_{NNN}$, respectively. Simplifying this complex arrangement leads to a version of the $J_1 - J_2$ model on a square lattice [111, 113, 114] which is sketched in the right part of Figure 5.6. Here, J_1 and J_2 represent the exchange interactions along the side (dashed line) and along the diagonal (solid line) of the square.

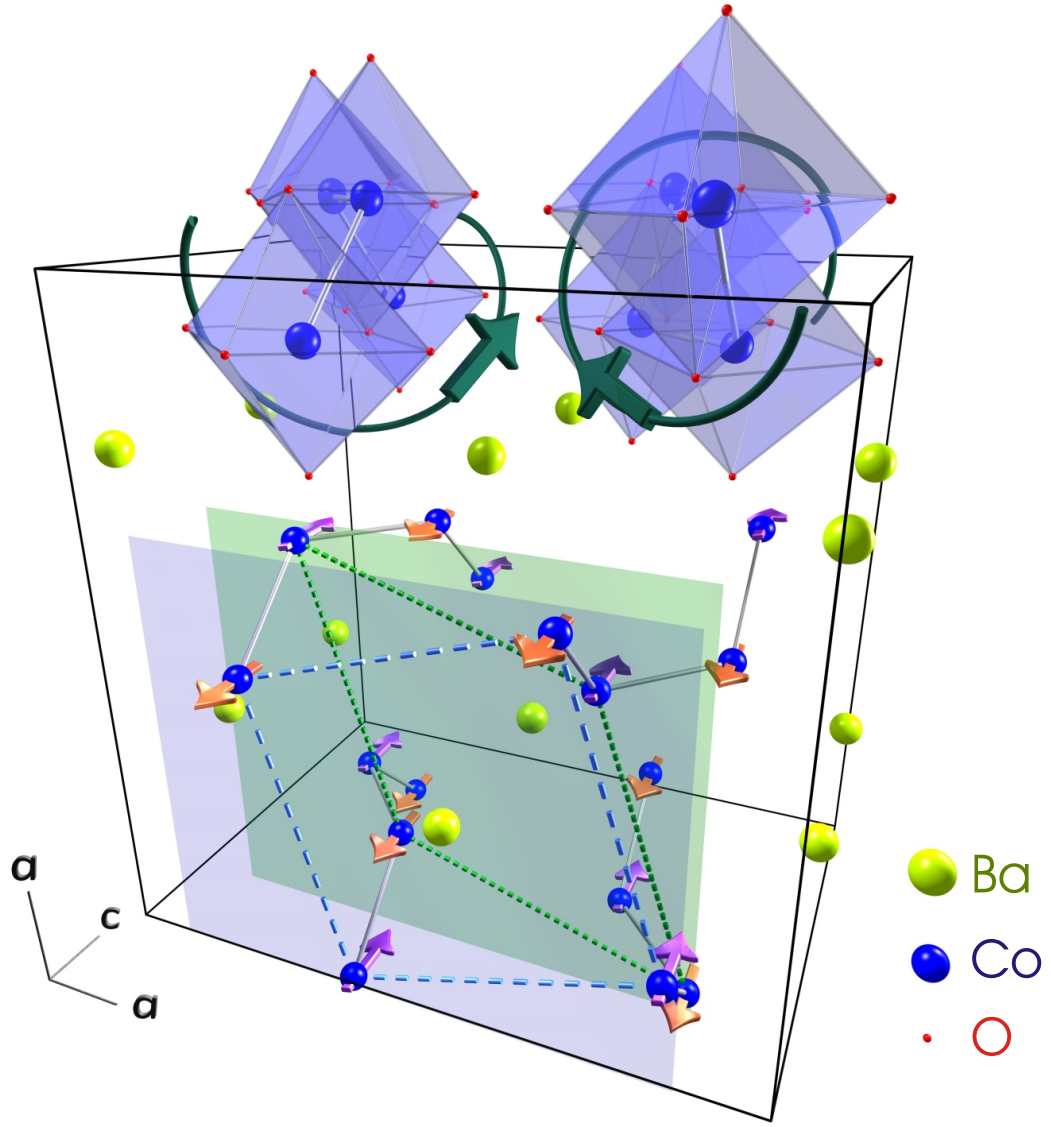

Figure 5.5: The structure of $BaCo_2V_2O_8$ contains right- and left-handed screw chains of corner sharing CoO_6 octahedra (top, blue) running along the c axis. Layers of Ba^{2+} ions (light green) are separating the chains. The VO_4 tetrahedra are not depicted for clarity. Four of the cobalt chains are depicted without the corresponding O^{2-} ions. The dominating NN interaction along the chains is given by the solid grey lines. The spins (orange and pink arrows) are antiferromagnetically ordered along the c axis. Within a certain ab plane, neighboring spins point either in the same or in the opposite direction for the [1 0 0] and the [0 1 0] direction, respectively. The coupling between NN Co^{2+} ions within this planes are exemplarily depicted as dashed and dotted lines (*cf.* Ref. 23).

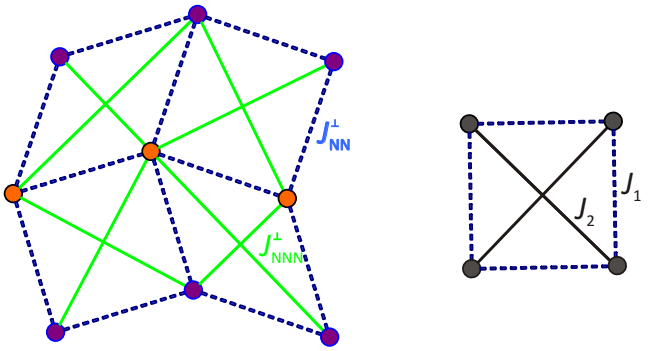

Figure 5.6: Geometrical arrangement of the Co^{2+} ions within the ab planes with the spins pointing out of (●) or into the plane (●). The NN inter-chain couplings $J^{\perp}_{NN}$ (dashed blue) are competing with corresponding NNN inter-chain couplings $J^{\perp}_{NNN}$ (green). A simpler version of this arrangement is described by the $J_1 - J_2$ model on a square lattice (right).

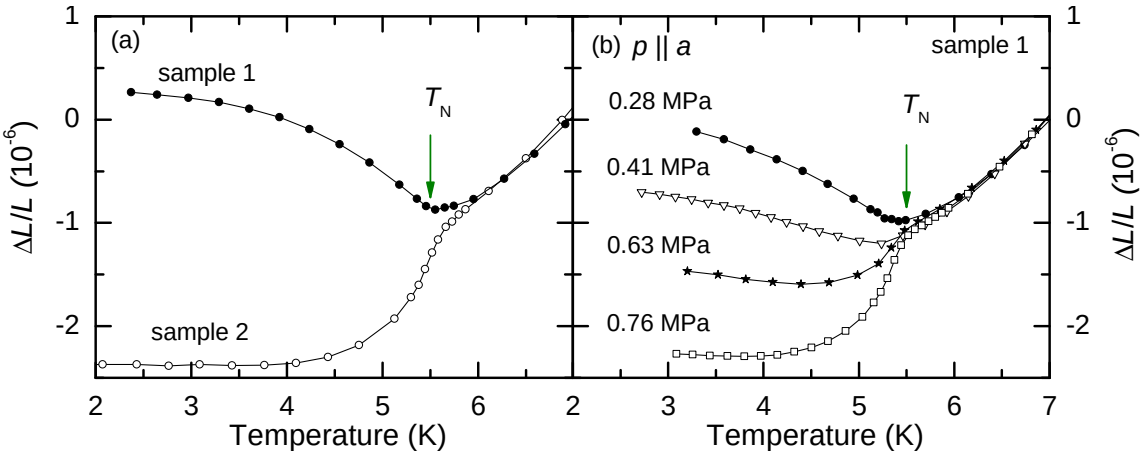

Figure 5.7: (a)-(b) Zero-field thermal expansion of the tetragonal a axis of $BaCo_2V_2O_8$. All length changes $\Delta L = L(T) - L_0$ are related to $L_0 = L(7\,\mathrm{K}; p_i)$. The different data sets in (a) were obtained on two different setups and samples. Panel (b) shows measurements on sample 1 during the same run but with varied uniaxial pressure along a (see text).

5.2 Domain Switching and Structural Distortion

Zero-field measurements of the thermal expansion along the tetragonal a axis are shown in Figure 5.7 (a)-(b). The relative length changes for two different samples of $BaCo_2V_2O_8$, shown in panel (a), were obtained in two different setups. In both cases the length change was measured along the tetragonal a direction and both measurements show that the onset of magnetic order, indicated by a green arrow, is accompanied by a spontaneous strain. But surprisingly, the spontaneous strains are of different signs. This finding is extraordinary because the tetragonal symmetry of the lattice requires an isotropic thermal expansion within the ab plane. Therefore, this behavior is a clear hint that the tetragonal symmetry is also broken by the nuclear structure when entering the Néel ordered phase, following the lower symmetry of the magnetic structure. One of the most obvious and simplest explanations for the different signs of strains is provided by the assumption that the antiferromagnetic ordering causes a small orthorhombic splitting $a \neq b$. Furthermore, a heavy twinning with respect to the orientations of the now orthorhombic axes a_o and b_o should occur and

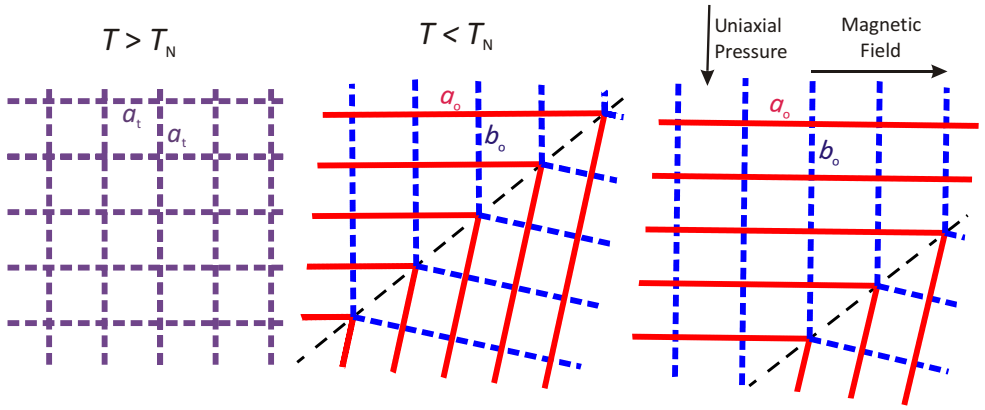

Figure 5.8: Schematic sketch of the process of partial detwinning by uniaxial pressure or by a magnetic field. The system has tetragonal symmetry for $T > T_N$ (left) which is spontaneously broken for $T < T_N$ (middle) and forming domains. Applying uniaxial pressure or magnetic fields (right) leads to partial detwinning of the domains. Note, that the influence of pressure and magnetic field applied along the same axis are opposing each other.

the measurements in panel (a) reflect, thus, different superpositions of the different a_o- and b_o-axis thermal expansion i.e. different twinning ratios in sample 1 and sample 2. In order to check this hypothesis a series of thermal expansion measurements along a certain tetragonal a axis on sample 1, which was an oriented piece of SN0075, were performed by M. Seher with varying uniaxial pressure in the TADNULL setup (see Sec. 2.3) [23, 59].

Figure 5.7 (b) shows the zero-field thermal expansion of sample 1 under varying uniaxial pressure. The pressure value p_i was changed from 0.28 MPa (closed circles) to 0.76 MPa (open squares). With increasing pressure one observes that this pressure range is sufficient to switch from a spontaneous expansion below T_N to a spontaneous contraction. In this low-pressure range the magnitude of the strain continuously varies with increasing pressure. This can be interpreted in terms of domain-switching as follows. For temperature above the Néel temperature ($T > T_N$) the system has tetragonal symmetry, as sketched in the left panel of Figure 5.8. But below the transition temperature (middle panel), the tetragonal a_t axes spontaneously develop an orthorhombic splitting, e.g. $a_o > a_t > b_o$. Due to twinning of these ferroelastic domains one measures a macroscopic length change that is an average of $a_o(T)$ and $b_o(T)$. Applying an increasing uniaxial pressure along one of the tetragonal a axes favors an orientation of the domains with the shorter orthorhombic axis (dashed blue) along the direction of pressure. Therefore, the amount of b_o-oriented domains along this direction is continuously enhanced until a single-domain crystal would be reached. In the present setup, the single-domain limit is, however, not reached because of the small amount of pressure applied. The hardness of the material most probably allows the application of higher pressures without destruction of the sample, but the setup used is not suitable for this kind of experiment. In order to prevent hysteresis effects that may occur below the transition temperature, "pressure-cooled" measurements were performed, which means that the uniaxial pressure was changed well above T_N at $T \approx 10$ K. Subsequently the sample was cooled down to about 3 K, and the data

collection was performed in the following heating run. As will be shown in detail in Section 5.4.2, this domain switching processes also occur for applying a magnetic field along the a axis where the magnetic field favors a domain orientation with the elongated lattice constant aligned along the field direction. Thus, if applied along the same a axis the domain switching effects of uniaxial pressure and magnetic field oppose each other because both favor different domain orientations. The pressure supports those domains with short axis along the direction of pressure while the magnetic field prefers the long-axis domains aligned along the direction of the field. Therefore, one could force the system into a single domain state when applying a transverse configuration of field and uniaxial pressure such that both favor the same domain orientation.

In none of the reported diffraction studies on $BaCo_2V_2O_8$ [24, 84, 106, 108, 109] this structural symmetry reduction in the Néel ordered state was discussed. This might be due to the fact that the average macroscopic strains $\Delta L/L$ are of the order of 10^{-6}, as the above shown zero-field data reveal. Judging from the thermal expansion along the ab-plane diagonal (see Sec. 5.4.1), which shows a strains of the order 10^{-5}, an orthorhombic splitting must, thus, be very small and even for a completely detwinned sample $\Delta L/L$ the splitting is estimated not to exceed 10^{-4} significantly which will be hard to detect by diffraction techniques. An investigation by single crystal and powder X-ray diffraction via synchrotron radiation will be presented below (Sec. 5.2.1)

The magnetic structure obtained by neutron scattering [24, 109] that was introduced above (cf. Fig. 5.6) gives further evidence for the observed structural distortion. The NN spins within the ab plane, indicated by orange and pink arrows according to the direction of the spin, are oriented parallel to each other along one of the tetragonal a axes, and antiparallel along the other. This kind of magnetic structure is a typical result of magnetic frustration, for example the competition between NN interactions $J^{\perp}_{\mathrm{NN}}$ along a (dashed blue line) and NNN interaction $J^{\perp}_{\mathrm{NNN}}$ along the diagonal [1 1 0] (solid green line) being both antiferromagnetic. Combined with a tetragonal symmetry where both a directions are equivalent, such a competition results in a perfect frustration. This frustration can be lifted by a distortion of the lattice if there is a finite magnetoelastic coupling, which means a change of $J^{\perp}_{\mathrm{NN}}$ and/or $J^{\perp}_{\mathrm{NNN}}$ with the lattice distortion. A simplified scenario for a lifting of frustration in $BaCo_2V_2O_8$ can be envisioned as follows. If $J^{\perp}_{\mathrm{NN}}$ decreases with increasing NN distance a small orthorhombic distortion $a_{\mathrm{o}} > a > b_{\mathrm{o}}$ lifts the frustration. The magnetic and the lattice structures are coupled such that NN spins are parallel along the shorter a_{o} and antiparallel along the longer b_o axis. This is only a qualitative, but reasonable explanation of the experimental observations described above and at present neither the sign nor the magnitude of the change of $J^{\perp}_{\mathrm{NN}}$ as a function of the distance is known, moreover, $J^{\perp}_{\mathrm{NNN}}$ can also depend on the lattice distortions.

5.2.1 Single Crystal X-ray Diffraction at XMaS

High resolution single crystal X-ray diffraction is a possible tool to verify the above presumed tetragonal-to-orthorhombic phase transition when entering the Néel ordered phase. The verification of an orthorhombic splitting would be the microscopic proof that the structure follows the (lower) symmetry of the magnetic structure and gave a more detailed view of the frustrated arrangement of the cobalt spins within the tetragonal ab plane.

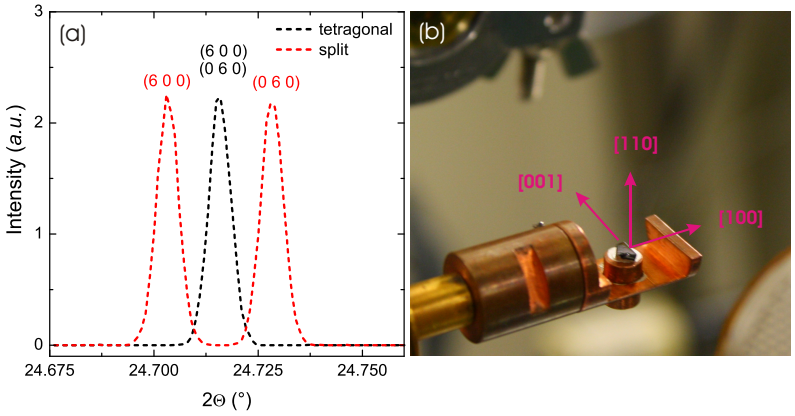

Figure 5.9: (a) Simulated spectra for a tetragonal (black) and orthorhombic (red) structure of $BaCo_2V_2O_8$ for (6 0 0) and (0 6 0) for a large splitting of $\Delta = a - b = 0.012$ Å. (b) Sample SN0133-C1 with polished (1 1 0) surface. The arrows mark the respective orientation of the sample.

An according measurement with the aim to determine the distortion factor $d = (a - b)/0.5(a + b)$ for different temperatures above and below T_N (10 K to 2 K) was carried out on the X-ray Magnetic Scattering (XMaS) facility located at the bending magnet BM28 at ESRF, Grenoble (France). It was planned to measure maps of $(h\,k\,0)$ with large h, k and with a large difference $|h - k|$, i.e. at large angles, that are most sensitive to an orthorhombic distortion, with high resolution as the distortion is expected to be very small, i.e. of the order of 10^{-5} as estimated from the zero-field thermal expansion measurements. In the tetragonal phase reflections like $(h\,k\,0)$ and $(k\,h\,0)$, e.g. (0 24 0) and (24 0 0), are indistinguishable in a powder because they are found at the same 2Θ value. For an orthorhombic distortion, the lattice constants a and b are no longer of the same value and the above mentioned reflections are split. In order to achieve as many reflections with large $(h\,k\,l)$ as possible the shortest wave length possible was chosen namely $\lambda = 0.8856$ Å corresponding to an energy of 14 keV. For a first approximation which reflections are most sensitive to a distortion, a FULLPROF simulation was carried out where the atom positions and symmetries were translated into the orthorhombic space group $Ibca$ (No. 73) which is a maximal translationengleiche subgroup of $I4_1/acd$ [66, 67]. In comparison with the respective calculations for the tetragonal space group it is possible to estimate the expectable angular shift between the two split reflections. Figure 5.9 (a) shows the reflections (6 0 0) and (0 6 0) for the tetragonal case (black) and the orthorhombic case (red) for a change in the lattice constants of $\Delta = a - b = 0.012$ Å and, thus, a distortion factor $d \approx 10^{-3}$. A splitting of one peak into two can be observed with an angular shift of $\approx 0.025°$. Note that this calculation represents an upper limit for the estimate of the angular shift since we expect a much smaller distortion from the thermal expansion measurements.

Sample

The sample used for this experiment was a part from the crystal SN0133 grown by the floating-zone technique which was also used for the neutron experiments (see Sec. 5.4.2). Three slices of about 2 mm thickness with surfaces perpendicular to [1 1 0] (2 samples) and [0 0 1] (1 sample) acting as scattering plane were prepared. Figure 5.9 (b) presents sample SN0133C1 with its (1 1 0) reflection surface mounted in the exper-

imental environment. Two edge of the slice were cut perpendicular to the [0 0 1] and [1 0 0] directions, respectively. The reflection surface was checked to have a proper orientation of less than 1° deviation and was thoroughly polished. The arrows indicate the respective orientation of the sample such that the c direction is oriented perpendicular to the incident beam.

Results

In the first step an alignment of the sample within the experimental setup was performed wherein the lattice parameter a was refined to $a = 12.4265$ Å. Scanning several intensities $(h\,k\,0)$ with $h = k$ (specular) and $(h\,k\,0)$ with $h \neq k$ (off-specular) it turned out that most of the reflections are very broad and show a shoulder. Figure 5.10 (a) shows exemplary scans of reflection (0 24 0) (black) which shows a very broad and, in this case, symmetric double peak structure. Grain boundaries can be suspected to cause such a double peak structure and in order to minimize such effects the configuration of the experimental setup was changed. For reduction of divergence effects and to increase the resolution the monochromator slit was closed to 0.2 mm (blue) and even 0.1 mm (green) yielding symmetric single reflections. However, due to the grain structure of the sample the measurement of the same intensity on different sample positions still caused troubles. As an example, scans of reflection (0 24 0), shown in Figure 5.10 (b), for three different sample positions reveal a change in shape and position. The angular shift can be understood by the grain structure assuming that each grain shows a slightly different orientation. For an orthorhombic splitting the reflections that are sensitive to changes each in a and b, respectively, they will show different signs in the angular shift (cf. Fig. 5.9). However, if for example (0 24 0) and (18 2 0) are measured on different grains it is possible for them to show a shift in the same direction simply because the grain orientation is different making the measurement incomparable. Thus, x and z scans at constant 2Θ were performed on the sample surface, see Figure 5.10 (c), showing a hilly structure. Sample positions at constant 2Θ, e.g. of (0 24 0), that showed a maximum in both x and z direction were chosen as "good" sample position, marked by arrows in panel (c) of Figure 5.10, assuming that they represent a single grain. The "same" grain at 2Θ of (18 2 0) and (18 18 0) was then identified through comparable $I(x, z)$ scans. This procedure should provide equal sample positions and, thus, equal sample quality to make the measurements comparable. This technique is far away from being waterproof but the best way to go under the given circumstances.

In order to obtain a statistic distribution of the angular shift as a function of temperature, two or more different intensities are measured on suitable grains. The best pair of reflections would have been a pair like $(h\,0\,0)$ and $(0\,h\,0)$ but there was always only one of those reflections reachable with a sufficient large h. Reflections (0 24 0) and (18 2 0) are each sensitive to changes in the lattice constants a_o and b_o, respectively and the angular shift should, thus, be of opposite sign at least within a certain grain. As a reference the reflection (18 18 0) was also measured which should be equally sensitive to a change in a_o and b_o.

Figure 5.11 shows 2Θ scans of the reflections (0 24 0) (a)-(d), (18 2 0) (e)-(h) and (18 18 0) (i)-(l) that were measured at 4 different sample positions, i.e. at each sample

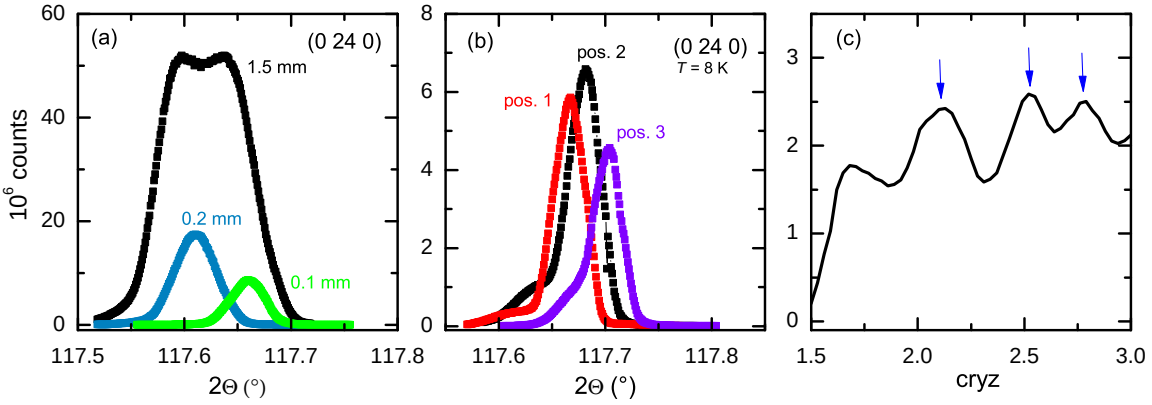

Figure 5.10: Exemplary scans of reflection (0 24 0) (a) for three different slit widths from 1.5 mm to 0.1 mm and (b) with the same slit (0.1 mm) at three different sample positions. Panel (c) shows a z scan of the sample at fixed x position. The arrows mark "good" sample positions (see text).

position all three reflections were measured for temperatures above and below T_N. In all scans one does not observe significant differences between the scans obtained above T_N, i.e. at 8 K (black) and 6 K (red). When entering the Néel ordered phase below 5.4 K (green and blue curves), however, the scans reveal a shift in 2Θ accompanied by a change in intensity and or the full width at half maximum (FWHM). Looking at a particular sample position, e.g. at position 1, we observe that (0 24 0) in panel (a) is shifted to lower 2Θ values, indicated by arrows, while for (18 2 0) in panel (e) the shift is positive. On position 3 the shift is vice versa for both reflections. This findings proof that we can measure shifts in 2Θ of opposite signs for reflections that are differently sensitive to changes in the lattice constants a_o and b_o. Thus, we observe an orthorhombic splitting. However, the behavior of (18 18 0) is not fitting into that picture but the shape of this reflection is not regular.

Several of these temperature dependent scans have been obtained on the two reflections (0 24 0) and (18 2 0) on a bunch of different sample positions. The single scans were fitted by a pseudo-Voigt line using PyMca [115] to obtain the values of 2Θ, the maximum intensity I_{max} and the FWHM in order to derive a statistic preference of these measures for the different kind of reflections. Panels (a) and (d) of Figure 5.12 show the shift $\Delta 2\theta$ of the scattering angle with respect to the value at 8 K. A tendency towards a negative shift for the (0 24 0) and a positive shift for (18 2 0) can be observed. If 2θ decreases (increases), the corresponding lattice parameter has to increase (decrease) to preserve Bragg's law. Consequently, the data reveal that b_t tends to increase while a_t decreases. The approximate shift of 0.003° in 2Θ corresponds to a relative change in the lattice constant of about $\frac{\Delta a}{a} \approx 2.4 \cdot 10^{-4}$. This change in the scattering angle seems to be accompanied by a change in I_{max}, see panels (b) and (e), such that the intensity increases below T_N for (0 24 0) and vice versa for (18 2 0). The FWHM, however, mainly increases for both reflections.

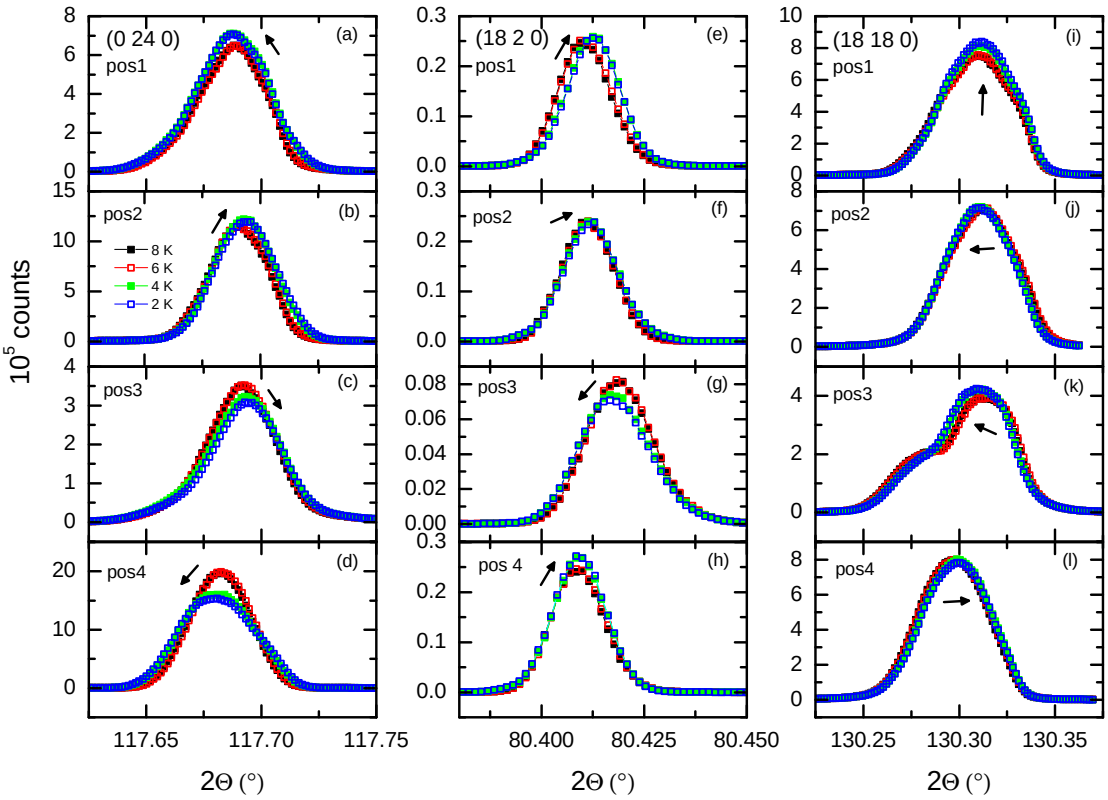

Figure 5.11: 2Θ scans of (0 24 0) (a)-(d), (18 2 0) (e)-(h) and (18 18 0) (i)-(l) at 4 different sample positions. At each position the reflections were measured each above and below T_N $=\approx 5.5\,K$, i.e. at $T = 8\,K$ (black), 6 K (red), 4 K (green) and 2 K (blue). The arrows indicate the direction of the shift when entering the Néel ordered phase.

5.2.2 Powder X-ray Diffraction at ID22

An additional high resolution X-ray powder diffraction (XRPD) measurement on $BaCo_2V_2O_8$ for different temperature above and below T_N was carried out on ID22 [43][3]. The sample was a well ground powder of crystallites that were synthesized by the spontaneous nucleation method that was mounted in a glass capillary. The measurements were carried out with a wavelength of $\lambda = 0.399$ Å corresponding to an energy of 31 keV. The full pattern and according results of the FULLPROF refinement are shown in the Appendix, Figure B.3. Panel (a)-(d) of Figure 5.13 show one exemplary reflection with $hkl = (6\,0\,0)$, $(0\,6\,0)$ for the different temperatures together with the FULLPROF refinement curve (black). The reflection shows a slight shift in 2Θ from $T = 100\,K$ to 10 K which corresponds to the thermal expansion. Neither a splitting or broadening nor a significant shift can be observed below T_N. Figure 5.14 shows the 3.2 K data (grey) together with the results of 4 FULLPROF simulations depicted as dashed lines. The blue pink curve represents a simulation where the structure is is already orthorhombic assuming a relative distortion $\Delta a/a = 10^{-4}$. Just above this value the peak starts splitting into two as can be seen when changing the distortion

[3]Thanks to the efforts of the local contact of XMaS, D. Wermeille, and the team of ID22!

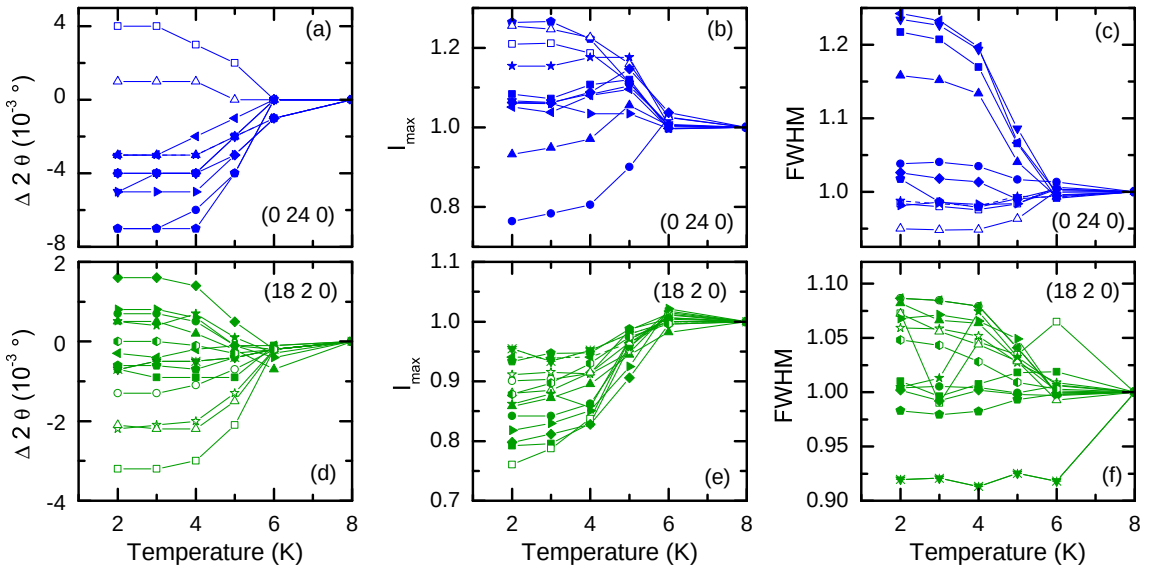

Figure 5.12: Different (fit) parameters of (0 24 0) (a)-(c) and (18 2 0)(d)-(f) as a function of the temperature. From left to right the panels show the shift $\Delta 2\Theta(T)$, the maximum intensity I_{max}, and the FWHM of the intensities. All measures were normalized to their value at $T = 8\,\mathrm{K}$ within each measurement.

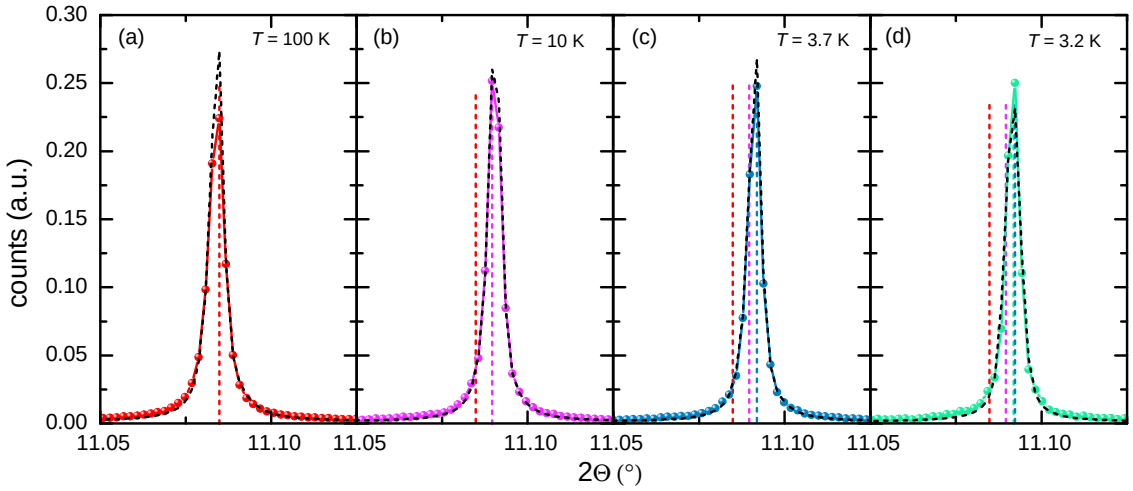

Figure 5.13: Reflections (6 0 0), (0 6 0) of $Ba\,Co_2V_2O_8$ for temperatures of (a) 100 K, (b) 10 K, (c) 3.7 K and (d) 3.2 K. Data points are depicted in red, the FULLPROF fit is the dashed line. The shift in 2Θ is marked by the colored vertical lines that represent the maximum positions at the respective temperatures.

from $5 \cdot 10^{-4}$ to 10^{-3}. Judging from this simulation, the orthorhombic distortion is smaller than $\Delta a/a = 10^{-4}$ which is consistent with the thermal expansion measurements where a relative length change of 10^{-5} was determined.

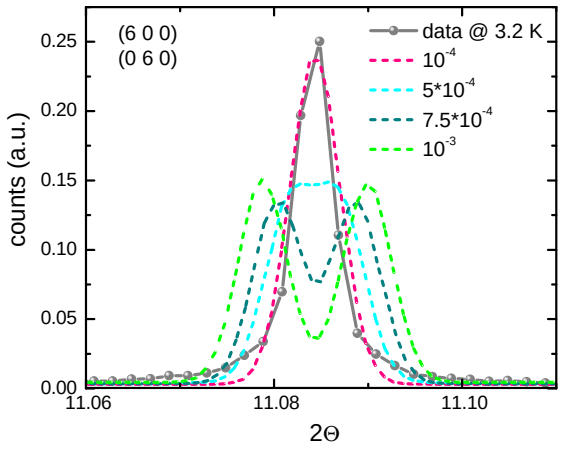

Figure 5.14: 3.2 K curve (gray) of reflection (6 0 0) in comparison with FULLPROF simulations for different orthorhombic splitting from 10^{-4} (pink) to 10^{-3} (green). A significant broadening of the peak starts at a relative splitting of $\Delta a/a = 5 \cdot 10^{-4}$.

5.2.3 Conclusion

Zero-field thermal expansion of $BaCo_2V_2O_8$ measured along the tetragonal a axis show a pressure-dependent spontaneous strain when entering the Néel ordered phase. Moreover, the sign of the strain can be changed, indicating that the structure of $BaCo_2V_2O_8$ undergoes an orthorhombic distortion due to the lower symmetry of the magnetic structure. Applying pressure yields a domain switching process with a preference for an alignment of the shorter orthorhombic axis along the direction of pressure. Thermal expansion yields a splitting of the order of $\Delta a/a = 10^{-5}$. Such a distortion would cause a change of $a \cdot (1 \pm 10^{-5}/2)$. Thus, the new lattice constants are $a_o = 12.426\,56$ Å and $b_o = 12.426\,44$ Å if assuming a symmetric change in both constants. This corresponds roughly to a change of the lattice constant by 0.0002 Å as the lower limit.

High resolution single crystal X-ray diffraction was applied to microscopically quantify the magnitude of the orthorhombic splitting. Reflections sensitive to changes in a_t and b_t show different signs in their shift of the scattering angle 2Θ with a preference of the reflection sensitive to b_t to show a negative $\Delta 2\Theta$. This corresponds roughly to a decrease in b_t of about 0.003 Å, i.e. $\frac{\Delta a}{a} \approx 2.4 \cdot 10^{-4}$. However, these results have to be handled with caution, because one finds only preferences in the shifts. The presented data in Section 5.2.1 are far from a good statistic, however, the tendencies can be extracted.

The mosaic of the sample does play a minor role in the thermodynamic measurements but becomes quite important in the high resolution single crystal diffraction experiment. The problems described in the first part of these experiments most probably occurred due to a poor mosaicity of the sample, i.e. the quality of the diffracting planes, either due to lattice defects/ impurities or due to damage of the sample through the polishing process. Other effects due to the mosaicity of the sample (e.g. measuring on a grain boundary) may give a biased interpretation of the data. Since a sample size of $5 \times 5 \times 2$ mm was requested for the experiment, a crystal prepared by spontaneous nucleation method was disregarded due to their much smaller size. Most probably such a crystal would have provided less crystal defects and reveals naturally grown planes with essentially no need for polishing.

High resolution X-ray powder diffraction were obtained at different temperatures

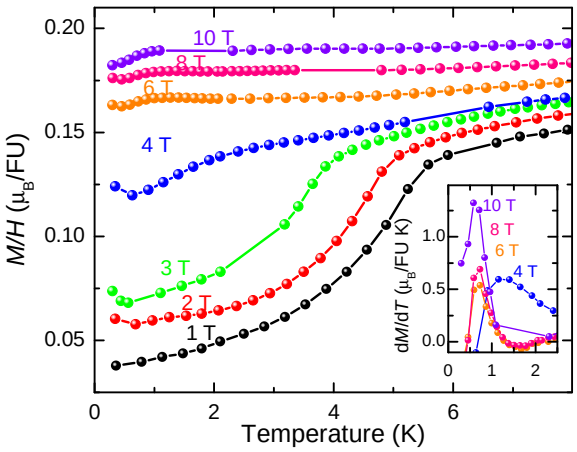

Figure 5.15: Low-temperature magnetic susceptibility of $BaCo_2V_2O_8$ for $H \,||\, c$ for different magnetic fields. The inset shows the temperature derivatives of the magnetization $dM(T)/dT$ which reveal sharp anomalies below $T \simeq 1\,\mathrm{K}$. This anomalies reflect the crossover to the incommensurate phase.

above and below T_N. Neither a splitting nor a broadening of reflections can be resolved below T_N, thus we can not extract a significant orthorhombic splitting from these data. Different estimations from the expected order of a angular splitting $\Delta 2\Theta$ and from FULLPROF simulations suggest that a distortion smaller than 10^{-4} can not be resolved in this setup which has an angular resolution of 0.005° [43]. Thus, this experiment is neither able to confirm or refute microscopically the orthorhombic splitting that was observed macroscopically.

5.3 *H* parallel *c*

As the c axis is the magnetic easy axis of $BaCo_2V_2O_8$, this field direction was elaborated in literature and, as introduced above, the magnetic phase diagram comprehends a variety of phenomena. In this section the investigation will be extended through low-temperature magnetization data as well as thermal expansion and magnetostriction measurements in magnetic fields up to 17 T.

Figure 5.15 (a) shows the temperature dependent magnetization M/H of $BaCo_2V_2O_8$ for different magnetic fields parallel to c down to 250 mK. The measurements were carried out with the Faraday magnetometer (see Sec. 2.3). For fields above 3 T a small kink is observed in the low-temperature region. This kink is reflected also in an anomaly of the temperature derivative of the magnetization $dM(T)/dT$, shown in the inset. $dM(T)/dT$ For a magnetic field of 4 T (c), which is located at the crossover region between Néel ordered and incommensurate state, the anomaly is relatively broad. For higher fields, the anomaly is shifted below a temperature of 1 K. This anomaly is located pretty close to the lowest reachable temperature. However, this sharp anomaly can be attributed to the crossover from the incommensurate phase into the paramagnetic phase. Due to experimental issues, the absolute values of the magnetization have to be handled cautiously.

Thermal expansion measurements further proof a signal of the incommensurate to paramagnetic crossover and extend the phase boundary to a magnetic field up to 17 T. Figure 5.16 summarizes the thermal expansion and magnetostriction data along the chain direction c for different magnetic fields applied along the same direction, i.e. along the Ising axis. The Néel ordering in low magnetic fields is accompanied by a

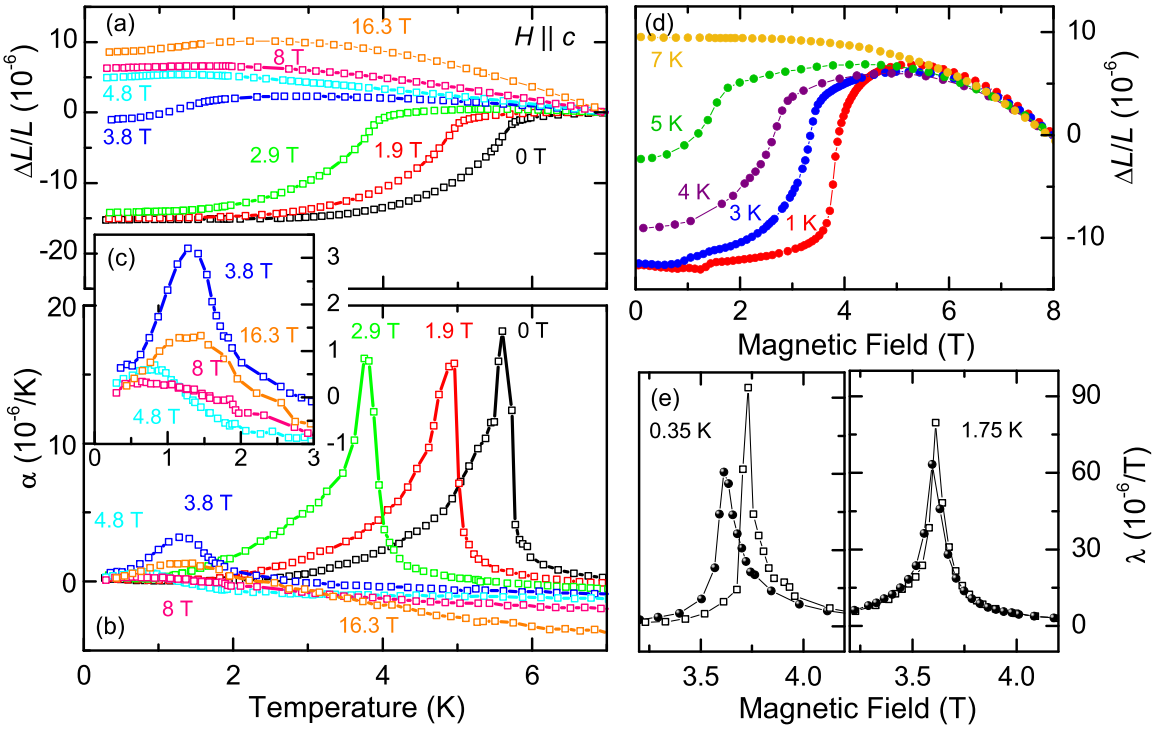

Figure 5.16: Thermal expansion (left) and magnetostriction (right) of $BaCo_2V_2O_8$ of the c axis for magnetic fields $H \,||\, c$. The upper panels depict the relative length changes related to $L_0 = L(7\,\mathrm{K}, H)$ and $L_0 = L(T, 0\,\mathrm{T})$, respectively. The lower panels show the derivatives of $\Delta L/L$ with respect to T or H. Panel (c) is an enlargement of the low-temperature range of (b). In all panels open (closed) symbols represent data measured with increasing (decreasing) temperature or magnetic field.

pronounced spontaneous contraction in the thermal expansion, see Figure 5.16 (a). The field dependence of T_N can easily be monitored by considering the shift of the anomalies in the corresponding temperature derivatives, i.e. in the thermal expansion coefficient $\alpha(T)$, which are shown in panel (b). The shape and the amplitude of the anomalies do hardly change up to about 3 T, but with further increasing magnetic field the anomalies rapidly drop in size and drastically broaden. As shown in panel (c), which is an enlargement of the low-temperature region of (b), the position as well as the magnitude of these anomalies non-monotonically vary with increasing H. The drastic change of the anomalies around 4 T is related to a transition from the Néel ordered state to an incommensurate high-field low-temperature phase as has been established by diffraction studies [24, 106].

The corresponding lengths changes have also been studied as a function of magnetic field at low-temperatures. Figure 5.16 (d) shows the magnetostriction measurements $\Delta L(H)/L$ for several temperatures below T_N. Below about $T = 1.5$ K the length changes at ≈ 4 T are almost discontinuous. Moreover, depending on the field-sweep direction a clear hysteresis occurs, see Figure 5.16 (e), confirming the proposed first order character of this transition from the Néel ordered to the incommensurate phase. For higher temperatures, the magnetostriction curves are more continuous and the hysteresis vanishes. The transition is, thus, of second order and marks the border

between Néel ordered and paramagnetic state.

Compared to the transition from Néel order to the paramagnetic state, the corresponding anomalies in the thermal expansion are rather broad for the crossover from the incommensurate phase into the paramagnetic state. An explanation for this behavior may be found considering the Spin-Peierls system $CuGeO_3$ where a similar change of the shape and broadening of the anomalies in the temperature-induced transitions when entering an incommensurate phase was observed [116–119]. This broadening effect was even enhanced in doped $CuGeO_3$ with increasing doping concentration, suggesting that the incommensurate phase is more severely disturbed by disorder than the commensurate phase [119]. Because the field-induced broadening in pure $BaCo_2V_2O_8$ is already more pronounced than that in weakly doped $CuGeO_3$, one may speculate that the rather complex structure of $BaCo_2V_2O_8$ could be very sensitive to defects which could be the reason for the drastic broadening of the transitions to the incommensurate phase. In $BaCo_2V_2O_8$, the microscopic nature of the high-field phase is not yet clear and a direct comparison of the spin-Peierls order in $CuGeO_3$ with the Néel order of $BaCo_2V_2O_8$ can not be made. Nevertheless, the mere fact that there is a pronounced spontaneous contraction of c in the Néel-ordered phase establishes a significant magnetoelastic coupling also in $BaCo_2V_2O_8$. Considering the most simple scenario of a NN interaction J_{NN} which increases with decreasing NN distance, the spontaneous contraction of c below T_{N} would result from a gain in magnetic energy ($E_{\mathrm{mag}} \propto -\Delta c$), which overcompensates the corresponding loss of elastic energy ($E_{\mathrm{el}} \propto \Delta c^2$). Together with the above discussion of the orthorhombic distortion (see Sec. 5.2), one can, thus, summarize that perhaps the most simple model of antiferromagnetic NN intra-chain (J) and inter-chain ($J_{\mathrm{NN}}^{\perp}$) interactions can explain the observed lattice distortions below T_{N}.

However, this scenario has to be handled cautiously because the considered NN couplings $J^i||i$ do not only depend on the corresponding longitudinal distortions parallel to i, but also on the distortions in the transverse directions $j, k \perp i$ and additionally, e.g., NNN, couplings and their dependencies on distortions along i, j, k may also be important for a quantitative description.

Magnetic Phase Diagram and Conclusion

Figure 5.17 summarizes the above presented data in the temperature *vs.* magnetic field phase diagram of $BaCo_2V_2O_8$ for magnetic fields applied along the c axis. The phase boundary was obtained by the extrema of the measured variables, i.e. of $\alpha(T)$ ($\triangleleft$), and $\lambda(H)$ ($\triangledown$) and the derivatives of the low-temperature magnetization $\frac{\mathrm{d}M(T,H)}{\mathrm{d}(T,H)}$ ($\square$). Additionally, thermal-conductivity measurements κ ($\circ$) (cf. Ref. 53) are also included.

In all measures, the anomalies attributed to the onset of Néel order are visible and rather sharp. The transition to the incommensurate phase, however, is detected only in the low-temperature magnetization and in the temperature dependent length change where the anomalies are very broad (see Fig. 5.16). The inset of Figure 5.17 shows three representative high-field anomalies in $\alpha(T)$ which rather indicate a broad crossover behavior instead of well-defined phase transitions. As a phenomenologi-

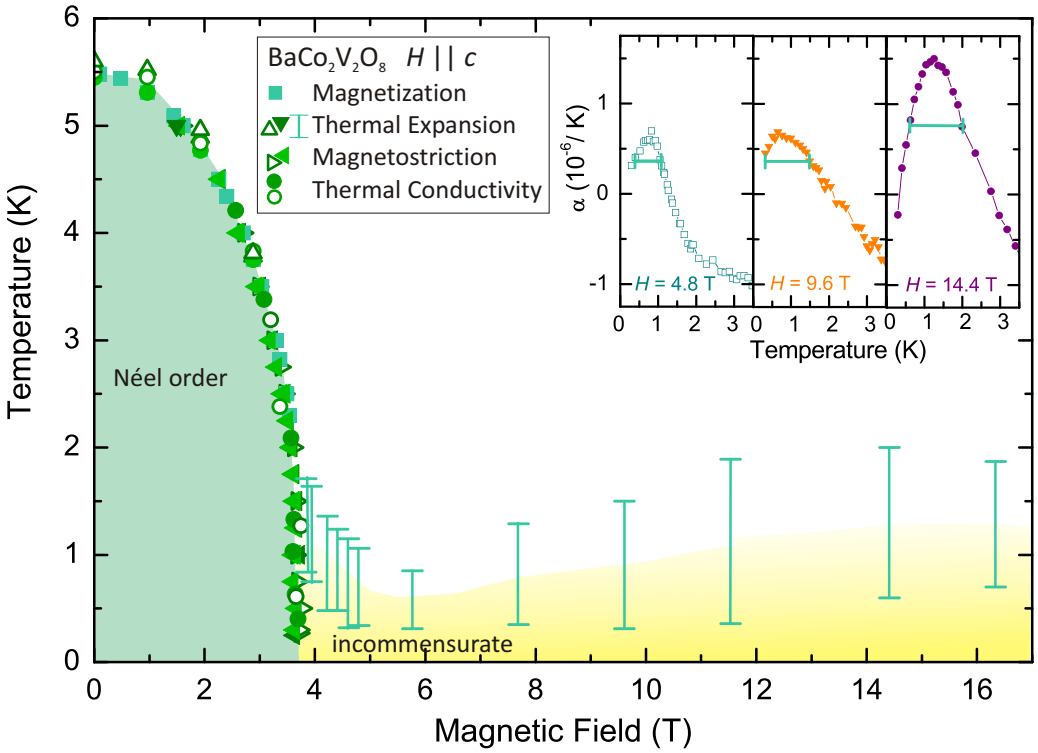

Figure 5.17: Magnetic phase diagram of $BaCo_2V_2O_8$ for $H \,||\, c$. The inset shows exemplary corresponding thermal expansion anomalies of the crossover region. The width at half maximum of theses anomalies are depicted as vertical bars in the higher-field range of the main panel to mark the broad crossover regions to the incommensurate phase (see text). Data points were obtained by measurements of the magnetization (■), thermal expansion (⋆), magnetostriction (▽), and thermal conductivity (○). Open and closed symbols represent measurements with increasing and decreasing field or temperature.

cal measure of the crossover region, the width at half maximum (green bars) of the corresponding thermal expansion anomaly was used. The corresponding positions of the maxima of $\alpha(T)$ were marked in the magnetic phase diagram as vertical bars representing the anomaly width in T.

The phase diagram agrees well with those reported previously by using other techniques [16, 24, 105–107, 110, 111]. For comparison, three of them are depicted in Figure 5.18. In the low-field range of the Néel-ordered phase all these reports essentially agree with each other, but some discrepancies are present in the high-field range. For example, experimental evidence for additional phase transitions in the region of the incommensurate phase probed by sound velocity measurements are reported, see panel (a) [110]. The additional features observed in this measurements are located in the field range close to the triple point but corresponding effects are neither seen in other literature data nor in the measurements presented here. As already discussed before, the data presented in this thesis reveal a 2^{nd} order transition from the Néel ordered to the paramagnetic phase, whereas the transition from Néel order to the incommensurate phase is accompanied by a field hysteresis in the magnetostriction marking the transition as 1^{st} order transition. These findings are confirmed by the

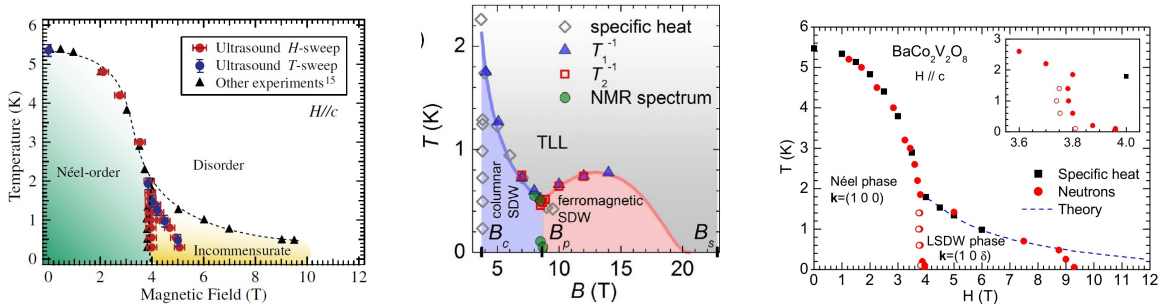

(a) taken from Ref. 110 **(b)** taken from Ref. 111 **(c)** taken from Ref. 24

Figure 5.18: Selection of temperature *vs.* magnetic-field phase diagrams of $BaCo_2V_2O_8$ for $H \,||\, c$ in several publications ordered by publication date. All of them show a steep decrease of the Néel temperature with $H_{crit} \approx 4\,\mathrm{T}$ where a first order transition into an incommensurate order occurs. All diagrams reveal additional features above 4 T. Yamaguchi *et al.* (a) detected additional features by sound velocity measurements in the region around 4 T to 6 T. NMR experiments (b) and neutron diffraction (c) give evidence for another crossover in the region around 9 T.

results of an extensive neutron diffraction study by Canévet et al. [24] where a similar field hysteresis that is dependent on the field-sweep rate is observed below $T \simeq 2\,\mathrm{K}$. The authors also report the coexistence of the Néel and incommensurate ordering in the respective field range. Most of the previous reports could follow the boundary to the high-field phase only up to a maximum magnetic field of $\approx 10\,\mathrm{T}$ [24, 105–110] and only recently the field range has been extended up to 14 T by an NMR study [111]. These measurements revealed a minimum of the phase boundary around 8.6 T and it was suggested to be related to a rearrangement concerning the magnetic inter-chain ordering. The theoretical approaches of Klanjšek et al. [111] predict a crossover from an antiferromagnetic spin density wave (SDW) to a ferromagnetic spin density wave. In these terms the antiferromagnetic SDW has to be identified with the incommensurate low spin density wave (LSDW) with a propagation vector $k = (1, 0, \delta)$ described in Ref. 24 which actually vanishes at $H \approx 9\,\mathrm{T}$, see Figure 5.18 (c). Within the ferromagnetic SDW the chains with LSDW are coupled ferromagnetically both in a and b direction. Signals of this phase were found in Ref. 111 but could, so far, not be confirmed in other reports [24]. Theoretical studies on the basis of bosonization combined with mean-field theory for the inter-chain interaction suggested an alternative possible origin for a non-monotonic phase boundary. The model proposes a possible change from the incommensurate phase with spins parallel to c towards a transverse staggered phase with spins oriented (mainly) perpendicular to c [120, 121].

Despite the drastic broadening of the high-field anomalies, the data presented here clearly support the occurrence of a minimum of the phase boundary around $\approx 8\,\mathrm{T}$, but the macroscopic data can neither confirm nor refute any of the proposed microscopic changes of the magnetic structure. The corresponding low-temperature magnetostriction data shown in Figure 5.16 (d) do not yield any indication for the occurrence of a field-induced phase transition around 8 T. Such a possible rearrangement of the magnetic structure, however, may be expected to be signaled also only by extremely

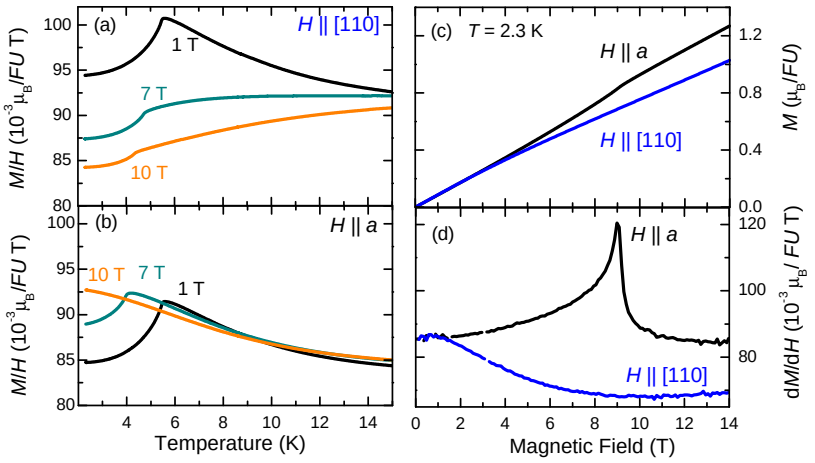

Figure 5.19: Magnetic susceptibility of $BaCo_2V_2O_8$ for $H \,||\, [1\,1\,0]$ (a) and $H \,||\, a$ (b). (c) Magnetization $M(H)$ for both field directions at $T = 2.3\,\mathrm{K}$ and (d) the derivative with respect to the magnetic field.

shallow anomalies, concerning the very broad and small anomalies of $\alpha(T)$ at the boundary to the incommensurate phase.

It is worth mentioning in this context, that the anomalies in the thermal expansion were observed only in crystals grown by the spontaneous nucleation method. All other samples that were grown via floating zone method, did not reveal according anomalies. However, the temperature dependent magnetization was obtained on floating zone sample (SN0075) and an anomaly can be resolved only in the magnetization. The question is, whether the absence of anomalies in the thermal expansion is attributed to lattice defects due to the rather fast cooling in a mirror furnace compared to the extremely slow crystal growth process in the spontaneous nucleation method. Another explanation would be a small misalignment of the sample orientation with respect to the magnetic field. The samples grown by spontaneous nucleation method have natural facets and do not necessarily have to be cut in shape in contrast to the floating zone samples. Additionally, experimental errors in the alignment within the measurement environment may occur. The features observed in e.g. the NMR measurements of Ref. 111 were also rather sensitive to the exact alignment [95].

5.4 In-plane Anisotropy: *H* perpendicular to *c*

Until recently, the field direction perpendicular to the easy c axis of $BaCo_2V_2O_8$ seemed to be of comparatively little interest. When our studies on $BaCo_2V_2O_8$ started, only few measurements for $H \perp c$ were presented in literature. The low-temperature magnetization $M(H)$ shown in Figure 5.4 [102], for example, yields a very high saturation field of about 40 T for the field direction perpendicular to the c axis which is nearly twice the saturation field for $H \,||\, c$. The phase boundary for $H \perp c$ was also probed by specific heat measurements [103] and expected to be rather flat. Together with a more recent study of the thermal conductivity [104], the reported phase boundaries in the region of 9 T are contradictory. Moreover, in both studies the explicit field direction within the ab plane has not been specified, but my measurements reveal a significant anisotropy between $H \,||\, a$ and $H \,||\, [1\,1\,0]$. Such an in-plane anisotropy is not in contradiction with the tetragonal symmetry of the paramagnetic

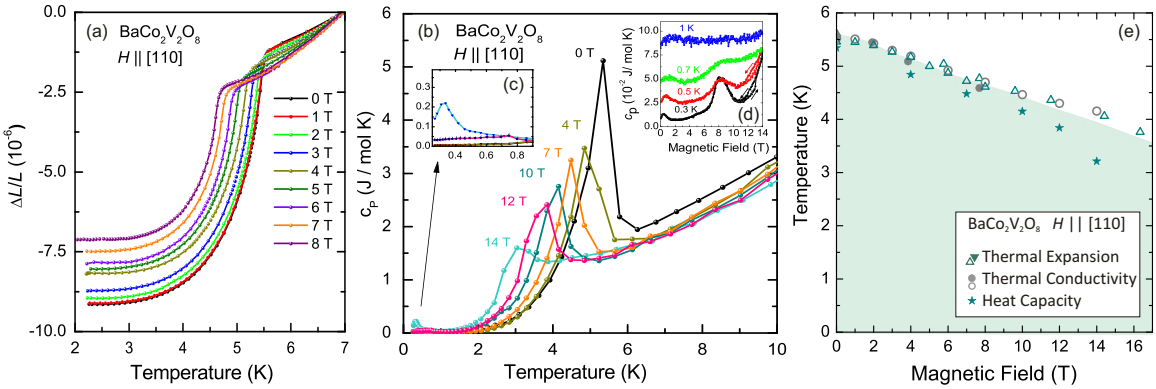

Figure 5.20: (a) Thermal expansion $\Delta L_{[1\,1\,0]}/L_{[1\,1\,0]}$ of $BaCo_2V_2O_8$. (b) Heat capacity for different fields. Inset (c) shows an enlargement of the low-temperature region. Inset (d) field-dependent heat capacity for low temperature. (e) Corresponding magnetic field *vs.* temperature phase diagram derived by thermal expansion ($\star$), thermal conductivity ($\circ$) and heat capacity ($\star$) measurements.

high-temperature phase and, anyway, the symmetry is reduced to orthorhombic in the Néel ordered phase as discussed in Section 5.2; although for macroscopic probes this is (at least partly) masked by the twinning of the crystals.

The anisotropy for magnetic field directions parallel a and $[1\,1\,0]$ can easily be seen in the magnetization of $BaCo_2V_2O_8$. Figure 5.19 compares representative magnetization data for both field directions where the left panels present the temperature-dependent magnetization and the right panels comprise the field-dependent measurements. For $H = 1\,\mathrm{T}$ the curves for both field directions only differ by about 10 % and show a sharp kink around the transition temperature. Further increasing the magnetic field to 7 and 10 T yields a pronounced anisotropy as is indicated by the change of the curvatures as well as by the different shift of the transition temperature with increasing magnetic field, see panels (a) and (b). While increasing the field to 10 T causes a continuous suppression of M/H and a weak decrease of T_N for $H \,||\, [1\,1\,0]$, T_N is so strongly suppressed for $H \,||\, a$ that it is no longer visible in the 10 T curve. Above T_N there is also little change of M/H with the field. The field dependent magnetization $M(H)$ measured at $T = 2.3\,\mathrm{K}$ for both field directions is depicted in panel (c). For $H \,||\, [1\,1\,0]$ the magnetization increases continuously with a slight downward curvature up to the maximum field of 14 T. For $H \,||\, a$, however, the $M(H)$ has a clear anomaly at $\approx 9.2\,\mathrm{T}$ signaling a phase transition which is best seen in the corresponding differential susceptibility $\partial M/\partial H$, shown in panel (d). In the following, the experimental results for the two in-plane field directions are discussed separately.

5.4.1 *H* parallel [110]

Figure 5.20 (a) shows the thermal expansion $\Delta L_{[1\,1\,0]}/L_{[1\,1\,0]}$ for different magnetic fields $H \,||\, [1\,1\,0]$. In zero magnetic field, a spontaneous contraction develops below T_N, which is roughly decreased by a factor of 2 on increasing the magnetic field. Concurrently, the transition temperature, derived from the maxima of the corresponding $\alpha_{[1\,1\,0]}(T)$ (not shown), continuously decreases with a slope $\partial T_\mathrm{N}/\partial H \simeq -0.1\,\mathrm{K/T}$.

This field dependence is revealed in the specific heat, Figure 5.20 (b). However, in a magnetic field of 14 T a small maximum arises in the low-temperature region, i.e. at $\simeq 0.3$ K see inset (b). The field dependent specific heat, inset (c), for temperatures below 1 K reveals a hysteresis for increasing and decreasing magnetic field located in the field region higher than 12 T. Moreover, a maximum is observed in the 0.3 K curve at $H = 8$ T that is already flattened at $T = 0.5$ K and is completely vanished at $T = 1$ K. Neither the origin of the low-T maximum in $c_p(T)$ nor the anomalies in $c(H)$ are known, so far, but similar behavior is also observed in the field direction $H \,||\, a$, see discussion in Section 5.4.2.

The phase boundary for $H \,||\, [1\,1\,0]$, shown in Figure 5.20 (e), was derived from the maximum positions in the thermal expansion coefficient and the heat capacity and, additionally of the thermal conductivity data presented in Refs. 23, 53. The specific heat data differ from that of the other two measurements, most probably due to a slight misalignment of the sample due to the technical setup. Also the point density is not the best to obtain sharp anomalies. Comparing the phase boundary for $H \,||\, [1\,1\,0]$ with former versions of a phase diagram in literature yields a very good agreement with the $H \perp c$ phase diagram based on specific heat data [103]. One may, thus, suppose that those data were measured with $H^{\perp c}||[1\,1\,0]$ in particular because such an orientation appears naturally due to the fact that the crystal of Ref. 103 was grown by spontaneous nucleation. The crystal grown by this method within this thesis has flat (1 1 0) surfaces which seems to be the preferred growth geometry (cf. Sec. 3.3.1).

As discussed previously, the Néel ordering causes an orthorhombic splitting $a_o > a_t > b_o$ and the crystal is twinned below T_N. Such a twinning does, however, not influence the expansion along [1 1 0] since both types of domains are rotated with respect to each other by 90° around the c axis. The relative length change along the diagonals of each domain is given by $\Delta L_{[1\,1\,0]}/L_{[1\,1\,0]} = (\Delta a_o/a_o + \Delta b_o/b_o)/2$ with the individual $\Delta a_o/a_o$ and $\Delta b_o/b_o$ being of opposite signs. Their absolute values can be expected to be of similar magnitude and not too much larger than the measured$\Delta L_{[1\,1\,0]}/L_{[1\,1\,0]} \simeq 10^{-5}$. The corresponding orthorhombic splitting $(a_o - b_o)/(a_o + b_o)$ should thus be in the 10^{-5} range.

5.4.2 *H* parallel [100]

Now the focus shall be set on the configuration with H applied along one of the tetragonal a_t axes. The thermal-expansion data measured along this direction are presented in Figure 5.21 (a). In this setup the domain structure below T_N is such that a small spontaneous contraction is present in zero field. On increasing the magnetic field, the magnitude of the spontaneous contraction rapidly decreases and around 3 T it even changes sign and turns into a spontaneous expansion, which is of maximum size around 6 T and finally completely vanishes above 10 T. The field dependence of T_N is best monitored by considering the shift of the maxima/minima of the corresponding thermal-expansion coefficient $\alpha(T)$ shown in Figure 5.21 (b). The curves are shown with an offset against each other for clarity. At first glance the sign change around 3 T might be interpreted as an indication for an additional structural or magnetic transition. However, we already know that the crystal is twinned and a more natural explanation arises from a magnetic-field induced (partial) detwinning by assuming that the

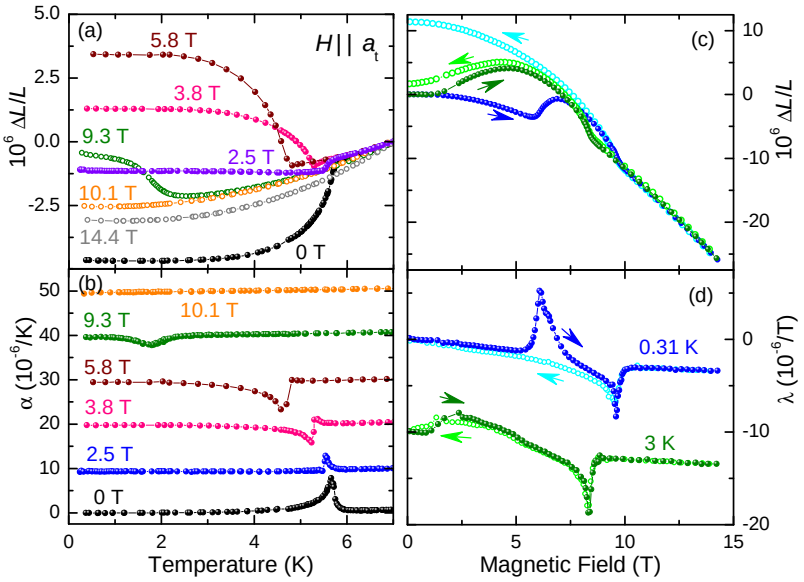

Figure 5.21: Thermal expansion (a) of the tetragonal a axis for magnetic fields $H \,||\, a$. A sign change occurs in $\Delta L/L$ and α (b) around 3 T due to field-induced partial detwinning. The magnetostriction data (c) depend on the field sweep direction (indicated by arrows) for the same reason in the low-T region. For clarity the curves in panel (d) are shifted with respect to each other by 10^{-6}/T.

magnetic field favors those domains which are aligned with the longer a_o axis parallel to H. An opposing impact has to be expected by applying a magnetic field or uniaxial pressure on the same a_t axis because H favors the "long" domains being aligned along $H \,||\, a_t$, whereas uniaxial pressure prefers the "short" domains along its direction. In a transverse configuration, i.e. when applied along two orthogonal a_t axes, however, magnetic field and pressure would support each other because both favor the same type of domain orientation (cf. Fig. 5.8 p. 70). In analogy to the pressure-cooled measurements of the zero-field thermal-expansion data that were discussed in Section 5.2, the $\Delta L(T, H)/L$ curves of Figure 5.21 were measured in a "field-cooled" mode where the magnetic field was only changed well above the transition temperature.

Panels (c) and (d) of Figure 5.21 display some exemplary $\Delta L(H)/L$ and $\lambda(T)$ curves, respectively, measured at constant temperature after the sample has been cooled in zero magnetic field. The field-sweep directions are indicated by arrows. At $T = 0.31$ K, $\Delta L(H)/L$ shows two anomalies on increasing the field (dark blue): a step-like increase at $\simeq 6$ T and a slope change at $\simeq 10$ T. While the slope change is reversible, the step-like change is absent in the field-decreasing run (light blue). At a higher temperature $T = 3$ K (green), broadened but still hysteretic anomalies occur in $\Delta L(H)/L$ around 2 T for both field-sweep directions. The analogous reversible slope change as in the low-temperature curves is observed now at $\simeq 8.5$ T. The slope changes at higher fields correspond to a field-driven crossing of the second-order phase boundary, which is already known from the temperature-dependent measurements as shown in the left panels of Figure 5.21.

The anomalies in the field dependence of $\frac{\Delta L}{L}$ at the lower magnetic fields feature a similar hysteresis behavior as it is known, e.g., from hysteresis loops of ferromagnets. Thus, the more or less step-like increase on increasing field is explained by the field-induced domain orientation as discussed above.

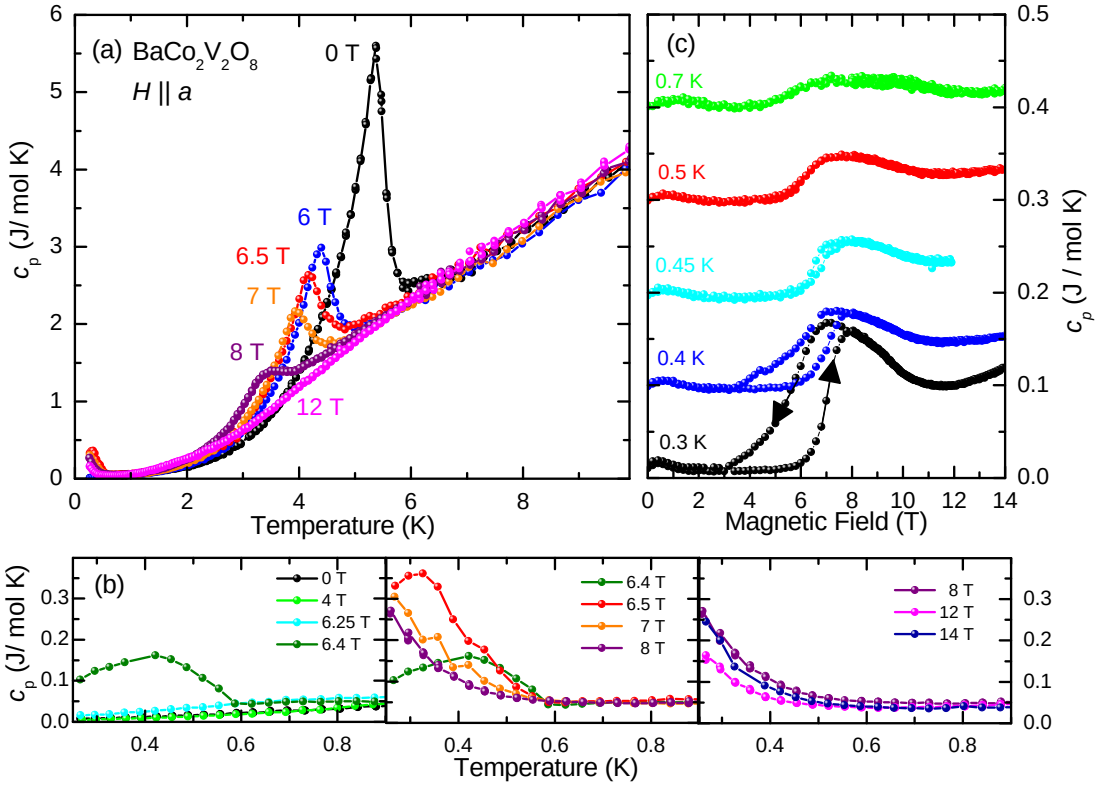

Figure 5.22: (a) Specific heat measurements for $H \,||\, a$ in different magnetic fields up to 12 T. Panels (b) show an enlargement of the low-temperature region below 1 K. (c) The field dependent specific heat at different temperatures between 0.3 K to 0.7 K. The curves are shifted by 0.1 J/mol K for clarity.

Specific Heat

The specific heat of $BaCo_2V_2O_8$ for field directions perpendicular to the c axis was, so far, reported without naming the explicit field direction. However, the phase boundary derived from those measurements could be identified with that for $H \,||\, (1\,1\,0)$, as discussed in Section 5.4.1. Figure 5.22 presents the specific heat of $BaCo_2V_2O_8$ for different magnetic fields parallel a measured down to a temperature of 250 mK. In zero magnetic field (black), the specific heat shows a sharp anomaly at T_N, below this transition temperature no further anomalies occur. Increasing the magnetic field brings several changes into the curve. First of all the transition temperature signaled by the maximum of the anomaly is shifted to lower temperatures. Secondly, the peak height strongly decreases while the peak is broadened. For fields above about 10 T, the anomaly has vanished, which further confirms the previously probed phase boundary in the temperature versus magnetic field phase diagram. Additionally, a small anomaly occurs below $T = 600$ mK for magnetic fields larger than 6 T, see Figure 5.22 (b), that increases in height and is shifted to even lower temperatures with further increasing field. In this temperature regime, the measured heat pulse curves show atypical temperature relaxation. One explanation could be a bad thermal coupling of the sample due to a small thermal conductivity. A Schottky anomaly, which reflects the specific heat of two states separated by an energy gap ΔE, could also be considered

to analyze the low-temperature anomaly. Using the high temperature approximation for $\Delta E << k_B T$ [122] the magnetic contribution to the specific heat can be written as

$$C_m \propto N_A k_B \left[\frac{\Delta E}{2k_B T}\right]^2 . \tag{5.1}$$

Indeed, a fit to the 12 and 14 T curves, i.e. above H_c yields an energy gap of about $\Delta E/k_B \simeq 80$ mK. However, a Schottky anomaly should be independent of the magnetic-field direction if originating from the moment of the nucleus, which is not the case for $BaCo_2V_2O_8$.

Considering the field dependence of the low-temperature specific heat suggests a relation to the domain switching processes. Figure 5.22 (c) shows the specific heat as a function of the magnetic field applied along a at different temperatures below 1 K. At $T = 0.3$ K (black) the curves for increasing and decreasing magnetic field (sweep direction marked by arrows) show a large hysteresis between 3 T to 7 T and a step-like increase of c_p with increasing field. The hysteresis vanishes already at 0.5 K and the step systematically flattens.

Thus, the previously discussed low T anomaly occurs exactly at the position where $c(H)$ shows the steepest increase and hysteretic behavior. Note that the critical magnetic field for the breakdown of the Néel ordered phase is not reflected in a sharp anomaly. Only an inflection point can be roughly identified at H_c. As the increase of c_p does not coincide with the field-induced transition from the antiferromagnetic phase, it possibly stems from the domain dynamics that pop up in α (and also in neutron experiments, see below) at the same field range.

So far, neither the origin of the low-temperature anomaly nor the hysteretic field dependent specific heat are completely understood and are only suspected to be correlated to the domain switching process in this compound. A further investigation to even lower temperatures could be of interest.

Magnetic Phase Diagram

Figure 5.23 shows the magnetic phase diagram of $BaCo_2V_2O_8$ for magnetic fields $H \,||\, a$. The phase boundary reveals a complete suppression of the Néel temperature for a critical magnetic field of about 10 T. The shape of the phase boundary was consistently confirmed by all the different measures labeled by different symbols. Small quantitative deviations of the critical fields obtained by one set of thermal-conductivity measurements compared to the other data most probably arise from a slight misalignment of the magnetic-field direction. A similar strong field dependence of T_N for $H \perp c$ has been reported for $SrCo_2V_2O_8$ in Ref. 25 and due to the structural alikeness a similar in-plane ansiotropy is observed also in $SrCo_2V_2O_8$ as will be shown in Section 6.1. As indicated by the dashed line in Figure 5.23, the partial field-induced detwinning of the sample causes some hysteresis behavior. The particular hysteresis measured depends on the one hand on the actual path in the $H - T$ plane and, on the other hand, is also sample dependent because it is probably influenced by internal strains and/or defects.

Concerning the actual phase boundary, however, no hysteresis effects connected

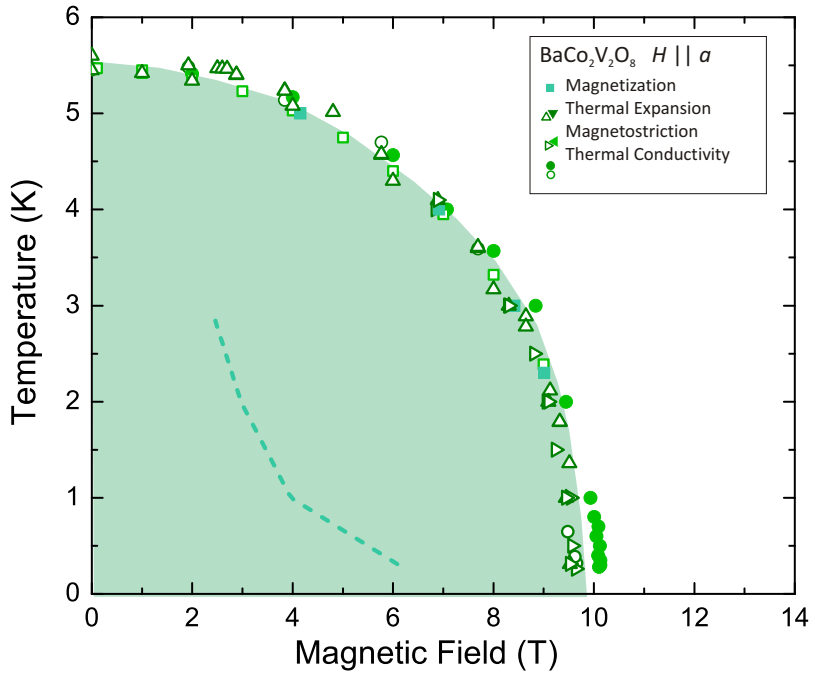

Figure 5.23: Magnetic phase diagram of $BaCo_2V_2O_8$ for magnetic fields parallel to the a_t axis. Data points were obtained by measurements of the magnetization (■), thermal expansion (⋆), magnetostriction (▽), and thermal conductivity (○). The dashed line marks the region of domain reorientation induced by the magnetic field.

to the phase transition are observed in any of the measurements which identifies the corresponding transition as a continuous second-order phase transition. Thus, the presented data may suggest that $BaCo_2V_2O_8$ has a quantum critical point at $H_{crit}^{||a} \simeq 10\,\mathrm{T}$. The thermal expansion coefficient $\alpha(T)$ also changes sign at 10 T which would be a typical signature of a quantum phase transition [123, 124]. For purely one-dimensional magnets, this sign change can even take place in form of a pole, i.e., $\alpha(T \to 0)$ diverges [125, 126], whereas for higher-dimensional systems, such a sign change via a divergence is only present for the Grüneisen ratio α/c, where c is the specific heat, and the magnetocaloric effect $\partial \ln T/\partial H$ [124, 127–130]. If at all, in the present case of $BaCo_2V_2O_8$ one would deal with a three-dimensional quantum phase transition from the Néel-ordered phase to a high-field phase whose microscopic nature remains to be clarified.

Figure 5.24 shows the magnetic phase diagrams of $BaCo_2V_2O_8$ for $H \perp c$ as formerly published in literature [96, 104]. Because the additional in-plane anisotropy was unknown, Zhao et al. interpreted the deviation of their $H \perp c$ -phase boundary from the previously known $H \perp c$ -phase boundary [103] as indication for the occurrence of a new phase around 10 T. This discrepancy is, however, caused by a mixing up of the different phase diagrams for $H \,||\, [1\,1\,0]$ and $H \,||\, a$ and is now fully resolved by considering the very different results for the different in-plane field directions presented above.

Modeling

Very recently, the in-plane anisoptropy has also been observed in high-field magnetization data, see Figure 5.24 (c), and the strong in-plane magnetic-field anisotropy of $BaCo_2V_2O_8$ has been explained by a structural peculiarity of the Co^{2+} screw chains. In this model the CoO_6 chains within $BaCo_2V_2O_8$ are treated from a crystallographic

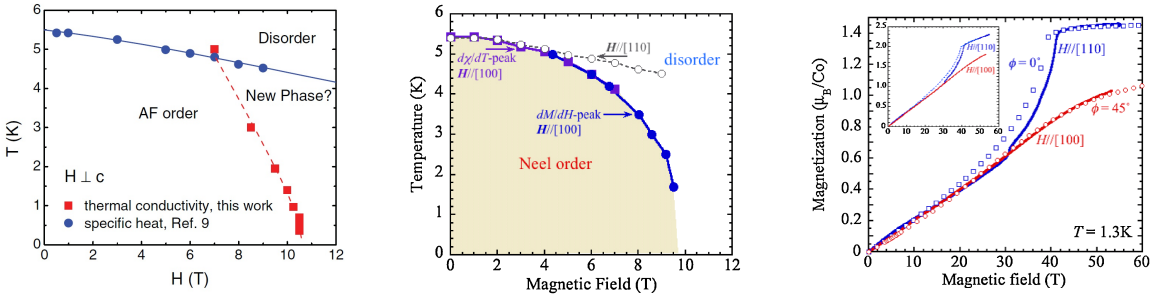

(a) taken from Ref. 104 **(b)** taken from Ref. 96 **(c)** taken from Ref. 96

Figure 5.24: (a) Magnetic phase diagram of $BaCo_2V_2O_8$ for fields perpendicular to c without distinction of the field directions [104]. (b) Magnetic phase diagram where the field directions are handled separately [96]. (c) In-plane high-field magnetization of $BaCo_2V_2O_8$ for $H \,||\, a$ (red) and $H \,||\, [110]$ (blue) are subtracted by Van-Vleck contributions (solid lines). The theoretical magnetization curves (open symbols) are calculated with the effective fields (see text) [96].

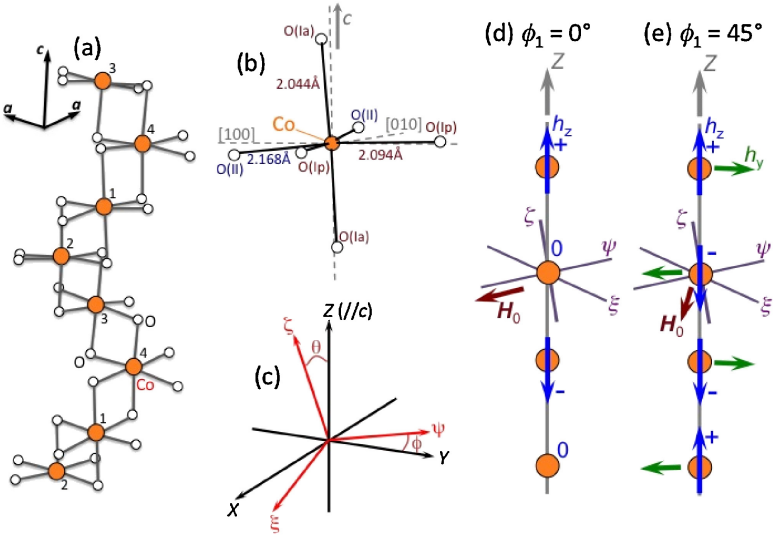

Figure 5.25: (a) Schematic view of the cobalt 4_1 screw chains. (b) A single CoO_6 octahedron in $BaCo_2V_2O_8$ with the different bond Co-O bond-lengths. (c) Relation between the global coordination system xyz and the local coordinates $\xi\psi\zeta$. The effective fields resulting from magnetic fields applied along [1 1 0] (d) and [1 0 0] (e) (taken from Ref. 96).

point of view, taking the alternating distortion of the CoO_6 octahedra into account. Figure 5.25 (a) shows the edge sharing octahedra which are rotated by 90° with respect to each other and form a fourfold screw axis along c. The upper apical oxygen shows a tilt away from the crystallographic c axis, see Figure 5.25 (b). A local coordinate system is defined, Figure 5.25 (c), where the angle Φ represents the rotation of the local coordinate system around the z axis. Resulting from the 90° rotation of the octahedra with respect to each other the magnetic principal axes change with a four-step periodicity. There are also two different planar Co-O bonds (*cf.* Fig. 5.2) which results in a rhombic anisotropy for the Co^{2+} ion.

The translation of the effective g tensor into the local coordinate system provides off-diagonal elements that lead to effective fields parallel to y and z when the external

General		Special	
hkl:	$h+k+l=2n$	hkl:	$l=2n+1 \vee 2h+l=4n$
$hk0$:	$h,k=2n$	hkl:	$l=2n+1 \vee h=2n$
$0kl$:	$k,l=2n$	hkl:	$h,k=2n,\ h+k+l=4n$
hhl:	$2h+l=4n$	hkl:	$2h+l=4n$
$00l$:	$l=4n$		
$h00$:	$h=2n$		
$h\bar{h}0$:	h=$2n$		

Table 5.2: Reflection conditions of space group $I4_1/acd$ [66] which can be attributed to the different symmetry elements of the space group discussed in Section 3.2.

magnetic field is applied along x. The effective Hamiltonian reads [96]

$$\mathcal{H} = J\sum_j \{S_{j,z}S_{j+1,z} + \epsilon(S_{j,x}S_{j+1,x} + S_{j,y}Sj+1,y)\} - \mu_{\mathrm{B}}\sum_i \left\{ g_{xx}H_0S_{j,x} + h_yS_{j,y}\sin(2\Phi_1+\pi(j-1)) + h_zS_{j,z}\cos\left(\Phi_1+\frac{\pi(j-1)}{2}\right)\right\}, \tag{5.2}$$

where h_y and h_z represent the absolute values of the effective fields which are comparatively high with $h_y = 0.4\cdot H_0$ and $h_z = 0.14\cdot H_0$. The resulting effective fields for applied magnetic fields $H \,||\, [1\,1\,0]$ and $H \,||\, a$, corresponding to the angles $\Phi_1 = 0°$ and $\Phi_1 = 45°$, respectively, are depicted in Figure 5.25 (d) and (e). Thus, according to this model, a homogeneous magnetic field $H \,||\, a$ is accompanied by a staggered transverse field component (h_y = "$+-+-$", h_z = "$+--+$"), whereas no such transverse component occurs for $H \,||\, [1\,1\,0]$ ($h_y = 0$, h_z = "$+0-0$"). As a consequence, the Néel order collapses already at rather small fields of $\simeq 7\,\mathrm{T}$ when the field is applied along the a direction.

Single Crystal Neutron Diffraction

Figure 5.26 shows the integrated intensities of several magnetic superstructure reflections of the zero-field Néel ordered phase ($\vec{k} = (1,0,0)$) at $T = 50\,\mathrm{mK}$ in an applied magnetic field $H \,||\, a$ up to 11 T. First of all, the data in panels (a)-(c) reveal a collapse of the superstructure reflections as a function of the magnetic field at $H^{||a} \simeq 10\,\mathrm{T}$ verifying the above discussed hypothesis. The suppression of the magnetic intensities is not homogeneous and a significant hysteresis is observed for measurements obtained with increasing (closed symbols) and decreasing (open symbols) magnetic field. As discussed in Section 5.2, two types of magnetic domains are present in the Néel ordered phase of $BaCo_2V_2O_8$. In fact, the reflections of panel (a) arise from one type of the magnetic domains while those of panel (b) represent the other type [24]. This different field dependence can be explained in terms of a field-induced domain reorientation in the field-decreasing run like it was suggested by the magnetostriction data presented above (cf. Fig. 5.21). The idea was stated that the magnetic field $H \,||\, a$ favors a certain structural domain that is intimately connected to the magnetic domains which

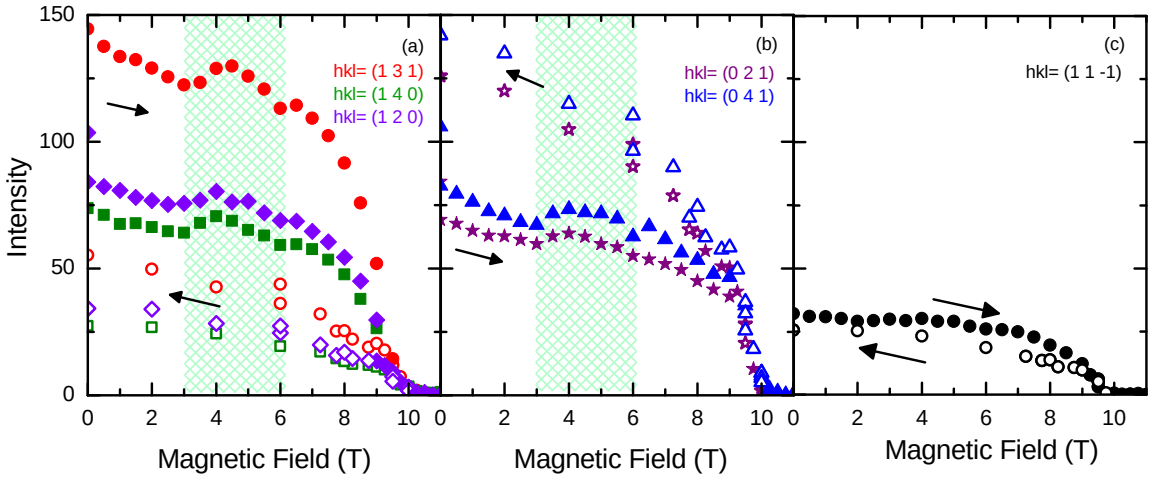

Figure 5.26: Intensities of several magnetic Bragg peaks of the Néel-ordered phase of $BaCo_2V_2O_8$ as a function of magnetic fields $H \,||\, a$ at $T \simeq 50\,\mathrm{mK}$. The intensities were either obtained with increasing (closed symbols) or decreasing (open symbols) magnetic field. Reflections in panels (a) and (b) belong to different magnetic domains, $(1\,1\,\bar{1})$ in panel (c) belongs to both domains. The size of the symbols is of the size of the error bars.

actually explains why the field-decreasing run results in a different intensity distribution as compared to the original zero-field data. Reentering the Néel phase coming from $H > H_c$ yields, thus, a stronger population of the domain that is favored by the magnetic field. These reorientation processes are actually also represented in the measurements for increasing field where the peak intensities of Figure 5.26 (a) rapidly decrease already at about 9 T whereas those of panel (b) only drop rapidly close to $H_c = 10\,\mathrm{T}$. Therefore, a microscopic confirmation of the macroscopically derived reorientation model is presented here. The $(1\,1\,\bar{1})$ reflection shown in panel (c) is equally sensitive to both domains. The distribution for both field sweep directions is only slightly different which might be caused by a slight field misalignment. Additionally, all representatives in panels (a) and (b) show an intermediate field anomaly in the field range between 3 to 7 T (green area) only for the curves measured with increasing magnetic field. Although, the absence of an anomaly in the curves measured with decreasing field would fit into the domain picture, the data have to be handled with caution because an anomaly could also simply be hidden due to the smaller database for the down measurements. However, since the anomaly is reflected in an increase of the intensity in the field-increased curves of both domains, this observation discards the reorientation of magnetic domains as the cause of the anomaly. So far the origin of this anomaly remains unresolved.

The suppression of the magnetic superstructure intensities shown above at $H_{crit}^{||a} \simeq 10\,\mathrm{T}$ could mean that another type of magnetic phase sets in above $H_{crit}^{||a}$, which is possibly accompanied by the occurrence of new reflections for fields above H_c. This was, however not confirmed by "fishing" within the Brillouin zone. A possible incommensurate phase would be accompanied by a splitting of the magnetic peaks above the critical field. Since no such splitting is observed but simply the disappearance of magnetic reflections, this option is discarded. Considering the above mentioned model

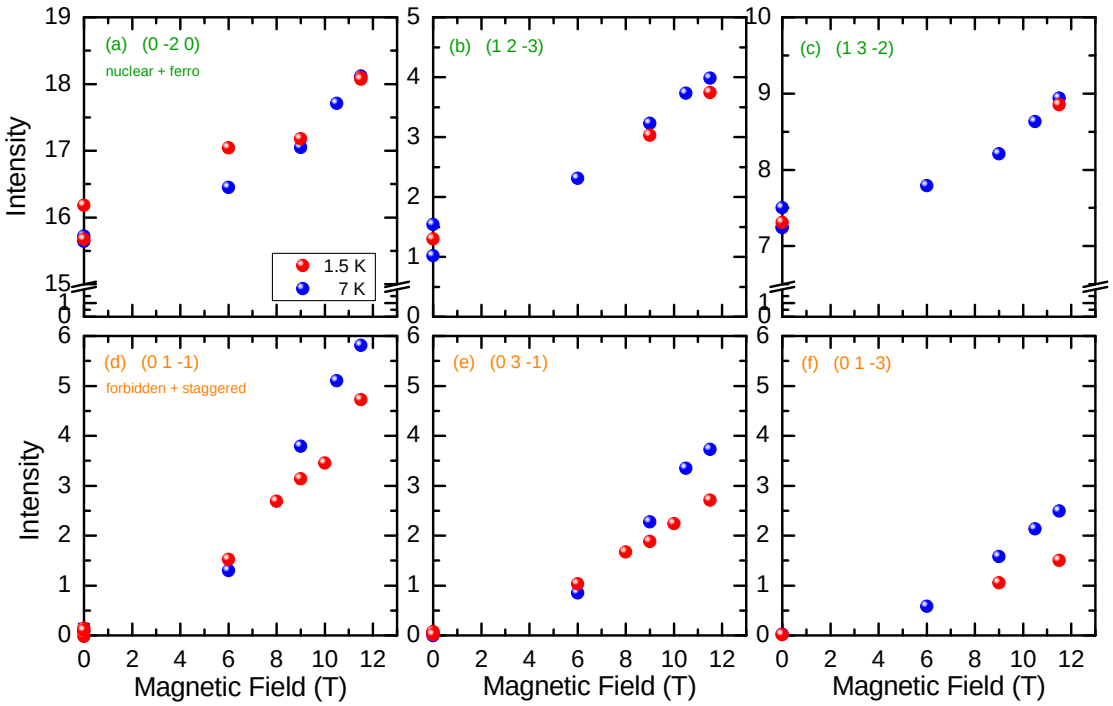

Figure 5.27: Field dependence of the integrated intensity of the nuclear reflections $(0\,1\,\bar{1})$ (a), $(0\,3\,\bar{1})$ (b) and the nuclear reflection $(1\,1\,\bar{2})$ (c) for temperatures above (red) and below (blue) T_N. Panels (d) and (e) show the reflection $(1\,1\,\bar{2})$ for different fields up to 11.5 T at $T = 1.5\,\mathrm{K}$ and 7 K, respectively. The size of the symbols is of the size of the error bars.

introduced by Kimura et al., the application of a magnetic field parallel a is accompanied by staggered effective field components perpendicular to the field direction, i.e. in b and c direction, due to the off-diagonal elements of the g tensor.

In panels (a)-(c) of Figure 5.27, the field dependence of the nuclear reflections $(0\,\bar{2}\,0)$, $(1\,2\,\bar{3})$ and $(1\,3\,\bar{2})$ are presented. The reflections were measured at two temperatures above T_N at $T \simeq 7\,\mathrm{K}$ (red) and below T_N at $T = 1.5\,\mathrm{K}$ (blue). At both temperatures the reflections show a similar increase of the intensity on increasing the magnetic field. This can naturally be explained by keeping in mind that an antiferromagnet in a transverse magnetic field tends to cant gradually into the field. A ferromagnetic component is induced by the magnetic field. However, this model can not explain the occurrence of forbidden reflections, like they are shown in panels (d)-(e) of Figure 5.27. Reflections $(0\,\bar{1}\,\bar{1})$, $(0\,3\,\bar{1})$ and $(0\,1\,\bar{3})$ are forbidden by the nuclear structure (see Table 5.2) and the antiferromagnetic zero-field structure with $\vec{k} = (1, 0, 0)$ (or $\vec{k} = (0, 1, 0)$), i.e. reflections hkl obtained by nuclear reflections and adding the propagation vector. It has to be mentioned that there is no reason for the forbidden reflections to have an intensity in zero-magnetic field. The occurring intensity was most probably caused by multiple scattering due to the irregular sample shape and large sample size. The intensities are, thus, corrected by the zero-field intensity. This is different for the nuclear reflections shown in panels (a)-(c) which, of course, yield an intensity also in zero-field. At both temperatures above and below T_N, the intensities of the forbidden reflections increase with increasing magnetic field and show basically the same field dependence

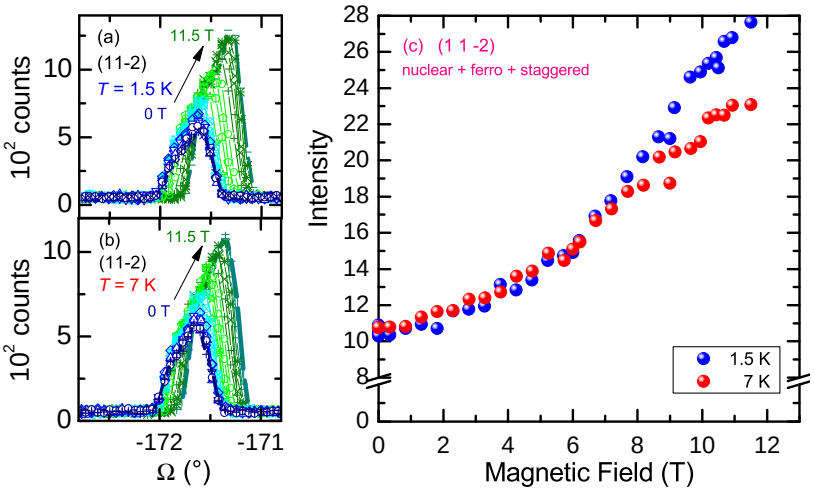

Figure 5.28: Ω scans of reflection $(1\,1\,\bar{2})$ in different magnetic fields up to 11.5 T for $T = 1.5$ K (a) and $T = 7$ K (b). (c) The integrated intensities of these scans for $T = 1.5$ K (blue) and $T = 7$ K (red). The size of the symbols is of the size of the error bars.

below $H_c \simeq 10$ T. However, for $H > 10$ T the intensity increases stronger for the measurements at $T = 1.5$ K. One can model the influence of a possible ferro-contribution by a FULLPROF simulation putting a uniform ferro-component M_x (for $H \,||\, a$) on each magnetic moment of the cobalt ions. Such a simulation indeed yields an additional intensity for the nuclear reflections shown in the upper panels of Figure 5.27. Coming back to the model of Kimura et al. one can also simulate the effect of a staggered component induced by the effective field h_y ($\propto H^{||\,a}$) with the sequence $''+-+-''$ on the M_y component of the Co ions, i.e. perpendicular to the field direction. This effective field yields, indeed, finite intensities for otherwise forbidden reflections, e.g., for those shown in the lower panels of Figure 5.27. In both cases it is no surprise that the reflections show a field dependence above T_N as they originate from the staggered moments that linearly depend on H. The derived models also yield nuclear reflections that are sensitive to both the uniform $M_x \propto H \,||\, a$ and the staggered $M_y \,||\, h_y \propto H \,||\, a$ moments. Figure 5.28 shows the measurements of such a nuclear reflection $(1\,1\,\bar{2})$ as a function of the magnetic field. Panels (a) and (b) show the originally obtained Ω scans at $T = 1.5$ K and $T = 7$ K, respectively. The reflections gain intensity with increasing field, the obtained integrated intensities are plotted in panel (c). Again, for both temperatures the field dependence is basically the same below about 9 T. However, on further increasing the field, the curves separate which was not the case for the "nuclear+ferro" reflections but for the "forbidden+staggered" reflections. Therefore, the qualitative microscopic proof of the staggered field theory is given by the results presented here. The next step should be a determination of the specific magnetic moment that has to be put into the model to obtain the observed intensities. The present database does not allow a determination of the magnetic structure. The complete list of nuclear and forbidden reflections and their intensities at different magnetic fields $H \,||\, a$ (and different temperatures) are summarized in Table B.2 in the Appendix B.

5.4.3 Conclusion

In this section an in-plane anisotropy for magnetic fields applied along the a axis and along the in-plane diagonal [1 1 0] is presented. Thermal expansion, and specific heat measurements presented above as well as thermal conductivity [23, 53] and magnetization data [96] reveal a fundamentally different field dependence for both field directions. In former literature, this anisotropy was unknown or spuriously interpreted as a new phase [104]. On the one hand, the phase boundary for $H \,||\, [1\,1\,0]$ is rather flat and the field behavior of the magnetization can be well described by the model of an Ising chain in a transverse magnetic field [96]. On the other hand one finds a strong field dependence in all anomalies that are related to the onset of long range magnetic order for fields applied along a. Moreover, a complete breakdown of the magnetic order is observed for fields above about 10 T as was confirmed in different thermodynamic measures as well as in single crystal neutron diffraction experiments. This suppression of the antiferromagnetic order can be explained by effective staggered fields occurring due the special arrangement and distortion of the CoO_6 octahedra [96]. A possible incommensurate phase above H_c, like it is present in $BaCo_2V_2O_8$ above 4 T for $H \,||\, c$ [24, 106], is not observed in this field direction.

The two magnetic domains present in the Néel ordered phase of $BaCo_2V_2O_8$ are represented by sets of magnetic Bragg peaks that show a different field-dependence for increasing and decreasing magnetic field (cf. Fig. 5.26). The different intensities for the different field sweep directions can be explained by the stronger population of the domain that is favored by the magnetic field. This microscopically confirms the respective domain-switching mechanisms that were already discussed for the magnetostriction results. The application of the magnetic field parallel to the a axis yields an increasing intensity of some nuclear reflections and the presence of reflections that are either forbidden by the nuclear structure or the magnetic structure with $\vec{k} = (1, 0, 0)$ (or $\vec{k} = (0, 1, 0)$). These reflections show an increasing intensity with increasing magnetic field and are present at temperatures above and below the zero-field T_N and for all magnetic fields up to $\simeq 11.5$ T. These reflections occur, on the one hand, due to a gradual adjustment of the magnetic moment along the field direction in case of the nuclear reflections and, on the other hand, due to the staggered moments in case of the forbidden reflections. Reflections that are sensitive to the staggered moment show a different increase of the intensity for fields above about 9 T. The origin of this difference remains unclear so far. For $H \,||\, a$, the low-temperature specific heat reveals an anomaly emerging in magnetic fields above 6 T. Hysteretic behavior is observed in the field-dependent heat capacity in this low-temperature region. Other measures like the thermal conductivity (*cf.* Ref. 53) and the field dependent intensity of magnetic Bragg peaks in the neutron diffraction experiments also reveal an anomaly in the field range 3 T to 7 T. So far the origin of these anomalies remains unknown.

6 Substitution

In the first part of this chapter, the influence of a partial or complete substitution of Ba by Sr on the magnetic behavior will be investigated. Four different substitution levels, including pure $SrCo_2V_2O_8$, have been synthesized and characterized. The second part of this chapter describes the substitution into the magnetic subsystem of $BaCo_2V_2O_8$. Single crystals of $BaCo_{1.9}M_{0.1}V_2O_8$ with four different in-chain substitutions M= Mn, Cu, Ni, or Mg were investigated.

6.1 $Ba_{1-x}Sr_xCo_2V_2O_8$

6.1.1 Introduction

Replacing some percentage of the barium ions within $BaCo_2V_2O_8$ by the much smaller strontium was chosen in analogy to cation substitution in the $S = 1$ Haldane chain $SrNi_2V_2O_8$ [131]. There, the substitution of Sr by a smaller ion, in that case calcium, yields an antiferromagnetic order whereas a spin-liquid state was reported to be stabilized by substitution with the larger barium ion. Small changes in the lattice constant a were discussed to change the effective inter-chain interactions. Substituting Ba by Sr in the spin-chain system $BaCo_2V_2O_8$ at first glance is a manipulation of the inter-chain distance since the alkaline-earth ion separates the spin chains. In this sense, this substitution enters the nonmagnetic subsystem. Due to a change of the resulting inter-chain coupling, at the same time, also the magnetic system is influenced. This way, similar effects as in $SrNi_2V_2O_8$ might lead to a change in the magnetic properties as well. Ba already is the largest of the alkaline earths, thus, only the substitution of a smaller ion is possible. As discussed in the previous chapter, the direction of the local easy axis is related to structural distortions. A substitution of Sr is supposed to change the degree of distortion and, in consequence, also the degree of anisotropies. To date, no other investigations of $BaCo_2V_2O_8$ with respect to the influence of any kind of substitution within the system are available besides my paper [132] which covers the main aspects of this chapter.

The end member of the substitution series $Ba_{1-x}Sr_xCo_2V_2O_8$ is $SrCo_2V_2O_8$ which is known from literature since 1994 but only few studies of that compound are available [25, 86–89]. The structure of $SrCo_2V_2O_8$ is reported to lack centrosymmetry but except that it is isostructural to $BaCo_2V_2O_8$. $SrCo_2V_2O_8$ enters a long-range ordered magnetic phase at an ordering temperature of $T_N \simeq 5\,K$ [25, 86, 88, 89]. He et al. report a second transition around 3 K and describe $SrCo_2V_2O_8$ as a quasi-one-

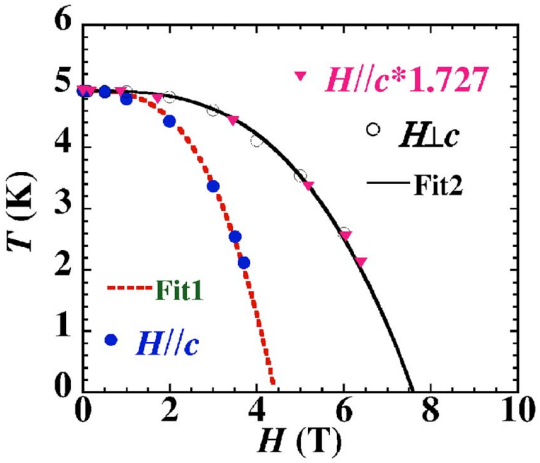

Figure 6.1: Magnetic phase diagram of $SrCo_2V_2O_8$ taken from Ref. 25 for magnetic fields parallel to c (blue circles) and perpendicular to c (black open circles). The data for $H \,||\, c$ were scaled on the other field direction represented by the pink triangles. The lines represents fits based on a power law (see text).

dimensional spin-chain, which shows weak ferromagnetism at low temperature due to spin canting introduced by Dzyaloshinskii-Moriya interactions. Moreover, the temperature *vs.* magnetic field phase diagram for field directions parallel and perpendicular to the c axis is claimed to be quite different from that of $BaCo_2V_2O_8$ [88]. The phase diagrams of $SrCo_2V_2O_8$, shown in Fig. 6.1, were obtained from the magnetization and the specific heat measured down to 2 K. The phase boundaries for $H \,||\, c$ and $H \perp c$ are reported to scale by a factor of 1.727 (see Fig. 6.1) and the critical magnetic fields $H_{\mathrm{crit}}^{\|c}(T \to 0) = 4.4\,\mathrm{T}$ and $H_{\mathrm{crit}}^{\perp a}(T \to 0) = 7.6\,\mathrm{T}$ are derived using the equation $H = H_{\mathrm{c}}(1 - T/T_{\mathrm{N}})^{\beta}$ which is stated to be based on a mean-field power law. $SrCo_2V_2O_8$ and $BaCo_2V_2O_8$ are argued to show completely different magnetic behavior. It is worth mentioning, that the field direction perpendicular to the c axis is not named explicitly in the references. However, in the course of this thesis it turned out that the particular orientation of the magnetic field $H \perp c$ plays an important role and the in-plane anisotropy reported recently for $BaCo_2V_2O_8$ [23, 96] was not discussed for $SrCo_2V_2O_8$ so far. These findings and in particular the proposed non-collinear spin structure [25, 88, 89], however, are challenged by more recent magnetization measurements which reveal only one critical temperature and show that $SrCo_2V_2O_8$ is much more similar to $BaCo_2V_2O_8$ [86]. This paper from 2011 is also the first paper that reports the single crystal growth of $SrCo_2V_2O_8$ and $BaCo_2V_2O_8$ by the floating-zone technique.

The discussion about the alikeness or difference of the two end members of the substitution series $Ba_{1-x}Sr_xCo_2V_2O_8$ with respect to their phase diagrams and magnetic structures is extended in this chapter. Single crystals of four levels of Sr substitution, $x = 0.1$ (SN0087), $x = 0.5$ (SN0091), $x = 0.9$ (SN0111), and $x = 1$ (SN0135), have been synthesized (see Sec. 3.3.2) and investigated by means of magnetization, specific heat, thermal conductivity [53], thermal expansion, and magnetostriction. Selected data are shown in this section, all other data that were also used to derive the magnetic phase diagrams can be found in Appendix B.

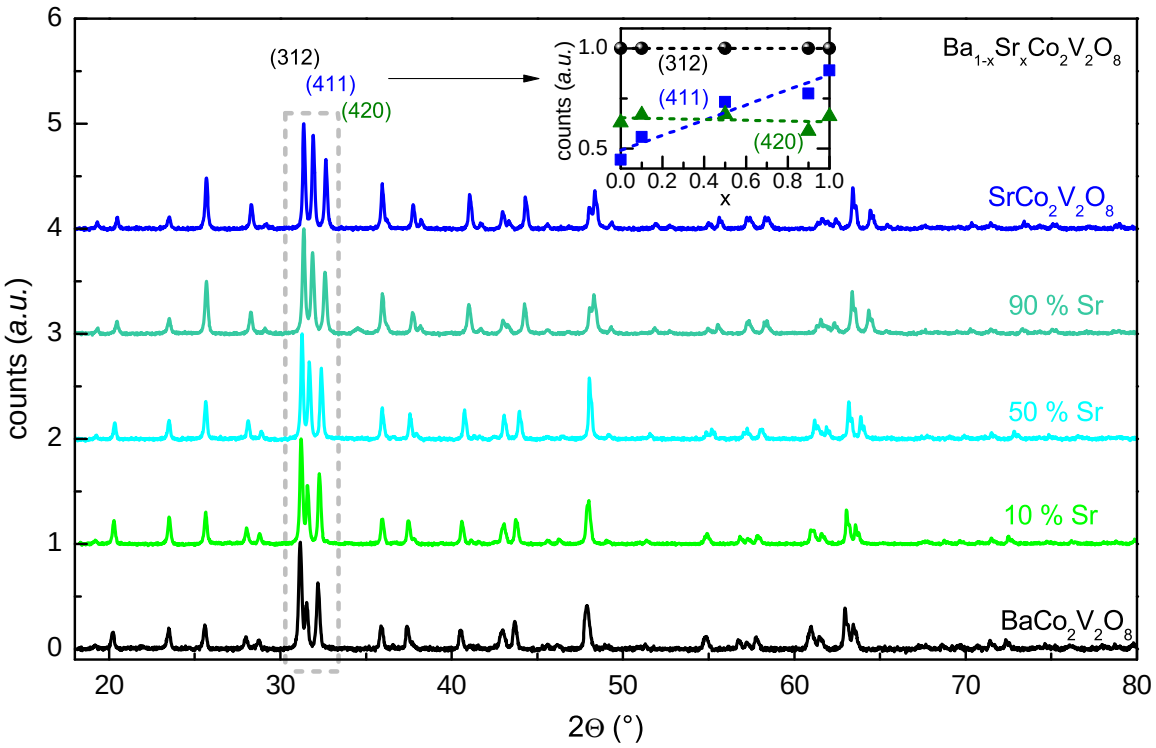

Figure 6.2: X-ray powder diffraction pattern of $Ba_{1-x}Sr_xCo_2V_2O_8$ from pure $BaCo_2V_2O_8$ (bottom) to pure $SrCo_2V_2O_8$ (top). The three largest intensities (gray box) belong to (hkl) = (3 1 2), (4 1 1) and (4 2 0). The inset shows the peak height of these three intensities in dependence of the Sr content, dashed lines are linear fits.

6.1.2 Structure

Phase purity of the compounds was checked by X-ray powder diffraction, as reported in Section 3.3.2. Figure 6.2 shows the powder patterns of $BaCo_2V_2O_8$ and the $Ba_{1-x}Sr_xCo_2V_2O_8$ samples with increasing Sr content from bottom to top. The structures of the two end members are known to belong to the centrosymmetric space group $I4_1/acd$ for $BaCo_2V_2O_8$ and the non-centrosymmetric $I4_1cd$ for $SrCo_2V_2O_8$. From the powder pattern both structures cannot be distinguished unambiguously because they mainly differ in their relative intensities. For the $Ba_{1-x}Sr_xCo_2V_2O_8$ samples with $x = 0.1, 0.5, 0.9$ this means that only based on X-ray powder diffraction one may not easily judge which space group they belong to. The three largest peaks, marked by a dashed box, belong to (hkl) = (3 1 2), (4 1 1) and (4 2 0). In $BaCo_2V_2O_8$, the central (4 1 1) peak is the weakest of the three but in $SrCo_2V_2O_8$, it is the (4 2 0) reflection to the right. For all samples, the intensities are normalized to the maximum of the (3 1 2) reflection. The inset of Fig. 6.2 shows the intensity of these three reflections as a function of the Sr content. While reflection (4 2 0) remains nearly constant,the (4 1 1) reflection shows a linear increase with increasing Sr content x. This change could either be explained by the alteration of the space group or the different form factors of Ba and Sr. FULLPROF simulations of the X-ray pattern for both compounds $BaCo_2V_2O_8$ and $SrCo_2V_2O_8$ each in the space groups No. 110 and No. 142 are shown in Figure 6.3. The calculation shows that the proportions of the

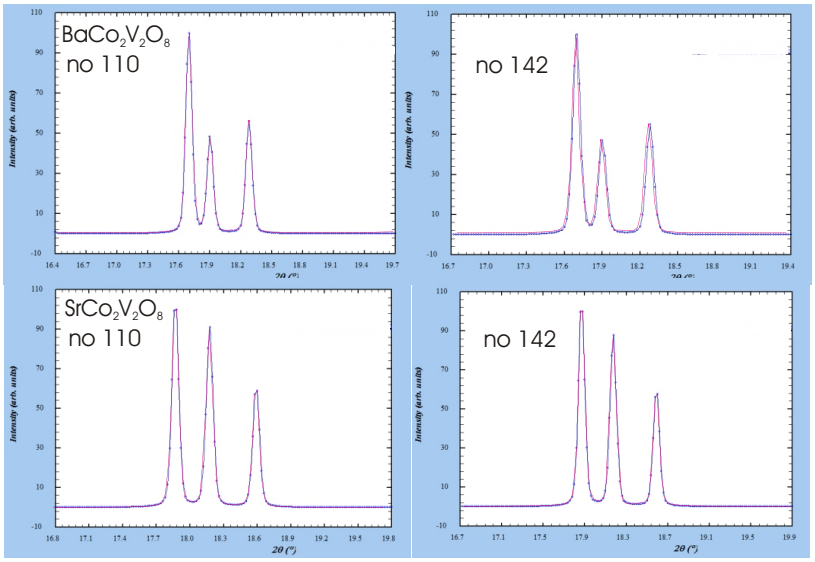

Figure 6.3: FULLPROF simulation for the X-ray pattern of $BaCo_2V_2O_8$ and $SrCo_2V_2O_8$ calculated each for the space groups No. 110 and 142 at the position of the three reflections (hkl) = (3 1 2), (4 1 1) and (4 2 0).

peak within each compound is irrespective of the space group indicating that the intensity of that peak is mainly sensitive to the form factor of the respective ion. But since the end members actually belong to different space groups a transition from a centro- to non-centrosymmetric structure is expected but cannot be located to a certain Sr content. By the by, in $SrNi_2V_2O_8$, which belongs to the non-centroymmetric space group No. 110, a structural change was observed when 50 % of the Sr are replaced by Ba. The mixed compound $Ba_{0.5}Sr_{0.5}Ni_2V_2O_8$ is centrosymmetric and was refined using space group No. 142 [17][1].

The loss of centrosymmetry when changing from $I4_1/acd$ to $I4_1cd$ (see Sec. 3.2) is reflected in a much stronger distortion of the building blocks of $SrCo_2V_2O_8$ as shown in Figures 6.4 and 6.5. The pictures were derived using the crystallographic data provided by the ICSD for the two end members [15, 41, 87]. The cubeoctahedron formed by the oxygen coordination of the Sr (left, Fig. 6.4) shows two elongated bond lengths (dashed lines) that lower the coordination almost to ten. Compared to the BaO_{12} polyhedron (right) the Sr holds an off-center position.

Concerning the magnetic properties of the cobalt, the distortion of the CoO_6 octahedra within $SrCo_2V_2O_8$ as depicted in Figure 6.5 is even more important. The $SrCo_2V_2O_8$ octahedron is quite distorted and reveals no equal Co-O bond lengths (solid lines). Also the O-O bond lengths (dashed lines) are all different and therefore, depicted in gray. This presentation of the CoO_6 octahedron has to be considered with some caution. The crystallographic data of $SrCo_2V_2O_8$ were taken from ICSD No. 400765 and the structure contains 4 different oxygen positions. In this reference identical z positions of the oxygens O2 and O3 are given, which result in case of the O2 in an unphysically short Co-O2 bond length of ≈ 0.2 Å. This z position of the lower apical oxygen O2 (see Fig. 6.5) must be erroneous and was, thus, changed such that the apical distances Co-O2 and Co-O3 along c have the same lengths. But the discussion of possibly different tilt angles of the local quantization axes of the CoO_6

[1] Note that the pure $BaNi_2V_2O_8$ is a 2D honeycomb antiferromagnet having a rhombohedral structure [83].

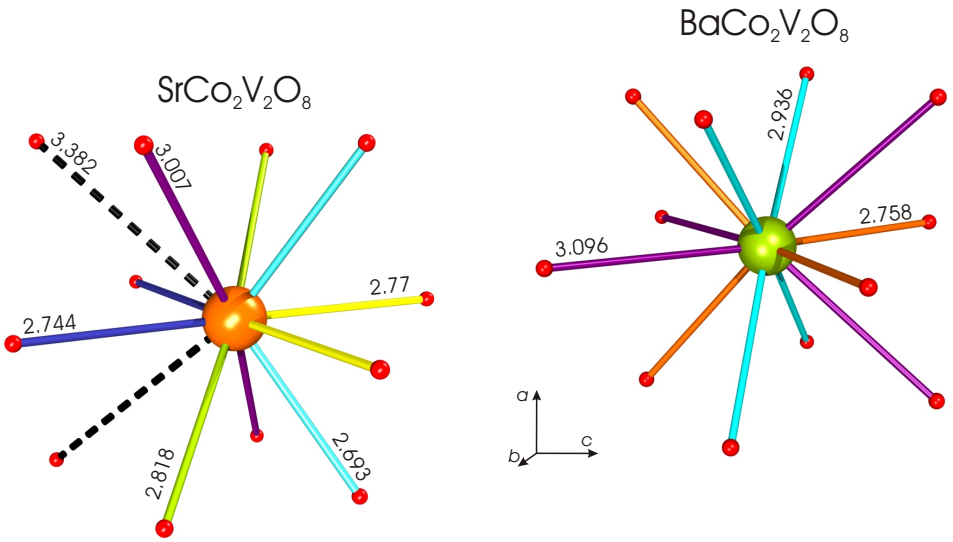

Figure 6.4: Comparison of the oxygen coordination of Sr in $SrCo_2V_2O_8$ (left) and Ba in $BaCo_2V_2O_8$ (right). The bond lengths are given in Å and equal colors (within each cubeoctahedron) represent equal lengths.

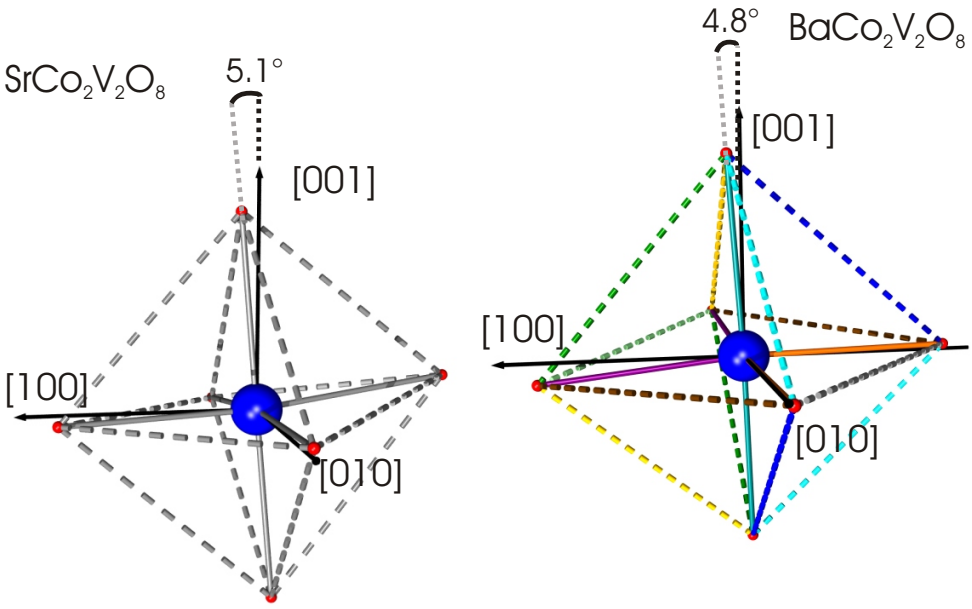

Figure 6.5: Comparison of the oxygen coordination of the cobalt sites in $SrCo_2V_2O_8$ (left) and $BaCo_2V_2O_8$ (right). Equal colors are equal lengths in the Ba case. In the Sr case all bond lengths are different and are, thus, depicted in grey.

octahedra (cf. Section 5.4) refers only to the upper apical oxygen O3 and is, therefore, unaffected by this assumption. In $SrCo_2V_2O_8$ this tilt angle is about 0.3° larger than in $BaCo_2V_2O_8$ which might be important for the magnetism as will be discussed later (see Sec. 6.1.5).

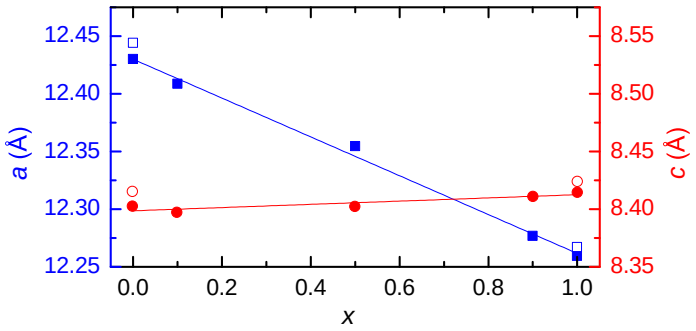

Figure 6.6: Lattice constants a (blue) and c (red) of the $Ba_{1-x}Sr_xCo_2V_2O_8$ series in dependence of the nominal Sr content x. Open symbols are taken from Refs. 15, 87. Solid lines are linear fits of a and c as a function of x.

Table 6.1: Nominal concentration x_{nom} of Sr compared to the values x_{EDX} from EDX measurements and the calculated concentration x_{mix} via the lattice constants.

sample	SN0075	SN0087	SN0091	SN0111	SN0135
x_{nom}	0	0.1	0.5	0.9	1
x_{EDX}		0.09	0.5	0.9	
x_{mix}	0	0.13	0.44	0.90	1

The Sr contents of the $Ba_{1-x}Sr_xCo_2V_2O_8$ samples are the nominal values, i.e. the aimed substitution levels in the growth process. In order to verify the real Sr content EDX measurements were performed [38] and yield resilient results for the Sr content x_{EDX}, see Tab. 6.1. Another possibility for verifying the Sr content is given by the analysis of the refined lattice constants. Figure 6.6 shows the refined lattice constants a (blue) and c (red) as a function of the nominal Sr content x. Open symbols are reference data for $BaCo_2V_2O_8$ and $SrCo_2V_2O_8$ taken from Refs. 15, 87 which lie systematically slightly above the data obtained on the current samples. With increasing Sr content the lattice constant a, which is a measure of the mean inter-chain distance, significantly decreases almost linearly, while c shows a weak increase. The linear decrease of a can be explained using Vegard's law [133, 134] which is known as an (empirical) law that gives a linear relation between the lattice constant of an alloy a_{mix} and the concentration x_{mix} of the substituted element at a given temperature, i.e. $a_{\mathrm{mix}} = \mathrm{mix} \cdot a_A + (1 - \mathrm{mix}) \cdot a_B \Leftrightarrow x_{\mathrm{mix}} = \frac{a_{\mathrm{mix}} - a_B}{a_A - a_B}$, where a_A and a_B are the lattice constants of the pure compounds A and B given that those compounds have the same crystal symmetry. Since $BaCo_2V_2O_8$ and $SrCo_2V_2O_8$ have basically the same structure type, this relation was used with the lattice parameters of sample SN0135 for $A = SrCo_2V_2O_8$, SN0075 for $B = BaCo_2V_2O_8$ and a_{mix} the lattice constants of the substituted samples. The Sr concentration of the first two alloys show deviations of 30 % for $Ba_{0.9}Sr_{0.1}Co_2V_2O_8$ and 12 % for $Ba_{0.5}Sr_{0.5}Co_2V_2O_8$ (see Table 6.1), as suggested by their deviations from the ideal linear curve in Figure 6.6. Considering the good concordance of the EDX results with the nominal value, the nomenclature of the $Ba_{1-x}Sr_xCo_2V_2O_8$ compounds sticks to the nominal value.

Orthorhombic Distortion

As discussed in the previous chapter, in $BaCo_2V_2O_8$ the magnetic structure is coupled to the lattice structure. Zero-field thermal expansion measurements under uniaxial pressure reveal an orthorhombic distortion when entering the Néel phase. The struc-

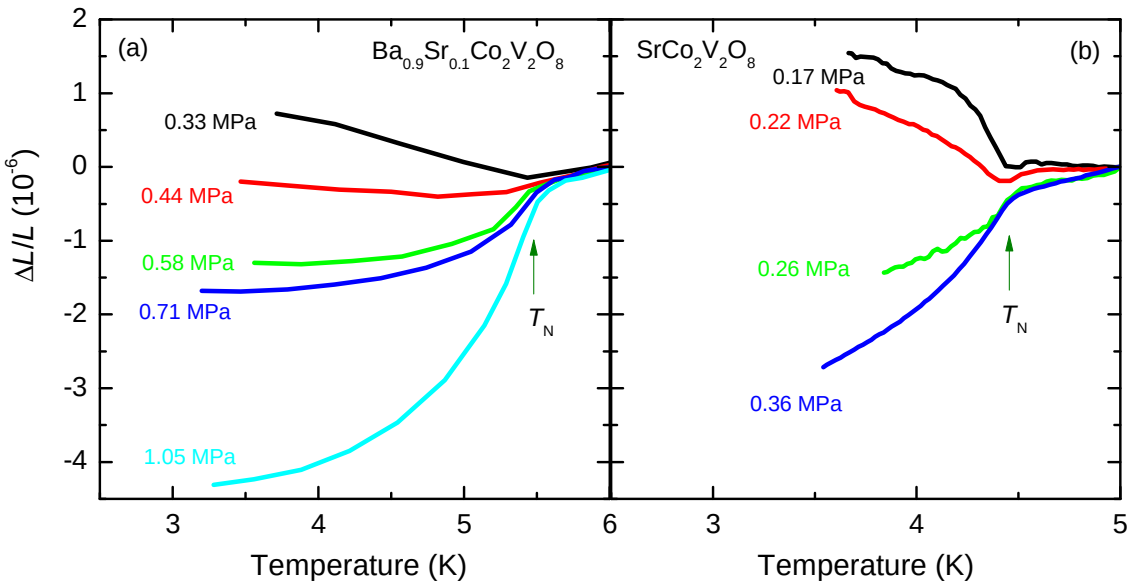

Figure 6.7: Zero-field thermal expansion of (a) $Ba_{0.9}Sr_{0.1}Co_2V_2O_8$ and (b) $SrCo_2V_2O_8$ measured for different uniaxial pressures applied along one of the tetragonal a axes, $p_i||a$.

tural domains following the magnetic domains can be switched by increasing uniaxial pressure, where one of the domain alignments is preferred, see Sec.5.2, [23]. A substitution in the system that is likely to influence the mean inter-chain distance could change or even suppress this domain forming. In order to clarify whether similar domains are present in the Sr-substituted samples, analogous measurements of the zero-field thermal expansion, i.e. the relative length change $\Delta L(T)/L_0$ as described in Sec. 5.2, were performed on the samples $Ba_{0.9}Sr_{0.1}Co_2V_2O_8$ and $SrCo_2V_2O_8$. The uniaxial pressure $p_i||a$ was applied at temperatures $T > T_N$ along one of the tetragonal a axes. Figure 6.7 shows the length changes $\Delta L = L(T) - L_0$ of $Ba_{0.9}Sr_{0.1}Co_2V_2O_8$ (a) and $SrCo_2V_2O_8$ (b) which are related to the length change L_0 at about 0.5 K above the transition temperature, i.e. 6 and 5 K for $Ba_{0.9}Sr_{0.1}Co_2V_2O_8$ and $SrCo_2V_2O_8$, respectively. Below T_N, both samples evolve a spontaneous strain whose magnitude and sign can systematically be changed by increasing the uniaxial pressure. Both samples show the very same characteristic behavior as $BaCo_2V_2O_8$. Consequently, the orthorhombic splitting and formation of structural domains is observed over the full range of Sr substitution. From the close resemblance of the presented measurements to $BaCo_2V_2O_8$ a similar zero-field magnetic structure to that in $BaCo_2V_2O_8$ is very likely. Thus, a magnetic non-collinear structure for $SrCo_2V_2O_8$ as proposed in Ref. 18 is not supported by the thermodynamic data presented here. This kind of spin structure was also questioned in Ref. 86. And indeed, a very recent neutron diffraction investigation by Bera et al. verifies the magnetic structure of $SrCo_2V_2O_8$ to be equal to that of $BaCo_2V_2O_8$ [100]. The refined magnetic moment at 1.5 K is determined to $\approx 2.25\mu_B/Co^{2+}$ ($BaCo_2V_2O_8$: $2.267(3)\mu_B/Co^{2+}$ [24]) which is smaller than the expected $3\mu_B/Co^{2+}$. Strong quantum fluctuations are suspected to cause this reduction.

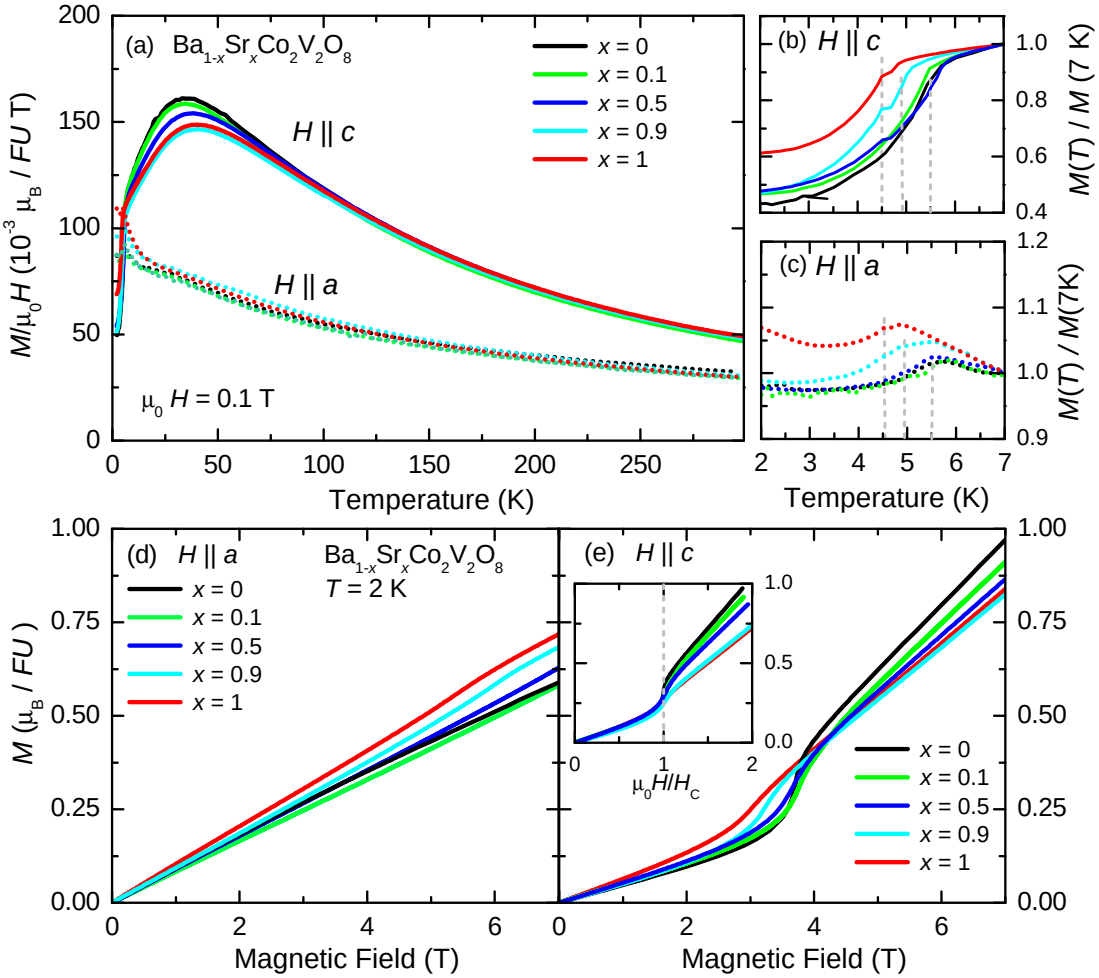

Figure 6.8: (a) Temperature dependent magnetization $M(T)/\mu_0 H$ at a magnetic field of 0.1 T applied along the c axis (solid lines) and along the a axis (dashed lines) for the $Ba_{1-x}Sr_xCo_2V_2O_8$ compounds with $0 \leqslant x \leqslant 1$. Panels (b) and (c) show $M(T)/M(7\,\mathrm{K})$ for $H \,||\, c$ and $H \,||\, a$. Panels (d) and (e) show the field dependent magnetization at $T = 2\,\mathrm{K}$ applied along the a axis and the c axis.

6.1.3 Ising Anisotropy

In order to probe the magnetic Ising anisotropy of the substituted systems, field- and temperature-dependent magnetization measurements were performed for field directions along the c and the a axis. The magnetization was measured in a SQUID magnetometer in magnetic fields up to 7 T at temperatures from 2 K to 300 K.

The temperature dependent magnetization at an applied magnetic field of 100 mT for the $Ba_{1-x}Sr_xCo_2V_2O_8$ compounds with Sr contents $0 \leqslant x \leqslant 1$ is shown in Figure 6.8 for the magnetic field applied along the c axis (solid lines) and the a axis (dashed lines). The strong Ising anisotropy of $BaCo_2V_2O_8$ in the paramagnetic high-temperature phase, i.e. $\chi^{H||c}/\chi^{H\perp c} \approx 1.5 - 2$ for $T > 50\,\mathrm{K}$, remains essentially preserved for all substitution levels up to the pure $SrCo_2V_2O_8$ and the overall shapes are close to that of the pure compound. In $BaCo_2V_2O_8$ the susceptibility shows a maximum around 35 K which signals the short-range correlations and is a fingerprint

of the one-dimensional nature of the magnetic subsystem. This low dimensionality is conserved in the substituted compounds and the maximum is shifted to higher temperatures with increasing substitution level while the absolute value of the maximum susceptibility is decreased at the same time. Thus, the antiferromagnetic exchange J is slightly increased with increasing substitution ($T/J = const.; \chi \cdot J = const.$).

Panels (b) and (c) show an enlargement of the curves for $H \,||\, c$ and $H \,||\, a$ in the low-temperature region next to the transition where a clear anomaly signals the onset of long-range order. The data were normalized to $M(7\,\mathrm{K})$ to visualize the shift of the transition temperature, which is marked by vertical dashed lines. With increasing substitution level T_N decreases from $\approx 5.4\,\mathrm{K}$ in $BaCo_2V_2O_8$ to $\approx 4.5\,\mathrm{K}$ in $SrCo_2V_2O_8$ (see also Table 6.2). Up to 50 % Sr, however, the transition temperature remains nearly unaffected, only the curvature changes. The values of the transition temperatures were obtained using the maximum of the respective derivatives in magnetization, thermal expansion/magnetotriction, and, if at hand, other quantities like the heat capacity or the thermal conductivity. The transition temperatures and other critical values are summarized in Table 6.2.

Panels (d) and (e) of Figure 6.8 show the field dependent magnetization measurements for all substitution levels in magnetic fields applied parallel to a and parallel to the c axis, respectively. For magnetic fields applied along the a axis, the lower substitution levels show a simple linear behavior like $BaCo_2V_2O_8$ which indicates that at $T = 2\,\mathrm{K}$ the transition from the Néel order to short range order is lying at higher magnetic fields ($H_c \approx 10\,\mathrm{T}$ in $BaCo_2V_2O_8$). $Ba_{0.1}Sr_{0.9}Co_2V_2O_8$ and $SrCo_2V_2O_8$, however, reveal a small kink around 5 and 6 T, respectively, (cf. Figs. B.6 and B.7 in the Appendix) indicating that the critical field is shifted to lower values with increasing Sr content. In the second field direction, $H \,||\, c$, the critical fields are much lower and are shifted to slightly lower values for $x = 0.9$ and 1. It is worth noticing, that the absolute value of the magnetization at 7 T is decreased from 0.97 to 0.84 μ_B/FU while at the same time the maximum value for $H \,||\, a$ is increased with increasing Sr content by exactly the same value from 0.59 to 0.72 μ_B/FU which is reasonable since the magnetic moment of the Co is preserved. Together with the decrease of the maximum susceptibility with increasing substitution level, which itself also depends on J, this "magnetization transfer" could be interpreted as an indication for a slight decrease of the magnetic anisotropy.

6.1.4 *H* parallel *c*

Figure 6.9 displays the thermal expansion and magnetostriction $\Delta L(T,H)/L$ measured along the c axis of the samples $Ba_{0.9}Sr_{0.1}Co_2V_2O_8$ and $SrCo_2V_2O_8$ for magnetic fields applied along c. In zero magnetic field, represented by the black curves in panels (a) and (c), the onset of the antiferromagnetic ordering is accompanied by a spontaneous contraction in the thermal expansion. The magnitude of the contraction does not change with the Sr content. The field dependence of the thermal expansion is only slightly different from that of $BaCo_2V_2O_8$ and the anomaly associated with the transition is observed in magnetic fields below 4 T. In $BaCo_2V_2O_8$, an incommensurate order is present for magnetic fields above 4 T and below temperatures of 1 K [24]. This temperature dependent paramagnetic-incommensurate transition is very broad

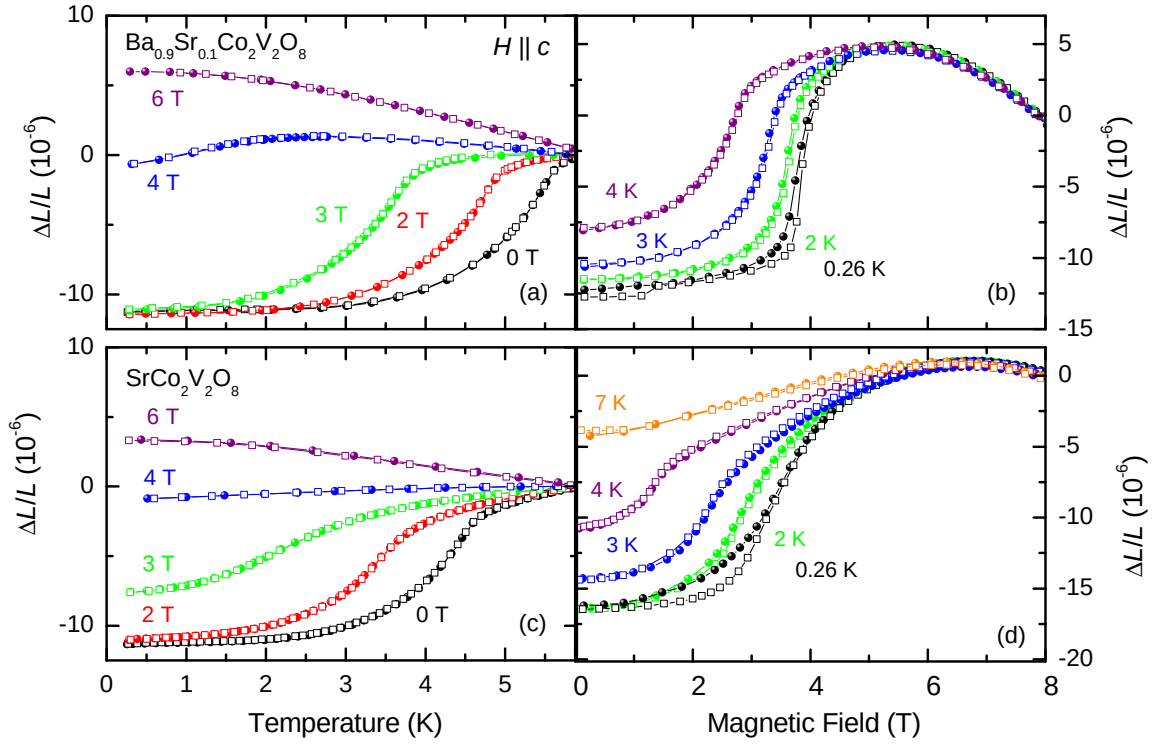

Figure 6.9: Thermal expansion (left) and magnetostriction (right) $\Delta L(T,H)/L$ measured along the c axis of $Ba_{0.9}Sr_{0.1}Co_2V_2O_8$ and $SrCo_2V_2O_8$ for $H \,||\, c$. Open and closed symbols represent measurements with increasing and decreasing temperature or magnetic field.

and causes only tiny anomalies in the thermal expansion data, cf. Chapter 5.

In case of $Ba_{1-x}Sr_xCo_2V_2O_8$ and $SrCo_2V_2O_8$ no such anomalies could be resolved, but this does not exclude the presence of an incommensurate order in the high-field low-temperature regime. An indirect hint for the occurrence of an incommensurate phase is given by the magnetostriction measurements of $Ba_{0.9}Sr_{0.1}Co_2V_2O_8$ and $SrCo_2V_2O_8$, Figure 6.9. From the zero-field T_N down to a temperature of 2 K, the magnetostriction signals continuous transitions without hysteresis effects between measurements obtained with increasing and decreasing magnetic field. Below about 1 K, however, magnetic field hysteresis is present indicating first-order phase transitions. This change from continuous to discontinuous, i.e. 2^{nd}- to 1^{st} order phase transitions, is also found in $BaCo_2V_2O_8$ where the transition between antiferromagnetic ordered and paramagnetic phase is of 2^{nd} order while the transition from the antiferromagnetic to incommensurate order is of 1^{st} order.

6.1.5 In-plane Anisotropy

With respect to the in-plane anisotropy known from $BaCo_2V_2O_8$ the substitution levels $x = 0.1$ and 1, i.e. $Ba_{0.9}Sr_{0.1}Co_2V_2O_8$ and $SrCo_2V_2O_8$, were investigated by means of the thermal expansion and the specific heat applying magnetic fields parallel to the tetragonal a axis and along the in-plane diagonal [1 1 0].

Figure 6.10 shows the thermal expansion and magnetostriction data $\Delta L(T,H)/L$

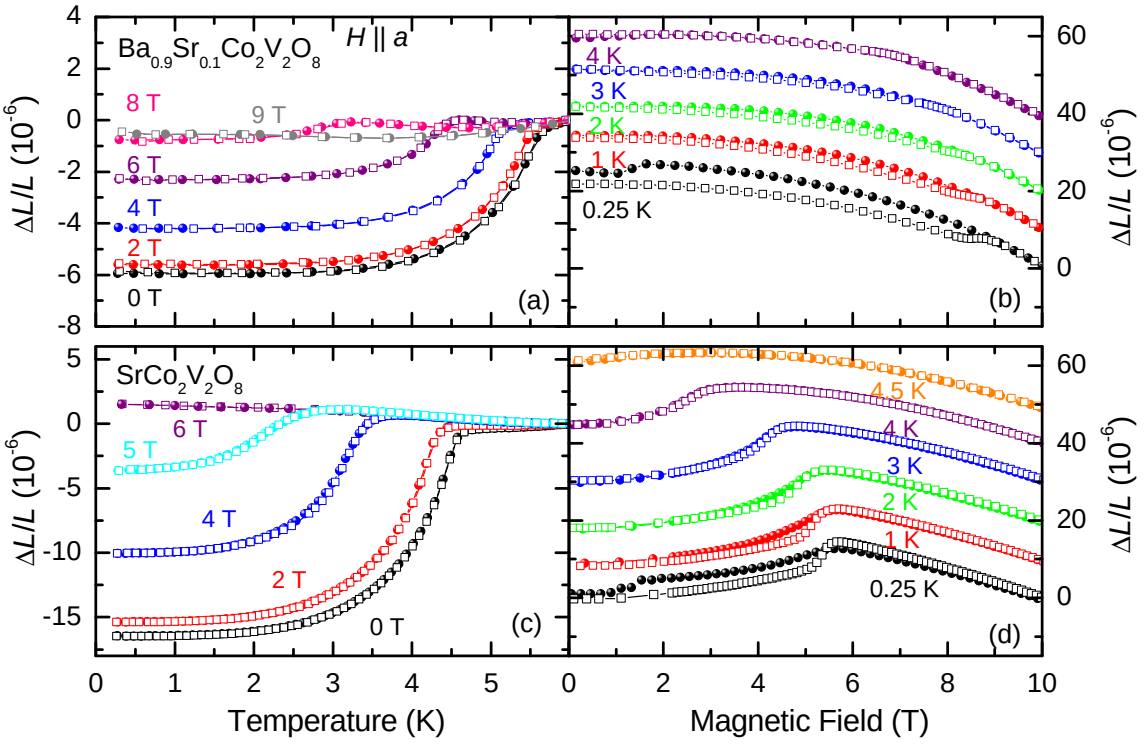

Figure 6.10: Thermal expansion (left) and magnetostriction (right) $\Delta L(T,H)/L$ measured along the a axes of $Ba_{0.9}Sr_{0.1}Co_2V_2O_8$ (a)-(b) and $SrCo_2V_2O_8$ (c)-(d) for $H \,||\, a$. Open and closed symbols represent measurements with increasing and decreasing temperature or magnetic field, respectively. The magnetostriction data were shifted to each other by 10^{-5} for clarity.

of $Ba_{0.9}Sr_{0.1}Co_2V_2O_8$ (a)-(b) and $SrCo_2V_2O_8$ (c)-(d) for $H \,||\, a$ which were measured along the a axis. All measurements were obtained with increasing and decreasing temperature or magnetic field. The zero-field thermal expansion shows that T_N is nearly unaffected for $Ba_{0.9}Sr_{0.1}Co_2V_2O_8$ and the relative length change is comparable to that of $BaCo_2V_2O_8$ (*cf.* Figure 5.21). In $SrCo_2V_2O_8$, however, the relative length change is three times larger and T_N lies at 4.5 K, which is about 1 K lower than in $BaCo_2V_2O_8$. Note that the zero-field curve shows a different slope than the previously discussed pressure-dependent thermal-expansion measurements. The measurements are not directly comparable because the sign and magnitude of the spontaneous strain is sample specific due to the present domain ratio.

Applying magnetic fields shifts the transition to lower temperatures. For $x = 0.1$ it is suppressed completely at an applied magnetic field of 9 T, while the transition in $SrCo_2V_2O_8$ has vanished already at 6 T. For temperatures below T_N, the magnetostriction data, shown in the right panels, reveal pronounced anomalies. The magnetostriction curves at the lowest temperature of 250 mK reveal a transition at ≈ 8.5 T for $Ba_{0.9}Sr_{0.1}Co_2V_2O_8$ giving an estimate of the critical magnetic field value for $T \to 0$. In $SrCo_2V_2O_8$ this value lies much lower at about 5.5 T. In both cases the samples show a hysteresis in the curves that were obtained for increasing and decreasing magnetic field below a temperature of 3 K. This hysteresis can be interpreted as

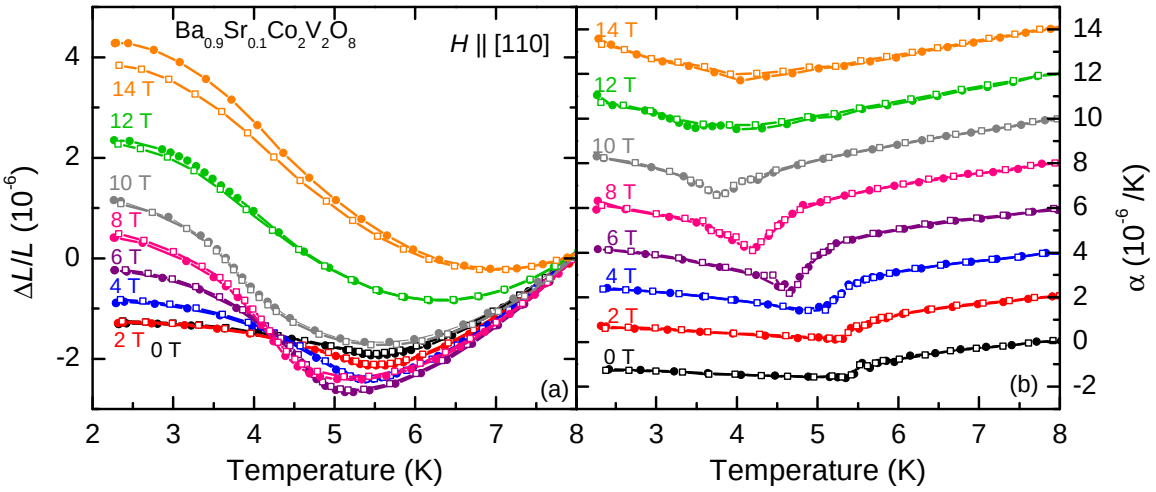

Figure 6.11: Thermal expansion $\Delta L(T)/L$ (left) of $Ba_{0.9}Sr_{0.1}Co_2V_2O_8$ measured along [1 1 0] for magnetic fields applied along the same direction and the corresponding thermal expansion coefficient (right).

partial detwinning process similar to that observed in $BaCo_2V_2O_8$ (see Sec. 5.4.2).

For a field direction along the in-plane diagonal [1 1 0] the thermal expansion in Figure 6.11, exemplarily measured on $Ba_{0.9}Sr_{0.1}Co_2V_2O_8$, clearly differs from the according data measured along a shown before. The sample does not show a well defined spontaneous length change below the transition but rather a small anomaly that is mainly visible in the thermal expansion coefficient, shown in panel (b), where the onset of the magnetic ordering is signaled by a minimum in α. The nearly linear suppression of the transition temperature is rather weak compared to the other field direction $H \,||\, a$ but the decrease of about $-0.17\,\mathrm{K/T}$ is slightly larger than for the pure compound (cf. Sec. 5.4.1). However, the transition is significantly broadened with increasing magnetic field which is not the case for $BaCo_2V_2O_8$. Moreover, the sign of the strain in the thermal expansions of the pure $BaCo_2V_2O_8$ and the substituted sample are of different signs. So far the origin of this discrepancy is unknown.

In literature, the magnetic phase diagram of $SrCo_2V_2O_8$ for the field direction perpendicular to the c axis was derived by specific heat measurements that were obtained for magnetic fields up to 6 T in a temperature range down to 2 K [25]. Figure 6.12 shows the specific heat of $SrCo_2V_2O_8$ for the field directions $H \,||\, a$, panel (a), and $H \,||\, [1\,1\,0]$, panel (d), for magnetic fields up to 14 T. In zero-magnetic field, the sample shows a sharp anomaly at 4.5 K, whereas a slightly higher T_N of 4.8 K was measured by He et al.. The peak height, however, reaches only 60 % of the peak height in the reference. The anomaly in the specific heat is strongly shifted for the field direction parallel to the a axis and is completely suppressed above 5 T which is in good agreement with the thermal expansion results presented above. In the other field direction, $H \,||\, [1\,1\,0]$, an anomaly remains present in magnetic fields up to 14 T. The nearly linear shift of T_N is roughly the same as for $Ba_{0.9}Sr_{0.1}Co_2V_2O_8$. It becomes clear, that a pronounced in-plane anisotropy is also present in $SrCo_2V_2O_8$. Since the measurements in Ref. 25 revealed a strong field dependence of T_N this field direction was most probably parallel to the a direction.

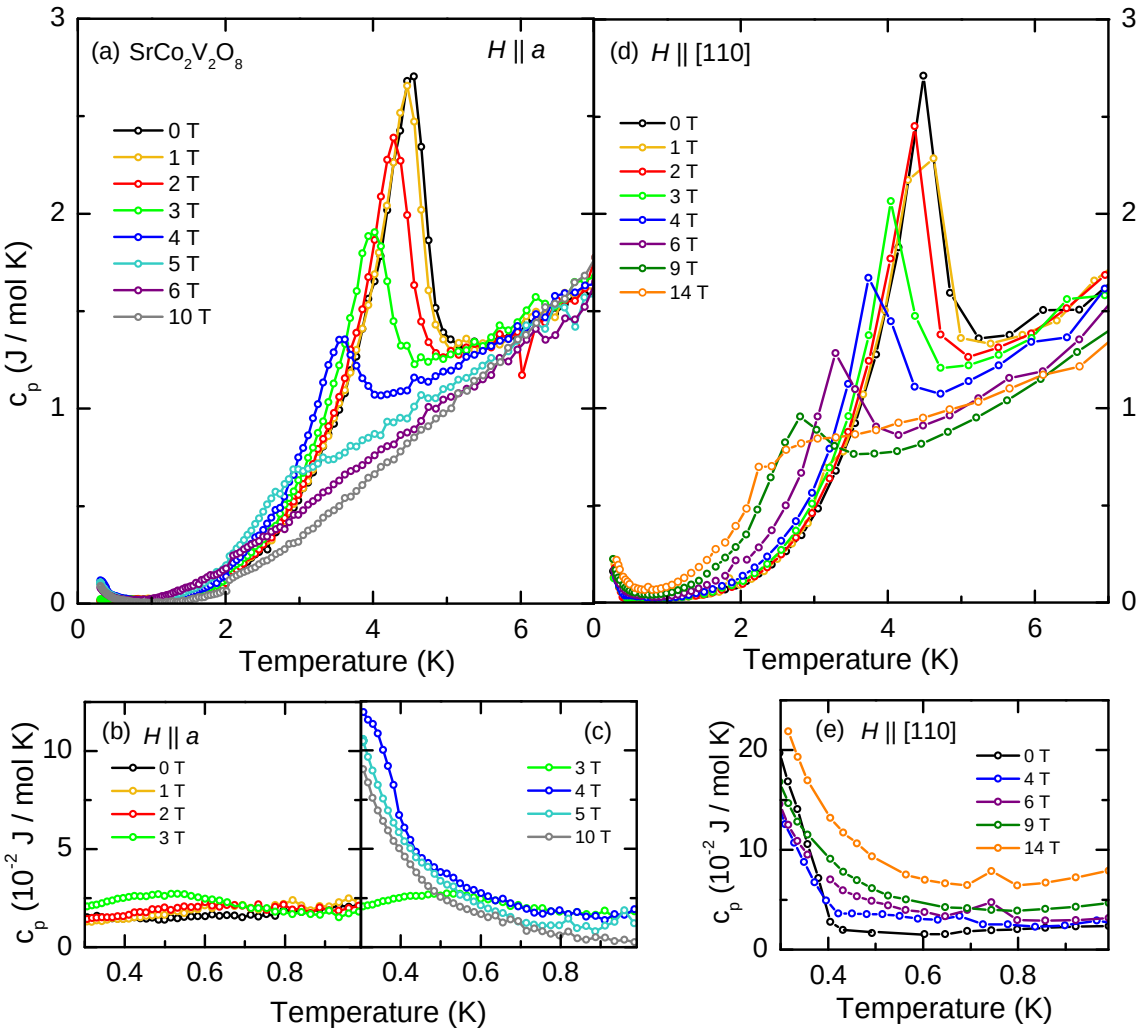

Figure 6.12: Specific heat of $SrCo_2V_2O_8$ for $H \,||\, a$ (a)-(c) and $H \,||\, [1\,1\,0]$ (d)-(e). The onset of antiferromagnetic order is signaled by a sharp anomaly. In the low-temperature regime, panels (b), (c), and (e), an anomaly evolves with increasing magnetic field.

Panels (b) and (c) show an enlargement of the low-temperature region, i.e. $T < 1\,\mathrm{K}$ for $H \,||\, a$. For low magnetic fields up to 3 T the specific heat does not change. Further increasing the field leads to a significant increase of c_p at temperatures below 0.6 K. For the other field direction, see panel (f), this upturn is present already in zero-magnetic field and remains nearly field independent. The measurements for both field directions were obtained on two different samples. The difference in the zero-field curves indicates an impurity effect in at least one of the samples. A similar anomaly was already discussed for the pure $BaCo_2V_2O_8$ compound in Section 5.4.2. In $BaCo_2V_2O_8$ this feature does not appear until an applied magnetic field of 6 T (see Sec. 5.4). The low-temperature anomalies are again accompanied by anomalous heat-pulse curves. The origin of this anomaly remains unknown.

Table 6.2: Critical temperatures T_N in zero magnetic field and critical magnetic fields obtained by extrapolating $H_{crit}^{\|a,c}(T)$ to $T \to 0$. The corresponding ratios $H_{crit}^{\|a,c}(T \to 0)/T_N(H = 0)$ are displayed in Fig. 6.14. The average decrease of T_N for $H\|[110]$ is given in the last column.

$Ba_{1-x}Sr_xCo_2V_2O_8$	T_N	$H_{crit}^{\|c}$	$H_{crit}^{\|a}$	$-\frac{\partial T_N}{\partial H^{\|[110]}}$
$x =$	(K)	(T)	(T)	(K/T)
0	5.5	3.9	9.7	0.1
0.1	5.5	3.9	8.7	0.17
0.5	5.5	3.9	8.0	–
0.9	4.9	3.7	6.4	–
1	4.5	3.5	5.3	0.17

6.1.6 Magnetic Phase Diagrams and Conclusion

The temperature *vs.* magnetic field phase diagrams for the $Ba_{1-x}Sr_xCo_2V_2O_8$ series were derived from the maximum positions of the temperature/field derivatives of the thermal expansion/magnetostriction and of the magnetization. If not shown here, the full data sets can be found in the Appendix B. The resulting temperature *vs.* magnetic field phase diagrams for the $Ba_{1-x}Sr_xCo_2V_2O_8$ series for $H \,||\, c$, $H \,||\, a$ and $H \,||\, [1\,1\,0]$ are shown in Figure 6.13. As a reference, in all panels the Néel and incommensurate ordered phases of pure $BaCo_2V_2O_8$ are marked by green and yellow shaded areas, respectively. The critical parameters discussed in the following are also summarized in Table 6.2.

The upper panels of Figure 6.13 show the phase diagrams for the field direction along the magnetic easy axis c. For a Sr content of 10 % and 50 % the zero-field Néel temperature as well as the complete phase boundary is nearly unchanged and the critical magnetic fields are close to H_{crit} of $BaCo_2V_2O_8$. Further increasing the substitution yields a suppression of the zero-field T_N to 4.9 K and 4.5 K for $Ba_{0.1}Sr_{0.9}Co_2V_2O_8$ and $SrCo_2V_2O_8$. The critical magnetic field, however, is suppressed only by 0.4 T over the full substitution range. For $x = 0.5$ and $x = 0.9$ the critical magnetic fields $H_{crit}(T \to 0)$ have to be extrapolated because the data were obtained only above $T = 2$ K. As can be seen in the phase boundaries of the other substitution levels and the pure compound, the value can be estimated by $H(T = 2\,\mathrm{K})$, because the slope of the curves is very steep below that temperature. In order to evaluate the influence of the substitution on the critical parameters, i.e. to visualize possible scaling behavior, the ratio $H_c(T \to 0)/T_N(H = 0)$ is plotted against the substitution level x in Figure 6.14. In case of $H \,||\, c$ (green) this ratio is basically constant over the whole substitution range, the overall influence of the substitution is, thus, rather weak. The incommensurate order found in $BaCo_2V_2O_8$, however, is not represented directly in our measurements in the $Ba_{1-x}Sr_xCo_2V_2O_8$ compounds. Only the small hysteresis observed in low-temperature magnetostriction data gives indirect evidence for an occurrence of such a phase above the critical field $H_{crit}^{\|c}(T \to 0)$. There is a certain amount of disorder in all substituted materials, which disturbs the evolution of a well-defined incommensurability in the low-temperature high-field range. However, this topic needs further investigation e.g. in terms of magnetic neutron diffraction.

The lower panels of Figure 6.13 show the magnetic phase diagrams for fields applied within the *ab* plane. A dashed line marks the phase boundary of $BaCo_2V_2O_8$ for magnetic fields applied parallel to the [1 1 0] direction. $Ba_{0.9}Sr_{0.1}Co_2V_2O_8$ and

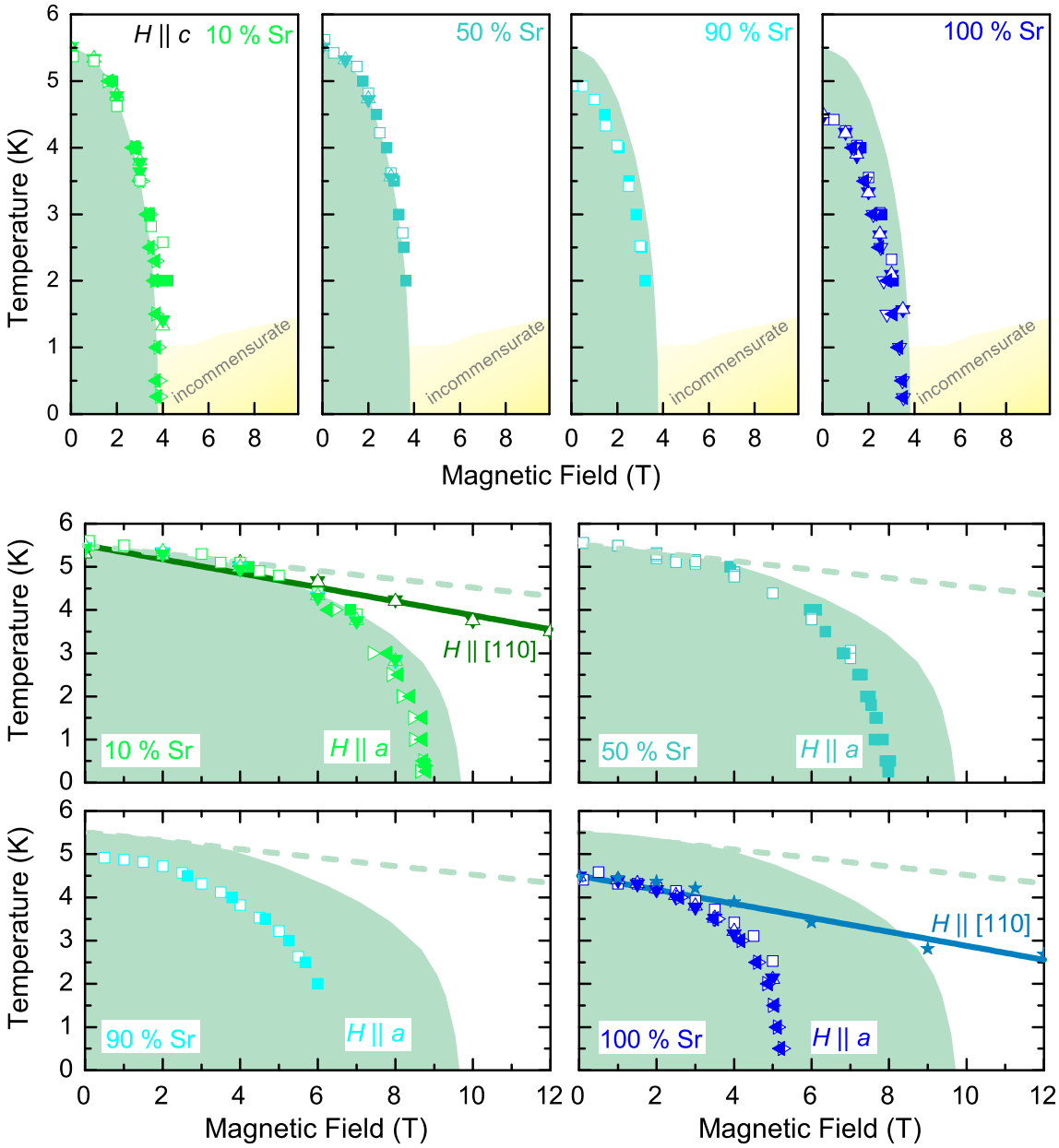

Figure 6.13: Magnetic phase diagrams of the $Ba_{1-x}Sr_xCo_2V_2O_8$ series for $H \,||\, c$ (upper panels) and within the *ab* plane (lower panels). Phase boundaries for $H \,||\, 110$ are included in the phase diagrams for 10 % Sr and 100 % Sr with respective reference data of $BaCo_2V_2O_8$ (blue bar). As a reference, the Néel (and incommensurate) ordered phases of $BaCo_2V_2O_8$ are depicted as green (and yellow) areas, respectively. Points are obtained from thermal expansion (△), magnetostriction (◀), magnetization (■), and specific heat data (⋆).

$SrCo_2V_2O_8$ both show a linear decrease of T_N of about $-0.17\,K/T$ in that field direction which is slightly larger than in $BaCo_2V_2O_8$. For magnetic fields applied parallel to *a* one observes a much stronger influence on the suppression of the transition temperature both with increasing magnetic field and increasing substitution level. The phase boundaries become steeper with increasing Sr content, i.e. the critical mag-

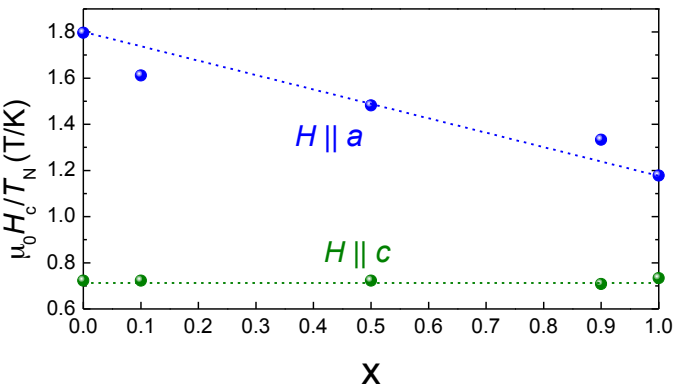

Figure 6.14: Ratio $H_{\mathrm{crit}}^{\|a,c}(T \to 0)/T_{\mathrm{N}}(H=0)$ of the critical magnetic field and the Néel temperature as a function of the strontium substitution level x for $H \,||\, a$ (blue) and $H \,||\, c$ (green).

netic field $H_{\mathrm{crit}}^{\|a}(T \to 0)$ is strongly decreased from 9.7 T in $BaCo_2V_2O_8$ to 5.3 T in $SrCo_2V_2O_8$. Thus, $H_{\mathrm{crit}}^{\|a}(T \to 0)$ is reduced by about 45 % when Ba is replaced by Sr, while T_{N} is only reduced by about 20 %. This is also reflected in the ratio $H_{\mathrm{crit}}^{\|a}(T \to 0)/T_{\mathrm{N}}(H=0)$ which shows a linear decrease (cf. Fig. 6.14, blue line) in contrast to the rather constant ratio for $H \,||\, c$. The in-plane anisotropy for magnetic fields parallel a and [1 1 0] is preserved upon doping. Moreover, the data reveal that the anisotropy becomes even more pronounced with increasing Sr content as seen in the strong decrease of $H_{\mathrm{crit}}^{\|a}$.

In summary, one finds that concerning the paramagnetic phase, i.e. for temperature above ≈ 6 K, the strong Ising anisotropy of the magnetic susceptibility remains almost unchanged, that is the pronounced easy-axis anisotropy of the Co^{2+} spins due to the crystal electric field is essentially preserved despite a stronger distortion of the CoO_6 octahedra e.g. in $SrCo_2V_2O_8$ (cf. Fig. 6.5). One observes that the in-plane anisotropy systematically increases with increasing Sr content. Given through the local orientation of the CoO_6 octahedra, the tilt of the upper apical Co-O bond from the c axis is the crucial parameter according to the calculations of Ref. 96. Figure 6.5 compares the CoO_6 octahedra of $SrCo_2V_2O_8$ and $BaCo_2V_2O_8$ which were obtained using the refined data of Refs. 15, 87. For $BaCo_2V_2O_8$, the octahedra consists of three pairs of equal Co-O and five pairs of equal O-O bond lengths, whereas such pair-wise equal bond lengths are not present in $SrCo_2V_2O_8$ and the octahedra are, thus, significantly more distorted. Especially the tilt angle of the short upper apical Co-O bond increases from $\approx 4.8°$ in $BaCo_2V_2O_8$ to 5.1° in $SrCo_2V_2O_8$. The systematic decrease of $H_{\mathrm{crit}}^{\|a}(T \to 0)/T_{\mathrm{N}}(H=0)$ could be naturally explained through the increasing tilt angle of the local quantization axes with increasing Sr content and, thus, an increase of the staggered g-factor. Consequently, an external magnetic field $H \,||\, a$ would cause larger staggered fields h_b resulting in a systematic decrease of $H_{\mathrm{crit}}^{\|a}(T \to 0)/T_{\mathrm{N}}(H=0)$ with increasing x. Note that the oxygen coordination is known only for the two end members. Further verification of this theory could be given through structure determination and, thus, of the tilt angles of the intermediate samples in a neutron scattering experiment.

The preservation of the Ising anisotropy for $T > T_{\mathrm{N}}$ over the entire substitution series $Ba_{1-x}Sr_xCo_2V_2O_8$ suggests that the Sr substitution mainly influence the inter-chain interaction $J_i^{\perp}$. Because the inter-chain distance considerably decreases with increasing Sr content, one may expect the inter-chain exchange couplings to increase,

which seems to be in conflict with the observed weakly decreasing T_N. The magnetic structure of $BaCo_2V_2O_8$ typically arises in the presence of frustrated NN ($J^{\perp}_{NN}$) and NNN ($J^{\perp}_{NNN}$) inter-chain interactions (cf. Fig. 5.6). The decreasing inter-chain distance in the $Ba_{1-x}Sr_xCo_2V_2O_8$ series may, thus, change $J^{\perp}_{NN}$ and $J^{\perp}_{NNN}$ in a way that the resulting frustration increases, which in turn weakens the effective inter-chain interaction resulting in a weakly decreasing T_N with increasing Sr content.

The very same orthorhombic distortion and coupling of the magnetic structure to the structural domains which is known in $BaCo_2V_2O_8$ is also observed in the full range of Sr substitution. This gives evidence that the zero-field magnetic structure, with the spins within the (0 0 1) plane pointing either parallel or antiparallel to each other (see Chap. 5), is essentially preserved in the $Ba_{1-x}Sr_xCo_2V_2O_8$ compounds and in particular in $SrCo_2V_2O_8$ which contradicts previous assumptions in Refs. 25, 88, 89 and supports the suggestions made in Ref. 86. Only recently these assumptions have been confirmed for $SrCo_2V_2O_8$ by a single-crystal neutron diffraction experiment [100].

6.2 $BaCo_{1.9}M_{0.1}V_2O_8$

6.2.1 Introduction

Now the manipulation of the magnetic subsystem represented by the CoO_6 chains will be discussed. Partial substitution of the Co site by another transition metal (Mn, Fe, Ni, Cu, Zn) or the non-magnetic alkaline earth Mg is expected to create defect sites directly within the magnetic chains. Substitution by a non-magnetic impurity is the theoretically best described limiting case (see e.g. Refs. 26, 135, 136). $BaCo_2V_2O_8$ represents a quasi-one-dimensional spin system and such a substitution will cut the chains into finite segments. Neglecting inter-chain interactions, the spin chain then consists of finite non-interacting units. In real quasi-one-dimensional systems, however, three dimensional long-range magnetic order is induced below a low-enough critical temperature T_C due to existing finite inter-chain interactions which in turn will be influencing the 1D segmentation effects. Thus, a strong influence on the zero field value of T_N is expected (see e.g. Ref. 26).

Such an impurity substitution was investigated, e.g., in $SrNi_2V_2O_8$ where 5 % Mg doped polycrystalline samples show an impurity-induced phase transition at 3.7 K [137] instead of a non-magnetic spin-singlet ground state in the undoped $SrNi_2V_2O_8$ [13]. For $BaCo_2V_2O_8$, however, no such investigations are available in literature. Thus, single crystals of the $BaCo_{1.9}M_{0.1}V_2O_8$ series were grown where 5 % of Co^{2+} were replaced either by non-magnetic Mg^{2+} or by the magnetic ions Mn^{2+}, Ni^{2+}, and Cu^{2+}. The degree of (de-) coupling now depends on the magnetic properties of the substituted M^{2+} ion and this will be subject of this section. Measurements of the magnetization, thermal expansion, and magnetostriction and the resulting magnetic phase diagrams of the $BaCo_{1.9}M_{0.1}V_2O_8$ series will be discussed.

Structure

The discussion whether the centro- or non-centrosymmetric space group is present, has to be mooted analogously for the $BaCo_{1.9}M_{0.1}V_2O_8$ series. Figure 6.15 shows the X-ray diffraction patterns of the $BaCo_{1.9}M_{0.1}V_2O_8$ samples with M = Mg, Cu, Ni, Mn from top to bottom.

The structure of $BaCo_{1.9}Mg_{0.1}V_2O_8$[2] was also refined using space group $I4_1cd$ which yields similar results to those presented in Section 3.3.3 with $a = 12.3528(7)$ Å and $c = 8.4016(5)$ Å ($\chi^2 = 2.5$). The lattice constants remain basically unchanged, independent of the chosen space group. In principle, these substitutions could induce a change of the space group, e.g. from No. 142 to No. 110. Such a change is, anyway, not resolvable through powder X-ray diffraction and due to the very low substitution level, the structure refinement of the obtained powder patterns (see also Section 3.3.2) was carried out using the space group of $BaCo_2V_2O_8$ $I4_1/acd$. The resulting lattice parameters a and c as a function of the ionic radius of the substituted M^{2+} ion given in Å are shown in Figure 6.16 (a). For comparison the lattice constants of the pure compound $BaCo_2V_2O_8$ are marked by dashed lines. Literature values taken from

[2] The pure compound $BaMg_2V_2O_8$ belongs to the centrosymmetric space group [15].

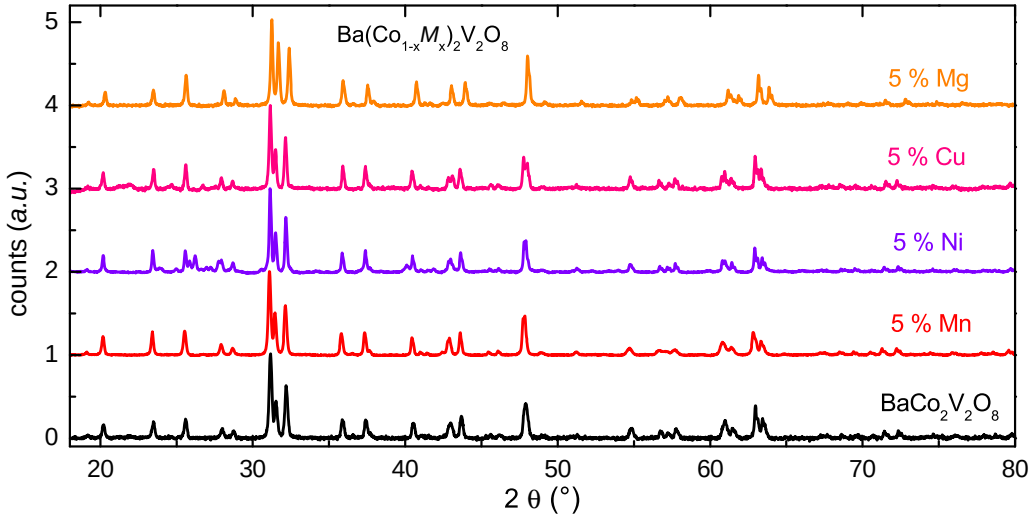

Figure 6.15: X-ray powder diffraction pattern of the $BaCo_{1.9}M_{0.1}V_2O_8$ sample with M =Mg, Cu, Ni, Mn and pure $BaCo_2V_2O_8$ (from top to bottom).

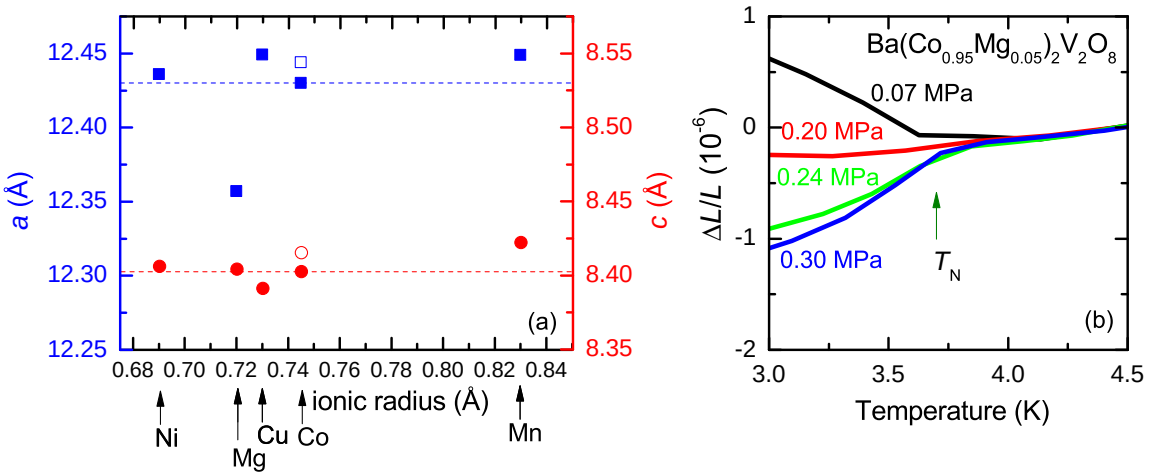

Figure 6.16: (a) Lattice constant a (blue) and c (red) as a function of the ionic radii of the substituted M^{2+} ions. The dashed lines mark the lattice constants of $BaCo_2V_2O_8$. Open symbols are reference data for $BaCo_2V_2O_8$ taken from Ref. 15. (b) Zero-field thermal-expansion of $BaCo_{1.9}Mg_{0.1}V_2O_8$ with applied uniaxial pressure $p_i||a$.

Ref. 15 are depicted as open symbols. For the substitution with the transition metal ions Mn, Cu, and Ni the lattice constants remain almost unchanged as might be expected from the rather low substitution level of 5 %. $BaCo_{1.9}Mg_{0.1}V_2O_8$, however, reveals a significant reduction of a despite the fact that its tabulated ionic radius (see Table 3.1, 27) is similar to that of the transition metal ions.

Orthorhombic Distortion

Figure 6.16 (b) shows representative zero-field thermal expansion measurements of $BaCo_{1.9}Mg_{0.1}V_2O_8$ measured for different uniaxial pressures $p_i||a$ applied along the a

axis. All length changes $\Delta L = L(T) - L_0$ in the figure are related to L_0 at 4.5 K. The curves show that the Néel temperature of $BaCo_{1.9}Mg_{0.1}V_2O_8$ is strongly reduced compared to pure $BaCo_2V_2O_8$. This reduction to $T_N = 3.7$ K is much stronger than for any other compound of the $Ba_{1-x}Sr_xCo_2V_2O_8$ series. For weak uniaxial pressure of 0.07 MPa the sample shows a spontaneous expansion when entering the Néel ordered phase. Increasing the pressure switches the expansion into a spontaneous contraction. Note that the scale of the ordinate is half of that shown in Figure 6.7 for the Sr substituted samples. This switching indicates that also for a substitution of 5 % Mg into $BaCo_2V_2O_8$ an orthorhombic splitting is still present. The formation of structural domains in $BaCo_2V_2O_8$ seems to basically sustain the segmentation of the spin chains by the non-magnetic impurity. The substitution by nonmagnetic Mg represents the extreme case of complete blocking of the NN exchange within the chains. For the substitution by the magnetic ions where the exchange is not completely blocked the very same structural distortion is expected. Thus, this result strongly suggests that the magnetic structure of all these crystals does not change significantly. Nevertheless, a definite proof of this claim requires a microscopic determination of the magnetic structure.

6.2.2 Ising Anisotropy

Figure 6.17 (a) shows the temperature-dependent magnetization $M(T)/\mu_0 H$ in a weak magnetic field of 100 mT for the field directions parallel and perpendicular to the c axis. The black curves (M = Co) mark the reference data of the pure $BaCo_2V_2O_8$. For all substitutions, the maxima in the $\chi^{||c}$ curves remain nearly unaffected in their position at $\approx$ 34 K and their absolute values. Moreover, the overall slope and the Ising anisotropy ($\approx \chi^{||c}/\chi^{\perp|c}$) remain essentially preserved. The kink in the $BaCo_{1.9}Mn_{0.1}V_2O_8$ data (yellow) around 150 K and the larger absolute value below this temperature most probably stem from an impurity of some Mn-oxide. Panels (b) and (c) show the normalized magnetization $M(T)/M(7\,\mathrm{K})$ in the low-temperature region for $H \,||\, c$ and $H \,||\, a$, respectively. The transition temperatures are indicated by vertical grey lines. For M = Mn, T_N is slightly increased to 5.8 K. The Ni substitution does not change T_N but for Cu and even more for Mg the transition temperature is strongly decreased to 4.4 K and 3.7 K, respectively.

Panels (d) and (e) show the field-dependent magnetization at $T = 2$ K. For $H \,||\, a$, the overall behavior is nearly unchanged compared to $BaCo_2V_2O_8$ (black) and only small deviations in the absolute value are observed. Again, $BaCo_{1.9}Mg_{0.1}V_2O_8$ behaves exceptional. The absolute value of $M(7\,\mathrm{T})$ is slightly enhanced and the magnetization reveals a small kink at a magnetic field of $\approx$ 6 T marked by an arrow. This kink indicates the breakdown of the Néel order already at this strongly reduced critical magnetic field at a temperature of 2 K compared to the critical field $H_{crit}^{||a} = 9.5$ T for $BaCo_2V_2O_8$.

For the field direction parallel to the magnetic easy axis the substitutional influence is much stronger. At $T = 2$ K $BaCo_2V_2O_8$ shows a field-induced transition around 4 T. The Ni substitution does not change the critical field, but the slope of the curve above H_c is reduced. In case of manganese the critical field at $T = 2$ K is decreased in comparison to $BaCo_2V_2O_8$. The absolute value of $M(7\,\mathrm{T})$ above H_c is reduced,

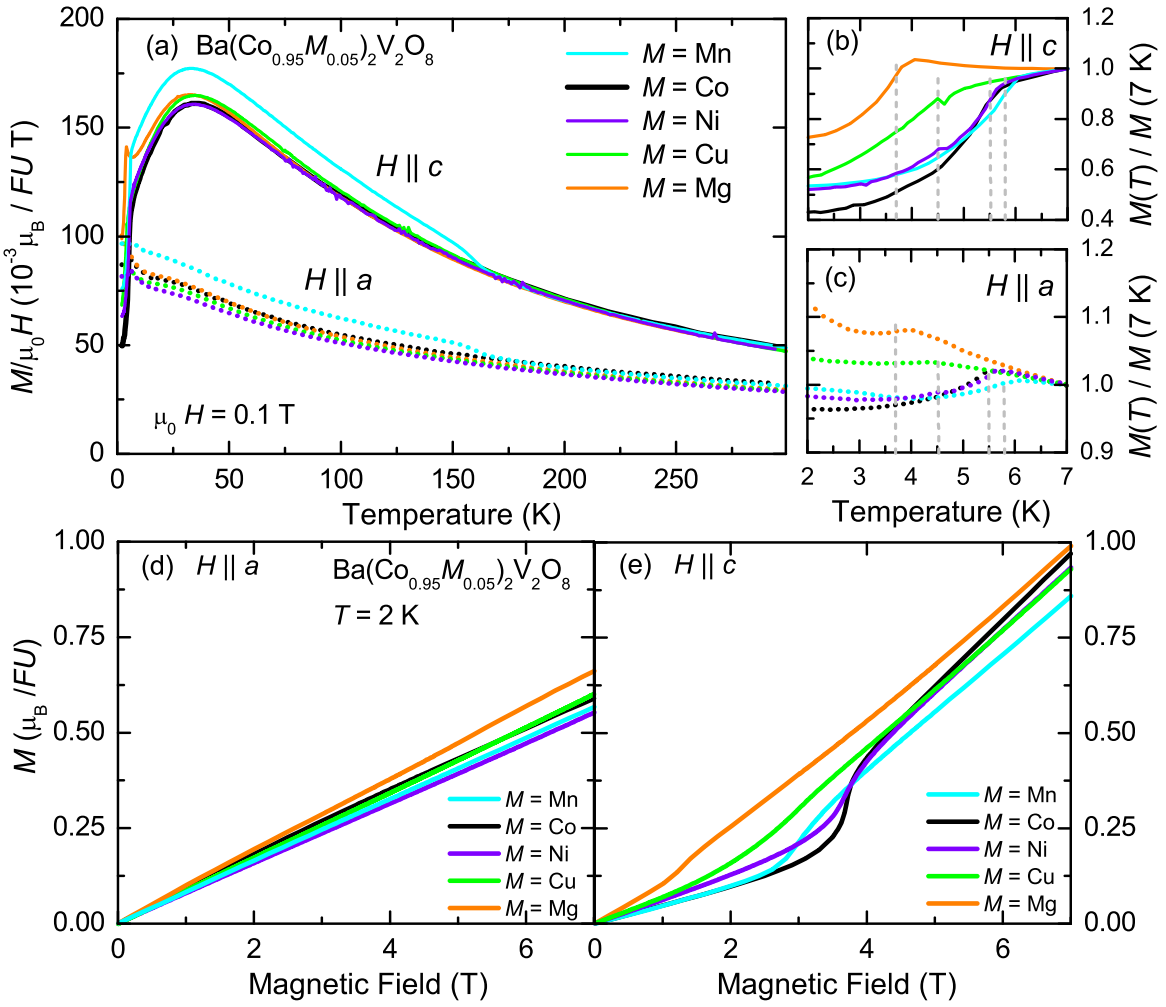

Figure 6.17: Temperature-dependent magnetization (a) of the $BaCo_{1.9}M_{0.1}V_2O_8$ series at a magnetic field of 100 mT applied along the c axis (solid lines) and along the a axis (dashed lines). Panels (b) and (c) show an enlargement of the respective low-temperature region. The extracted transition temperatures are marked by vertical lines. Panels (d) and (e) depict the field-dependent magnetization at $T = 2$ K with H along a and c axis, respectively.

kept in mind that the zero-field T_N was enhanced. The influence of copper and the non-magnetic magnesium is even stronger and the critical field is lowered to only 1.4 T in case of M =Mg. The data presented above are only an exemplary selection, the complete magnetization data are shown in Appendix B).

6.2.3 *H* parallel *c*

For two samples, $BaCo_{1.9}Cu_{0.1}V_2O_8$ and $BaCo_{1.9}Mg_{0.1}V_2O_8$, the investigation of the magnetic phase diagram for $H \,||\, c$ was extended to temperatures down to 250 mK using thermal expansion and magnetostriction measurements. Figure 6.18 shows the temperature- and field-dependent length changes of the samples $BaCo_{1.9}Cu_{0.1}V_2O_8$ and $BaCo_{1.9}Mg_{0.1}V_2O_8$. The thermal expansion of $BaCo_{1.9}Cu_{0.1}V_2O_8$ shows a suppression of the transition temperature by magnetic fields similar to $BaCo_2V_2O_8$, i.e.

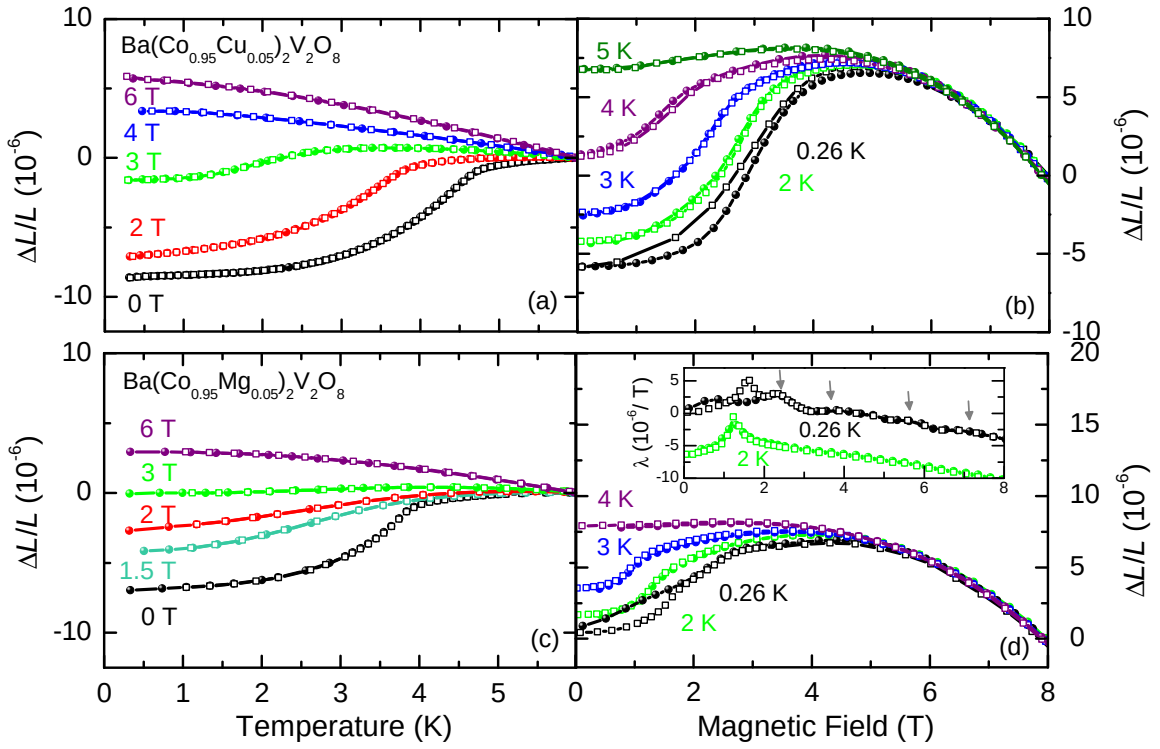

Figure 6.18: Thermal expansion (left panels) and magnetostriction (right panels) of $BaCo_{1.9}Cu_{0.1}V_2O_8$ (a)-(b) and $BaCo_{1.9}Mg_{0.1}V_2O_8$ (c)-(d) for magnetic fields $H \,||\, c$. Open and closed symbols represent measurements with increasing and decreasing temperature/field, respectively. The inset of panel (d) shows the magnetostriction coefficient $\lambda(H)$ for $T = 260\,\mathrm{mK}$ and 2 K. The low-temperature data reveal a sequence of broad anomalies, marked by arrows.

the transition vanishes above a critical field of 4 T. In the magnesium substituted case, panel (c), this critical field $H_{crit}^{||c}(T \to 0)$ lies lower and the transition temperature is suppressed already between 2-3 T. The low-temperature magnetostriction data reveal critical magnetic fields of 3 T for the Cu substitution and 2 T for the Mg substitution. Both samples also reveal a hysteresis in the field-dependence giving an indirect hint for the possible occurrence of an incommensurate phase. Be reminded, that in $BaCo_2V_2O_8$ the transition "Néel $\to$ paramagnetic" is of 2^{nd} order while the "Néel $\to$ incommensurate" transition is of 1^{st} order and accompanied by a hysteresis in the magnetostriction. The corresponding thermal expansion measurements $\Delta L_c(T; H \,||\, c > 4\,\mathrm{T})$ (see panels (a) and (c)) do not show any resolvable anomalies in the low-temperature region which should be present if there were well defined transitions in the incommensurate phase. Thus, in all cases the evolution of a well defined incommensurability in the low-temperature high-field range seems to be disturbed. Similar to the discussion for the $Ba_{1-x}Sr_xCo_2V_2O_8$ series in the previous section this issue needs further investigation through, e.g., neutron scattering.

For the $BaCo_{1.9}Mg_{0.1}V_2O_8$ crystal, however, a particular feature is observed in the low-temperature magnetostriction coefficient λ. As depicted in the inset of Figure 6.18 (d), at $T = 260\,\mathrm{mK}$ the magnetostriction coefficient λreveals a sequence of

broad anomalies indicated by arrows. At higher temperatures this feature disappears. In the pure compound $BaCo_2V_2O_8$ an incommensurate phase is observed above a magnetic field of about 4 T which shows a continuous variation of the propagation vector $\Delta k(H)$ with increasing magnetic field [105]. This continuous variation can be compared to the mechanisms in the incommensurate phase of Spin-Peierls systems. Here, the number of (soliton/anti-soliton) kinks continuously increases with increasing external magnetic field. In order to keep the domain walls equidistant, the system has to rearrange with increasing magnetic field [117, 138–140]. Such a mechanism will be significantly disturbed due to a segmentation of the spin chains as it is the case in $BaCo_{1.9}Mg_{0.1}V_2O_8$. The continuous variation of $\Delta k(H)$ is no longer possible because the Mg^{2+} ions form a blockade for the rearrangement processes. The additional anomalies in the low-temperature magnetostriction data of $BaCo_{1.9}Mg_{0.1}V_2O_8$ may, thus, be seen as an indication for discontinuous changes in the field dependence of $\Delta k(H)$. Since these anomalies do not occur, e.g., in $BaCo_{1.9}Cu_{0.1}V_2O_8$, a plausible explanation is given through a less effective segmentation by the Cu ions which is consistent with the weaker influence of Cu and the other transition metals on T_N.

6.2.4 In-plane Anisotropy

Figure 6.19 shows the thermal expansion (left panels) and representative magnetostriction data (right panels) of the $BaCo_{1.9}M_{0.1}V_2O_8$ samples for magnetic fields applied along a. The thermal expansion for M = Mn reveals a slightly enhanced transition temperature of 5.8 K which is shifted to $\approx$ 3 K in a magnetic field of 9 T. For even larger fields the transition is shifted below $T = 2.5$ K which is the lowest temperature that was reachable in the used VTI setup. The critical magnetic field lies approximately around 12 T as the magnetostriction data for $T = 2.3$ K, shown in panel (b), reveal an anomaly at 11 T. The Cu-substituted sample shows a suppression of T_N above 7 T. Again, the critical magnetic field, however lies a little higher as the low-temperature magnetostriction data reveal. $BaCo_{1.9}Mg_{0.1}V_2O_8$ with its strongly reduced zero-field transition temperature of 3.7 K shows a switching from a spontaneous contraction below T_N to an elongation in an external magnetic field between 3 and 5 T. The change of the spontaneous strains can be related to the orthorhombic twin domains and a partial magnetic field induced detwinning as discussed for $BaCo_2V_2O_8$. Moreover, such detwinning effects also explain the hysteresis between the $\Delta L(H)$ curves obtained with increasing field after zero-field cooling, as seen in panel (f) represented by open symbols, and those measured either with decreasing field (closed symbols) or in the subsequent field-increasing run (pink symbols) as marked by the arrows. In general, the anomalies in the magnetostriction data of the $BaCo_{1.9}M_{0.1}V_2O_8$ compounds are broadened compared to $BaCo_2V_2O_8$ which is probably related to the disorder induced by the substitution.

For $BaCo_{1.9}Mn_{0.1}V_2O_8$ and $BaCo_{1.9}Mg_{0.1}V_2O_8$ the thermal expansion was also measured for the field direction parallel to [1 1 0] in order to study whether an in-plane anisotropy is conserved in the $BaCo_{1.9}M_{0.1}V_2O_8$ compounds. Figure 6.20 shows the respective thermal expansion (left panels) and the corresponding derivatives (right panels), i.e. the thermal expansion coefficient α. Both compounds reveal a rather weak shift of the transition temperature with increasing magnetic field, which can

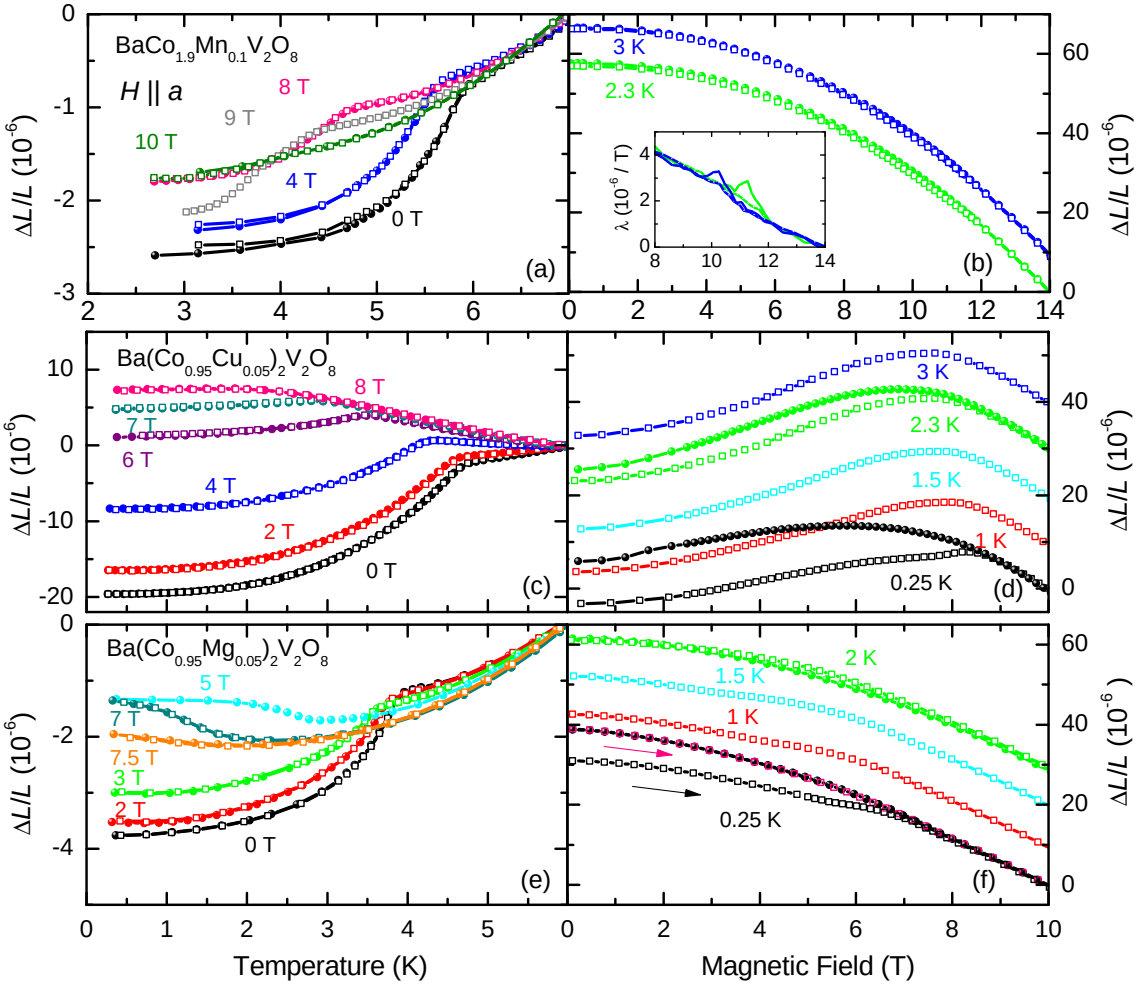

Figure 6.19: Thermal expansion (left panels) and magnetostriction (right panels) for $H \,||\, a$ of $BaCo_{1.9}Mn_{0.1}V_2O_8$ (a)-(b), $BaCo_{1.9}Cu_{0.1}V_2O_8$ (c)-(d) and $BaCo_{1.9}Mg_{0.1}V_2O_8$ (e)-(f). The data were obtained with increasing (open symbols) and decreasing (closed symbols) temperature or field. Note the different scales in panels (a)-(b). For clarity, the magnetostriction data are offset by 10^{-5} with respect to each other. The arrows in (f) mark the zero-field cooled and subsequent field-cooled measurements.

be tracked by the extrema of α. Remarkably, like in the Sr-substituted sample, the sign of the strain in the thermal expansions is of different sign than that of the pure $BaCo_2V_2O_8$. The presented measurements and those in Appendix B were used to derive the magnetic phase boundaries of the $BaCo_{1.9}M_{0.1}V_2O_8$ compounds for magnetic fields parallel to a and $[1\,1\,0]$, respectively.

6.2.5 Magnetic Phase Diagrams and Conclusion

The upper panels of Figure 6.21 show the phase diagrams of the $BaCo_{1.9}M_{0.1}V_2O_8$ compounds for magnetic fields applied along c. For comparison the Néel and incommensurate phases of $BaCo_2V_2O_8$ are marked as green and yellow shaded areas. Apart from a slight enhancement of the zero-field T_N for M = Mn ($S = 5/2$) it decreases for

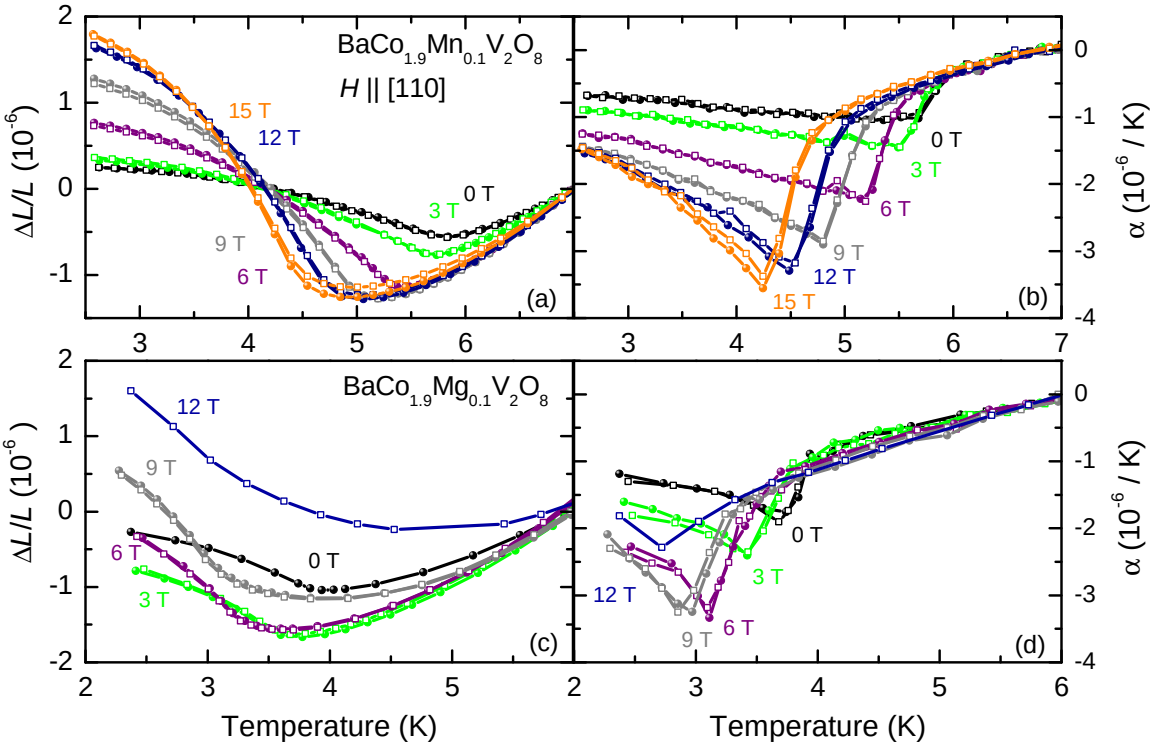

Figure 6.20: Thermal expansion $\Delta L/L$ and the thermal expansion coefficients α of $BaCo_{1.9}Mn_{0.1}V_2O_8$ (a)-(b) and $BaCo_{1.9}Mg_{0.1}V_2O_8$ (c)-(d) for magnetic fields parallel to [1 1 0]. Note the different scale of the abscissa.

the other transition metals and Mg substitutions. For the substitution of Ni ($S = 1$) the phase diagram almost coincides with that of $BaCo_2V_2O_8$ ($H_{crit}^{\|c} = 3.9\,\mathrm{T}$). The critical magnetic fields $H_{crit}^{\|c}$ can be estimated to a slightly lower value of 3.1 T and 3.7 T for Mn and Ni, respectively. All extracted parameters T_N, $H_{crit}^{\|a,c}$, $\frac{\partial T_\mathrm{N}}{\partial H}\|[110]$ of the $BaCo_{1.9}M_{0.1}V_2O_8$ series are summarized in Table 6.3.

For $BaCo_{1.9}Cu_{0.1}V_2O_8$ (Cu^{2+} $S = 1/2$) and $BaCo_{1.9}Mg_{0.1}V_2O_8$ (Mg^{2+} $S = 0$) the zero-field T_N is significantly lower. The phase boundary of $BaCo_{1.9}Cu_{0.1}V_2O_8$ yields an even lower critical field of 3 T, however, the substitution of the non-magnetic Mg seems to have the largest impact on the phase boundary. The critical field is decreased to 1.6 T. Moreover, hysteresis effects are observed in the low-temperature magnetostriction of $BaCo_{1.9}Cu_{0.1}V_2O_8$ and $BaCo_{1.9}Mg_{0.1}V_2O_8$ (cf. Fig. 6.18 (b),(d)) giving an indirect hint for the presence of an incommensurate phase, but this issue cannot be solved by the present data, as for both compounds, e.g., the thermal expansion does not give any sign for an anomaly in the low- temperature range (cf. Fig. 6.18 (a),(c)). Nevertheless, additional kinks in the low-temperature magnetostriction of $BaCo_{1.9}Mg_{0.1}V_2O_8$ appear which can be related to discontinuous changes in the field dependence of $\Delta k(H)$ (see Fig. 6.19 (f)) revealing a possible indication for an incommensurate phase similar to the parent compound.

All crystals of the $Ba_{1-x}Sr_xCo_2V_2O_8$ and $BaCo_{1.9}M_{0.1}V_2O_8$ series that were investigated in this chapter, were grown by the floating-zone technique in an image-furnace. None of them reveals resolvable anomalies of $\Delta L_c(T; H \,||\, c > 4\,\mathrm{T})$. The appearance of

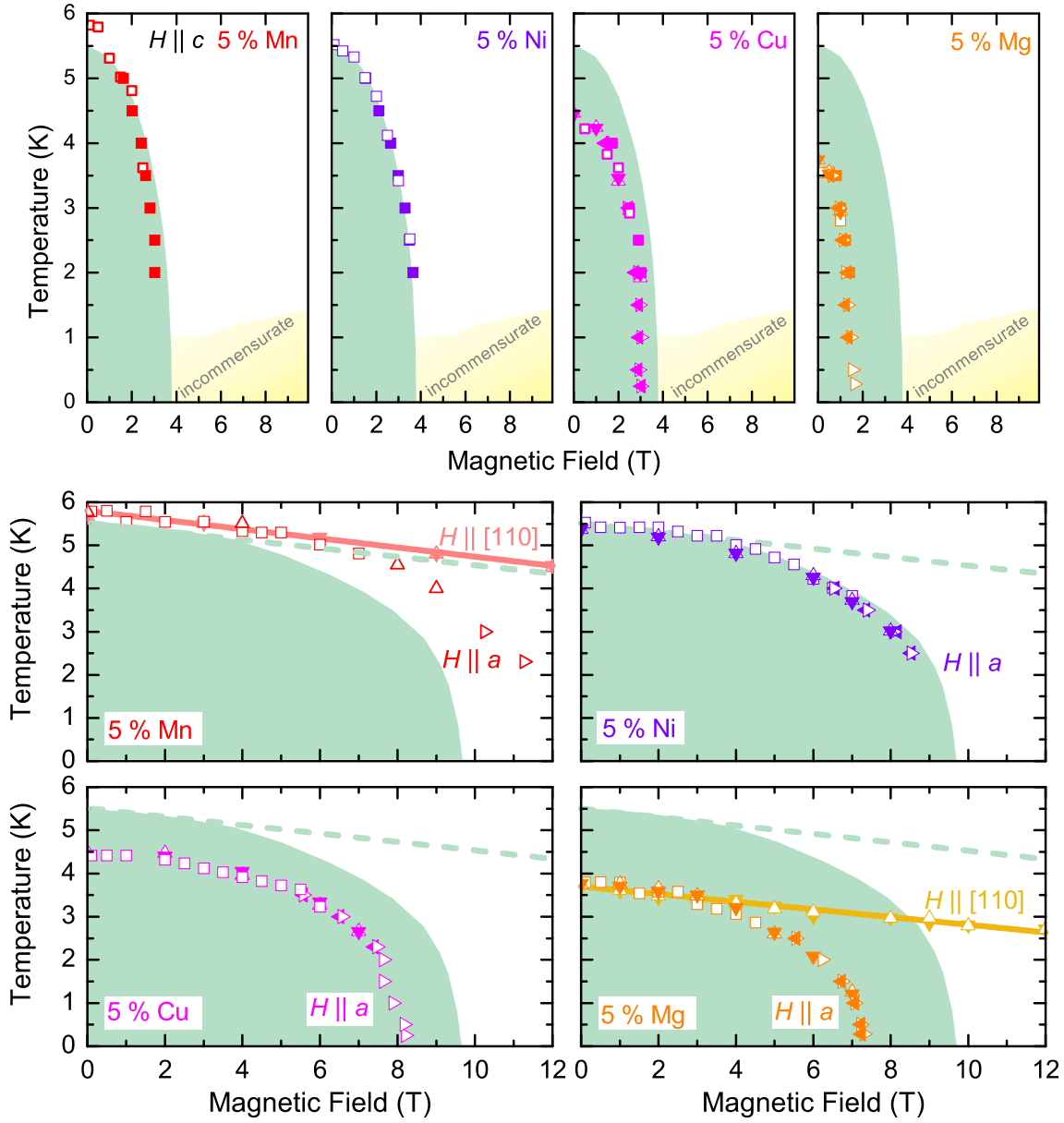

Figure 6.21: Temperature *vs.* magnetic field phase diagram of the $BaCo_{1.9}M_{0.1}V_2O_8$ compounds with $M =$ Mn, Ni, Cu or Mg for $H \,||\, c$ (upper panels) and within the ab plane (lower panels). Phase boundaries for $H \,||\, 110$ are included in the phase diagrams for 5 % Mn and 5 % Mg with respective reference data of $BaCo_2V_2O_8$ (dashed green line). As a reference, the Néel (and incommensurate) ordered phases of $BaCo_2V_2O_8$ are depicted as shaded areas. Data are obtained by thermal expansion (△), magnetostriction (◀), and magnetization (■).

the incommensurate phase in the thermodynamic properties might be related to the applied growth technique. The anomalies of $BaCo_2V_2O_8$ in $\Delta L_c(T; H \,||\, c > 4\,\mathrm{T})$ were observed only in the sample grown by spontaneous nucleation method. Samples of $BaCo_2V_2O_8$ grown by the floating-zone technique did hardly or not at all show such a signal in the thermal expansion. One has to argue whether this is due to sample quality, because the samples experience comparatively fast cooling rates during the

$Ba\,Co_{1.9}M_{0.1}V_2O_8$ $M =$	T_N (K)	$H_{crit}^{\parallel c}$ (T)	$H_{crit}^{\parallel a}$ (T)	$\frac{\partial T_N}{\partial H^{\parallel[110]}}$ (K/T)
Mn	5.8	3.1	12	0.1
Co	5.5	3.9	9.7	0.1
Ni	5.5	3.7	9.5	–
Cu	4.4	3.0	8.2	–
Mg	3.7	1.6	7.2	0.09

Table 6.3: Critical temperatures T_N in zero magnetic field and critical magnetic fields obtained by extrapolating $H_{crit}^{\parallel a,c}(T)$ to $T \to 0$. The average decrease of T_N for $H \parallel [110]$ was measured for $Ba\,Co_{1.9}Mn_{0.1}V_2O_8$ and $Ba\,Co_{1.9}Mg_{0.1}V_2O_8$.

growth process in an image furnace compared to the extremely slow nucleation processes for the other method. Another explanation could be that the occurrence of an incommensurate phase is extremely sensitive to the precise direction of the magnetic field.

The lower panels of Figure 6.21 depict the temperature *vs.* magnetic field phase diagrams for the in-plane field directions. The dashed green line marks the phase boundary of $Ba\,Co_2V_2O_8$ for $H \,||\, [1\,1\,0]$. The thermal expansion measurements of $Ba\,Co_{1.9}Mn_{0.1}V_2O_8$ and $Ba\,Co_{1.9}Mg_{0.1}V_2O_8$ (Fig. 6.20) for this field direction reveal a similar nearly linear decrease of T_N. The respective phase boundaries are marked by solid lines. For the field direction parallel to the a axis $Ba\,Co_{1.9}Mn_{0.1}V_2O_8$ also shows a much weaker decrease of T_N than the pure compound. Here, the estimated critical magnetic field $H_{crit}^{\parallel a}(T \to 0)$ is $\approx 12\,\mathrm{T}$.

Similar to the field direction along the chains, the substitution of Ni leaves the phase boundary almost unchanged. Only a slight decrease of $H_{crit}^{\parallel a}(T \to 0)$ is observed. The T *vs.* H phase boundaries of $Ba\,Co_{1.9}Cu_{0.1}V_2O_8$ and $Ba\,Co_{1.9}Mg_{0.1}V_2O_8$ roughly scale with the boundary of the pure $Ba\,Co_2V_2O_8$ by a factor of 1:1.2 and 1:1.4 both in T and H. Thus, substitution of manganese seems to weaken the in-plane anisotropy while the other in-chain substitutions do not influence the anisotropy at all. Concerning the changes in the zero-field Néel temperature, theoretical approaches yield a strong suppression of T_N for a quasi 1D system with non-magnetic impurities [26, 27, 136]. For a substitution level of 5 % the average distance of two impurity ions is 20 lattice sites. In the high-temperature regime, where no long range order is present, one can expect little changes in the magnetic susceptibility due to the fact that the correlation length $\xi(T)$ is anyway significantly shorter than this average distance. For lower temperatures the correlation length typically increases. A significant influence is expected for T_N, because the spin chains are cut into finite chain segments and thus the low-temperature increase of $\xi(T)$ is limited, if the intra-chain magnetic coupling via the substituted M ion is effectively blocked [26, 141]. The degree of (de-)coupling of the finite chain segments depends on the magnetic properties of the substituting ion M, which obviously influences the NN intra-chain exchange. In addition, the next nearest neighbor (NNN) intra-chain exchange may contribute and an effective coupling of the finite chain segments via the neighboring chains due to the finite inter-chain coupling might be important, too.

Due to the fact that the substitution of the non-magnetic Mg causes such a strong suppression of the Néel temperature in contrast to e.g. Ni it seems obvious that the NN intra-chain interaction is the dominant coupling mechanism of the finite chain

segments. The coupling via the $S = 1/2$ ion copper shows an intermediate suppression of T_N compared to the other substitutions. A reduction of the effective intra-chain exchange by partial replacement of the $S = 3/2$ Co^{2+} ions by the $S = 1/2$ Cu^{2+} ion is likely. This difference to the replacement by $S = 1$ or $5/2$ may be explained by the difference in the electron configuration within these ions. Co^{2+}, Ni^{2+}, and Mn^{2+} have half-filled e_g orbitals, whereas there is only a single hole in the e_g orbital of Cu^{2+} and, additionally, for such a small spin quantum number of $S = 1/2$, quantum fluctuations are considerably enhanced.

The topic of substitution is for sure not exhausted by the studies present in this chapter and could be extended to address open issues concerning, e.g., the different sign in thermal expansion for $BaCo_2V_2O_8$ and the substituted samples. Other possible substitutions or simply higher substitution level could be of interest. Since $BaNi_2V_2O_8$, for example, has rhombohedral structure substitution of larger amounts of Ni into $BaCo_2V_2O_8$ could lead to interesting structural peculiarities.

7 Summary

The aim of this thesis was the synthesis and characterization of a group of spin-chain compounds $Ba_{1-x}Sr_x(Co_{1-y}M_y)_2V_2O_8$ (M = Mn, Cu, Ni, Mg) and (Ba ,Sr)$Mn_2V_2O_8$ and the determination of the temperature *vs.* magnetic-field phase diagrams of the compounds for different field directions.

The tetragonal structure of these compounds consists of screw chains of edge-sharing MO_6 octahedra where M is a transition metal. The chains are separated by nonmagnetic Ba or Sr ions and by VO_4 tetrahedra. Depending on the M^{2+} transition metal, different spin values are realized. This thesis examined the large-spin ($S = 5/2$) compounds $AMn_2V_2O_8$ (A = Ba, Sr), the effective Ising $S = 1/2$ compounds $ACo_2V_2O_8$ (A = Ba, Sr) as well as intermediate substitutions between Ba and Sr, and, furthermore, $BaCo_{1.9}M_{0.1}V_2O_8$ compounds with partial substitution of Co by other transition metals. This report about the crystal growth and the comprehensive investigations on $BaCo_2V_2O_8$ concerning different types of substitution are the first of their kind for that compound.

Several diffraction techniques were brought to bear comprising X-ray techniques and single crystal neutron diffraction. The thermodynamic properties were obtained by means of the magnetization, thermal expansion/magnetostriction, and the heat capacity. In previous studies single crystals were grown by the spontaneous nucleation method as reported for $BaCo_2V_2O_8$, $SrCo_2V_2O_8$ and $BaMn_2V_2O_8$ [15, 17, 84, 85, 87, 88]. For the analysis of the anisotropic magnetism of these compounds and the full evaluation of the temperature *vs.* magnetic-field phase diagrams, however, large, oriented and specifically shaped single crystals are required. The crystals were grown via the floating-zone method in a mirror furnace under several optimizations, e.g. a very slow growth rate and employing the twice scanning method.

The first single crystal investigations of the two $S = 5/2$ Heisenberg spin chains $BaMn_2V_2O_8$ and $SrMn_2V_2O_8$ are reported here. Both compounds are nearly isotropic, one-dimensional spin chains as is represented by a broad maximum in the temperature dependent magnetization. The Néel temperatures of 37 K and 42 K for $BaMn_2V_2O_8$ and $SrMn_2V_2O_8$, respectively, are one order of a magnitude higher compared to the transition temperature of $BaCo_2V_2O_8$ ($T_N = 5.4$ K) and show a very weak positive field dependence $\frac{dT_N}{dH} > 0$ which is reflected in a very flat phase boundary in the temperature *vs.* magnetic field phase diagram. $BaMn_2V_2O_8$ shows a spin-flop transition in small magnetic fields of $\simeq 300$ mT applied perpendicular to the c axis as is observed in the temperature-dependent magnetization and the magnetostriction data. The presence of a spin-flop transition suggests a zero magnetic field spin structure

where the spins prefer to lie within the ab plane. Concerning $SrMn_2V_2O_8$, the respective critical field is lower than 300 mT, if a spin flop transition is present at all. Recently, the spin structure of $SrMn_2V_2O_8$ was resolved [100] and reveals a ferromagnetic alignment of the spins within the ab plane where the spins are oriented along a. Along c which is along the chains, the NN exchange is still antiferromagnetic, resulting in ferromagnetic planes that are ordered antiferromagnetically to each other along c. Due to the assumptions derived from the magnetization of $BaMn_2V_2O_8$ and the structural similarity to $SrMn_2V_2O_8$, a similar order pattern of the zero-field magnetic structure can most probably be transferred to $BaMn_2V_2O_8$.

Within the $AM_2V_2O_8$ compounds, $BaCo_2V_2O_8$ represents the quasi-one dimensional effective $S = 1/2$ Ising chain type. The Ising chains are running along c with the spin direction alternating along c due to the antiferromagnetic NN intra-chain exchange The inter-chain coupling, however, is frustrated leading to the presence of two magnetic domains. In zero-magnetic field the system undergoes a tetragonal to orthorhombic distortion when entering the Néel ordered phase at $T_N = 5.4$ K. This structural distortion is confirmed in zero-field pressure-dependent thermal-expansion measurements where the spontaneous strains can be switched by increasing uniaxial pressure. Via magnetoelastic coupling the structural domains of $BaCo_2V_2O_8$ couple to the two magnetic domains. The structural domains in the Néel ordered phase can, furthermore, be manipulated in magnetic fields applied parallel to one of the a axes. Thus, the domains can be oriented either by applying uniaxial pressure or magnetic fields along a, favoring the shorter/longer domains, respectively. Nevertheless, the expected distortion of the order of 10^{-5} could hardly be detected in high-resolution single crystal diffraction under difficult circumstances due to the mosaicity of the sample. However, the experiment gives evidence that the structural transition is accompanied by a slight shift in the scattering angle that is of different sign for reflections sensitive on a and b. These extremely small distortions could not be resolved in high resolution powder X-ray diffraction.

For magnetic fields applied along the magnetic easy c axis, the Néel ordered state breaks down at $H_c(T \to 0) = 3.9$ T where an incommensurate phase is entered in the low-temperature region [24, 110]. A hysteresis in the low-temperature magnetostriction of $BaCo_2V_2O_8$ gives evidence for a first-order transition from the Néel ordered into the incommensurate phase. Furthermore, the thermal expansion yields very broad anomalies in the low-temperature region of the high-field curves. The phase boundary between incommensurate and paramagnetic phase was traced up to a maximum magnetic field of 17 T showing a tendency of an increase of T_{IC} after a minimum around 8 T. In this field range theoretical predictions and experimental findings suppose the transition between two types of spin density waves [111]. However, this transition can not be resolved by the macroscopic data presented here.

For field directions perpendicular to the magnetic easy axis, an in-plane anisotropy was found. For $H \,||\, [1\,1\,0]$, $BaCo_2V_2O_8$ shows only a weak field dependence of T_N, whereas the magnetic order can be completely suppressed in magnetic fields $H \,||\, a$ of about 10 T. Former contradictory reports for the field direction $H \perp c$ (e.g. Refs. 103, 104) could, thus, be resolved. Motivated by the experimental findings presented here, Kimura et al. developed a model where an applied magnetic field $H \,||\, a$ is accompanied by a staggered transverse field component via a staggered g tensor and which predicts

Table 7.1: Critical temperatures T_N in zero magnetic field and critical magnetic fields obtained by extrapolating $H_{crit}^{\|a,c}(T)$ to $T \to 0$. Note that for $H\|c$ and $H\|a$ different phases are realized above the respective critical fields. The average decrease of T_N for $H\|[110]$ is given in the last line.

		$Ba_{1-x}Sr_xCo_2V_2O_8$					$BaCo_{1.9}M_{0.1}V_2O_8$			
	$x =$	0	0.1	0.5	0.9	1	$M =$ Mn	Ni	Cu	Mg
T_N(K)		5.5	5.5	5.5	4.9	4.5	5.8	5.5	4.4	3.7
$H_{crit}^{\|c}$(T)		3.9	3.9	3.9	3.7	3.5	3.1	3.7	3.0	1.6
$H_{crit}^{\|a}$(T)		9.7	8.7	8.0	6.4	5.3	(12)	(9)	8.2	7.2
$-\frac{\partial T_N}{\partial H}$(K/T)	$H\|[110]$	0.1	0.17	–	–	0.17	–	–	–	0.09

the breakdown of the magnetic order at $H \simeq 7\,\mathrm{T}$, whereas no such transverse component occurs for $H \,||\, [1\,1\,0]$ [96]. The breakdown of the magnetic order for $H \,||\, a$ is not only evidenced in magnetostriction measurements but also by the collapse of magnetic superstructure peaks in single-crystal neutron experiments. The field-induced detwinning of the structural/magnetic domains is clearly observed in the different field hysterses of magnetic Bragg peaks which are sensitive to the different magnetic domains [24]. Another effect, when applying the magnetic field perpendicular to the antiferromagnetically ordered spins, is the induction of a ferromagnetic component due to a gradual alignment of the spins along the field, which is observed in the increasing intensity of some nuclear reflections. However, due to the staggered g tensor, the field induces staggered field components perpendicular to the field direction which is consistent with the field-induced increasing intensity of otherwise forbidden reflections. Thus, the model of Kimura et al. is qualitatively confirmed. The quantitative evaluation of the induced moments is pending.

It has to be noted that for $H \,||\, a$ in different measures like the thermal conductivity, the temperature and field dependent heat capacity and in the magnetic reflections as a function of temperature additional anomalies are observed around 6 T. So far, the origin of these anomalies remains unresolved.

$BaCo_2V_2O_8$ was manipulated by different types of substitutions represented by the $Ba_{1-x}Sr_xCo_2V_2O_8$ series (out-of-chain substitution) and the $BaCo_{1.9}M_{0.1}V_2O_8$ series (in-chain substitution) where $M = \mathrm{Mn, Ni, Cu, Mg}$. All compounds have in common that an orthorhombic distortion is observed when entering the Néel ordered phase. Also the magnetic anisotropies, both the Ising anisotropy for $H \,||\, c$ and $H \perp c$ and the in-plane anisotropy for $H \,||\, a$ and $H \,||\, [1\,1\,0]$, are essentially preserved. Judging from these experimental results also the magnetic structure of $BaCo_2V_2O_8$ is essentially preserved for all substituted samples and especially for $SrCo_2V_2O_8$ where a different magnetic structure was proposed [25, 88, 89]. This was confirmed for $SrCo_2V_2O_8$ recently by neutron diffraction investigation of the magnetic structure [100]. Only indirect hints for a transition from the Néel ordered into an incommensurate phase for $H \,||\, c$ are given by hysteretic magnetostriction curves in the low-temperature regime. The thermal expansion did not show respective anomalies like they were observed in the pure $BaCo_2V_2O_8$.

The Sr substitution yields a slight decline of the Ising anisotropy but an increase of the in-plane anisotropy as can best be traced by the magnetic phase diagrams for all of the three relevant field directions (*cf.* Figure 6.13). These changes in the anisotropies can be understood by a systematic increase of distortion of the CoO_6 octahedra with increasing Sr content which results in an increasing tilt of the local quantization axis away from the z direction. This in turn might lead to a change in the staggered g tensor and increasing staggered transverse fields h_y, h_z. Due to the decreasing inter-chain distance with increasing Sr content a change of $J^{\perp}_{\mathrm{NN}}$ and $J^{\perp}_{\mathrm{NNN}}$ is suggested in a way that the resulting frustration increases, which in turn results in a weakened effective inter-chain interaction and the observed weakly decreasing T_{N} with increasing Sr content.

The substitution of e.g. Cu and Mg yields a drastic reduction of the ordering temperature. Due to the fact that the substitution of the non-magnetic Mg causes such a strong suppression of the Néel temperature in contrast to, e.g., Ni one may conclude that the NN intra-chain interaction is the dominant coupling mechanism of the finite chain segments. The coupling via the $S = 1/2$ ion copper shows an intermediate suppression of T_{N} compared to the other substitutions.

A subgroup of the $AM_2V_2O_8$ compounds was investigated in this work considering different aspects starting at the crystal growth and continued by structural and magnetic investigations. There is still work to be done for crystal growers as is reflected in the example of $PbCo_2V_2O_8$, which was first synthesized only a couple of year ago [90, 91], but still no reports about single crystal growth are available. Concerning the compounds investigated here, there are still open questions that were already enunciated above. Furthermore, other aspects could step into focus as there are, for example, practically no optical investigations known for $BaCo_2V_2O_8$.

Appendices

A Further Growth Processes

In this section growth processes of other systems that are not directly related to $BaCo_2V_2O_8$ or were not investigated further are described.

A.1 $Ba_{1-x}A_xCo_2V_2O_8$, A= Ca, K

$Ba_{0.9}Ca_{0.1}Co_2V_2O_8$ SN0119

Introduction

In case of $SrNi_2V_2O_8$, two kinds of substitutions on the strontium site, with the larger barium and the smaller calcium, have been performed with the aim to manipulate the spin liquid ground state [131]. In case of substitution with a larger cation the system was expected to stabilize the spin liquid ground state while substitution with a smaller cation should drive the system into an Ising-like Néel ordered state.

In case of$BaCo_2V_2O_8$ a larger cation for entering the Ba site is hard to find. A partial substitution of strontium was discussed before, therefore, it was of interest if the even smaller calcium can enter this site as well. Thus, a substitution of 10 % calcium into $BaCo_2V_2O_8$ was aspired.

Crystal Growth

A mixture of $BaCO_3$, $CaCO_3$ (Alfa Aesar, 99.95 %), $CoCO_3$ (Alfa Aesar, 99.5 %), and V_2O_5 according to Eq. (A.1) was prepared and put in a platinum crucible for the pre-reaction. The mixture was heated to a temperature of 950 °C for 5 hours. The

Figure A.1: Single crystals of $Ba_{0.9}K_{0.1}Co_2V_2O_8$, SN0127 and $Ba_{0.9}Ca_{0.1}Co_2V_2O_8$, SN0119. The complete potassium substitution (SN0125) did not yield a single phase crystal.

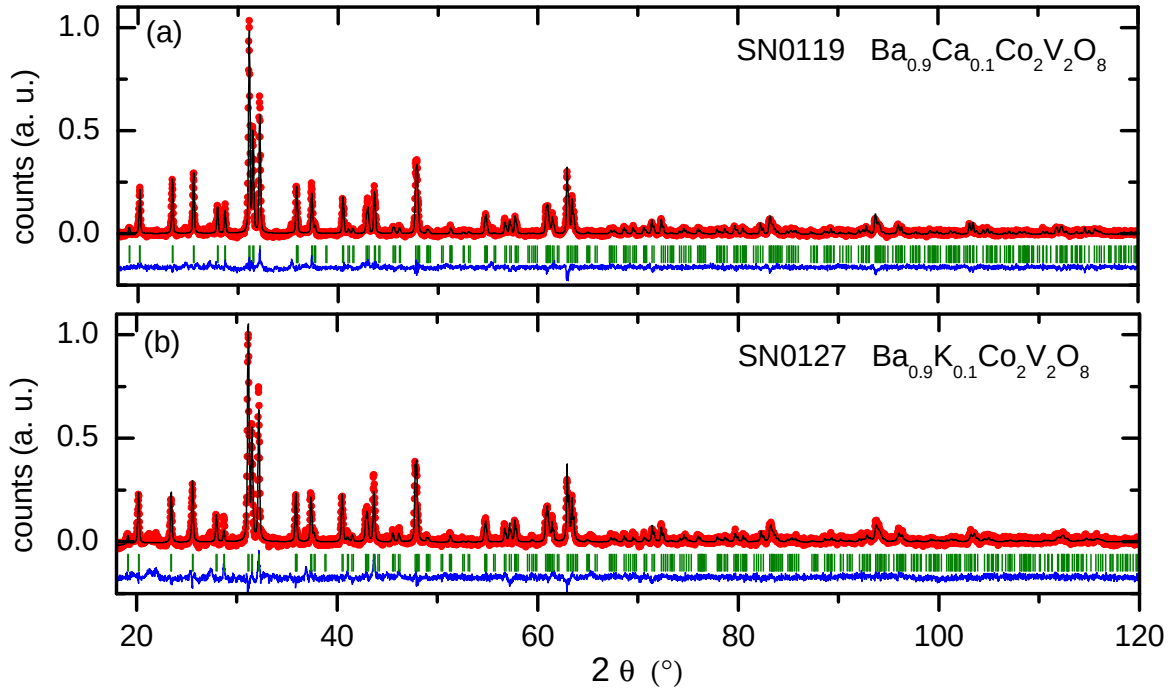

Figure A.2: X-ray powder patterns of (a) $Ba_{0.9}K_{0.1}Co_2V_2O_8$, SN0119 and (b) $Ba_{0.9}Ca_{0.1}Co_2V_2O_8$, SN0127 . Green bars are calculated reflection positions, measured data are red points, the black line is the fitted intensity, and the blue line gives the difference between measurements and fit.

resulting material was pressed into a rod and sintered at 550 °C for 8 hours.

$$0.9\,BaCO_3 + 0.1\,CaCO_3 + 2\,CoCO_3 + V_2O_5 \rightarrow Ba_{0.9}Ca_{0.1}Co_2V_2O_8 + 3\,CO_2\uparrow \quad \text{(A.1)}$$

The crystal growth by the floating-zone technique was performed in three runs, all of them with 300 W lamps and ambient air as atmosphere. The first run was carried out very fast in order to compress the material. The second run was done with a growth rate of about 1 mm/h to 1.5 mm/h and relatively high rotations. The third run was basically done under similar conditions but this time rotation rates were chosen more slowly (10 r/min and 6 r/min). The resulting crystal is shown on the right side of Fig. A.1 and is of some irregular shape due to an intermediate breakdown of the melt. Laue pictures confirmed the single crystallinity but cutting the crystal showed that there is some stress inside. Figure A.2 shows the X-ray powder pattern of SN0119 in panel (a). The tetragonal space group $I4_1/acd$ (no. 142) was used for fitting and gives unit cell parameters of $a = 12.4364(6)$ Å and $c = 8.4107(4)$ Å ($\chi^2 = 1.6$).

$Ba_{0.9}K_{0.1}Co_2V_2O_8$ SN0127

Introduction

Potassium is an alkali metal with a slightly larger atomic radius than barium (CN10: 1.59 Å; CN12: 1.64 Å[70]). The idea to dope the barium site with potassium was to

influence the valence of cobalt which is 2+ in $BaCo_2V_2O_8$. In contrast to the alkaline earth Ba^{2+} the valence of the alkaline metal potassium is only 1+. Partial or complete substitution of K on the Ba site should, therefore, produce a mixed cobalt valence of 2+/3+ depending on the level of substitution.

Crystal Growth

$$0.9 \cdot BaCO_3 + 0.1 \cdot KNO_3 + 2/3 \cdot Co_3O_4 + V_2O_5 \rightarrow$$
$$Ba_{0.9}K_{0.1}Co_2V_2O_8 + 0.9\ CO_2 \uparrow + 0.1\ NO_2 \uparrow + \frac{1}{3}\ O_2 \uparrow \quad \text{(A.2)}$$

A mixture of the educts $BaCO_3$, KNO_3 (Merck, $\geq$ 99 %), Co_3O_4 and V_2O_5 was mixed according to Eq. (A.2) and put in a platinum crucible to heat it to 700 °C for 10 hours which is not that high but was chosen to prevent an evaporation of the potassium. Assuming that the potassium did react with the other educts the sample was ground intermediately and heated to 800 °C for 12 hours. The pressed rod was shortly sintered at 700 °C and put in the mirror furnace (300 W lamps, air 1.5 bar) two times (2 mm/h first run, 0.5 mm/h second run). The resulting single crystal (see Fig. A.1, left) showed a smooth surface.

The X-ray powder pattern of SN0127 is shown in panel (b) of Figure A.2. The tetragonal space group $I4_1/acd$ was used for fitting and reveals unit cell parameters of $a = 12.4364(6)$ Å and $c = 8.4107(4)$ Å ($\chi^2 = 2.2$). The sample seems to have small impurities (extra peaks in the low-angle region) and according to EDX measurements (not shown) there was basically no potassium in the sample. Most probably the potassium evaporated during crystal growth.

Figure A.3 shows measurements of the specific heat of $Ba_{0.9}K_{0.1}Co_2V_2O_8$ in zero magnetic field an for different magnetic field $H \,||\, a$ (see inset) and the derived phase diagram, panel (c).

$KCo_2V_2O_8$ SN0125

Crystal Growth

The precursor for $KCo_2V_2O_8$ was mixed according to Eq. (A.3), carefully ground and put in a platinum crucible for the pre-reaction.

$$3\ KNO_3 + 2\ Co_3O_4 + 3\ V_2O_5 \longrightarrow 3\ KCo_2V_2O_8 + 3\ NO \uparrow + O_2 \uparrow \quad \text{(A.3)}$$

The mixture was heated to 500 °C for 60 hours with intermediate grinding. The resulting material was pressed into a rod and directly prepared for crystal growth in the mirror furnace (300 W lamps, air, ambient pressure). The lamp power could be kept at about 20 % which is only half the value that was necessary for the growth of, e.g., $BaCo_2V_2O_8$. The growth velocity was chosen very slow with 2 mm/h but the melt was very unstable which could be improved by a very high growth velocity of 27 mm/h. However, the crystal growth was not stable at all and the resulting crystal, shown in Fig. A.1, shows a very irregular shape and different areas of red and

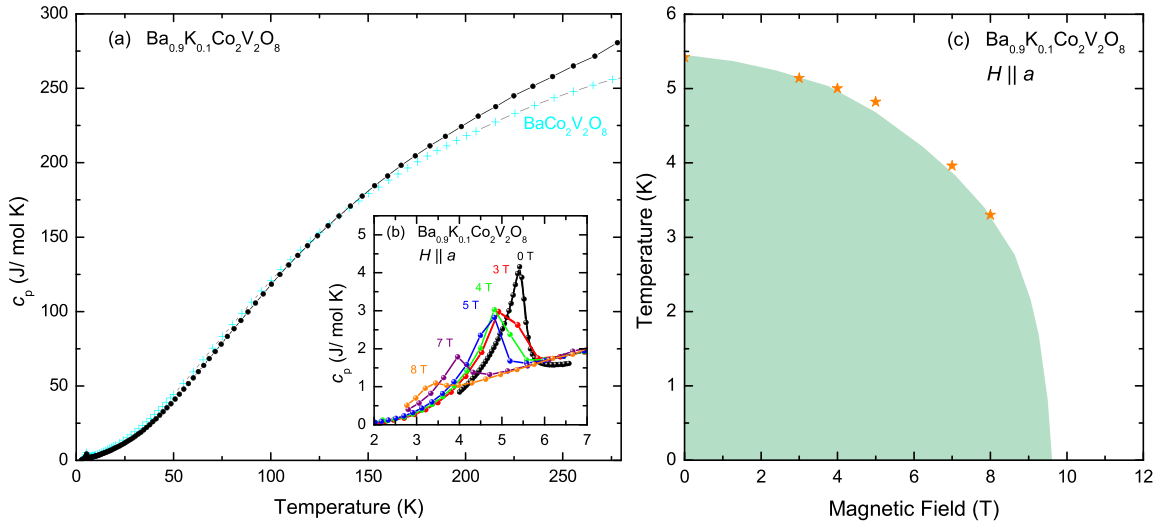

Figure A.3: Specific heat of $Ba_{0.9}K_{0.1}Co_2V_2O_8$ (a) in zero-magnetic field for temperatures up to 280 K. The data show an anomaly at 5.5 K. The inset (b) shows the specific heat for different magnetic fields $H \,||\, a$. Panel (c) depicts the temperature versus magnetic-field phase diagram of $Ba_{0.9}K_{0.1}Co_2V_2O_8$ for $H \,||\, a$ derived from specific heat measurements. The shaded area marks the Néel ordered phase of $BaCo_2V_2O_8$ as reference.

Figure A.4: Ternary diagram of the constituents BaO, CoO and V_2O_5. The diagram gives information about percentage compositions of three constituents.

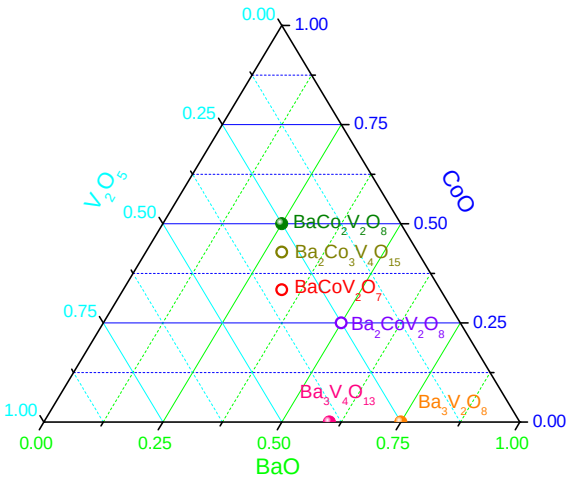

gray color. Part of the red crystalline areas were investigated by single crystal X-ray diffraction (APEX) by M. Valldor who suggested a possible composition of $Ba_3V_5O_{14}$ which was tried out to grow purposely in collaboration with him (see below).

A.2 Other Vanadates

The ternary diagram in Figure A.4 shows the percental composition for the three constituents BaO, Co and VO_5. The diagram has to be read such that one has to follow the colored bars on which the data points are lying to the according scale. $BaCo_2V_2O_8$, for example, lies on the cross section of 25 % BaO (green), 50 % CoO (blue), and 25 % V_2O_5 (cyan) leading to a proportion of 1:2:1 for BaO:CoO:V_2O_5.

Figure A.5: Microscopic picture of SN246 (left panel) grown from melt and sample SN0087 grown in the mirror furnace (right panel).

The compositions given in the diagram are only partly existing yet, therefore, existing compounds are marked with closed balls, non-existing compositions are marked with open circles . $BaCo_2V_2O_8$ (green) is well known and investigated, see Chapter 5. $Ba_2Co_3V_4O_{15}$ (dark yellow) was one project of N. Amuneke of Prof. A. Möllers work group at the University of Houston. To the best of my knowledge, this compound could not be synthesized so far. $BaCoV_2O_7$ (red) and in analogy $SrMnV_2O_7$, are unknown compounds. The synthesis attempts are described below. $Ba_2CoV_2O_8$ (purple) is also an unknown compound that was part of my Diploma project [92]. Compositions of only BaO and VO_5 are existing in larger variety, only two of them are marked in the diagram. $Ba_3V_2O_8$ (orange) is known since 1970 and in the focus of present research [142, 143]. $Ba_3V_4O_{14}$ (pink) is an unknown compound and was tried to be synthesized which will be described below.

$BaCoV_2O_7$

SN246

The first attempt to grow $BaCoV_2O_7$ was carried out in Houston. The educts were mixed according to Eq. (A.4) and put in a corundium crucible.

$$Ba(OH)_2 \cdot 8\ H_2O + CoCO_3 \cdot H_2O + V_2O_5 \rightarrow BaCoV_2O_7 + CO_2 \uparrow + 10\ H_2O \uparrow \quad \text{(A.4)}$$

The mixture was heated to 600 °C in a box furnace (without automatic ramping) and was kept there for about 2 days. After one-hour heating at 700 °C the sample was cooled down. The result from this melt is shown in the left panel of Fig. A.5 which is a picture taken under the microscope. The dark-gray material shows no clear shapes and looks like it was cooled down too fast which might be due to the fact that the cooling process had to be regulated manually.

Further experiments of growing the material in a melt of $LiVO_3$ with different amounts of the flux material were performed via Differential Scanning Calorimetry (DSC). With this thermoanalytical technique the different amounts of needed heat for increasing the temperature in a sample and a reference system is measured as a function of temperature. With this technique it is possible to detect phase transitions because, e.g., a phase transition will consume or free energy during the transition (endothermic or exothermic processes) compared to the reference. The DSC measurements are presented for pure $BaCoV_2O_7$ (Fig. A.6) and proportions of $BaCoV_2O_7$ to $LiVO_3$ of 4:1 (Fig. A.7), 1:1 (Fig. A.8) and 1:4 (Fig. A.9).

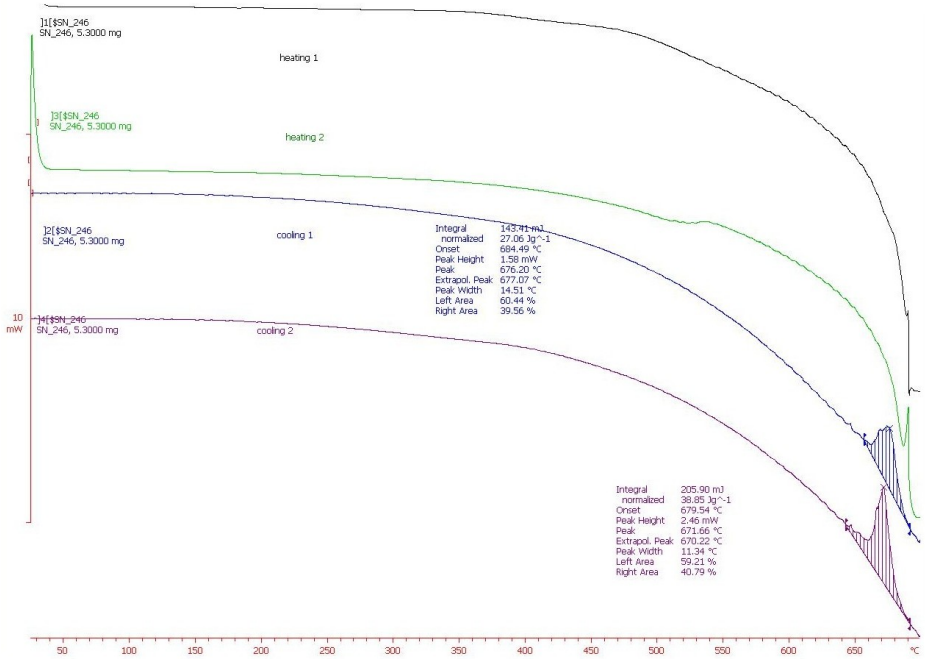

Figure A.6: DSC measurement of $BaCoV_2O_7$.

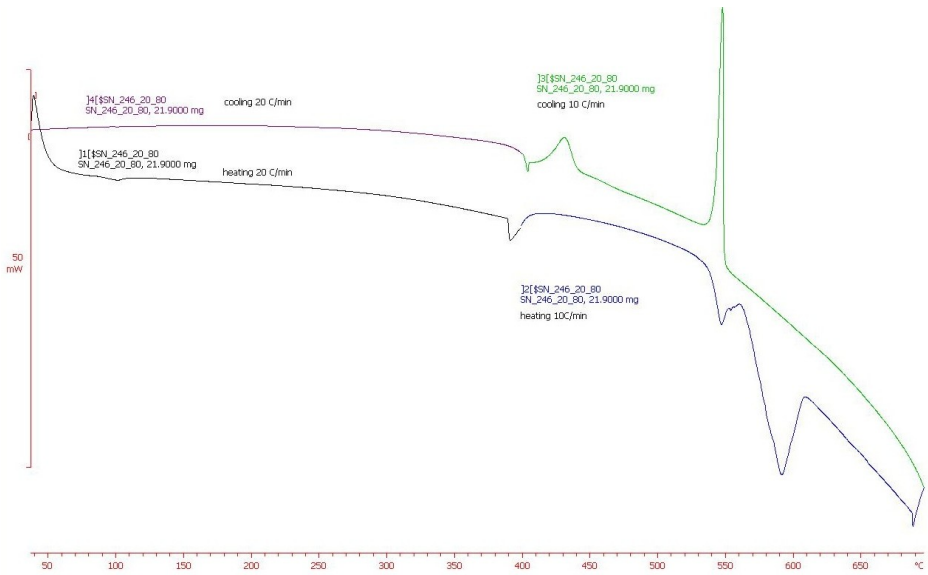

Figure A.7: DSC measurement for $BaCoV_2O_7$:$LiVO_3$ is 4:1.

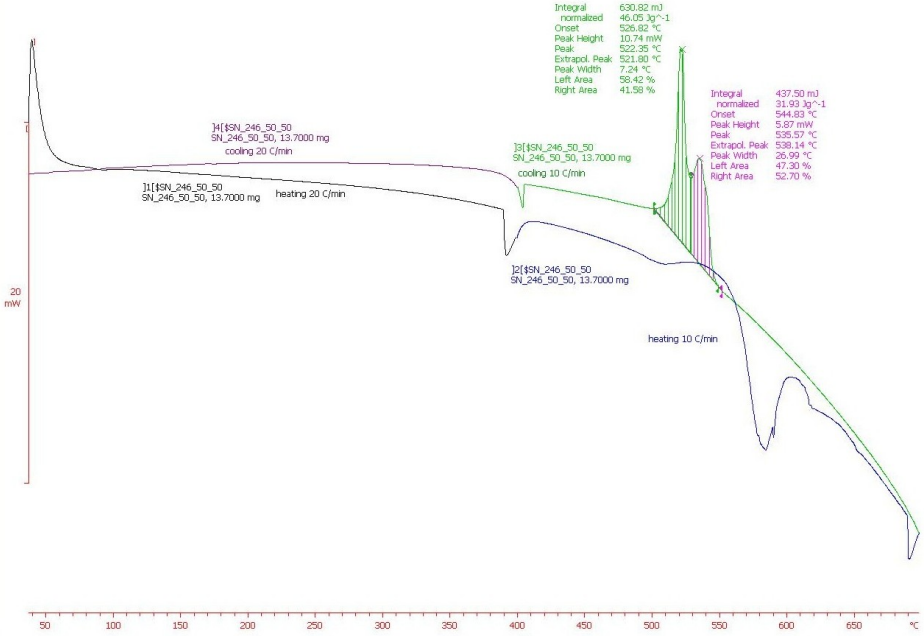

Figure A.8: DSC measurement for $BaCoV_2O_7$:$LiVO_3$ is 1:1.

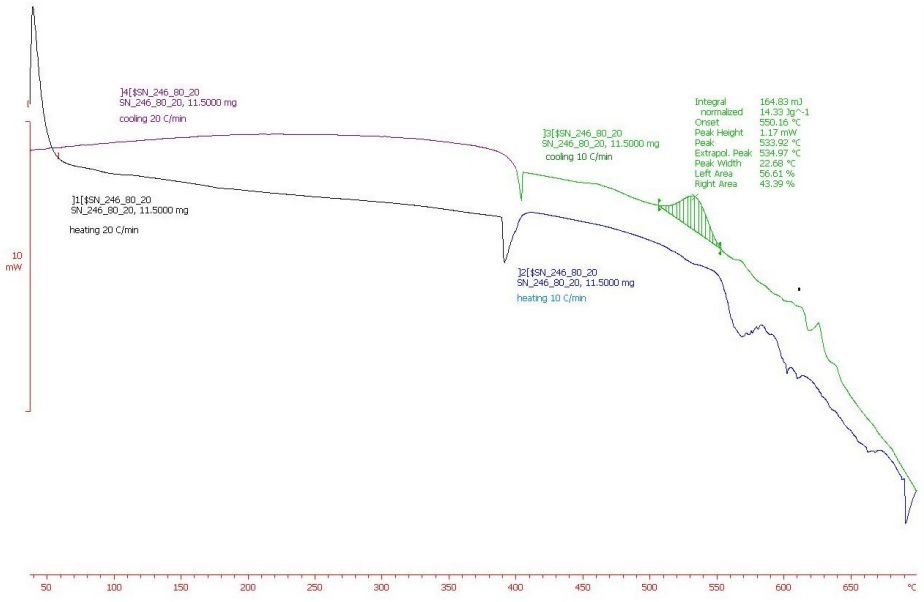

Figure A.9: DSC measurement for $BaCoV_2O_7$:$LiVO_3$ is 1:4.

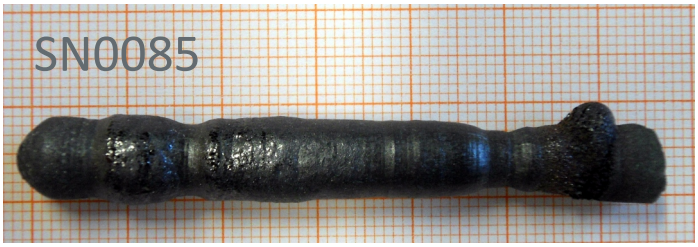

Figure A.10: Sample SN0085 of $SrMnV_2O_7$. The sample is no pure single crystal and contains yellow impurities.

SN0083

A precursor of $BaCO_3$, Co_3O_4 and V_2O_5 was mixed in the ratio 3:1:3 according to Eq. (A.5).

$$3\ BaCO_3 + Co_3O_4 + 3\ V_2O_5 \rightarrow BaCoV_2O_7 + 3\ CO_2 \uparrow + 1/2\ O_2 \uparrow \qquad (A.5)$$

The mixture was put in a platinum crucible and heated to 700 °C for 48 hours with intermediate grinding. After the pre-reaction the product was silvery and was molten. A powder X-ray diffraction was performed before the material was pressed into a rod and sintered at 600 °C for 5 hours. The crystal growth in the mirror-furnace (300 W lamps) was done in Ar atmosphere with relatively high rotation (20-23 r/min) and a growth velocity of 4 mm/h in the beginning which was soon enhanced to 10 mm/h. The resulting crystal is shown in the right panel of Fig. A.5 and shows a green color but with an undulated surface.

$SrMnV_2O_7$

The reaction of $SrMnV_2O_7$ (SN0085) was done in two steps. As a pre-reaction SrV_2O_6 was synthesized according to Eq. (A.6) (SN0059). Subsequently, SrV_2O_6 was mixed with MnO in the ratio 1:1 according to Eq. (A.6) and directly prepared for the mirror furnace.

$$SrCO_3 + V_2O_5 \longrightarrow SrV_2O_6 + CO_2 \uparrow\ SrV_2O_6 + MnO \longrightarrow SrMnV_2O_7 \qquad (A.6)$$

The crystal growth in the mirror furnace (300 W lamps) performed under ambient pressure in an Ar atmosphere with a growth velocity of 7 mm/h to 10 mm/h. The resulting sample is shown in Fig. A.10 but the sample was not a single phase and showed yellow grains within a dark gray main part.

$Ba_3V_5O_{14}$

The analysis of the failed reaction of $KCo_2V_2O_8$ (SN0125) suggested an impurity with the composition $Ba_3V_5O_{14}$. As far as one can tell from literature research (e.g. in ICSD) $Ba_3V_5O_{14}$ would be a new compound. The reaction for $Ba_3V_5O_{14}$ (SN0129) took place in two steps.

$$3\ BaCO_3 + 2.2\ V_2O_5 \rightarrow Ba_3V_2O_8 \qquad (A.7)$$

$$Ba_3V_2O_8 + 3\ VO_2 \rightarrow Ba_3V_5O_14 \qquad (A.8)$$

As a precursor $BaCO_3$ and V_2O_5 were mixed according to Eq. (A.8) to react into $Ba_3V_2O_8$. The mixture was put in a platinum crucible and heated to 600 °C for 48 hours. In the second step (Eq. (A.8)) the resulting composition was mixed with VO_2. The mixture was pressed into a rod and directly prepared for the crystal growth in the four-mirror furnace (300 W lamps, ambient pressure, Ar). The crystal growth was carried out by M. Valldor and did not yield a crystal of homogeneous composition.

$LiCuVO_4$

Introduction

$LiCuVO_4$ crystallizes in the orthorhombic space group (Imma, No. 74) and realizes a distorted inverse spinel type. Jahn Teller effects are very prominent in this system and lead to Cu^{2+} chains that are running along the b axis. Literature is consistent in the description as a quasi-one-dimensional spin-1/2 chain but the nature of the dominant magnetic character seems to be still under discussion [144]. $LiCuVO_4$ is a Mott-Hubbard insulator that shows helical spin order and multiferroic properties (e.g. Ref. 145). Another related system that has drawn attention is $AgCuVO_4$ which is also a quasi-one dimensional $S = 1/2$ chain [146].

The aim of my abode of two months in the chemical department of the University of Houston in the work group of Prof. Dr. A. Möller, was the growth of larger single crystals of $LiCuVO_4$ by the top-seed method. Unfortunately, the special furnace was not available during that period. Therefore, crystals were grown in a solution of $LiCuVO_4$ in a $LiVO_3$ melt, in analogy to e.g. Refs. 147, 148.

Crystal growth

Former attempts of the crystal growth were always carried out using only small amounts of the chemicals. For the process described below, a larger amount of about 12 g of the mixture was prepared. Lithium carbonate, copper oxide and vanadium(V) oxide were mixed in the molar ratio 1:2:1 (see Eq. (A.9)), carefully ground and put in a corundum crucible. The mixture was heated to 600 °C within 6 hours and during the similar period heated to 660 °C where it was kept for 1 hour. Afterward it was cooled down to 600 °C where it stayed for 30 hours.

$$Li_2CO_3 + 2\ CuO + V_2O_5 \rightarrow 2\ LiCuVO_4 + CO_2 \uparrow \tag{A.9}$$

Afterwards, the product was carefully ground and mixed with $LiVO_3$ (SN0079) in the ratio 40 mol% : 60 mol%. The mixture was put into a corundum crucible and covered with a lit. The following heat circle contained heating to 675 °C and a very slow cooling rate of only 0.9 °C/hour down to 580 °C so that in summary the sample was in the furnace for about 130 hours. The lit was stuck on the crucible when removing the setup from the box furnace. A bunch of crystals of the size of about 2 mm were found within the flux. They were removed from the crucible by solving the flux in hot water and putting it into the ultrasonic device. The crystals were removed by washing them

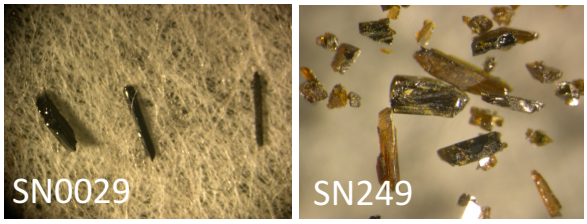

Figure A.11: Samples of $LiCuVO_4$ grown in solution in a LiVO3 melt are of the size of about 2 mm.

out through a filter paper. Some of the resulting crystals are shown in Fig. A.11 which have specific habit of their shape. Laue check of exemplary crystals showed that the largest plane usually is perpendicular to the [0 0 1] direction. Additionally, the fragile crystals can be cleaved easily along that plane which makes the crystals split very easily [147]. An arrangement of the sample with a large area perpendicular to (1 0 0) for optical and dielectric spectroscopy was of great interest [149], which could not be realized because the crystals always broke.

A.3 $(Dy_{1-x}Ho_x)_2Ti_2O_7$

Introduction

$Dy_2Ti_2O_7$ and $Ho_2Ti_2O_7$ are both so called spin-ice compounds. The Dy/Ho ions form a pyrochlore sublattice of corner-sharing tetrahedra with the spin moments lying on local easy axes pointing in or out of the tetrahedron. The magnetic ions interact via competing nearest neighbor exchange and long range dipole-dipole interactions leading to a highly frustrated situation [53]. The field-dependent magnetization of a spin-ice shows plateaus. The position of those plateaus depends, amongst others, on the magnetic moment and the relative size of the interactions present in the spin-ice compound. Comparing the field-dependent magnetization curves of $Dy_2Ti_2O_7$ and $Ho_2Ti_2O_7$ they can be matched almost perfectly by rescaling the magnetic field axis by a factor of 1.5. This can be understood by an enhanced effective coupling constant in holmium titanate. The following models have been derived by O. Breunig. In a naive microscopic model, this can be treated by a site-dependent coupling constant J_{ij} between the spins $\vec{S}_i$ and $\vec{S}_j$. For a partial substitution of Dy by Ho, one could define $J_{ij} = \sqrt{1.5}J$ for i or j Ho. In case of full substitution this would, thus, result in $J_{\text{eff}} = 1.5J$. Modeling single tetrahedra (partially occupied by 1,2,3 and 4 Ho replacing Dy) with this site-selective exchange gives magnetization curves that range from the Kagome-plateau ending at 1 T up to magnetization curves with a saturation field of 1.5 T (as in holmium titante). By a simple weighted average of these curves a multi-plateau magnetization arises. However, this approach neglects the long-ranged dipolar interactions. In fact, a Monte Carlo-like simulation performed on a lattice of 3000 ions does not show multiple plateaus. Thus, one might conclude that the simple assumption of a site selective coupling constant $J_{i,j}$ is oversimplified and the physics is mainly governed by the long-range dipolar interactions. Due to these theoretical considerations two samples were grown where 10 % and 50 % of the Dy ions were replace by Ho.

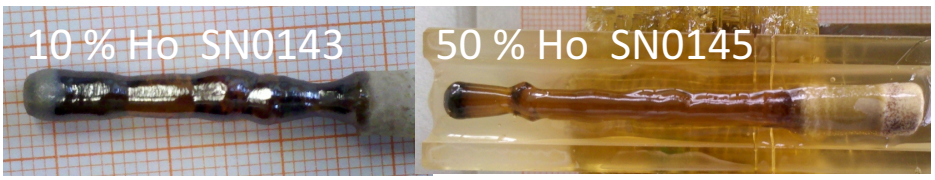

Figure A.12: Single crystals of $(Dy_{0.9}Ho_{0.1})_2Ti_2O_7$ (SN0143) and $(Dy_{0.5}Ho_{0.5})_2Ti_2O_7$ (SN0145). SN0145 is glued on a sample holder for cutting in an annular saw.

Crystal Growth

SN0143

The precursor was prepared according to Eq. (A.10) with $x = 0.1$, carefully ground and put into a platinum crucible. The pre-reactions took place in a box furnace where the mixture was heated to 1300 °C for 70 hours with intermediate grinding. After grinding and compressing in rod-shape, the sample was sintered in a Pt ship at 1300 °C for 5 hours.

$$(1-x)\ Dy_2O_3 + x\ Ho_2O_3 + 2\ TiO_2 \rightarrow (Dy_{1-x}Ho_x)_2Ti_2O_7 \qquad (A.10)$$

The sample was grown twice in the four-mirror-furnace with 1000 W lamps in an oxygen atmosphere and under pressure of 1.5 bar to 3 bar. The growth was very difficult due to technical problems with the furnace (e.g. a bad focus) and a strong compactification of the material after melting. The sample was grown a third time in the two-mirror furnace (1000 W lamps, 3 bar O 2) with counter rotating rods (20 and 12 r/min) and a growth velocity of about 5 mm/h. The resulting crystal is shown in the left panel of Fig. A.12 and was tempered in oxygen for about 3 days. The resulting lattice parameter is $a = 10.118\,18(16)$ Å as obtained by a LeBail Fit using Jana 2000.

SN0145

The precursor was prepared according to Eq. (A.10) with $x = 0.5$ and heated to 1300 °C in a Pt crucible for 48 hours with intermediate grinding. The pressed rod was sintered 1350 °C for 10 hours.

The sample was grown in the two-mirror furnace with 1000 W lamps under 3 bar O_2 atmosphere in two steps. In the first run the rod was molten with a volt level of about 62 V to 63 V and a growth velocity of 20 mm/h to 25 mm/h. The diameter of the bar was reduced from 6 mm to 3 mm which shows that the material undergoes a large compactification. In the next run the same atmosphere was chosen but this time the growth rate was much slower with 8 mm/h for the lower rod and 10 mm/h for the seed rod to produce a slightly larger diameter of the resulting sample. The resulting crystal is shown in the right panel of Fig. A.12. The sample was tempered in an oxygen atmosphere for 48 hours. The resulting lattice parameter is $a = 10.115\,29(7)$ Å obtained by a LeBail fit using JANA 2000 [1]. The magnetization $M(B)$ is shown in Figure A.14 for temperatures $0.28\,K \leq T \leq 3\,K$. Solid (dashed) lines represent

[1] Both data refinements were carried out by J. Engelmayer

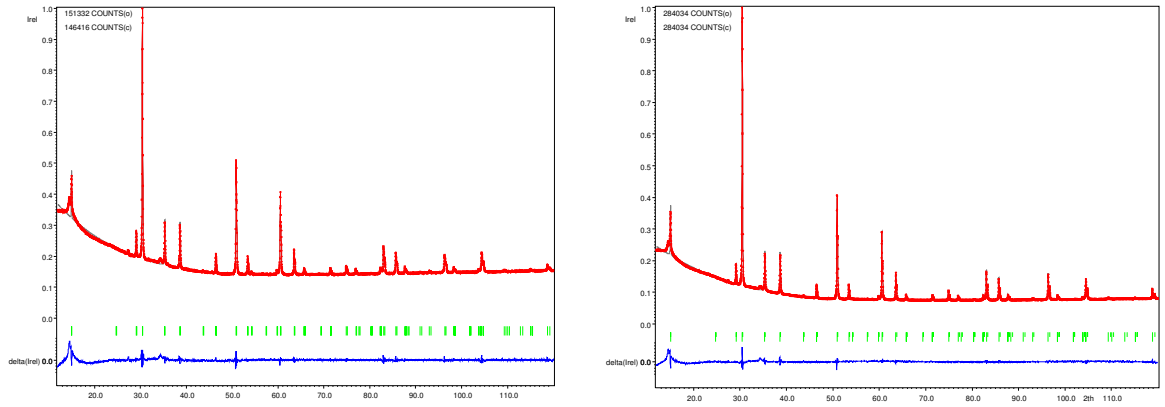

Figure A.13: X-ray powder diffraction pattern of SN0134 (left) and SN0145 (right).

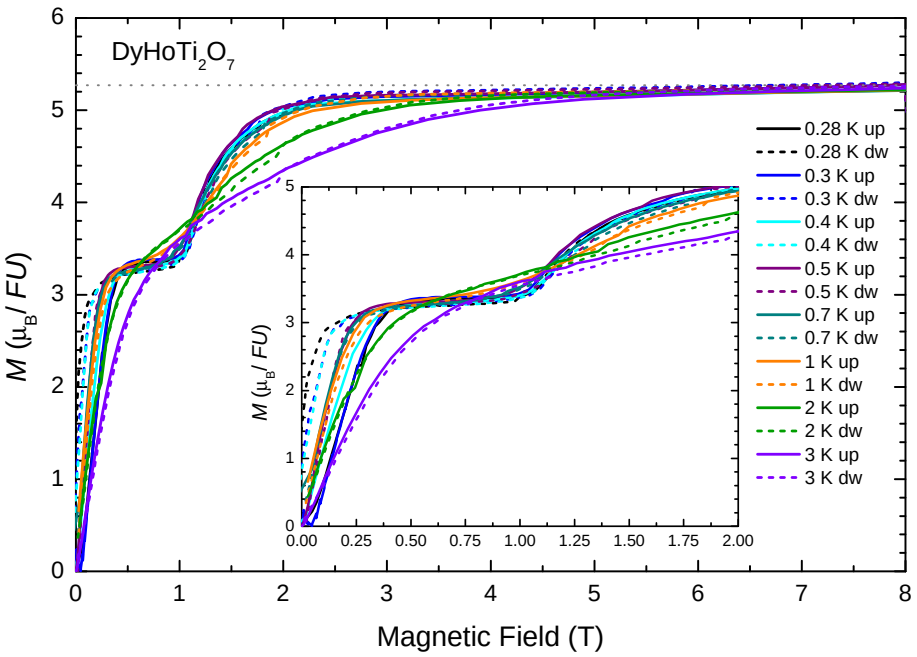

Figure A.14: Magnetization of $DyHoTi_2O_7$ for different temperatures $0.28\,\mathrm{K} \leq T \leq 3\,\mathrm{K}$. Solid and dashed lines represent data measured with increasing or decreasing magnetic field, respectively. The gray horizontal line marks the saturation value at maximum field.

measurements with increasing (decreasing) magnetic field. The data were obtained by S. Scharffe, *cf.* Ref. 33.

Figure A.15: Samples of $La_{1-x}Sr_xCoO_3$ with $X = 0.005$ (SN0067), $X = 0.007$ (SN0069), $X = 0.002$ (SN0071), and $X = 0.004$ (SN0073).

A.4 $La_{1-x}Sr_xCoO_3$

Introduction

Partial substitution of $LaCoO_3$ by Sr represents a hetero-valent doping of the system. In consequence, the valence of the Co ions is affected resulting in a mixed valence of +3 and +4 inducing magnetism into the system. This mixed valence leads to a variety of phenomena (e.g. orbital order) and spin-state transitions, see, e.g., Ref. 150.

Crystal Growth

Crystal of the $La_{1-x}Sr_xCoO_3$ series with $0.002 \leq x \leq 0.007$ grown in the four-mirror furnace in analogy to single crystal growth in Ref. 151.

All samples were mixed according to Eq. (A.11):

$$(1-x)\cdot 1/2\, La_2O_3 + 1/3\, Co_3O_4 + x\, SrCO_3 \xrightarrow{O2} La_{1-x}Sr_xCoO_3 + xCO\uparrow + (1/2x - 1/6)O\uparrow \quad \text{(A.11)}$$

The La_2O_3 (Alfa Aesar, 99.99 %) was dried in a platinum crucible at 800 °C for 50 hours. After mixing the educts, the powder was heated for $\simeq$ 80 hours at 1200 K with intermediate grinding and pressing into a rod. The crystal growth in the mirror furnace (1000 W lamps) was carried out in oxygen atmosphere with 5 bar pressure. The rotation was kept between 15-20 r/min and the growth velocity was kept at $\simeq$ 5 mm/h. The samples are growing nicely and the resulting crystals of $La_{1-x}Sr_xCoO_3$ with $x = 0.005$ (SN0067), $x = 0.007$ (SN0069), $x = 0.002$ (SN0071), and $x = 0.004$ (SN0073), shown in Fig. A.15, have a smooth and shiny surface. The difficulties in this crystals growth lie in oxygen defects which easily occur. This is the reason for using a high oxygen pressure during the growth process in the mirror furnace. The oxygen defects as well as the explicit substitution level have a large impact on the magnetic behavior. Measurements of the magnetization, shown in Fig. A.16, of these samples have been carried out by D. Löwen. The thermo power of all samples was measured by G. Kolland but are not shown here.

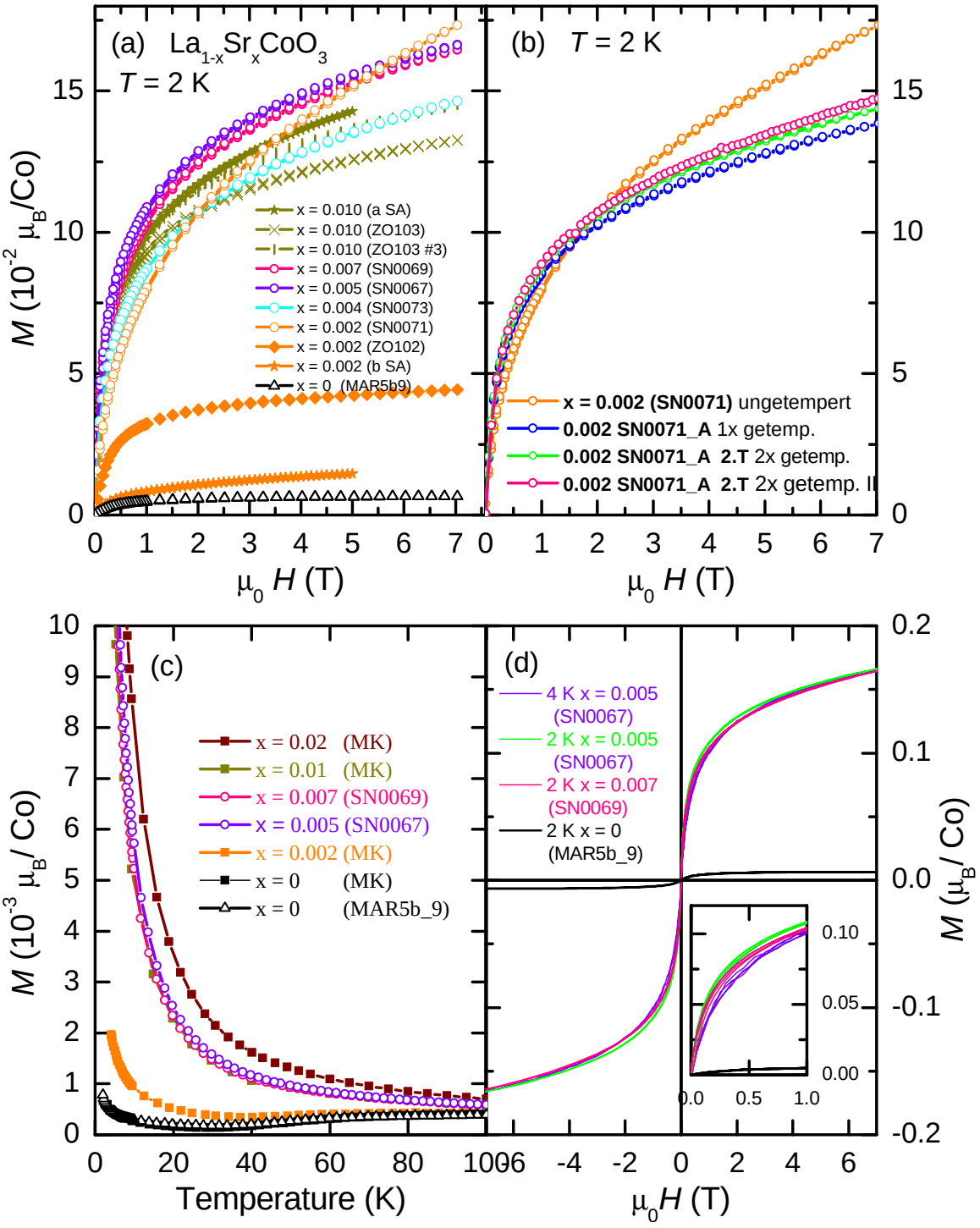

Figure A.16: (a) Magnetization at $T = 2\,\mathrm{K}$ compared for $La_{1-x}Sr_xCoO_3$ with different $0 \leq x \leq 0.1$. Same colors represent the same x. Different symbols represent samples grown by different persons. (b) Magnetization of SN0071 ($x = 0.002$) after crystal growth and subsequent tempering. (c) Temperature dependent magnetization of several samples. (d) Magnetization loops of different samples. The inset shows an enlargement of the positive low-field region.

B Measurements

Table B.1: Single crystal data from X-ray diffraction. U_{iso} and U_{ij} are given in (10^{-3} Å^2) with standard deviations in parentheses.

Atom, Wyck.	**Coordinates** (x, y, z)	**Occupancy, U**$_{iso}$	**U**$_{11}$, **U**$_{22}$, **U**$_{33}$, **U**$_{12}$, **U**$_{13}$, **U**$_{23}$
Sr, *8a*	0, 0, 0	1.0, 14.8(1)	15.0(2), 13.6(2), 15.6(2), 3.6(2), 0, 0
V, *16b*	0.26406(4), 0.07899(4), 0.0779(1)	1.0, 6.68(10)	7.4(2), 5.5(2), 7.1(2), 0.2(2), -0.5(2), -0.2(2)
Mn, *16b*	0.33080(4), 0.33215(4), 0.21024(9)	1.0, 8.4(1)	9.1(2), 8.8(2), 7.3(2), -1.0(2), -0.6(2), 0.8(2)
O1, *16b*	0.1408(2), 0.4981(2), -0.0080(3)	1.0, 12.5(6)	12(1), 8.5(9), 17(1), -0.9(8), -1.9(9), -0.9(8)
O2, *16b*	0.1533(2), 0.6869(2), 0.7009(3)	1.0, 12.0(6)	12(1), 16(1), 8.1(8), 4.2(9), 0.7(8), -2.0(8)
O3, *16b*	0.3239(2), 0.4995(2), 0.1710(3)	1.0, 12.9(6)	14(1), 10.2(9), 15(1), 1.8(8), -3.6(8), 2.2(8)
O4,*16b*	0.3328(2), 0.1560(2), 0.2124(3)	1.0, 11.1(6)	14(1), 10(1), 9(1), -2.1(8), -0.9(7), -0.7(7)

Space group: $I4_1cd$ (No.110), $a = 12.4422(9)$ Å, $c = 8.6833(6)$ Å, cell volume= 1350.697 Å^3, $Z = 8$, R(obs)= 0.0268, R_W(obs)= 0.0666, R(all)= 0.0305, R_W(all)= 0.0677, S(obs)= 1.20, S(all)= 1.15

Unit cell parameters were adapted from the powder X-ray diffraction experiment.

CSD No. 421422 (Data obtainable from FIZ, Karlsruhe, Abt. PROKA, 76344 Eggenstein-Leopoldshafen, Germany.)

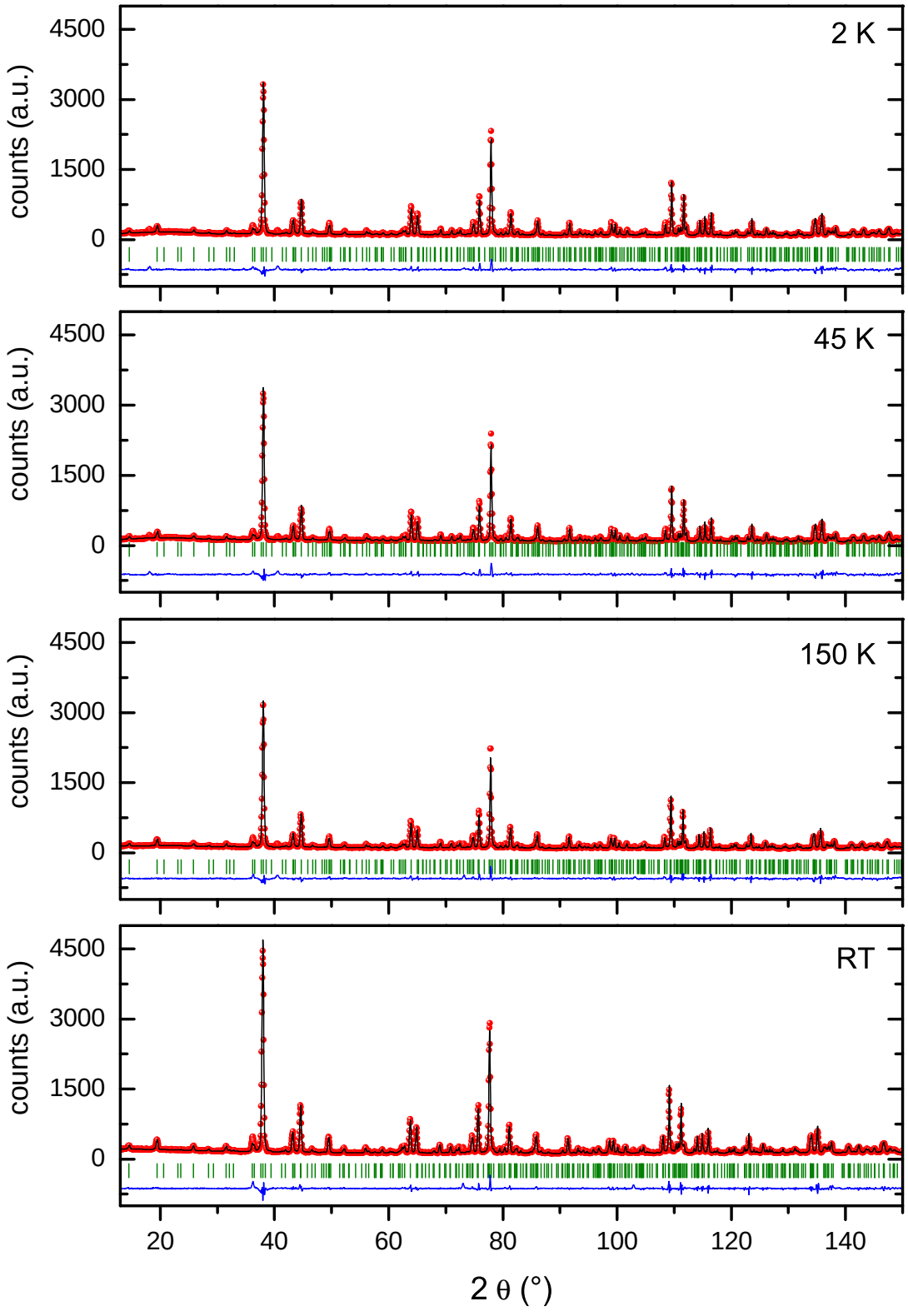

Figure B.1: Refined neutron powder diffraction pattern of $BaMn_2V_2O_8$. Green bars are calculated Bragg positions, measured data are red points, black line is the fitted intensity, and the blue line gives the difference between measurements and fit.

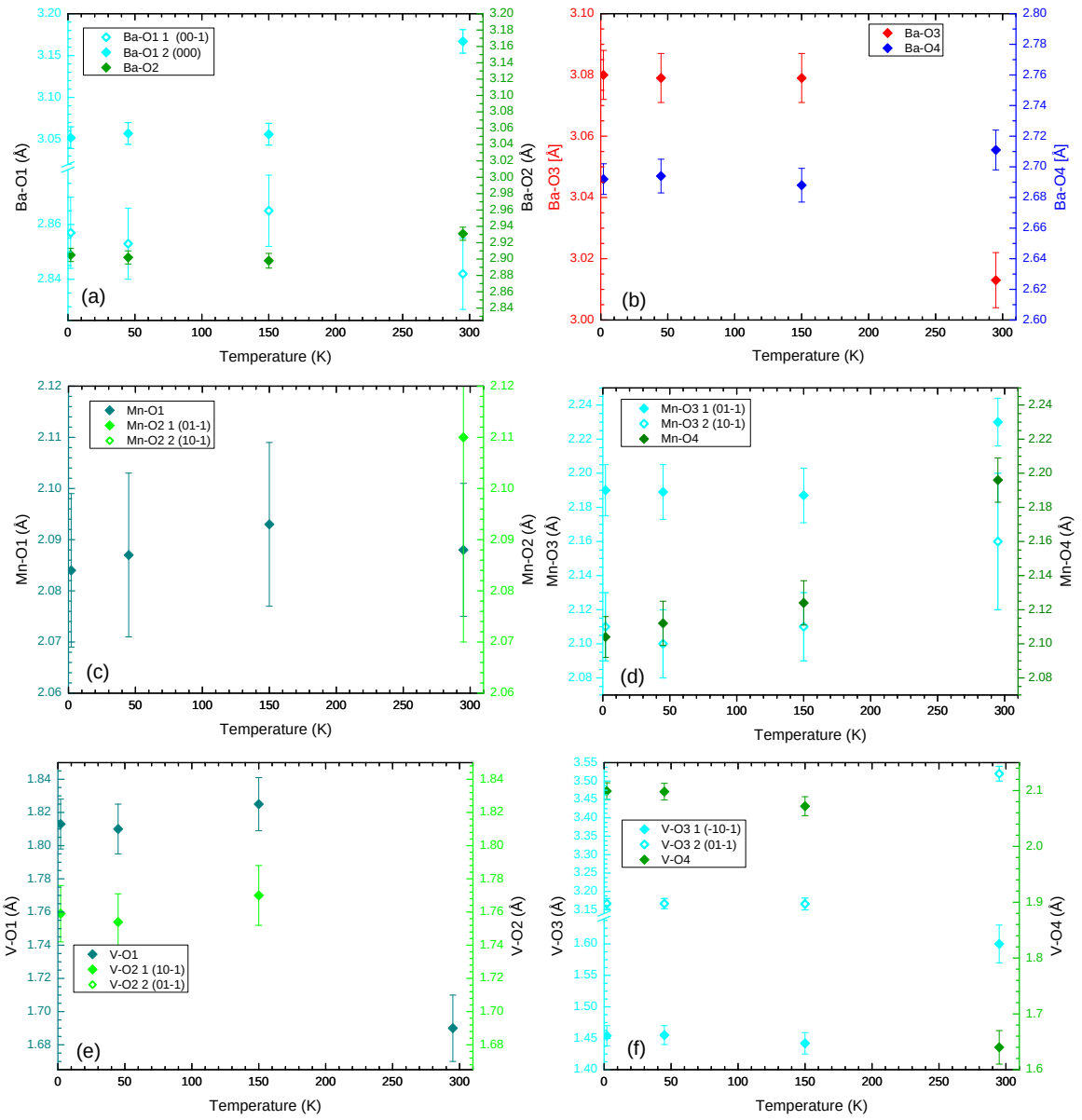

Figure B.2: Ba–O (a)-(b), Mn–O 8c)-(d) and V–O (e)-(f) bond lengths within $BaMn_2V_2O_8$ as a function of temperature.

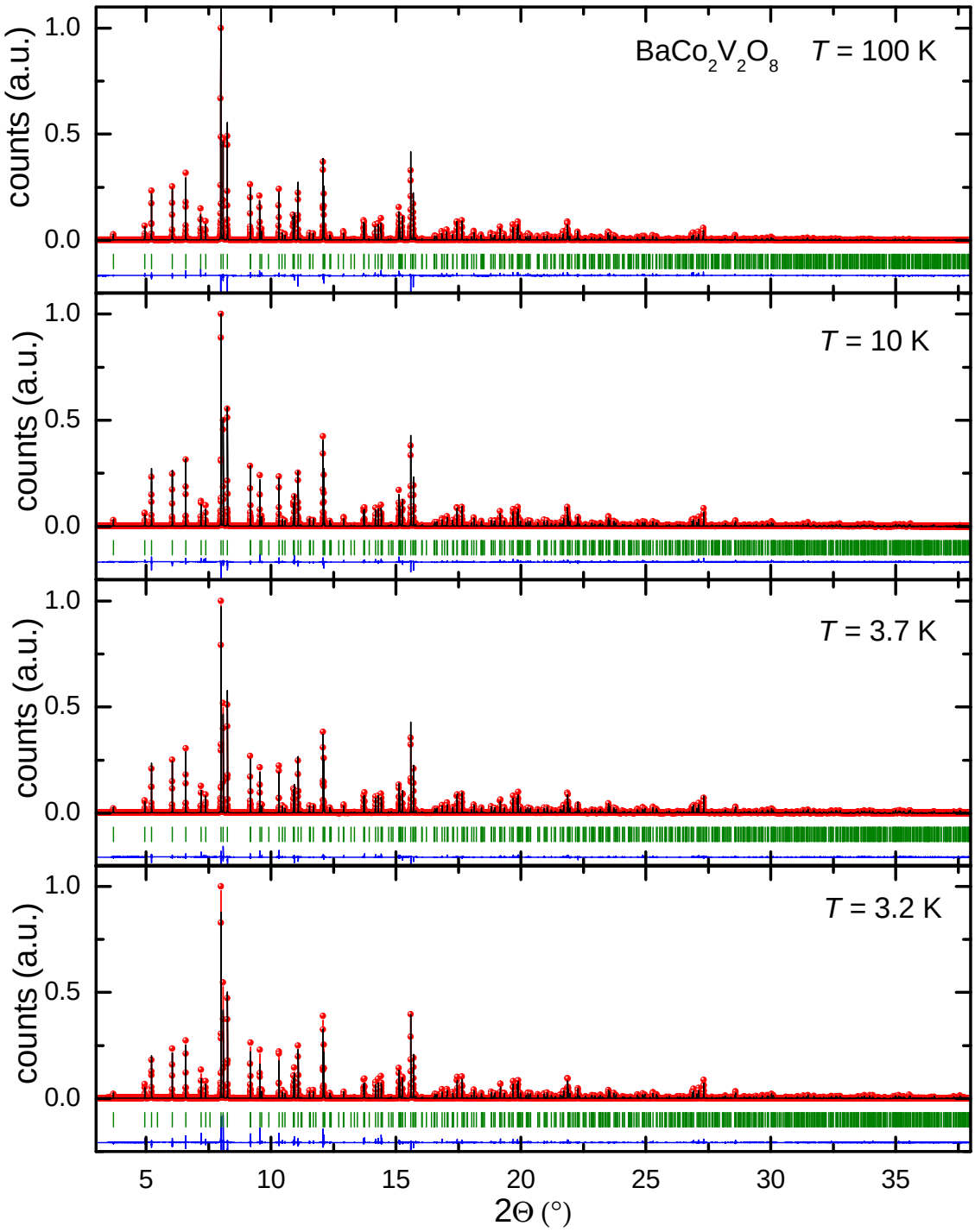

Figure B.3: High resolution XRPD of $BaCo_2V_2O_8$ as a function of temperature. Green bars are calculated Bragg positions, measured data are red points, black line is the fitted intensity, and the blue line gives the difference between measurements and fit.

Table B.2: Summary of forbidden and nuclear reflections that were obtained as a function of temperature and magnetic field in the single crystal neutron diffraction experiment on D23. The integrated intensities and their errors are given for each (temperature/ field combination).

$(h\,k\,l)$	T (K)	$\mu_0 H = 0$ T	6 T	8 T	9 T	10 T	10.5 T	11.5 T
forbidden								
$(0\,0\,\overline{2})$	1.5	1.23 ± 0.01	1.24 ± 0.01	–	1.25 ± 0.01	–	1.27 ± 0.01	1.3 ± 0.01
	7	1.41 ± 0.04	1.46 ± 0.04	1.56 ± 0.05	–	1.5 ± 0.04	–	1.65 ± 0.03
$(0\,1\,\overline{1})$	1.5	2.04 ± 0.05	3.26 ± 0.05	–	5.75 ± 0.05	–	7.06 ± 0.05	7.77 ± 0.05
	7	1.99 ± 0.05	–	–	5.03 ± 0.05	–	–	6.61 ± 0.06
$(0\,1\,\overline{2})$	7	0.73 ± 0.05	0.77 ± 0.05	0.66 ± 0.04	–	0.72 ± 0.04	–	–
$(0\,1\,\overline{3})$	1.5	1.54 ± 0.05	2.1 ± 0.05	–	3.1 ± 0.06	–	3.65 ± 0.05	4.01 ± 0.06
	7	1.67 ± 0.05	–	–	2.71 ± 0.05	–	–	3.16 ± 0.05
$(0\,3\,0)$	7	0.73 ± 0.05	0.77 ± 0.05	0.66 ± 0.04	–	0.72 ± 0.04	–	–
$(0\,\overline{3}\,3)$	1.5	0.4 ± 0.14	1.88 ± 0.2	–	5.04 ± 0.21	–	6.87 ± 0.17	7.95 ± 0.18
	7	0.13 ± 0.15	–	–	3.69 ± 0.18	–	–	5.29 ± 0.23
$(0\,3\,\overline{1})$	1.5	0.97 ± 0.03	1.82 ± 0.04	–	3.25 ± 0.05	–	4.32 ± 0.05	4.7 ± 0.04
	7	1 ± 0.06	1.96 ± 0.05	2.6 ± 0.05	2.74 ± 0.07	3.17 ± 0.06	–	3.57 ± 0.07
$(1\,3\,0)$	1.5	5.82 ± 0.03	6.07 ± 0.03	–	5.57 ± 0.03	–	5.76 ± 0.03	6.3 ± 0.03
	7	6.07 ± 0.06	5.92 ± 0.06	5.71 ± 0.06	–	5.64 ± 0.06	–	–
nuclear								
$(0\,\overline{2}\,0)$	1.5	15.72 ± 0.21	16.45 ± 0.03	–	17.05 ± 0.03	–	17.71 ± 0.04	18.12 ± 0.03
	7	16.18 ± 0.03	17.04 ± 0.16	–	17.18 ± 0.03	–	–	18.09 ± 0.04
$(1\,2\,\overline{3})$	1.5	1.54 ± 0.06	2.31 ± 0.06	–	3.23 ± 0.06	–	3.73 ± 0.07	3.98 ± 0.07
	7	1.3 ± 0.11	–	–	3.03 ± 0.07	–	–	3.74 ± 0.06
$(1\,3\,\overline{2})$	1.5	7.24 ± 0.03	7.79 ± 0.04	–	8.21 ± 0.04	5.64 ± 0.06	–	8.94 ± 0.04
	7	7.31 ± 0.03	–	–	–	–	8.63 ± 0.04	8.85 ± 0.04
$(1\,1\,\overline{2})$	1.5	10.29 ± 0.22	15.56 ± 0.26	20.19 ± 0.29	22.91 ± 0.29	24.88 ± 0.31	25.68 ± 0.31	–
	7	10.76 ± 0.23	15.49 ± 0.26	18.63 ± 0.28	20.46 ± 0.3	21.03 ± 0.3	22.52 ± 0.29	23.08 ± 0.16

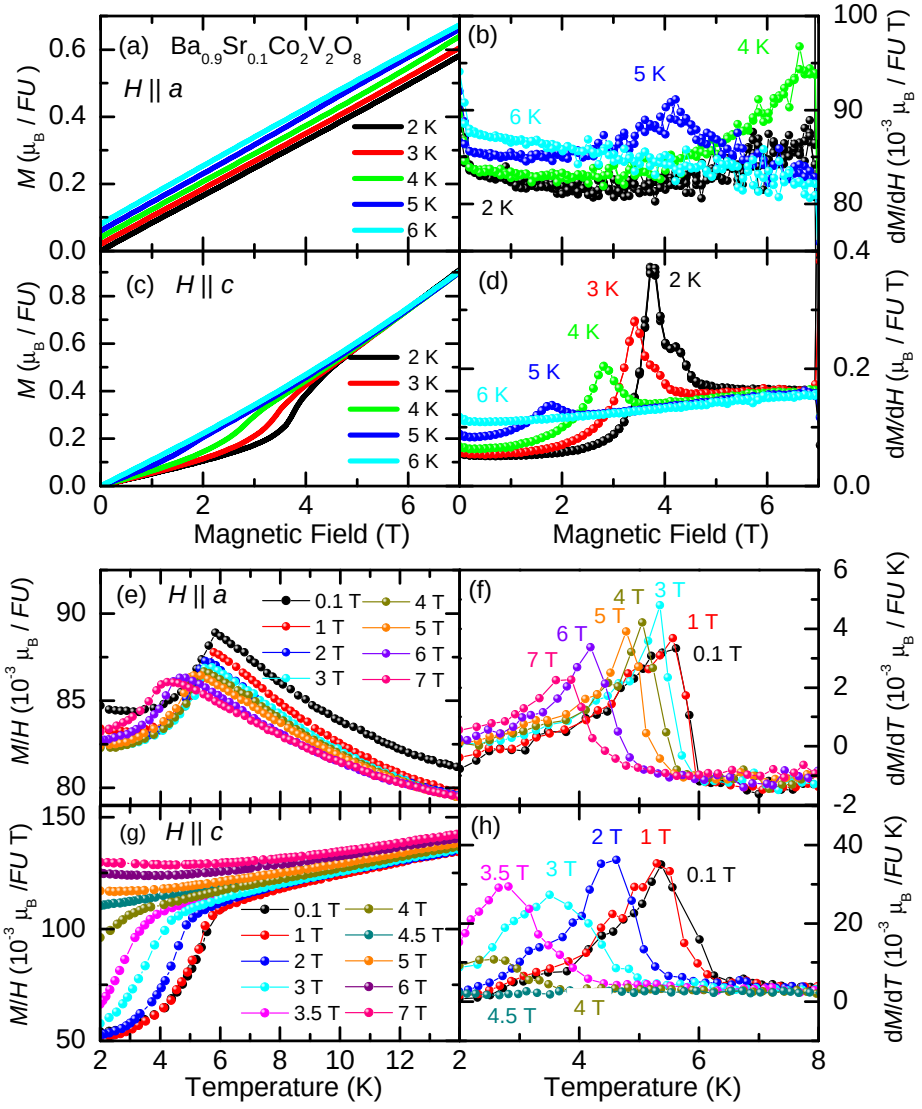

Figure B.4: Field- (a)-(d) and temperature- (e)-(h) dependent magnetization of $Ba_{0.9}Sr_{0.1}Co_2V_2O_8$ for magnetic fields $H \,||\, a$ and $H \,||\, c$ measured in the SQUID and VSM setups, respectively. The curves in (a) are shifted with respect to each other for clarity.

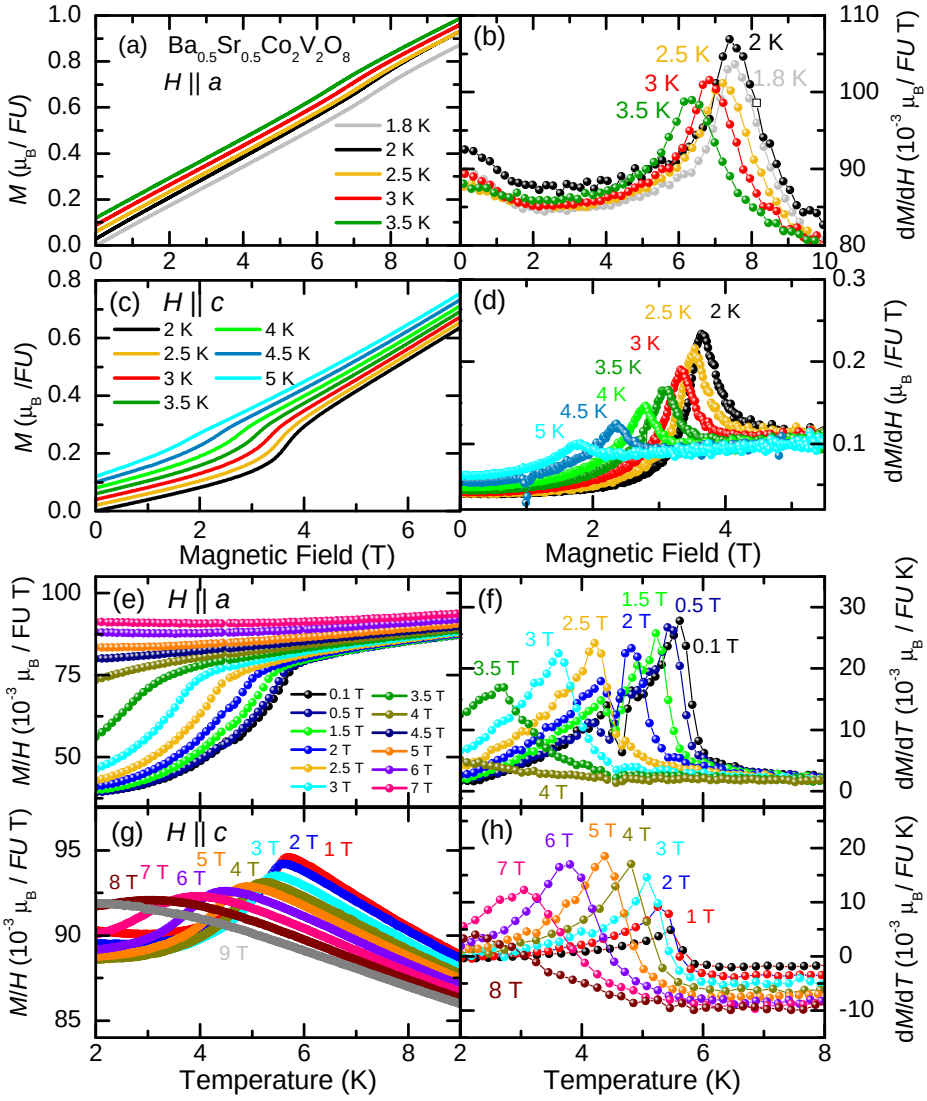

Figure B.5: Field- (a)-(d) and temperature- (e)-(h) dependent magnetization of $Ba_{0.5}Sr_{0.5}Co_2V_2O_8$ for magnetic fields $H \,||\, a$ and $H \,||\, c$ measured in the SQUID and VSM setups, respectively. The curves in (a) and (b) are shifted with respect to each other for clarity.

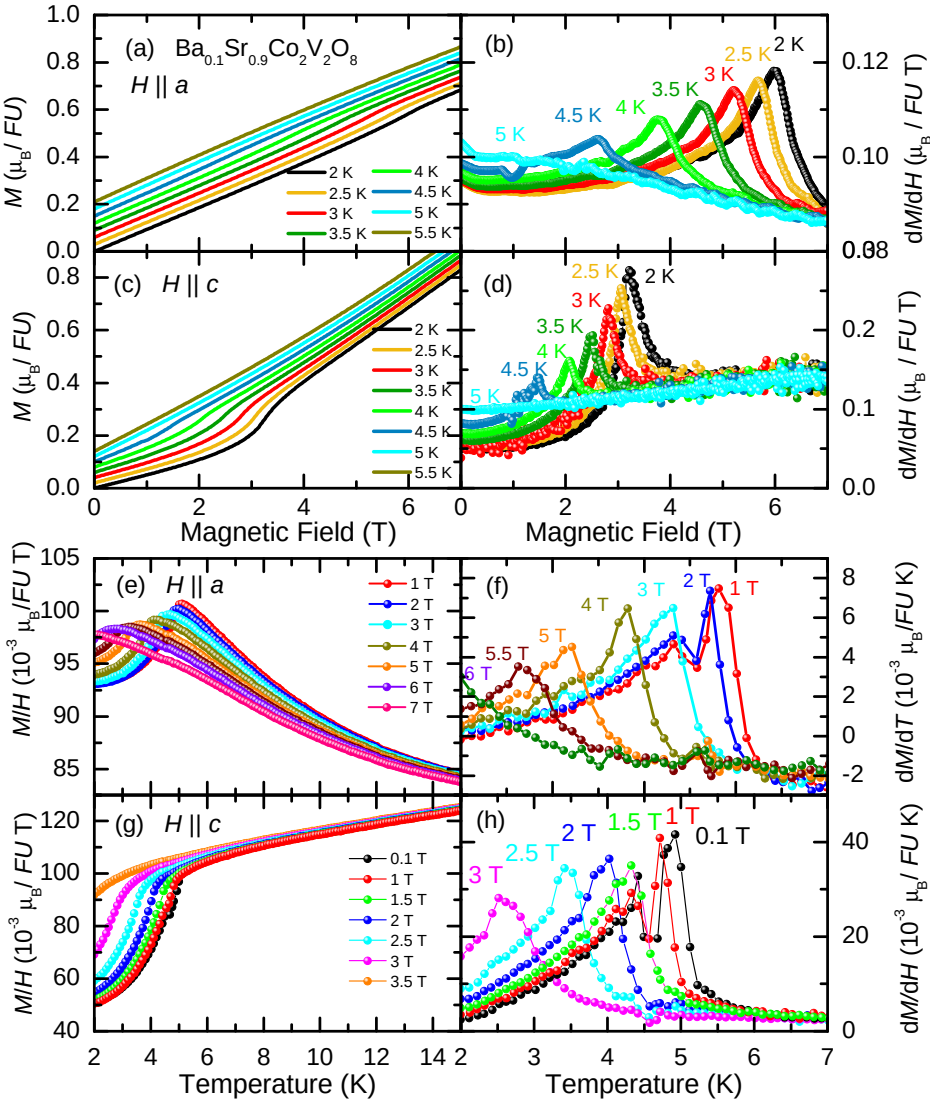

Figure B.6: Field- (a)-(d) and temperature- (e)-(h) dependent magnetization of $Ba_{0.1}Sr_{0.9}Co_2V_2O_8$ for magnetic fields $H \,||\, a$ and $H \,||\, c$ measured in the SQUID and VSM setups, respectively. The curves in (a) and (c) are shifted with respect to each other for clarity.

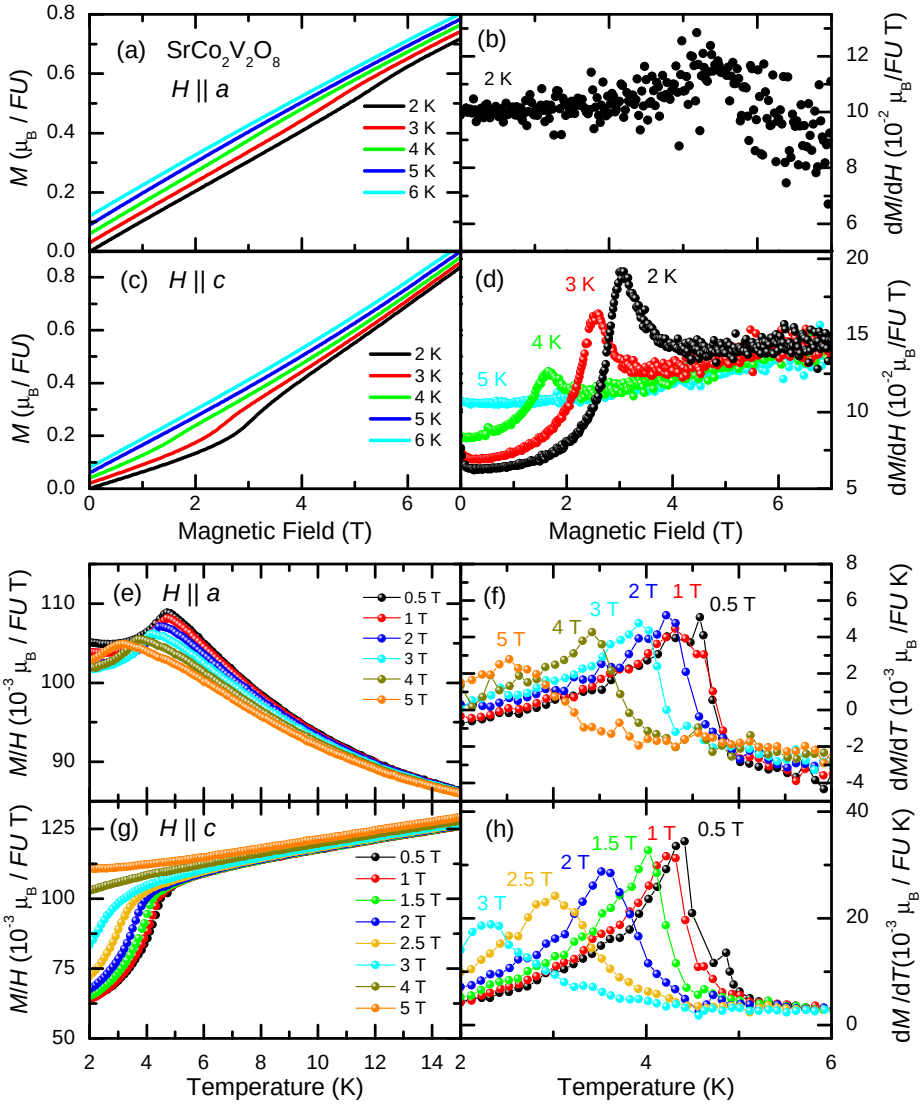

Figure B.7: Field- (a)-(d) and temperature- (e)-(h) dependent magnetization of $SrCo_2V_2O_8$ for magnetic fields $H \,||\, a$ and $H \,||\, c$ measured in the SQUID. The curves in (a) and (c) are shifted with respect to each other for clarity.

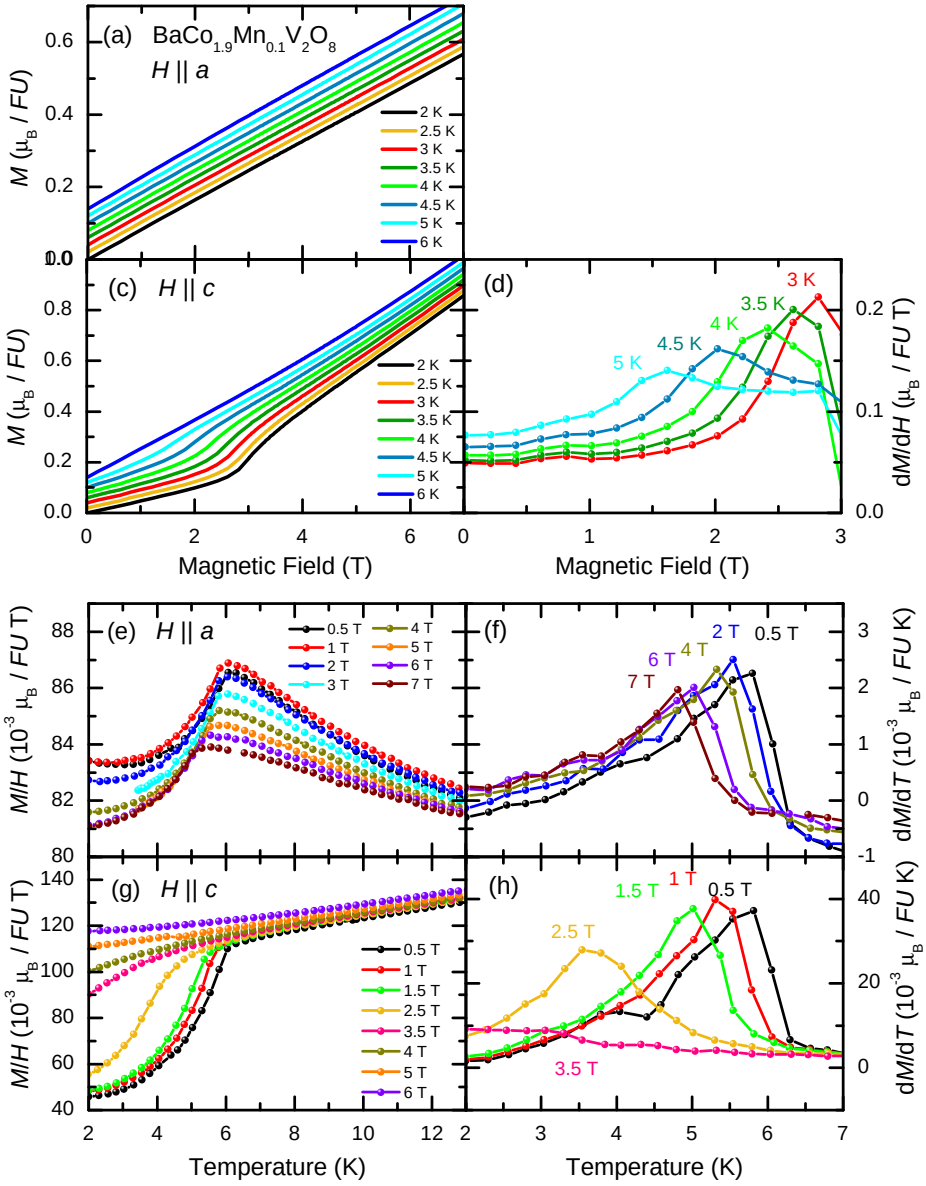

Figure B.8: Field- (a)-(d) and temperature- (e)-(h) dependent magnetization of $BaCo_{1.9}Mn_{0.1}V_2O_8$ for magnetic fields $H \,||\, a$ and $H \,||\, c$ measured in the SQUID. The curves in (a) and (c) are shifted with respect to each other for clarity.

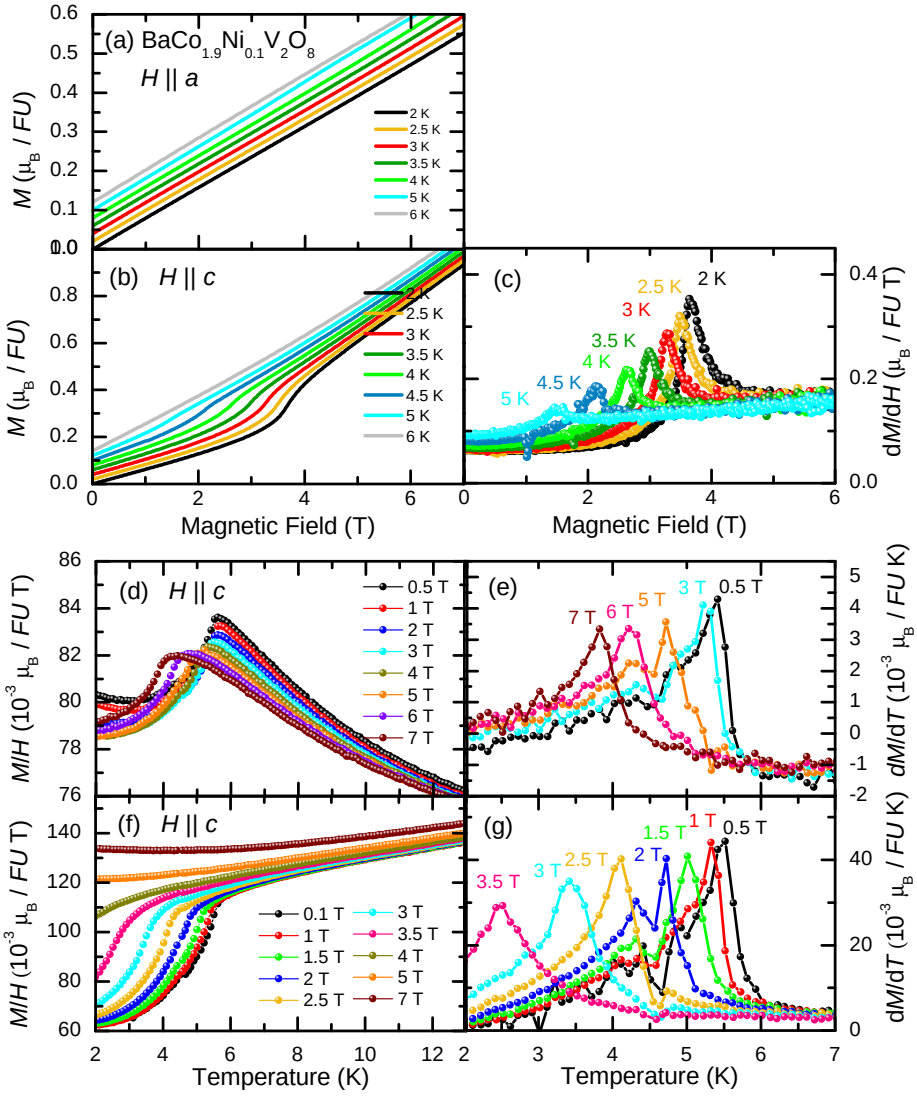

Figure B.9: Field- (a)-(c) and temperature- (d)-(g) dependent magnetization of $BaCo_{1.9}Ni_{0.1}V_2O_8$ for magnetic fields $H \,||\, a$ and $H \,||\, c$ measured in the SQUID. The curves in (a) and (b) are shifted with respect to each other for clarity.

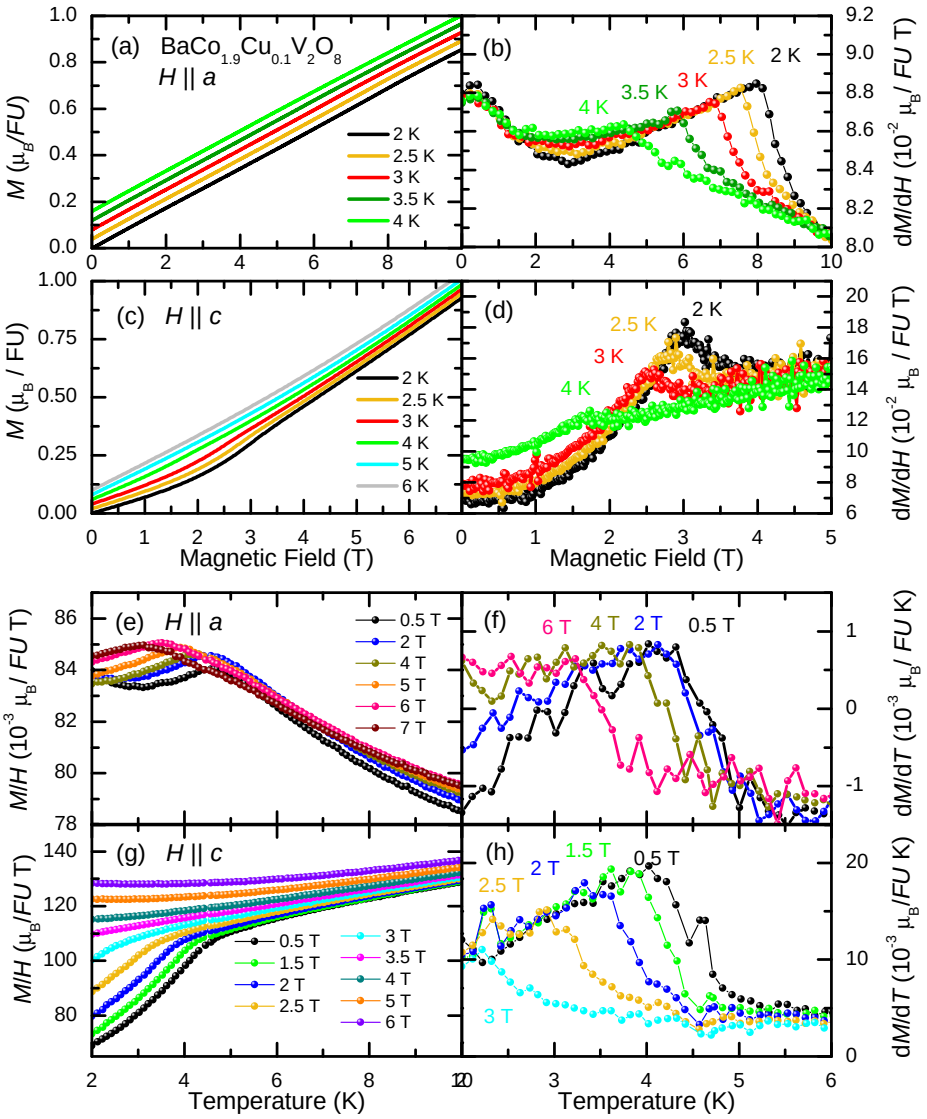

Figure B.10: Field- (a)-(d) and temperature- (e)-(h) dependent magnetization of $BaCo_{1.9}Cu_{0.1}V_2O_8$ for magnetic fields $H \,||\, a$ and $H \,||\, c$ measured in the VSM and the SQUID, respectively. The curves in (a) and (c) are shifted with respect to each other for clarity.

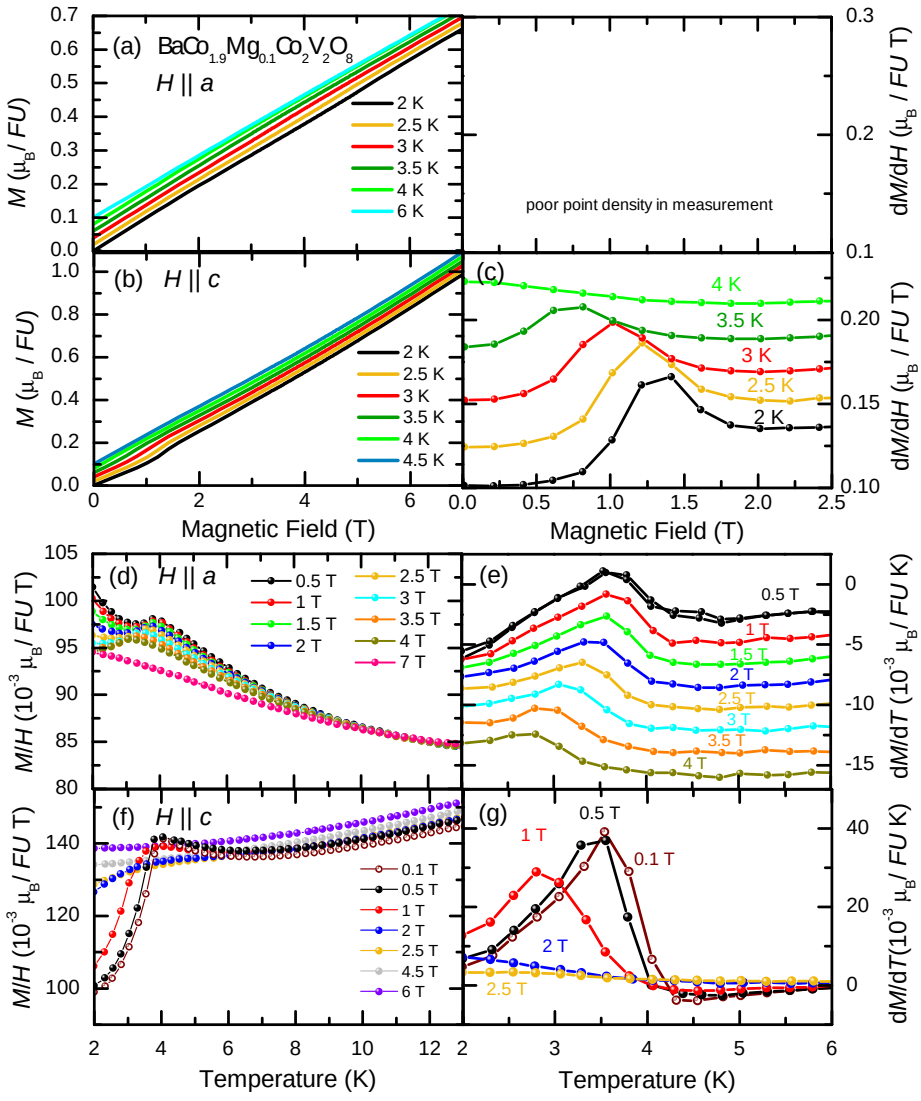

Figure B.11: Field- (a)-(c) and temperature- (d)-(g) dependent magnetization of $BaCo_{1.9}Mg_{0.1}V_2O_8$ for magnetic fields $H \,||\, a$ and $H \,||\, c$ measured in the SQUID. The curves in (a) and (b) are shifted with respect to each other for clarity.

List of Figures

List of Tables

Bibliography

[1] R. Schrott, *Tropen. Über das Erhabene* (Fischer, 2002).

[2] H.-J. Mikeska and A. K. Kolezhuk, *Quantum Magnetism*, edited by U. Schollwöck, J. Richter, D. J. Farnell, and R. F. Bishop, Lecture Notes in Physics (Springer Berlin Heidelberg, 2004) pp. 1–83.

[3] N. D. Mermin and H. Wagner, Physical Review Letters **17**, 1133 (1966).

[4] S. Blundell, *Magnetism in Condensed Matter* (Oxford University Press, 2008).

[5] K. Everschor-Sitte, Ph.D. thesis, Universität zu Köln (2012).

[6] F. Anfuso, M. Garst, A. Rosch, O. Heyer, T. Lorenz, C. Rüegg, and K. Krämer, Physical Review B **77**, 235113 (2008).

[7] K. Kudo, S. Ishikawa, T. Noji, T. Adachi, Y. Koike, K. Maki, S. Tsuji, and K. Kumagai, Journal of Low Temperature Physics **117**, 1689 (1999).

[8] A. V. Sologubenko, K. Giannó, H. R. Ott, U. Ammerahl, and A. Revcolevschi, Physical Review Letters **84**, 2714 (2000).

[9] C. Hess, C. Baumann, U. Ammerahl, B. Büchner, F. Heidrich-Meisner, W. Brenig, and A. Revcolevschi, Physical Review B **64**, 184305 (2001).

[10] M. Hase, I. Terasaki, and K. Uchinokura, Physical Review Letters **70**, 3651 (1993).

[11] I. U. Heilmann, G. Shirane, Y. Endoh, R. J. Birgeneau, and S. L. Holt, Physical Review B **18**, 3530 (1978).

[12] Z. Wang, M. Schmidt, A. K. Bera, A. T. M. N. Islam, B. Lake, A. Loidl, and J. Deisenhofer, Physical Review B **87**, 104405 (2013).

[13] A. K. Bera, B. Lake, A. T. M. N. Islam, B. Klemke, E. Faulhaber, and J. M. Law, Physical Review B **87**, 224423 (2013).

[14] M. Norman, Journal of Superconductivity and Novel Magnetism **25**, 2131 (2012).

[15] R. Wichmann and H. Müller-Buschbaum, Zeitschrift für anorganische und allgemeine Chemie **534**, 153 (1986).

[16] Z. He, T. Taniyama, T. Kyômen, and M. Itoh, Physical Review B **72**, 172403 (2005).

[17] M. von Postel and H. Müller-Buschbaum, Zeitschrift für anorganische und allgemeine Chemie **615**, 97 (1992).

[18] Z. He, Y. Ueda, and M. Itoh, Solid State Communications **141**, 22 (2007).

[19] S. Niesen, O. Heyer, T. Lorenz, and M. Valldor, Journal of Magnetism and Magnetic Materials **323**, 2575 (2011).

[20] M. Valldor, O. Heyer, A. C. Komarek, A. Senyshyn, M. Braden, and T. Lorenz, Physical Review B **83**, 024418 (2011).

[21] T. Smith and S. A. Friedberg, Physical Review **176**, 660 (1968).

[22] V. Tkáč, K. Tibenská, a. Orendáčová, M. Orendáč, J. Šebek, V. Sechovský, a. G. Anders, V. Pavlík, and a. Feher, Physica Status Solidi (B) **248**, 2834 (2011).

[23] S. K. Niesen, G. Kolland, M. Seher, O. Breunig, M. Valldor, M. Braden, B. Grenier, and T. Lorenz, Physical Review B **87**, 224413 (2013).

[24] E. Canévet, B. Grenier, M. Klanjšek, C. Berthier, M. Horvatić, V. Simonet, and P. Lejay, Physical Review B **87**, 054408 (2013).

[25] Z. He, T. Taniyama, and M. Itoh, Physical Review B **73**, 6 (2006).

[26] S. Eggert, I. Affleck, and M. D. Horton, Physical Review Letters **89**, 047202 (2002).

[27] S. Eggert and I. Affleck, Journal of Magnetism and Magnetic Materials **272-276**, E647 (2004).

[28] E. Ising, Zeitschrift für Physik **31**, 253 (1925).

[29] D. Baeriswyl and L. Degiorgi, eds., *Strong Interactions in Low Dimensions*, Physics and Chemistry of Materials with Low-Dimensional Structures (Kluwer Academic Publishers, 2004).

[30] P. Lemmens, G. Guntherodt, and C. Gros, Physics Reports **375**, 1 (2003).

[31] D. Bitko, T. F. Rosenbaum, and G. Aeppli, Physical Review Letters **77**, 940 (1996).

[32] A. Kinross, M. Fu, T. Munsie, H. Dabkowska, G. Luke, S. Sachdev, and T. Imai, Physical Review X **4**, 031008 (2014).

[33] S. Scharffe, Ph.D. thesis, Universität zu Köln (in progress).

[34] M. Vojta, Physik Journal **1**, 55 (2002).

[35] M. Vojta, Physik Journal **13**, 23 (2014).

[36] L. D. Carr, *Understanding Quantum Phase Transitions*, edited by L. Carr, Condensed Matter Physics (CRC Press, 2011).

[37] S. Sachdev, *Quantum Phase Transitions* (Cambridge University Press, 2011).

[38] P. Warzanowski, Bachelor thesis, Universität zu Köln (2014).

[39] http://clip.berlios.de/ (2014).

[40] G. Hölzer, M. Fritsch, M. Deutsch, J. Härtwig, and E. Förster, Physical Review A **56**, 4554 (1997).

[41] (2014), http://icsd.rrz.uni-koeln.de/icsd/.

[42] J. Rodríguez-Carvajal, Physica B: Condensed Matter **192**, 55 (1993).

[43] http://www.esrf.eu/id22 (2014).

[44] http://www.esrf.eu/UsersAndScience/Experiments/CRG/BM28 (2014).

[45] S. Brown, L. Bouchenoire, D. Bowyer, J. Kervin, D. Laundy, M. Longfield, D. Mannix, D. Paul, A. Stunault, P. Thompson, M. Cooper, C. Lucas, and W. Stirling, Journal of Synchrotron Radiation **8**, 1171 (2001).

[46] T. Brückel, G. Heger, D. Richter, and R. Zorn, eds., *Neutron Scattering. Lectures of the Laboratory Course*, Matter and Materials (Forschungszentrum Jülich, 2005).

[47] A.-J. Dianoux and G. Lander, eds., *Neutron Data Booklet* (Institut Laue-Langevin, 2003).

[48] G. Shirane, S. Shapiro, and J. Tranquada, eds., *Neutron Scattering with a Triple-Axis Spectrometer- Basic Techniques* (Cambridge University Press, 2004).

[49] http://www.ill.eu/d23 (2014).

[50] D. Löwen, Diploma thesis, Universität zu Köln (2011).

[51] S. Scharffe, Diploma thesis, Universität zu Köln (2012).

[52] O. Breunig, Diploma thesis, Universität zu Köln (2011).

[53] G. Kolland, Ph.D. thesis, Universität zu Köln (2012).

[54] P. Carruthers, Review of Modern Physics **33**, 92 (1961).

[55] G. Brändli and R. Griessen, Cryogenics **13**, 299 (1973).

[56] R. Pott, Diploma thesis, Universität zu Köln (1977).

[57] O. Heyer, Diploma thesis, Universität zu Köln (2005).

[58] J. Rohrkamp, Diploma thesis, Universität zu Köln (2007).

[59] M. Seher, Diploma thesis, Universität zu Köln (2012).

[60] J. Hulliger, Angewandte Chemie **106**, 151 (1994).

[61] F. Kohlrausch, *Praktische Physik 2* (Teubner Verlag, 2012).

[62] T. Duffar, ed., *Crystal Growth Processes Based on Capillarity. Czochralski, Floating Zone, Shaping and Crucible Techniques* (John Wiley & Sons Ltd., 2010).

[63] G. Dhanaraj, K. Byrappa, V. Prasad, and M. Dudley, eds., *Springer Handbook of Crystal Growth* (Springer, 2010).

[64] K. A. Jackson, *Kinetic Processes. Crystal Growth, Diffusion, and Phase Transitions in Materials* (WILEY-VCH Verlag GmbH & Co. KGaA, Weinheim, 2004).

[65] http://webelements.com/ (2014).

[66] T. Hahn, ed., *International Tables for Crystallography*, 5th ed., Vol. A: Space-group symmetry (Springer, 2005).

[67] H. Wondratschek and U. Müller, eds., *International Tables for Crystallography*, 1st ed., Vol. A1: Symmetry relations between space groups (Springer, 2004).

[68] W. Kleber, *Einführung in die Kristallographie*, 18th ed., edited by H.-J. Bautsch and J. Bohm (Verlag Technik, 1998).

[69] Z. Dauter and M. Jaskolski, Journal of Applied Crystallography **43**, 1150 (2010).

[70] R. D. Shannon, Acta Crystallographica **A2**, 751 (1976).

[71] D.-G. Chen, W.-D. Cheng, D.-S. Wu, H. Zhang, Y.-C. Zhang, Y.-J. Gong, and Z.-G. Kan, Journal of Solid State Chemistry **177**, 3927 (2004).

[72] E. Murashova, Y. Velikodnyi, and V. Trunov, Zhurnal Neoganicheskoi Khimii **34**, 1388 (1989).

[73] R. Vogt and H. Müller-Buschbaum, Zeitschrift für Anorganische und Allgemeine Chemie **591**, 167 (1990).

[74] H.-J. Koo and M.-H. Whangbo, Inorganic Chemistry **45**, 4440 (2006).

[75] Z. He, T. Kyômen, and M. Itoh, Physical Review B **69**, 220407 (2004).

[76] Z. He, T. Kyômen, and M. Itoh, Journal of Crystal Growth **274**, 486 (2005).

[77] R. Wichmann and M. B. H., Revue de Chimie Minérale **23**, 1 (1986).

[78] B. Pahari, K. Ghoshray, R. Sarkar, B. Bandyopadhyay, and A. Ghoshray, Physical Review B **73**, 012407 (2006).

[79] Y. Uchiyama, Y. Sasago, I. Tsukada, K. Uchinokura, a. Zheludev, T. Hayashi, N. Miura, and P. Böni, Physical Review Letters **83**, 632 (1999).

[80] A. Zorko, Ph.D. thesis, University of Ljubljana (2004).

[81] N. Tsujii, H. Suzuki, H. Kitazawa, and G. Kido, Physical Review B **72**, 104402 (2005).

[82] R. Wichmann and H. Müller-Buschbaum, Revue de Chimie Minérale **21**, 824 (1984).

[83] N. Rogado, Q. Huang, J. Lynn, A. P. Ramirez, D. Huse, and R. J. Cava, Physical Review B **65**, 144443 (2002).

[84] Z. He, D. Fu, T. Kyômen, T. Taniyama, and M. Itoh, Chemistry of Materials **17**, 2924 (2005).

[85] Z. He, T. Taniyama, and M. Itoh, Journal of Crystal Growth **289**, 734 (2006).

[86] P. Lejay, E. Canevet, S. Srivastava, B. Grenier, M. Klanjsek, and C. Berthier, Journal of Crystal Growth **317**, 128 (2011).

[87] D. Osterloh and H. Müller Buschbaum, Zeitschrift für Naturforschung B **49**, 923 (1994)).

[88] Z. He, T. Taniyama, and M. Itoh, Journal of Crystal Growth **293**, 458 (2006).

[89] Z. He, T. Taniyama, M. Itoh, J.-I. Yamaura, and Y. Ueda, Solid State Communications **141**, 667 (2007).

[90] Z. He, Y. Ueda, and M. Itoh, Journal of Solid State Chemistry **180**, 1770 (2007).

[91] Z. He, Y. Ueda, and M. Itoh, Solid state communications **142**, 404 (2007).

[92] S. Niesen, Diploma thesis, Universität zu Köln (2009).

[93] G. J. Redhammer, G. Roth, W. Treutmann, W. Paulus, G. André, C. Pietzonka, and G. Amthauer, Journal of Solid State Chemistry **181**, 3163 (2008).

[94] http://www.ill.eu/d2b (2014).

[95] private communication.

[96] S. Kimura, K. Okunishi, M. Hagiwara, K. Kindo, Z. He, T. Taniyama, M. Itoh, and K. Watanabe, Journal of the Physical Society of Japan **82**, 033706 (2013).

[97] M. E. Fisher, American Journal of Physics **32**, 343 (1964).

[98] Y. Kim, M. Greven, U.-J. Wiese, and R. Birgeneau, The European Physical Journal B **4**, 291 (1998).

[99] B. Bauer, L. Carr, H. Evertz, A. Feiguin, J. Freire, S. Fuchs, L. Gamper, J. Gukelberger, E. Gull, S. Guertler, A. Hehn, R. Igarashi, S. Isakov, D. Koop, P. Ma, P. Mates, H. Matsuo, O. Parcollet, G. Pawlowski, J. Picon, L. Pollet, E. Santos, V. Scarola, U. Schollwöck, C. Silva, B. Surer, S. Todo, S. Trebst, M. Troyer, M. Wall, P. Werner, and S. Wessel, Journal of Statistical Mechanics , 05001 (2011).

[100] A. Bera, B. Lake, W.-D. Stein, and S. Zander, Physical Review B **89**, 094402 (2014).

[101] Y. Ideta, Y. Kawasaki, Y. Kishimoto, T. Ohno, Y. Michihiro, Z. He, Y. Ueda, and M. Itoh, Physical Review B **86**, 094433 (2012).

[102] S. Kimura, H. Yashiro, M. Hagiwara, O. Okunishi, K. Kindo, Z. He, T. Taniyama, and M. Itoh, Journal of Physics: Conference Series **51**, 99 (2006).

[103] Z. He, T. Taniyama, and M. Itoh, Applied Physics Letters **88**, 132504 (2006).

[104] Z. Zhao, X. Liu, Z. He, X. Wang, C. Fan, W. Ke, Q. Li, L. Chen, X. Zhao, and X. Sun, Physical Review B **85**, 1 (2012).

[105] S. Kimura, T. Takeuchi, O. Okunishi, M. Hagiwara, Z. He, K. Kindo, T. Taniyama, and M. Itoh, Physical Review Letters **100**, 057202 (2008).

[106] S. Kimura, M. Matsuda, T. Masuda, S. Hondo, K. Kaneko, N. Metoki, M. Hagiwara, T. Takeuchi, K. Okunishi, Z. He, K. Kindo, T. Taniyama, and M. Itoh, Physical Review Letters **101**, 207201 (2008).

[107] S. Kimura, T. Takeuchi, M. Hagiwara, K. Okunishi, Z. He, T. Taniyama, and M. Itoh, Journal of Physics: Conference Series **150**, 042090 (2009).

[108] S. Kimura, Y. Narumi, N. Terada, Y. Tanaka, M. Iwaki, K. Katsumata, M. Hagiwara, K. Kindo, Z. He, T. Taniyama, M. Itoh, H. Toyokawa, T. Ishikawa, and H. Kitamura, Journal of the Physical Society of Japan **79**, 043706 (2010).

[109] Y. Kawasaki, J. Gavilano, L. Keller, J. Schefer, N. Bech Christensen, A. Amato, T. Ohno, Z. Kishimoto, Y.and He, Y. Ueda, and M. Itoh, Physical Review B **83**, 064421 (2011).

[110] H. Yamaguchi, S. Yasin, S. Zherlitsyn, K. Omura, S. Kimura, S. Yoshii, K. Okunishi, Z. He, T. Taniyama, M. Itoh, and M. Hagiwara, Journal of the Physical Society of Japan **80**, 033701 (2011).

[111] M. Klanjšek, M. Horvatić, C. Berthier, H. Mayaffre, E. Canévet, B. Grenier, P. Lejay, and E. Orignac, arXiv:1202.6374v1 cond-mat.str-el (2012).

[112] C. Kuo, C. Lue, Z. He, and M. Itoh, Solid State Communications **149**, 341 (2009).

[113] P. Chandra and B. Doucot, Physical Review B **38**, 9335(R) (1988).

[114] R. Melzi, P. Carretta, A. Lascialfari, M. Mambrini, M. Troyer, P. Millet, and F. Mila, Physical Review B **85**, 1318 (2000).

[115] http://pymca.sourceforge.net (2014).

[116] T. Lorenz, U. Ammerahl, T. Auweiler, B. Büchner, A. Revcolevschi, and G. Dhalenne, Physical Review B **55**, 5914 (1997).

[117] T. Lorenz, B. Büchner, P. H. M. van Loosdrecht, F. Schönfeld, G. Chouteau, A. Revcolevschi, and G. Dhalenne, Physical Review Letters **81**, 148 (1998).

[118] T. Lorenz, Ph.D. thesis, Universität zu Köln (1998).

[119] B. Büchner, T. Lorenz, R. Walter, H. Kierspel, A. Revcolevschi, and G. Dhalenne, Physical Review B **59**, 6886 (1999).

[120] K. Okunishi and T. Suzuki, Physical Review B **76**, 224411 (2007).

[121] K. Okunishi and T. Tanabe, Journal of Physics: Conference Series **200**, 022043 (2010).

[122] F. Pobell, *Matter and Methods at Low Temperatures* (Springer, 2007).

[123] L. Zhu, M. Garst, A. Rosch, and Q. Si, Physical Review Letters **91**, 066404 (2003).

[124] M. Garst and A. Rosch, Physical Review B **72**, 205129 (2005).

[125] T. Lorenz, O. Heyer, M. Garst, F. Anfuso, A. Rosch, C. Rüegg, and K. Krämer, Physical Review Letters **100**, 067208 (2008).

[126] J. Rohrkamp, M. Phillips, M. Turnbull, and T. Lorenz, Journal of Physics: Conference Series **200**, 012169 (2010).

[127] R. Küchler, N. Oeschler, P. Gegenwart, T. Cichorek, K. Neumaier, O. Tegus, C. Geibel, J. A. Mydosh, F. Steglich, L. Zhu, and Q. Si, Physical Review Letters **91**, 066405 (2003).

[128] R. Küchler, P. Gegenwart, K. Heuser, E.-W. Scheidt, G. R. Stewart, and F. Steglich, Physical Review Letters **93**, 096402 (2004).

[129] T. Lorenz, S. Stark, O. Heyer, N. Hollmann, A. Vasiliev, A. Oosawa, and H. Tanaka, Journal of Magnetism and Magnetic Materials **316**, 291 (2007), proceedings of the Joint European Magnetic Symposia.

[130] Y. Tokiwa, T. Radu, C. Geibel, F. Steglich, and P. Gegenwart, Physical Review Letters **102**, 066401 (2009).

[131] Z. He and Y. Ueda, Journal of the Physical Society of Japan **77**, 013703 (2008).

[132] S. K. Niesen, O. Breunig, S. Salm, M. Seher, M. Valldor, P. Warzanowski, and T. Lorenz, Physical Review B **90**, 104419 (2014).

[133] L. Vegard, Zeitschrift für Physik **5**, 17 (1921).

[134] A. R. Denton and N. W. Ashcroft, Physical Review A **43**, 3161 (1991).

[135] Y. Imry, P. Montano, and D. Hone, Physical Review B **12**, 253 (1975).

[136] A. Zvyagin, Low Temperature Physics **32**, 158 (2006).

[137] J. Giapintzakis, J. Androulakis, E. Syskakis, T. P. Papageorgiou, G. Apostolopoulos, S. Thanos, and C. Papastaikoudis, Physica Status Solidi (B) **243**, 1366 (2006).

[138] P. Bak, Reports on Progress in Physics **45**, 587 (1982).

[139] A. Buzdin, M. Kulić, and V. Tugushev, Solid State Communications **48**, 483 (1983).

[140] V. Kiryukhin, B. Keimer, J. Hill, and A. Vigliante, Physical Review Letters **76**, 4608 (1996).

[141] Y. Imry, P. Pincus, and D. Scalapino, Physical Review B **12**, 1978 (1975).

[142] S. J. Mugavero, M. Bharathy, J. McAlum, and H.-C. zur Loye, Solid State Sciences **10**, 370 (2008).

[143] M. Azdouz, B. Manoun, R. Essehli, M. Azrour, L. Bih, S. Benmokhtar, a. A. Hou, and P. Lazor, Journal of Alloys and Compounds **498**, 42 (2010).

[144] M. Mourigal, M. Enderle, B. Fåk, R. K. Kremer, J. M. Law, A. Schneidewind, A. Hiess, and A. Prokofiev, Physical Review Letters **109**, 027203 (2012).

[145] Y. Matiks, P. Horsch, R. K. Kremer, B. Keimer, and A. V. Boris, Physical Review Letters **103**, 187401 (2009).

[146] A. Möller and J. Jainski, Zeitschrift für anorganische und allgemeine Chemie **634**, 1669 (2008).

[147] A. Prokofiev, D. Wichert, and W. Assmus, Journal of Crystal Growth **220**, 345 (2000).

[148] A. Prokofiev, I. Vasilyeva, and W. Assmus, Journal of Crystal Growth **275**, e2009 (2005).

[149] C. Grams, Ph.D. thesis, Universität zu Köln (in progress).

[150] M. Kriener, Ph.D. thesis, Universität zu Köln (2005).

[151] C. Zobel, Ph.D. thesis, Universität zu Köln (2002).

Publications

1. *Antiferromagnetic Heisenberg S=5/2 spin chain compound* $SrMn_2V_2O_8$
   S.K. Niesen, O. Heyer, T. Lorenz, and M. Valldor.
   Journal of Magnetism and Magnetic Materials **323**, 2575 (2011)

2. *Magnetic phase diagrams, domain switching and a quantum phase transition of the quasi-1D Ising-like antiferromagnet* $BaCo_2V_2O_8$
   S.K. Niesen, G. Kolland, M. Seher, O. Breunig, M. Valldor, M. Braden, B. Grenier, and T. Lorenz
   Physical Review B **87**, 224413 (2013)

3. *Substitution effects on the temperature versus magnetic field phase diagrams of the quasi-one-dimensional effective Ising spin-1/2 chain system* $BaCo_2V_2O_8$
   S.K. Niesen, M. Seher, S. Salm, O. Breunig, M. Valldor, P. Warzanowski, and T. Lorenz
   Physical Review B **90**, 104419 (2014)

- Teilnahme an den DPG Frühjahrstagungen in den Jahren 2008-2014
- Aufenthalt an der University of Houston, April-Juni 2011 in der Forschungsgruppe von Prof. Dr. A. Möller
- SCES 2011, Cambridge, UK
- Lotherm Summerschool 2012, Ljubljana, Slowenien

Abstract

Different representatives of the group of quasi-one-dimensional spin-chain compounds $Ba_{1-x}Sr_x(Co_{1-y}M_y)_2V_2O_8$ with M = Mn, Cu, Ni, Mg and (Ba,Sr)$Mn_2V_2O_8$ were synthesized, characterized and their magnetic phase diagrams determined for $H \,||\, c$, $H \,||\, a$ and $H \,||\, [1\,1\,0]$. The tetragonal structure of these compounds consists of screw chains of edge-sharing MO_6 octahedra, where depending on the transition metal M different spin values are realized. The chains are separated by nonmagnetic Ba or Sr and V ions. Large single crystals were grown via the floating-zone method in a mirror furnace employing the twice scanning method.

The single crystal studies of the $S = 5/2$ Heisenberg spin chains $BaMn_2V_2O_8$ ($T_N = 37\,K$) and $SrMn_2V_2O_8$ ($T_N = 42\,K$) reveal a weak positive field dependence. $BaMn_2V_2O_8$ shows a spin-flop transition at $H^{\perp c} \simeq 300\,mT$ as is observed in the susceptibility and the magnetostriction. Deduced from this data a magnetic structure is suggested similar to the magnetic structure of $SrMn_2V_2O_8$ which reveals ferromagnetic planes (spins along $\pm a$) that are ordered antiferromagnetically to each other along the chain direction c [100].

$BaCo_2V_2O_8$ is a quasi-one dimensional effective $S = 1/2$ Ising chain where the antiferromagnetic Ising chains along c have a frustrated inter-chain arrangement leading to the presence of two magnetic domains. Below $T_N = 5.4\,K$ the system undergoes a structural distortion as confirmed by zero-field high-resolution thermal-expansion. Via magnetoelastic coupling the structural domains couple to the magnetic domains and can be manipulated by uniaxial pressure or magnetic fields along a. The expected distortion of the order of 10^{-5} could hardly be detected in high-resolution single crystal X-ray diffraction. For $H \,||\, c$, the Néel ordered state breaks down at $H_c = 3.9\,T$ where an incommensurate (IC) phase is entered in the low-T region [24, 110]. A first order transition is confirmed by a hysteresis in the low-T magnetostriction. Thermal expansion yields very broad anomalies in the low-T region of the high-field curves and the IC-to-paramagnetic phase boundary was traced up to 17 T. For $H \perp c$, an in-plane anisotropy was found with a weak field dependence of T_N for $H \,||\, [1\,1\,0]$, but a complete suppression of T_N at $H^{||\,a} \simeq 10\,T$. Kimura et al. developed a model where a magnetic field $H \,||\, a$ is accompanied by a staggered transverse field component via a staggered g tensor [96]. The predicted breakdown of the magnetic order for $H \,||\, a$ is evidenced in magnetostriction and the collapse of magnetic superstructure peaks in single-crystal neutron diffraction. The field-induced detwinning of the structural/magnetic domains is clearly observed in the different field hysterses of magnetic Bragg peaks being sensitive to different domains. Moreover, the magnetic field

induces an increasing intensity for nuclear reflections due to a uniform ferromagnetic component parallel to to the external field. In addition, the presence of forbidden reflections and their field-dependent behavior are explained by the presence of the staggered moments giving a qualitative confirmation of the Kimura model. Different measures (thermal conductivity, heat capacity, neutron diffraction) show additional anomalies around 6 T whose origin remains unknown.

The investigation of out-of-chain substitutions in the $Ba_{1-x}Sr_xCo_2V_2O_8$ series and of in-chain substitutions in the $BaCo_{1.9}M_{0.1}V_2O_8$ series ($M = \mathrm{Mn, Ni, Cu, Mg}$) yields a preservation of the orthorhombic distortion (below T_N) and of both the Ising and in-plane anisotropy. Judging from these experimental results the magnetic structure is essentially preserved for all substitutions which was recently confirmed for $SrCo_2V_2O_8$ by neutron diffraction [100]. Only indirect hints for a transition from the Néel ordered into an IC phase for $H \,||\, c$ are given by hysteretic magnetostriction curves in the low-T regime. The Sr substitution yields a slight decline of the Ising anisotropy but an increase of the in-plane anisotropy as is reflected in the magnetic phase diagrams. These changes in the anisotropies can be understood by a systematic increase of the distortion of the CoO_6 octahedra with increasing Sr content. Due to the decreasing inter-chain distance with increasing Sr content a change of $J^{\perp}_{\mathrm{NN}}$ and $J^{\perp}_{\mathrm{NNN}}$ is suggested in a way that the resulting frustration increases, which in turn results in a weakened effective inter-chain interaction and a weakly decreasing T_N with increasing Sr content. The substitution of, e.g., Cu and Mg yields a drastic reduction of the ordering temperature. Due to the strong suppression of T_N by Mg in contrast to, e.g., Ni the NN intra-chain interaction is suggested to be the dominant coupling mechanism of the finite chain segments.

Zusammenfassung

Die quasi-eindimensionalen Spinketten Systeme $Ba_{1-x}Sr_x(Co_{1-y}M_y)_2V_2O_8$ mit M = Mn, Cu, Ni, Mg und (Ba ,Sr)$Mn_2V_2O_8$ wurden synthetisiert, charakterisiert und die Magnetfeld-Temperatur Phasendiagramme für die Feldrichtungen $H \,||\, c$, $H \,||\, a$ und $H \,||\, [1\,1\,0]$ erstellt. In der tetragonalen Struktur formen die eckenverknüpften MO_6 Oktaeder Schraubketten entlang c, die durch die nicht-magnetischen Ionen Ba oder Sr und V separiert sind. Das Übergansmetall M bestimmt den Magnetismus dieser Systeme. Große Einkristalle wurden mit dem Schmelzzonenverfahren in einem Spiegelofen hergestellt unter Anwendung der sog. twice-scanning Methode.

Die Einkristallstudie der $S = 5/2$ Heisenberg Spinketten $BaMn_2V_2O_8$ ($T_N = 37\,K$) und $SrMn_2V_2O_8$ ($T_N = 42\,K$) ergibt eine schwach positive Feldabhängigkeit der Ordnungstemperatur. Im Fall von $H \perp c$ zeigt $BaMn_2V_2O_8$ einen Spin-Flop Übergang bei $H^{\perp c} \simeq 300\,mT$ sowohl in der Suszeptibilität, als auch in der Magnetostriktion. Aus diesen Daten leitet sich eine ähnliche Magnetstruktur ab, wie sie für $SrMn_2V_2O_8$ bereits publiziert wurde und welche ferromagnetische Ebenen (mit Spins $\pm a$) beinhaltet, die untereinander antiferromagnetisch entlang c geordnet sind [100].

In der quasi-eindimensionalen effektiven $S = 1/2$ Ising Spinkette $BaCo_2V_2O_8$ weisen die antiferromagnetischen Ising Ketten (entlang c) eine frustrierte Zwischenketten-Anordnung auf, die zu der Ausbildung zweier magnetischer Domänen führt. Druckabhängige Messungen der thermische Ausdehnung im Nullfeld lassen auf eine strukturelle Verzerrung unterhalb von $T_N = 5.4\,K$ schließen, bei der die strukturellen Domänen via magnetoelastischer Kopplung den magnetischen Domänen folgen und welche durch uniaxialen Druck oder Magnetfelder entlang a ausgerichtet werden können. Die erwartete geringe Aufspaltung von 10^{-5} konnte ansatzweise auch in hoch-auflösender Einkristall-Röntgendiffraktion beobachtet werden. Für $H \,||\, c$ bricht der geordnete Zustand bei $H_c = 3.9\,T$ zusammen und geht bei tiefen Temperaturen in eine inkommensurable Phase über [24, 110]. Eine Hysterese in der Magnetostriktion belegt dort einen Phasenübergang erster Art. Die Phasengrenze zwischen paramagnetischem und inkommensurablem Zustand konnte bis zu 17 T verfolgt werden. Für $H \perp c$ wurde eine Anisotropie in der Ebene entdeckt, bei der sich nur eine schwache Feldabhängigkeit von T_N für $H \,||\, [1\,1\,0]$, jedoch ein kompletter Zusammenbruch der Ordnung für $H \,||\, a$ zeigt. Kimura et al. entwickelten ein Modell, bei dem ein Magnetfeld $H \,||\, a$ durch einen alternierenden g Tensor auch transversale (gestaffelte) Feldkomponenten induziert [96]. Der vorhergesagte Zusammenbruch der magnetischen Ordnung für $H \,||\, a \simeq 10\,T$ konnte anhand von Magnetostriktionsmessungen und dem Verschwinden magnetischer Überstrukturreflexe in Neutronen-Diffraktionsexperimenten belegt werden. Auch

die feldinduzierte Entzwilligung der strukturellen/magnetischen Domänen wurde in Form einer Feld-Hysterese in der Intensität von magnetischen Reflexen mikroskopisch nachgewiesen. Zusätzlich verursacht das Magnetfeld einen Intensitätsanstieg einiger nuklearer Reflexe, sowie das Auftreten verbotener Reflexe, deren Feldabhängigkeit durch die gestaffelten Feldkomponenten bestimmt sind, wie sie durch das Modell von Kimura et al. festgelegt sind. Unterschiedliche Messgrößen (Thermische Leitfähigkeit, Wärmekapazität, Neutronen-Diffraktion) weisen zusätzliche Anomalien bei 6 T auf, deren Ursprung bislang ungeklärt ist.

Der Einfluss von Substitutionen auf magnetische und unmagnetische Plätze wurde anhand der $Ba_{1-x}Sr_xCo_2V_2O_8$ und $BaCo_{1.9}M_{0.1}V_2O_8$ (M = Mn, Ni, Cu, Mg) Serien untersucht. Die strukturelle Verzerrung sowie die magnetischen Anisotropien bleiben in allen Systemen nahezu unberührt. Daraus kann man auch auf den Erhalt der magnetischen Struktur schließen, was für $SrCo_2V_2O_8$ bereits gezeigt wurde [100]. Für $H \,||\, a$ weisen Hysteresen in der Tieftemperatur-Magnetostriktion nur indirekt auf einen Übergang von der Néel-Phase zu einer inkommensurablen Ordnung hin. Die Sr-Substitution führt zu einer leichten Reduktion der Ising Anisotropie, jedoch auch zu einer Zunahme der Ansiotropie in der Ebene, was durch einen systematischen Anstieg der Oktaeder-Verzerrung mit zunehmendem Sr-Gehalt verstanden werden kann. Die Reduzierung der Zwischenkettenabstände mit höherem Sr-Gehalt legt eine Veränderung von $J^{\perp}_{\mathrm{NN}}$ und $J^{\perp}_{\mathrm{NNN}}$ nahe, welche die vorhandene Frustration erhöht und somit den Effekt der Zwischenketten-Kopplung stört und die geringe Verringerung von T_{N} erklärt. Die Substitution von beispielsweise Cu und Mg führt hingegen zu einer drastischen Reduzierung von T_{N}. Die starke Unterdrückung von T_{N} für Mg, im Gegensatz zu Ni, identifiziert die NN Wechselwirkung als den dominanten Kopplungsmechanismus der endlichen Kettensegmente.

Erklärung

Ich versichere, dass ich die von mir vorgelegte Dissertation selbständig angefertigt, die benutzten Quellen und Hilfsmittel vollständig angegeben und die Stellen der Arbeit – einschließlich Tabellen, Karten und Abbildungen –, die anderen Werken im Wortlaut oder dem Sinn nach entnommen sind, in jedem Einzelfall als Entlehnung kenntlich gemacht habe; dass diese Dissertation noch keiner anderen Fakultät oder Universität vorgelegen hat; dass sie – abgesehen von den angegebenen Teilpublikationen – noch nicht veröffentlicht worden ist sowie, dass ich eine solche Veröffentlichung vor Abschluss des Promotionsverfahrens nicht vornehmen werde. Die Bestimmungen der Promotionsordnung sind mir bekannt. Die von mir vorgelegte Dissertation ist von Priv.-Doz. Dr. Thomas Lorenz betreut worden.

Köln, 1. Dezember 2014 Sandra Niesen

Danksagung

Ich habe immer gedacht, ich würde eine besonders tolle Danksagung schreiben, aber jetzt ist es 6 Uhr morgens und ich habe die Nacht durch gemacht.
Zuallererst geht der Dank an alle, die inhaltlich viel zu der Arbeit beigetragen haben, an alle Unterstützer, Kollaborationen und Mitdenker, insbesondere meinem Doktorvater und "Chefchen" Thomas und an Martin, den “Alchemisten”, Oliver, dem “Simulator” und natürlich meinen verbrauchten Diplomanden. Dank an die local contacts Béatrice Grenier und Didier Wermeille, an Prof. Angela Möller für die lehrreiche Zeit in Houston. Danke an Prof. Braden und Navid für die Unterstützung in der Welt der Neutronen.
Danke an “meine” Arbeitsgruppe für viel Zusammenhalt und Freude an der Arbeit wie am Leben. Jetzt gerade freue ich mich darauf, dass (hoffentlich) für mich gebastelt wird und ein paar mir lieb gewordene Menschen über mich lästern und alle peinlichen Geschichten ausgraben- fantastisch! Dank an all die Charakterköpfe auf allen Ebenen, Sekretariat, Werkstätten, Studenten, Doktoranden, Profs... Danke meinen Mädels für 20 Jahre Freundschaft durch alle Höhen und Tiefen. Danke an alle meine Eltern und Geschwister und die Ommas und Oppas.
Zuletzt der größte Dank an O für alle Unterstützung, auf jede erdenkliche Art. The story goes on! Aiki, aiki!